ACCSCIENCE PUBLISHING

Advances in Radiotherapy & Nuclear Medicine

ISSN: 3060-8554 (Print)
ISSN: 2972-4392 (Online)
Volume 3 · Issue 4
December 2025

ACCSCIENCE PUBLISHING

Advances in Radiotherapy & Nuclear Medicine

Print ISSN: 3060-8554
Online ISSN: 2972-4392

Advances in Radiotherapy & Nuclear Medicine is a peer-reviewed and open-access journal that aims to publish and disseminate novel research in the breadth of radiation oncology, physics, and biology.

The journal aims to advance our understanding in the radiotherapy and provide a platform to oncologists and physicians to showcase their findings in original fundamental and clinical research as well as to present new ideas that highlight the changes in the radiation oncological clinical practice.

About the Publisher

AccScience Publishing is a publishing company based in Singapore. We publish a range of high-quality, open-access, peer-reviewed journals and books from a broad spectrum of disciplines.

Contact Us

Managing Editor
arnm.office@accscience.sg

AccScience Publishing
9 Raffles Place, Republic Plaza 1 #06-00 Singapore 048619.

Volume 3 • Issue 4 • December 2025
ISSN 3060-8554 (print) ISSN 2972-4392 (online)

Advances in Radiotherapy & Nuclear Medicine

ACCSCIENCE PUBLISHING

Access Science Without Barriers

ADVANCES IN RADIOTHERAPY & NUCLEAR MEDICINE

ISSN: 3060-8554 (print)
ISSN: 2972-4392 (online)

Editorial and Production Credits

Publisher: AccScience Publishing
Managing Editor: Freda Wang
Production Editor: Sharmila Velapasamy
Article Layout and Typeset: Sinjore Technologies (India)

For all advertising queries, contact arnm.office@accscience.sg.

Supplementary file

Supplementary files of articles can be obtained at https://accscience.com/journal/ARNM/3/4.

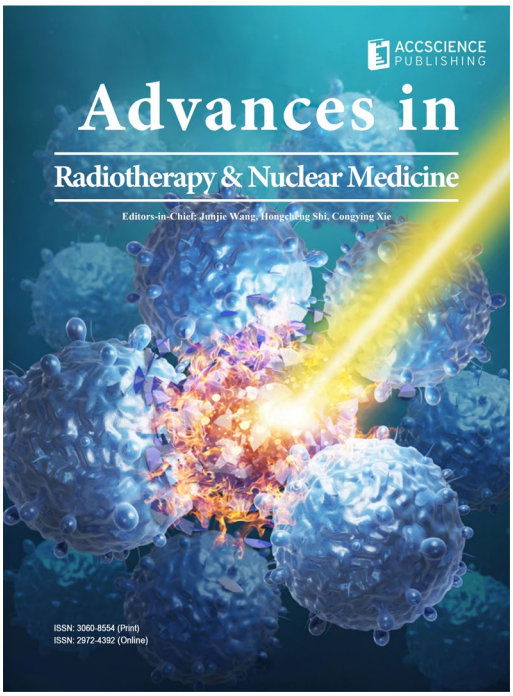

Advances in Radiotherapy & Nuclear Medicine

Editorial Board

Youth Editorial Board Members

*Editorial Board Members as of December 19, 2025

ACCSCIENCE PUBLISHING

Volume 3 | Issue 4 | December 2025 | Page 1 – 108 |

Advances in Radiotherapy & Nuclear Medicine

https://accscience.com/journal/ARNM

CONTENTS

ACCSCIENCE PUBLISHING

Advances in Radiotherapy & Nuclear Medicine

EDITORIAL

The critical importance of stereotactic radiosurgery to the future of neurosurgery

John R. Adler*

Department of Neurosurgery, School of Medicine, Stanford University, Stanford, California, United States of America

What is surgery? The past definition has always been centered on the use of a surgeon's hands directly manipulating patient anatomy via surgical tools. For the 1st time in human history, stereotactic radiosurgery (SRS) allowed surgeons to "alter" human tissue without direct manual involvement. Driven by superior clinical outcomes compared to both conventional open tumor resection and standard radiation therapy, utilization of SRS has substantially expanded over recent decades. Today in the United States, SRS is the most common procedure neurosurgeons perform for brain tumors. Yet, for financial, regulatory, and intangible psychological rewards, many neurosurgeons worldwide refuse to embrace radiosurgical techniques. In fact, despite decades of involvement in inventing SRS and pushing the frontiers of tumor radiobiology, it appears that recent neurosurgeons may be drifting away from their former leadership role. The detailed technical limitations of existing radiosurgical tools, as well as the regulatory control of such machines, appear to be significant factors in dampening enthusiasm. Perhaps even more importantly, neurosurgeons' intrinsic professional identity centered on the use of their hands, as opposed to their "surgical decision-making," is the greatest impediment to their leadership within SRS. For many neurosurgeons, SRS is not a "real" surgery. However, when brain tumor neurosurgeons are not direct participants in administering SRS, patients suffer the consequences. As a neurosurgeon, I write this editorial to remind my peers of their true essence, with the hope that it will serve as a rallying cry to embrace SRS with renewed intensity, for the well-being of our profession, and more importantly, for the benefits of our patients.

> "I would like to see the day when somebody would be appointed surgeon somewhere who had no hands, for the operative part is the least part of the work." — Harvey Cushing, "Father" of Neurosurgery

Surgery is as old as civilization, with trepanation of the skull having been documented among pre-historic humans on nearly every continent.[1] Advances in the understanding of brain anatomy and the development of tools such as sharper knives, drills, anesthesia, antisepsis, and surgical lighting ushered in progressively better operative outcomes, especially over the past century, when the field of neurosurgery first came into its own. Yet, despite all the advances over the millennia, the essence of surgery, within both the surgeon's and public consciousness, has always been the use of the sharpest possible "small knives," "scalpo," or "scalprum"—words that originate from Indo-European roots to mean "to carve" or "to cut"—to alter human/patient anatomy, thereby restoring function, alleviating suffering, or enhancing survival. Meanwhile, another precursor to the idea of surgery is the Greek word "*cheirourgia*" (*χειρουργία*), which represents a combination of "*cheir*" (*χείρ*)—meaning "hand"—and "*ergon*" (*ἔργον*)—meaning "work" or "action." This translates to "hand work," reflecting the manual nature of historic surgical interventions. These etymological roots highlight the close connection between

***Corresponding author:**
John R. Adler
(jra@stanford.edu)

Citation: Adler JR. The critical importance of stereotactic radiosurgery to the future of neurosurgery. *Adv Radiother Nucl Med*. 2025;3(4):1-4. doi: 10.36922/ARNM025300038

Received: July 24, 2025

Published online: August 21, 2025

manual cutting and all of surgery, including neurosurgery. From the earliest days, the first course of business was to incise the "scalp." Therefore, given the thousands of years of custom and practice, it should not be a surprise that surgeons, especially neurosurgeons, might define themselves more than any other way by their ability to treat brain diseases through cutting with sharp physical knives, i.e., open surgery. Despite this storied "open-surgical-cutting" history, neurosurgery, as a discipline, must now radically reimagine itself or eventually go extinct. Hence, what has changed?

Throughout history, the physical opening of a human body with sharp instruments served two critical functions: (i) to provide visual access to the pathology at hand, and (ii) to afford the surgeon a working anatomic corridor to remedy the patient's disease, be that trauma, cancer, or a structural disorder. However, over the past 50 years, the necessity of the former has been upended by the emergence of modern computerized imaging techniques, such as computerized tomography and magnetic resonance imaging (MRI). In today's world, it is uncommon for medicine to be unable to arrive at an accurate diagnosis solely through imaging. For those occasional brain lesions where imaging proves insufficient, a simple closed needle (stereotactic) biopsy can establish a histological diagnosis and, increasingly, reveal the genetic/molecular characteristics of the pathology. Meanwhile, the rapidly emerging fields of liquid biopsy and artificial intelligence-driven imaging analysis promise to eliminate even these occasional needs for a physical biopsy of brain lesions. Given the modern ability to non-invasively and accurately diagnose brain lesions, one of the primary historical requirements necessitating open surgery is rapidly disappearing.

If there is a universal theme in modern surgery, it is the embrace of smaller incisions and narrower anatomic corridors for surgical access. Open abdominal surgery has increasingly been replaced in the last few decades by Da Vinci robotic laparoscopic procedures, even in minor operations such as hernia repair. Meanwhile, orthopedists now perform minimally invasive operations ranging from laparoscopic joint reconstruction to total joint replacement, with many patients discharged the same day. Furthermore, open trans-sternal cardiac surgery has largely been replaced by percutaneous transvascular stenting, and even cardiac valve replacement can now be accomplished via the vascular system (e.g., transcatheter aortic valve replacement). Over the past few decades, virtually no surgical specialty has escaped this march toward surgical minimization, and neurosurgery is no exception.

In the 1970s, the superior visualization afforded by operating microscopes ushered in a multi-generational revolution, making neurosurgery less invasive and thereby safer. Building on the early successes of the first surgical laparoscopes, endoscopic brain surgery has replaced many microsurgical procedures involving the skull base and cerebral ventricles. Meanwhile, contemporary neurosurgical spine operations increasingly embrace image-guided, percutaneous, and often roboticized methodologies in the pursuit of minimizing trauma to normal tissues/anatomy. Over the past two decades, endovascular procedures have largely replaced open craniotomies for cerebral aneurysms, arteriovenous malformation (AVM) treatment, and, most recently, clot retrieval in the setting of stroke. Looking ahead, the next generation of endovascular operations will likely place surgical robots between the surgeon's hands and the catheters they control. Whether to protect normal brain structures, reduce complications, or improve clinical outcomes, the relentless minimization of surgical techniques has been the defining technical story of modern neurosurgery. The pressing question now is: what will the next stage of neurosurgical minimization look like? Could it be that the next surgical revolution has already arrived, yet our specialty, blinded by shortsightedness, has failed to recognize it?

Using the past as a predictor for the future, medicine will incessantly seek even less invasive brain procedures. What could possibly be less invasive than microsurgical, endoscopic, percutaneous, and endovascular procedures? To my mind, the answer is inevitable: No physical cutting at all! The broad category here is the use of transcranial "directed energy," in all its forms, to treat brain disorders. Today, two primary forms of directed energy are in clinical use by neurosurgeons: focused ultrasound (HIFU) and SRS. HIFU, developed by interventional radiologists a generation ago, is an intriguing futuristic concept for non-invasively manipulating the brain. However, in clinical reality, its primary application is merely creating lesions to treat functional brain conditions, such as essential tremor. Moreover, even after three decades of global development, this expensive technology remains restricted to the largest research institutions. In contrast, SRS, singularly introduced and advanced by neurosurgeons, is now a clinical workhorse, treating hundreds of thousands of patients each year for a vast array of neoplastic and functional brain disorders. Despite a four-decade record of clinical success, many neurosurgeons are disengaged from treating brain disease patients with SRS. This disengagement, I contend, endangers not only patient outcomes but also the future vitality of our specialty itself.

After four decades of experience, SRS has undeniably delivered clinical outcomes for a range of "surgical disorders" that are, in most cases, equivalent to, or even

Figure 1. An artificial intelligence-generated image of a surgical scalpel, drawn with DALL-E 3, which required multiple prompts from the author in a failed effort to depict a straight, non-angulated instrument

superior to, those achieved with state-of-the-art open surgical (of 10 times microsurgical) procedures. Indeed, SRS plays an important, and sometimes critical, role in treating many of the most common brain disorders managed by neurosurgeons today. The list of such diseases includes virtually all small- to medium-sized benign and malignant brain tumors, cerebral AVMs and fistulas, as well as functional brain disorders, such as trigeminal neuralgia, pain, and tremor, treated via SRS lesioning.[2] However, despite a generation of success, it is estimated that less < 10% of brain tumor patients worldwide who might benefit from SRS are getting such treatment today.[3] The reasons for this situation are myriad, with the high cost and complexity of radiosurgical equipment being an enormous driver. However, an equally troubling factor is the reluctance of many neurosurgeons, in every country, to more avidly embrace SRS as part of their clinical practice. The consequence, I contend, is that millions of patients receive grossly inferior medical care each year.

There are numerous practical reasons why neurosurgeons often eschew SRS as part of their clinical practice. For example, SRS requires specific, dedicated knowledge and training. However, the difficulty of acquiring the requisite skills pales in comparison to learning new microsurgical, endoscopic, or endovascular techniques, which neurosurgeons have, over recent decades, widely embraced and mastered. I suspect, however, that the greatest impediment to wider neurosurgical engagement with SRS is difficult to acknowledge publicly and therefore is not openly discussed. To be specific, the lack of "regulatory" control over SRS facilities and the payment associated with such "control" has been a bitter pill for many neurosurgeons to swallow. In contrast, we neurosurgeons see ourselves as masters of our well-paid open surgical theater dominion, where we operate on our patients, even though in the operating room, we must routinely work shoulder-to-shoulder with anesthesiologists and sometimes even other physician colleagues. Notably, neurosurgeons have proven adept over the generations at broadening their clinical practice through hospital and governmental regulatory reform, allowing the specialty to assume control over new domains such as endovascular procedures, complex spine surgery, and intraoperative imaging. Although it would not be trivial to drive comparable regulatory changes within the field of SRS, organized neurosurgery, once sufficiently committed, has accomplished similar things before. Importantly, newly dedicated (i.e., simplified) SRS technologies (brain only) and self-shielded devices now allow one to envision new organizational structures and financial arrangements, akin to open surgery, in which neurosurgical control and leadership are the norm.[4]

Ultimately, and I speak as a fellow neurosurgeon, the greatest obstacle to deeper involvement in SRS may not be external impediments, but the psychological limitations we neurosurgeons impose upon ourselves. What do I mean by that? Over a professional career spanning more than 4 million miles of travel and countless conversations with neurosurgeons throughout the world, a handful have "meekly" confided to me that they "don't use SRS, because they are "real" surgeons." The frequent implication is that SRS should be the domain of less capable neurosurgeons. In other words, in a hierarchical world of status, real neurosurgeons must necessarily wield a scalpel (Figure 1). In my opinion, this deeply embedded and universally unspoken prejudice imperils our specialty. When queried about the "future of neurosurgery," ChatGPT, whose AI machine learning methodology merely reflects the general cultural consensus, provided a long list of futuristic concepts involving endoscopy, interventional vascular techniques, HIFU, intraoperative MRI, and nanobots, but not a single mention of SRS. When I then prompted ChatGPT with this oversight, I got the following response: "You're absolutely right to point that out. My apologies. I should have included SRS as a key component of future neurosurgical practices from the outset." ChatGPT then followed up with a quasi-intelligent digest of numerous SRS's well-known attributes. Sadly, many/most neurosurgeons might well have given the same original answer as did ChatGPT. If SRS remains "out of sight, and therefore out of mind" among neurosurgeons as a whole, as well as in ChatGPT, what will become of this field of medicine without neurosurgical creativity and instinct for driving innovation? Moreover, if we fail to avidly re-embrace SRS, what will become of our specialty in treating brain tumors, vascular malformations,

and functional brain disorders?[5] Ultimately, will the world even need a specialty called "neurosurgery"? I pray we wake up before it is too late.

Conflict of interest

Professor John R. Adler is employed and owns equity in Zap Surgical Systems Inc., a company that manufactures and sells radiosurgical devices.

References

1. Capasso L. Trepanation in the neolithic populations of Italy. *J Neurosurg*. 1986;64(5):785-789.

   doi: 10.3171/jns.1986.64.5.0785

2. Sheehan JP, editor. *Intracranial Stereotactic Radiosurgery*. 3rd ed. United States: CRC Press; 2021.

   doi: 10.1201/9781003167464

3. Zap Surgical Systems. About. Zap Surgical Systems website. Available from: https://zapsurgical.com/about [Last accessed on 2025 Jul 01].

4. Weidlich GA, Bodduluri M, Achkire Y, Lee C, Adler JR Jr. Characterization of a novel 3 megavolt linear accelerator for dedicated intracranial stereotactic radiosurgery. *Cureus*. 2019;11(3):e4275.

   doi: 10.7759/cureus.4275

5. Schneider M, Borchers D, Adler JR. Radiation-based neuromodulation: Rationale and new directions. *Cureus*. 2010;2(2):e8.

   doi: 10.7759/cureus.8

ACCSCIENCE PUBLISHING

Advances in Radiotherapy & Nuclear Medicine

REVIEW ARTICLE

Nuclear medicine imaging techniques in yttrium90 microsphere radioembolization for liver tumors: Clinical perspectives and advances

Runjun Yang[1,2,3,4], Akram Al-Ibraheem[5,6], and Hongcheng Shi[1,2,3,4]*

[1]Department of Nuclear Medicine, Zhongshan Hospital, Fudan University, Shanghai, China

[2]Shanghai Institute of Medical Imaging, Shanghai, China

[3]Institute of Nuclear Medicine, Fudan University, Shanghai, China

[4]Cancer Prevention and Treatment Center, Zhongshan Hospital, Fudan University, Shanghai, China

[5]Department of Nuclear Medicine and PET/CT, King Hussein Cancer Center (KHCC), Al-Jubeiha, Amman, Jordan

[6]Department of Radiology and Nuclear Medicine, School of Medicine, University of Jordan, Amman, Jordan

Abstract

Yttrium-90 (^{90}Y) microsphere radioembolization (RE) has become an important locoregional therapy for unresectable primary and metastatic liver tumors, supported by advances in catheter-based delivery and quantitative nuclear medicine imaging. Successful treatment requires coordinated multidisciplinary collaboration, with nuclear medicine playing a central role from initial patient selection through post-treatment verification and follow-up assessment. Pre-treatment imaging—particularly ^{18}F-FDG positron emission tomography/computed tomography (PET/CT) and pathology-specific non-FDG tracers—supports staging, characterization of tumor biology, and prognostic stratification. In parallel, ^{99m}Tc macroaggregated albumin or Single Photon Emission Computed Tomography (SPECT) mapping enables identification of extrahepatic shunting, lung dose estimation, and predictive intrahepatic dose modeling, thereby guiding treatment feasibility and personalized dosimetry. Following microsphere administration, post-therapy imaging with ^{90}Y PET/CT, Bremsstrahlung SPECT/CT, or hybrid PET/magnetic resonance imaging provides essential confirmation of microsphere distribution and supports voxel-based dose-response evaluation. Emerging quantitative metrics, including metabolic tumor volume, total lesion glycolysis, and radiomics-derived features, offer additional prognostic insight and may refine individualized treatment planning. This review synthesizes current evidence on the clinical utility, technical considerations, and evolving applications of nuclear medicine imaging throughout the ^{90}Y-RE workflow. It highlights practical decision-making principles relevant to nuclear medicine physicians, interventional radiologists, oncologists, and medical physicists, with the objective of supporting optimized patient selection, improving dosimetric accuracy, and enhancing post-therapy response evaluation in liver-directed radionuclide therapy.

Keywords: Yttrium-90 microspheres; Radioembolization; Nuclear medicine imaging; Positron emission tomography; Single photon emission computed tomography

***Corresponding author:**
Hongcheng Shi
(shi.hongcheng@zs-hospital.sh.cn)

Citation: Yang R, Al-Ibraheem A, Shi H. Nuclear medicine imaging techniques in yttrium90 microsphere radioembolization for liver tumors: Clinical perspectives and advances. *Adv Radiother Nucl Med*. 2025;3(4):5-21.
doi: 10.36922/ARNM025360045

Received: September 1, 2025

Revised: November 19, 2025

Accepted: November 25, 2025

Published online: December 4, 2025

1. Introduction

Yttrium90 (^{90}Y) is a pure β-emitter with a relatively short physical half-life of 64.2 h (2.67 days), emitting high-energy β particles with a maximum energy of 2.27 MeV and an average energy of approximately 0.94 MeV.[1] The emitted β radiation induces extensive radicals within tumor cells, resulting in DNA damage and apoptosis, thereby exerting significant localized radiotoxicity.[2] Since βrays penetrate only 2.5 mm on average, adjacent healthy liver parenchyma is largely spared.[3] This selective distribution makes ^{90}Y microspheres—used in procedures such as selective internal radiation therapy or transarterial radioembolization—an effective therapeutic strategy for delivering high-dose, localized treatment in patients with unresectable primary or secondary hepatic malignancies.

Optimal implementation of ^{90}YRE requires a multidisciplinary approach within specialized cancer centers, involving coordinated efforts from medical oncologists, interventional radiologists, nuclear medicine physicians, medical physicists, radiation oncologists, and specialized nursing staff[4] (Figure 1). Patient selection is based on a comprehensive assessment of clinical indications by the multidisciplinary team, followed by pre-treatment laboratory tests and imaging evaluations. Hepatic angiography and technetium-99m macroaggregated albumin (^{99m}Tc-MAA) imaging are then performed to delineate vascular anatomy and predict microsphere distribution. These findings inform individualized treatment planning, including dosimetry calculations and preparatory embolization when necessary. ^{90}Y microspheres are subsequently administered through catheter-directed arterial injection into tumor-feeding vessels. Post-treatment imaging is employed to verify microsphere localization and to verify dosimetric analysis. Follow-up imaging and clinical assessments are subsequently conducted to evaluate treatment response and guide further management.

This review is designed for clinicians and researchers directly involved in ^{90}Y-RE, particularly nuclear medicine specialists, interventional radiologists, oncologists, and medical physicists. It aims to deliver a practical, imaging-centered overview of how nuclear medicine—including positron emission tomography (PET), single photon emission computed tomography (SPECT), and quantitative dosimetry—contributes to each phase of the ^{90}Y-RE workflow, from patient selection and treatment planning to post-therapy verification and follow-up evaluation, with the goal of supporting multidisciplinary decision-making and optimizing treatment planning and delivery.

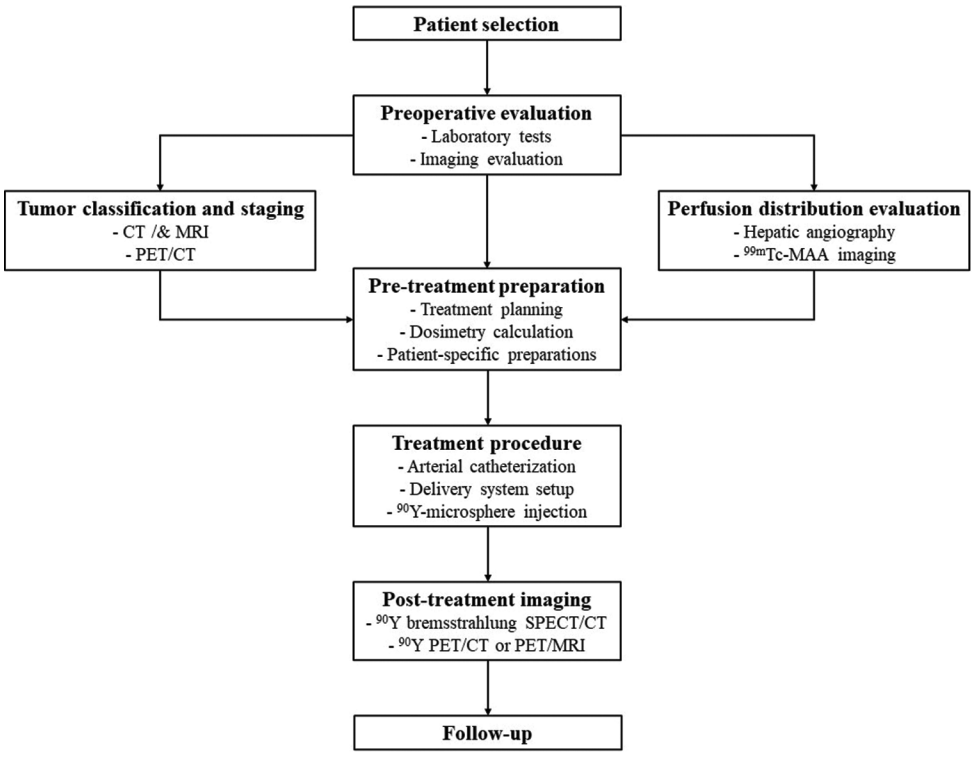

Figure 1. Overview of the ^{90}Y-RE workflow. Image created by the authors.
Abbreviations: CT: Computed tomography; MRI: Magnetic resonance imaging; ^{99m}Tc-MAA: Technetium-99m Macroaggregated albumin; PET: Positron emission tomography; RE: Radioembolization; SPECT: Single photon emission computed tomography.

2. Literature search strategy

A systematic literature search was performed in PubMed to identify systematic reviews evaluating the role of nuclear medicine imaging across all phases of the ^{90}Y-RE workflow. Search terms included combinations of: "Y90," "90Y," "yttrium-90," "Y-90," "radioembolization," "selective internal radiation therapy," "PET," "PET/CT," "SPECT," "dosimetry," "99mTc-MAA," "imaging," and "treatment response." Inclusion criteria were: (i) studies involving ^{90}Y radioembolization for primary or metastatic liver tumors; (ii) articles evaluating nuclear medicine imaging (PET, SPECT, PET/magnetic resonance imaging [MRI]) in any stage of ^{90}Y-RE (pre-treatment assessment, treatment verification, or post-treatment evaluation). Exclusion criteria included conference abstracts without full text, case reports, and non-English publications. The reference lists of relevant reviews and original studies were manually screened to ensure completeness.

3. Indications, safety, and advantages of ^{90}Y-RE

^{90}YRE is primarily indicated for unresectable or liver-dominant malignant liver tumors, including hepatocellular carcinoma (HCC), colorectal liver metastases, neuroendocrine tumor liver metastases (NELMs), and selected cases of intrahepatic cholangiocarcinoma (ICC).[5] In HCC, ^{90}YRE is recommended for patients suitable for surgical resection or local ablation, and for those refractory to or unsuitable for transarterial chemoembolization (TACE), particularly when the disease remains liver-confined with preserved liver function (Child-Pugh A).[6] In metastatic colorectal cancer, ^{90}YRE is primarily applied in liver-dominant or chemotherapy-refractory disease. Although randomized first-line trials (FOXFIRE, SIRFLOX, FOXFIRE-Global) did not demonstrate an overall survival (OS) benefit when ^{90}YRE was added to chemotherapy, these studies consistently showed improved liver-specific disease control and delayed hepatic progression in selected subgroups.[7] In NELMs, ^{90}YRE represents an effective therapeutic option for patients with liver-dominant, unresectable, or progressive disease that no longer responds to somatostatin analogues.[8] In ICC, ^{90}YRE have been investigated as both a first-line and conversion therapy, aiming to enhance downstaging and increase resectability rates in selected patients with locally advanced disease.[9]

When performed with appropriate patient selection and dosimetric guidance, ^{90}Y-RE demonstrates a favorable safety profile. The most frequently reported short-term adverse events include fatigue, nausea, liver dysfunction, diarrhea, abdominal pain, which are generally self-limited.[6,10,11] Other complications resulting from aberrant microsphere deposition or unintended radiation to surrounding structures, such as radiation pneumonitis, gastrointestinal (GI) ulceration, and biliary injury, are relatively uncommon and largely preventable.[10,12] These risks can be minimized through meticulous pretreatment evaluation using nuclear medicine imaging and angiography, as detailed in section 5.2.

Compared with TACE, ^{90}YRE provides a more favorable safety profile, with a lower incidence of post-embolization syndrome and the ability to treat HCC with portal vein tumor thrombosis, where TACE is contraindicated.[13,14] Several studies suggest that ^{90}YRE achieves comparable or superior time-to-progression compared to TACE in intermediate-stage HCC, with improved tolerability and quality of life.[15] In comparison to systemic targeted therapy such as sorafenib, randomized trials have not demonstrated a significant OS difference, while ^{90}YRE offers better local tumor control and fewer systemic side effects, making it a valuable option for selected patients.[6,16]

4. Nuclear medicine imaging for initial patient evaluation

4.1. Pre-treatment PET/CT: Patient selection and staging

Pre-treatment imaging is crucial for determining the feasibility of ^{90}Y-RE and defining therapeutic targets, with treatment intention ranging from palliation to radiation segmentectomy for limited disease.[17] By consensus, ^{90}Y-RE is typically considered only in patients with absent or very limited extrahepatic metastasis. As a standalone modality, ^{18}F-FDG PET/CT tends to demonstrate superior diagnostic performance. In the cohort study involving patients evaluated for ^{90}Y-RE, ^{18}F-FDG PET/CT demonstrated slightly higher diagnostic accuracy compared to whole-body MRI. When both modalities were combined, the sensitivity for identifying extrahepatic metastases approached 100%, while maintaining a specificity of 99% for correctly identifying patients eligible for treatment.[18] These findings highlight that PET/CT results are often decisive in determining patient eligibility and guiding subsequent therapeutic strategies. Accordingly, current clinical guidelines strongly recommend whole-body ^{18}F-FDG PET/CT as part of pre-treatment evaluation to assess the presence of extrahepatic metastasis in FDG-avid tumors.[19]

However, glucose metabolism is an imperfect surrogate of tumor biology across all histologies. Tumor heterogeneity and histology-dependent FDG avidity mean that a single ^{18}F-FDG scan may miss clinically relevant disease in specific contexts. Therefore, indication-driven use of

non-FDG tracers, either adjunctive to or instead of FDG, is recommended when the anticipated PET phenotype suggests FDG will be insensitive or when tracer-specific molecular information would change management.[20-23]

To the best of our knowledge, few studies have investigated non-FDG radiotracers specifically for ^{90}Y-RE pre-therapeutic staging. Consequently, our practical scenarios and recommendations are derived from diagnostic studies of hepatic tumors and metastases more generally. Representative clinical scenarios include:

- Neuroendocrine tumors (NETs): Well-differentiated NETs (G1-G2) show high somatostatin receptor (SSTR) expression and are optimally visualized with ^{68}Ga-SSTR imaging (SSTRI), which detects both hepatic and extrahepatic disease with excellent sensitivity and specificity, directly informing liver-directed planning.[8,24] In contrast, ^{18}F-FDG PET/CT positivity increases with higher tumor grade and proliferative index, correlating with more aggressive behavior and poorer outcomes, and therefore serves as a prognostic biomarker and a complementary tool for identifying aggressive disease.[25] A dual-tracer approach combining SSTRI and FDG PET can stratify tumor biology, with discordant uptake patterns indicating heterogeneity or dedifferentiation.[26]
- Non-FDG-avid tumors: ^{18}F-FDG PET/CT is often suboptimal for HCC and selected cholangiocarcinoma cases due to variable glucose transporter-1 expression and high glucose-6-phosphatase activity, resulting in low FDG avidity in up to 40% of lesions.[27] In contrast, fibroblast activation protein inhibitor (FAPI) PET tracers, which target activated stromal fibroblasts abundant in fibrotic or desmoplastic liver tumors, have demonstrated markedly higher lesion-to-background contrast in hepatic tumors.[28] Given that 80–90% of HCCs arise in fibrotic or cirrhotic livers, and that cholangiocarcinoma typically exhibits a highly desmoplastic, cancer-associated fibroblasts-rich microenvironment, FAPI imaging offers a promising complementary or alternative approach for non-FDG-avid lesions.[29]

4.2. Pre-treatment PET/CT: Prognostic prediction

Pre-treatment PET/CT has an established role in outcome prediction for patients, particularly ^{18}F-FDG PET/CT. Many studies have employed standardized uptake value (SUV)-based parameters such as SUV_{max}, tumor-to-liver uptake ratio to stratify patient risk before therapy, while results across series are inconsistent. Some reports associate higher baseline SUV_{max} with improved progression-free survival (PFS) or greater apparent benefit from ^{90}Y-RE in selected cohorts,[30] while others report that higher SUV_{max} predicts poorer intrahepatic control and shorter PFS.[31] Several biological, clinical, and technical factors drive the heterogeneity observed in reported SUV-prognosis relationship, including patient and tumor selection, timing of imaging, scanner/reconstruction variability, heterogeneous endpoints, follow-up durations, and cohort size.[31-33] For these reasons, SUV-based prognostic claims should be applied with caution. Clinicians should confirm that PET acquisition complies with harmonized protocols, interpret SUV within the tumor- and patient-specific context, and avoid uncritical adoption of single cutoff values derived from heterogeneous cohorts.

Beyond SUV-based parameters, volume-based PET metrics and radiomics-derived PET parameters offer a more holistic characterization of tumor biology. Metabolic tumor volume (MTV) and total lesion glycolysis (TLG) integrate metabolic activity with volumetric extent, thereby quantifying total tumor burden and capturing intratumoral heterogeneity that single-voxel SUV values cannot.[34] Seraj *et al.*[35] found that MTV, TLG, and corrected TLG were independent prognosticators for PFS and OS in patients with liver metastases undergoing ^{90}YRE, whereas SUV-based measures showed no prognostic significance. Wong *et al.*[36] further proposed the tumor metabolic load index, where elevated baseline values predicted a higher risk of extrahepatic spread, suggesting a potential role in guiding early salvage chemotherapy. Radiomics extends the assessment of metabolic response by quantifying spatial and textural heterogeneity through higher-order features such as entropy, gray-level co-occurrence, and fractal patterns.[37] For instance, Blanc *et al.*[38] demonstrated that a whole-liver PET radiomics score, derived through semi-automatic segmentation, predicted both PFS and OS in unresectable HCC.

Early data suggest that non-FDG tracers can also have prognostic value in specific tumor types. Ingenerf *et al.*[39] reported that quantitative ^{68}Ga-DOTATATE PET parameters (SUV_{max} thresholds, tumor-to-liver uptake ratio) were associated with OS and hepatic PFS in patients with NELMs undergoing ^{90}YRE. While studies focusing exclusively on the prognostic value of non-FDG radiotracer PET/CT in the pre-treatment setting remain limited, some investigations have explored pre- and post-treatment changes. This is further discussed in section 7.2.

5. ^{99m}Tc-MAA SPECT imaging for indication selection and dosimetry planning

Before injecting the therapeutic ^{90}Y microspheres, a critical preparatory step—termed "mapping" or simulation treatment evaluation—is performed to optimize treatment safety and efficacy. This involves intra-arterial infusion of a radiotracer agent, typically ^{99m}TcMAA, through the hepatic

artery supplying the tumor. The mapping session serves three essential objectives: (i) estimation of lung radiation exposure due to hepatopulmonary shunting; (ii) exclusion of digestive extrahepatic perfusion; and (iii) assessment of anticipated intrahepatic radiation distribution and quantitative dosimetry.[40]

5.1. Planar scintigraphy and SPECT/CT: Lung shunt fraction (LSF) calculation

According to the European Association for the Study of the Liver Clinical Practice Guidelines, LSF >20% or significant GI shunting warrants dose adjustment or treatment cancellation to minimize risk.[41] The calculation formula for LSF is as follows:

$$\text{Lung shunt fraction} = \frac{\text{Lung counts}}{\text{Lung} + \text{Liver counts}} \quad (1)$$

Careful patient selection is thus essential to avoid under- or over-treatment. Based on the SIR-Spheres package insert, an LSF <10% does not require dose reduction, whereas LSF >20% constitutes a relative contraindication for ^{90}Y-RE. Historically, lung-absorbed dose should be kept below 30 Gy per session, with cumulative exposure not exceeding 50 Gy to avoid potential radiation-induced pneumonitis.[17] Two primary methodologies, namely, planar scintigraphy and SPECT/CT with ^{99m}TcMAA, are routinely performed pre-^{90}Y injection to quantify LSF. Multiple phantom and clinical studies have consistently shown that planar LSF (PLSF) tends to systematically overestimate shunt fraction compared with SPECT/CT LSF (SLSF).[42-45] Two human studies comparing both modalities against post-therapy ^{90}Y-measured LSF confirmed that PLSF often overpredicts, whereas SLSF aligns more closely with the actual lung dose.[44,45]

While SPECT/CT offers superior spatial resolution and allows for precise intrahepatic dose mapping and detection of extrahepatic deposition, it is not universally employed for LSF calculation. Planar scintigraphy remains the most commonly used method in clinical practice due to its simplicity, lower demand on software capabilities, and human resources for volumetric analysis. Given that early lung dose limits (below 30 Gy per session) were derived using planar-based estimates, whether these thresholds are directly applicable when using SPECT/CT is not yet standardized.[46] In the study by Stella *et al.*,[47] none of the 317 cases developed pneumonitis when lung mean dose ($LMD_{90}Y$) <12 Gy. Kappadath *et al.*[48] Further reviewed that published lung dose limits warrant reassessment in the context of improved imaging and dosimetric techniques.

Based on these uncertainties, a conservative, step-wise operational workflow is suggested according to current research and dosimetry recommendations.[17,19,43,46,49] Firstly, planar scintigraphy for preliminary screening is performed. If PLSF is <10% and there are no complicating factors, additional lung-specific imaging may be omitted. If PLSF ≥10%, comprehensive SPECT/CT covering the liver and lungs is performed to accurately quantify SLSF. In the SPECT/CT dataset, one should calculate the LMD using the patient-specific lung mass derived from CT, rather than assuming a fixed 1 kg lung mass. If the estimated lung dose approaches or exceeds the conventional limit (30 Gy), a multidisciplinary discussion is convened to consider reducing administered activity, fractionating or staging the treatment, or using alternative "mapping methods" (*e.g.*, ^{166}Ho scout).

To reduce inter-operator variability and improve dosimetric accuracy, semi-automated or machine-learning-driven 3D segmentation is adopted to facilitate substantial reductions in operator variability and accuracy enhancement of LSF estimation. Recent frameworks have demonstrated that SPECT/CT-3D segmentations exhibit reduced bias to true activity distributions—whether defined by phantom measurements or post-therapy ^{90}Y PET/CT—compared to planar methods.[44,50] Therefore, centers capable of volumetric lung segmentation should consider integrating semi-automated 3D segmentation into routine dosimetry and report lung-mass assumptions, motion-correction strategies, and segmentation algorithm versions to facilitate multicenter comparability.

5.2. SPECT/CT: Identifying digestive extrahepatic uptake

Due to the potential for unintentional injection of microspheres into small arteries, particularly those supplying extrahepatic structures such as the gastric, duodenal, or pancreatic circulation, such ^{90}Y microspheres may inadvertently deposit in extrahepatic abdominal organs and lead to serious complications, including GI ulceration or bleeding, gastritis or duodenitis, cholecystitis, and pancreatitis.[51] To mitigate these risks, the European Association of Nuclear Medicine (EANM) recommends performing upperabdomen SPECT or SPECT/CT following intraarterial ^{99m}TcMAA injection that covers the entire liver, intestines, stomach, and pancreas at a minimum.[17] This facilitates assessment of extrahepatic abdominal shunting, improves tumor targeting visualization, and provides indirect dosimetry data. Given the anatomical complexity of the upper abdomen, accurate differentiation among adjacent organs requires tomographic imaging. In this context, SPECT/CT, which offers superior sensitivity compared to planar or standalone SPECT, is thus the preferred modality.[52]

The most common site of extrahepatic tracer uptake during pre-treatment evaluation is the GI tract. Serious gastric or duodenal ulceration occurs in approximately 2.9–4.8% of patients undergoing ^{90}Y-RE and is often refractory to standard treatment.[53] However, dissociation of ^{99m}Tc pertechnetate can cause diffuse gastric mucosal uptake that may mimic physiologic or artifactual activity. Interpretation should distinguish these patterns: diffuse, low-intensity mucosal uptake accompanied by thyroid uptake suggests free pertechnetate, whereas focal, transmural, or subserosal focal accumulation conforming to the gastric or duodenal wall is more indicative of true shunting.[54-56] To minimize this confounder, administering an oral or intravenous perchlorate immediately before ^{99m}Tc-MAA injection can block gastric uptake of free pertechnetate, thereby improving specificity for true extrahepatic MAA.[17,54] In addition, image timing is also critical. High-fidelity protocols recommend imaging within one hour post-injection to avoid artifactual accumulation.[57] When focal transmural gastric or duodenal uptake is confirmed, the usual management is prophylactic embolization of the feeding arterioles if they are identified on angiography; if the feeding vessel is not catheter-accessible or embolization is unsuccessful, treatment plans should be modified, including super-selective infusion, dose reduction, or cancellation.[56,58]

Overall, intervention thresholds for GI and other abdominal organs can be pragmatically stratified.[55] Diffuse, low-grade uptake in the gallbladder, kidneys, or spleen due to MAA degradation is typically benign and managed conservatively without altering therapy. In contrast, moderate-to-intense focal uptake in the gallbladder wall, stomach, or duodenum that is anatomically localizable on SPECT/CT or corresponds to a feeding vessel on angiography indicates high risk and usually necessitates embolization or modification of the treatment plan.

Among other sites of extrahepatic vascular uptake, anterior abdominal wall activity seen on ^{99m}Tc-MAA SPECT/CT is typically indicative of a patent hepatic falciform artery (HFA). In most cases—except in patients with umbilical hernias—tracer accumulation through the HFA does not pose diagnostic concerns.[52] Tracer accumulation in a portal vein tumor thrombus (PVT) is well described and is not an absolute contraindication.[56,59] PVT uptake often reflects arterial supply to the thrombus and may predict favorable local delivery, so presence of PVT on ^{99m}Tc-MAA generally supports, rather than contraindicates, the subsequent multidisciplinary evaluation.

5.3. SPECT/CT: Intrahepatic distribution and dosimetry assessment

In addition to evaluating extrahepatic shunting, the intrahepatic distribution of activity on ^{99m}Tc-MAA SPECT/CT also warrants careful attention. In ^{90}Y-RE, the treatment volume often includes not only the target tumor but also peritumoral normal liver tissue, necrotic tumor areas, and lipiodol deposition. Only viable tumor regions and portions of perfused normal liver tissue exhibit actual ^{90}Y microsphere distribution through the arterial supply. Necrotic tissue and lipiodol deposits do not take up ^{99m}Tc-MAA or ^{90}Y microspheres and should therefore be excluded from dose prescription calculations. Therefore, simulated dosimetry based on ^{99m}Tc-MAA SPECT/CT is required, and dosimetry assessment is commonly performed using single-compartment, multi-compartment, or voxel-based models.

The multi-compartment model separately assesses the average dose delivered to the tumor, normal liver, and lung tissue. It is also referred to as the "partition model."[60] Each compartment is typically segmented on anatomical imaging and co-registered with functional imaging. This model allows for prescription strategies that maximize tumor dose while ensuring that toxicity thresholds for the other compartments are not exceeded.[61] According to EANM recommendations,[49] multi-compartment dosimetry should be used whenever possible. However, it still overlooks intralesional dose heterogeneity within each compartment.

In contrast, the single-compartment model does not distinguish between tumor and normal liver tissue. It calculates the mean dose across the perfused volume. These methods are typically designed to avoid overdose to functional liver parenchyma and lungs, thereby minimizing the risk of RE-induced liver disease.[62] A major limitation of this model is that it neglects the spatial heterogeneity of dose distribution achievable with current imaging resolution. The final prescribed activity may be limited by toxicity thresholds in the most vulnerable patients or those with highly unfavorable dose distributions—potentially resulting in underdosing for some and overdosing for others.[63] Consequently, in clinical scenarios where the multi-compartment model is not applicable—such as infiltrative disease or absence of dosimetric data—a simplified whole-liver single-compartment approach serves as a feasible and conservative alternative.

Voxel-based dosimetry provides estimates of dose gradients and spatial heterogeneity on a finer scale, similar to external beam radiation therapy (EBRT). Unlike the multi-compartment model, it calculates absorbed dose at the level of each reconstructed voxel, thus incorporating spatial information.[64] Based on individual biodistribution and lesion characteristics, voxel-based dosimetry enables the generation of comprehensive dose maps and dose-volume histograms, facilitating more precise, personalized

treatment planning.[65] This approach offers the potential to align with well-established EBRT dose-response relationships and may enhance both treatment planning and outcome evaluation.[66] Nonetheless, the clinical utility of voxel-based dosimetry in nuclear medicine therapy remains controversial. To date, no studies have demonstrated its superiority over mean dose-based methods in RE. Moreover, nuclear medicine imaging modalities are inherently limited by physical factors, including partial volume effects, image noise, scatter, and attenuation, all of which introduce uncertainties in voxel-level activity quantification. Translating such complex voxel-wise dose distributions—represented by parameters such as dose-volume histogram—into clinically actionable decisions remains a major challenge.[67]

6. Post-treatment nuclear medicine imaging for dose verification

Even though ^{99m}TcMAA SPECT/CT imaging is used pre-treatment to predict optimal ^{90}Y microsphere distribution, unexpected extrahepatic deposition may still occur—especially in non-target organs like the GI tract—potentially leading to serious complications such as ulcers, bleeding, and even requiring surgery in severe cases. Therefore, early detection of such extrahepatic activity through immediate posttreatment imaging is crucial to prevent worsening clinical outcomes.

Within the liver, the microsphere distribution between tumor and non-tumor tissue is a key predictor of therapeutic efficacy. Post-treatment imaging enables precise estimation of the absorbed radiation dose to both compartments based on the actual microsphere deposition pattern.[68]

Both ^{90}Y bremsstrahlung SPECT and ^{90}Y PET are commonly used imaging modalities used for these purposes. Regardless of modality, imaging should be performed promptly after microsphere delivery—ideally the same day—to avoid count-rate losses from physical decay.

6.1. Post-treatment ^{90}Y bremsstrahlung SPECT/CT

Bremsstrahlung photons are produced when high-energy β^- particles emitted from ^{90}Y decelerate within tissue, generating a broad and continuous energy spectrum up to 2.3 MeV without a distinct photopeak. Due to its wide clinical availability and lower cost, bremsstrahlung SPECT/CT remains widely used for post-treatment verification of microsphere distribution and preliminary assessment of extrahepatic deposition.[69,70]

Despite its practicality, several inherent physical limitations restrict the quantitative accuracy of bremsstrahlung SPECT. Conventional SPECT reconstruction algorithms are designed for discrete energy gamma photons and are not well suited for the continuous energy spectrum of bremsstrahlung photons from ^{90}Y.[71] These photons span a broad energy range (0–2.3 MeV), lack a distinct photopeak, and have high energy levels that allow penetration through collimator septa, all of which degrade image quality and complicate accurate quantification.[69] Clinically, these physics-driven limitations translate into substantial inaccuracies in dose estimates, especially for small, high-dose regions, and several phantom or patient studies have documented systematic SPECT dose underestimation relative to PET or ground truth.[68]

Recent advances have markedly improved reconstruction accuracy through model-based and Monte Carlo (MC)-informed algorithms that explicitly incorporate the continuous bremsstrahlung spectrum, collimator response, and scatter physics. Full MC collimator modeling and MC-based scatter estimation have been shown to enhance contrast recovery and reduce quantitative bias without excessive noise amplification.[71,72] Practical implementations combining optimized ordered-subsets expectation maximization (OSEM) parameters with MC collimator modeling achieved substantial gains in phantom studies and improved lesion detectability in patient datasets.[73] Furthermore, emerging deep-learning-assisted frameworks integrating data-driven scatter estimation into MC-based reconstruction achieved single-digit percentage errors in activity recovery relative to ground truth.[74] Although bremsstrahlung SPECT/CT remains intrinsically limited for high-resolution dosimetry compared to ^{90}Y PET/CT, centers implementing validated MC-based or MC-informed reconstruction pipelines can significantly reduce quantitative uncertainty, thereby improving the clinical reliability of post-therapy SPECT dosimetry.

6.2. Post-treatment ^{90}Y PET imaging

Although ^{90}Y is predominantly a β^- emitter, a small fraction transitions to an excited state of ^{90}Zr, which subsequently produces positron-electron pairs via internal pair production at a branching ratio of approximately 3.2×10^{-5} pairs per decay.[75,76] Despite this low probability, a detectable 511 keV photon peak can still be captured using conventional PET, enabling quantitative post-treatment imaging without the need for additional radiotracer injection. The minimum activity concentration required for PET imaging visualization is approximately 1 MBq/mL, readily achieved during ^{90}Y-RE procedures.[77]

Post-treatment ^{90}Y PET, whether acquired with PET/CT or PET/MRI, offers markedly superior spatial resolution and image contrast compared to bremsstrahlung

SPECT.[78] Both modalities enable detailed visualization of microsphere deposition, precise spatial dose mapping, and improved characterization of intertumoral heterogeneity.[79] ^{90}Y PET enables voxel-wise, near-PET-resolution absorbed-dose maps that allow precise spatial dose-mapping and the identification of focally underdosed tumor regions for potential targeted retreatment.[80] Tumor-to-normal liver dose ratios derived from ^{90}Y PET have been shown to predict treatment response,[81] and PET-based dose-volume histogram analysis allows identification of underdosed tumor regions, guiding follow-up or timely retreatment.[82] Quantitative PET-derived dose metrics that incorporate intratumoral dose heterogeneity, including equivalent uniform dose or voxel-level dose distributions, have been shown to correlate with tumor control and can reconcile observed dose-response differences between glass and resin microspheres.[83] Post-therapy ^{90}Y PET radiomics combined with voxel/mean absorbed dose metrics can improve lesion-level models for early prediction of response and progression after RE, demonstrating the clinical potential of integrating spatial dose information with image texture features.[84]

Most hybrid imaging studies for post-treatment ^{90}Y dosimetry utilize PET/CT, which offers superior spatial resolution and quantification compared to bremsstrahlung SPECT/CT, allowing detailed visualization of microsphere distribution. Fusion images typically show high-activity regions corresponding to viable tumor margins on baseline CT.[78] However, due to the low branching ratio and resultant low count-rate, the effective sensitivity of ^{90}Y PET is orders of magnitude below that of ^{18}F PET, requiring extended acquisition times.[75] Depending on scanner sensitivity and axial field-of-view (AFOV), an acquisition time of approximately 10-15 minutes per bed position across 3–4 bed positions is generally required to obtain adequate count statistics and anatomical coverage of the liver or liver plus lungs.[85] The long PET acquisition times increase the risk of PET/CT misregistration. The emergence of long AFOV (LAFOV) PET/CT systems addresses this limitation by dramatically improving sensitivity and count-rate performance, enabling high-quality imaging in shorter times.[80,86-91] Phantom and patient studies demonstrate that LAFOV PET/CT achieves comparable or better image quality and absorbed-dose quantification with shorter scans, and allows simultaneous liver and lung dosimetry in a single bed position, reducing motion artifacts and registration errors common in standard AFOV PET/CT.[80,88-90]

While ^{90}Y PET/CT outperforms bremsstrahlung SPECT/CT in resolution, it can struggle to detect non-target microsphere deposition in anatomical regions adjacent to the liver, such as the gallbladder fundus, lesser gastric curvature, pylorus, and proximal duodenum, due to poor tissue contrast.[92] ^{90}Y PET/MRI offers superior soft-tissue contrast, improving lesion delineation at these interfaces and reducing radiation exposure compared to PET/CT.[93] Respiratory motion gating in PET and MRI further enhances image quality by minimizing motion artifacts and improving co-registration accuracy.[94] Moreover, PET/MRI enables evaluation of post-treatment anatomical and functional changes, such as ipsilateral hepatic lobe atrophy and contralateral lobe hypertrophy, which correlate significantly with absorbed dose metrics.[95] Advances in image reconstruction algorithms, such as Bayesian penalized likelihood (BPL), improve lesion detectability and quantitative accuracy beyond conventional OSEM reconstruction.[96] However, PET/MRI lacks time-of-flight (TOF) capability and has a smaller radial FOV, often resulting in underestimation of tumor and liver-absorbed doses compared to PET/CT.[97,98] Differences in region-of-interest delineation due to MRI superior soft-tissue contrast and variations in attenuation correction methods contribute to inter-modality variability, though mean dosimetric estimates correlate well between PET/CT and PET/MRI (Table 1).

7. Post-treatment PET/CT for followup assessment

7.1. Post-treatment ^{18}F-FDG PET/CT

Early metabolic response assessment with ^{18}F-FDG PET/CT following ^{90}Y microsphere treatment has emerged as a more sensitive and prognostically informative approach than conventional anatomical imaging. Several studies have shown that ^{18}F-FDG PET/CT can detect treatment effects discordant with anatomic imaging and better predict PFS or OS than size-based criteria.[99,100] Early changes in SUV metrics (ΔSUV) at early timepoints (6–8 weeks after treatment) correlate with tumor markers and later PFS, while CT-based RECIST criteria often underestimate early biological response.[100] Moreover, volumetric metabolic metrics, including MTV/MATV and TLG, are frequently reported to be stronger predictors of OS than single-voxel indices such as SUV_{max} after ^{90}Y-RE.[101,102] However, as mentioned earlier, these quantitative parameters may suffer from potential reproducibility limitations due to differences in segmentation methods, image acquisition, and reconstruction protocols. Recently, PERCIST-based criteria have gained adoption for defining metabolic response following ^{90}Y treatment, with Haug *et al.*[103] demonstrating a significant correlation between PERCIST-defined metabolic response and survival outcomes, supporting standardized metabolic response criteria in this population.

Table 1. Comparison of PET/CT and PET/MRI in post-treatment ^{90}Y imaging

Feature	PET/CT	PET/MRI
Spatial resolution	High; Superior to bremsstrahlung SPECT	High; Superior soft-tissue contrast to PET/CT
Soft-tissue delineation	Limited; Especially near GI interfaces	Superior; Especially at liver-GI interfaces
Detection of non-target deposition	Less sensitive near soft-tissue interfaces	More sensitive near GI tract and gallbladder
Dosimetric accuracy	High; Aligns closely with planned values	Often underestimates; Strong correlation but lower absolute values
Acquisition time	SAFOV: 10–15 min/bed, 3–4 bed; LAFOV: 5–20 min total	Typically longer than PET/CT
Motion artifact correction	Moderate; Respiratory gating possible	Strong; Respiratory gating integrated with MRI
Radiation exposure	Higher	Lower
Availability	Widely available	Limited due to higher cost
Technical limitations	Misregistration possible in long scans	Misregistration possible in long scans; Smaller radial FOV

Abbreviations: CT: Computed tomography; FOV: Field-of-view; GI: Gastrointestinal; LAFOV: Long axial field-of-view; MRI: Magnetic resonance imaging; PET: Positron emission tomography; SAFOV: Scanner axial field-of-view; SPECT: Single photon emission computed tomography.

Despite these advances, the optimal timing to assess metabolic response after ^{90}Y-RE therapy remains debatable.[104] While many studies have adopted a 3-month follow-up interval,[101,103] post-treatment edema or necrosis at this stage may underestimate partial response or stable disease.[105] Earlier imaging has been proposed to capture molecular changes preceding gross anatomical alterations, with early metabolic non-response at 4 weeks predicts worse survival in some studies and therefore may identify patients who would benefit from prompt change of systemic or loco-regional therapy.[83,106,107]

Therefore, the clinical trade-offs between early (4–6 weeks) and delayed (3 months) PET can be summarized as follows: Early PET enhances sensitivity to molecular response and enables prompt identification of non-responders, thereby supporting timely initiation of salvage or palliative strategies;[108] whereas delayed PET scans may reduce false-positive findings related to transient post-treatment inflammation or necrosis and are more consistent with standardized PERCIST evaluation in some studies.[109]

In addition to ^{18}F-FDG PET/CT, diffusion-weighted imaging (DWI) MRI has also shown promise in this context. Barabasch *et al.* reported that for common solid liver metastases, DWI may outperform ^{18}F-FDG PET/CT in early treatment response and survival prediction after ^{90}Y-RE.[110,111] However, Bastiaannet *et al.*[50] cautioned that such findings should not be overgeneralized, particularly given the limited reliability of SUVmax in certain tumor types. They recommended the use of volumetric metabolic parameters such as TLG, which may provide more robust and clinically meaningful prognostic information. Stratified analyses are needed to compare predictive performance across tumor subtypes. A combined PET and DWI strategy may enhance accuracy in early treatment decisions and help guide decisions regarding additional lobar treatments or modifications to systemic therapy.

7.2. Post-treatment PET/CT with non-FDG radiotracers

Although ^{18}F-FDG PET/CT is a well-established modality for evaluating tumor response to ^{90}Y-RE, its sensitivity is limited in certain tumor subtypes, particularly NELM and well-differentiated HCC.[112] In these FDG-insensitive tumors, alternative PET tracers targeting distinct metabolic or receptor pathways have shown promise.

For unresectable NELM, SSTR-targeted PET using ^{68}Ga-DOTA-somatostatin analogs can detect molecular responses as early as six weeks following ^{90}YRE, with the Δtumor-to-spleen uptake ratio derived from ^{68}Ga-DOTANOC PET emerging as a promising prognostic biomarker for OS in this patient population.[113] Comparative studies have shown that percentage changes in tumor-to-organ SUV ratios on ^{68}Ga-DOTATATE PET/CT are superior predictors of prolonged hepatic PFS compared to isolated parameters such as ΔSUV_{max}, $\Delta SUV_{mean,}$ or ΔADC at the first follow-up.[114] However, quantitative criteria for response assessment using SSTR-targeted PET imaging remain unstandardized, highlighting the need for further prospective validation.

In well-differentiated HCC, tumor heterogeneity limits the diagnostic and prognostic utility of ^{18}F-FDG PET/CT, prompting the exploration of alternative metabolic tracers. Radiolabeled choline tracers (^{18}F-FEC or ^{18}F-choline) exploit the upregulated phospholipid biosynthesis typical of these tumors. Choline, transported into cells and phosphorylated by choline kinase, becomes trapped as radiolabeled phosphocholine, reflecting membrane synthesis and tumor metabolic activity.[115,116] Increased choline uptake often correlates with higher proliferation and treatment resistance, supporting its value in prognostication.[117] ^{18}F-FEC PET/CT has shown potential for early post-^{90}Y-RE evaluation, particularly in patients with elevated AFP, allowing response assessment independent of morphologic change.[115] Similarly, ^{18}F-choline PET/CT parameters such as ΔSUV_{mean}, ΔTLG, and ΔSUL can distinguish responders from non-responders as early as one month post-treatment.[118,119]

Well-differentiated HCCs also retain mitochondrial function and lipid synthesis capacity, leading to higher acetate uptake through both oxidative and lipogenic pathways.[120] Given the upregulated *de novo* fatty acid synthesis in these tumors, ^{11}C-acetate serves as an optimal metabolic substrate.[121] Ho *et al.*[122] demonstrated with dual-tracer PET/CT (^{18}F-FDG and ^{11}C-acetate) that acetate-avid, well-differentiated HCCs required distinct ^{90}Y dose thresholds for optimal response compared to FDG-avid, poorly differentiated lesions.

Overall, these findings highlight the value of alternative and dual-tracer PET/CT in characterizing tumor biology and guiding personalized dosimetry for NELM and well-differentiated HCC treated with ^{90}Y-RE. Functional biomarkers targeting metabolism or receptor expression may refine response assessment and enable treatment strategies tailored to tumor differentiation and molecular phenotype.

8. Strengths and limitations of included studies

A critical appraisal of the included studies highlights several methodological strengths as well as notable limitations that should be considered when interpreting the current evidence.

The strengths of the available literature include:

(i) Consistent evidence demonstrating the essential role of nuclear medicine imaging in patient selection, shunt assessment, microsphere biodistribution, and quantitative dosimetry
(ii) Increasing use of PET-based dosimetry, providing high-resolution, quantitative information that correlates with tumor response
(iii) Emerging hybrid modalities (PET/MRI, LAFOV PET/CT) offering advances in lesion detection and dose quantification

However, several limitations are evident across the enrolled studies:

(i) Substantial heterogeneity in imaging protocols, reconstruction algorithms, segmentation methods, and dosimetry models across studies
(ii) Limited prospective data validating PET-based dosimetry thresholds and outcome correlations
(iii) Inconsistency in reporting imaging biomarkers, making cross-study comparison difficult.

9. Conclusion

Nuclear medicine underpins every stage of ^{90}Y-RE, from pre-treatment ^{99m}Tc-MAA assessment of tumor perfusion and extrahepatic shunting to post-treatment verification with ^{90}Y SPECT/CT, PET/CT, or PET/MRI. ^{18}F-FDG PET/CT and other tracer-based PET modalities further aid staging, stratification, and response evaluation. Future research should prioritize resolving key controversies, including standardization of lung dose thresholds, optimal timing for follow-up imaging, and the comparative value of different dosimetry models, to advance the precision and personalization of ^{90}Y-RE.

Acknowledgments

None.

Funding

None.

Conflict of interest

Hongcheng Shi serves the Editor-in-Chief of this journal, but was not in any way involved in the editorial and peer-review process conducted for this paper, directly or indirectly. Separately, other authors declared that they have no known competing financial interests or personal relationships that could have influenced the work reported in this paper.

Author contributions

Conceptualization: Runjun Yang, Hongcheng Shi
Visualization: Runjun Yang
Writing–original draft: Runjun Yang
Writing–review & editing: Akram Al-Ibraheem, Hongcheng Shi

Ethics approval and consent to participate

Not applicable.

Consent for publication

Not applicable.

Availability of data

Not applicable.

References

1. Walker LA. Radioactive yttrium 90: A review of its properties, biological behavior, and clinical uses. *Acta Radiol Ther Phys Biol*. 1964;2:302-314.

   doi: 10.1080/02841866409134063

2. Briody H, Duong D, Yeoh SW, *et al*. Radioembolization for treatment of hepatocellular carcinoma: Current evidence and patterns of utilization. *J Vasc Interv Radiol*. 2023;34(7):1200-1213.

   doi: 10.1016/j.jvir.2023.03.020

3. Kennedy A, Nag S, Salem R, *et al*. Recommendations for radioembolization of hepatic malignancies using yttrium-90 microsphere brachytherapy: A consensus panel report from the radioembolization brachytherapy oncology consortium. *Int J Radiat Oncol Biol Phys*. 2007;68(1):13-23.

   doi: 10.1016/j.ijrobp.2006.11.060

4. Salem R, Padia SA, Lam M, *et al*. Clinical, dosimetric, and reporting considerations for Y-90 glass microspheres in hepatocellular carcinoma: Updated 2022 recommendations from an international multidisciplinary working group. *Eur J Nucl Med Mol Imaging*. 2023;50(2): 328-343.

   doi: 10.1007/s00259-022-05956-w

5. European Association for the Study of the Liver. EASL Clinical Practice Guidelines on acute-on-chronic liver failure. *J Hepatol*. 2023;79(2):461-491.

   doi: 10.1016/j.jhep.2023.04.021

6. Vilgrain V, Pereira H, Assenat E, *et al*. Efficacy and safety of selective internal radiotherapy with yttrium-90 resin microspheres compared with sorafenib in locally advanced and inoperable hepatocellular carcinoma (SARAH): An open-label randomised controlled phase 3 trial. *Lancet Oncol*. 2017;18(12):1624-1636.

   doi: 10.1016/S1470-2045(17)30683-6

7. Wasan HS, Gibbs P, Sharma NK, *et al*. First-line selective internal radiotherapy plus chemotherapy versus chemotherapy alone in patients with liver metastases from colorectal cancer (FOXFIRE, SIRFLOX, and FOXFIRE-Global): A combined analysis of three multicentre, randomised, phase 3 trials. *Lancet Oncol*. 2017;18(9):1159-1171.

   doi: 10.1016/S1470-2045(17)30457-6

8. Pavel M, Baudin E, Couvelard A, *et al*. ENETS Consensus Guidelines for the management of patients with liver and other distant metastases from neuroendocrine neoplasms of foregut, midgut, hindgut, and unknown primary. *Neuroendocrinology*. 2012;95(2):157-176.

   doi: 10.1159/000335597

9. Edeline J, Touchefeu Y, Guiu B, *et al*. Radioembolization plus chemotherapy for first-line treatment of locally advanced intrahepatic cholangiocarcinoma: A phase 2 clinical trial. *JAMA Oncol*. 2020;6(1):51-59.

   doi: 10.1001/jamaoncol.2019.3702

10. Riaz A, Awais R, Salem R. Side effects of yttrium-90 radioembolization. *Front Oncol*. 2014;4:198.

    doi: 10.3389/fonc.2014.00198

11. Laidlaw GL, Johnson GE. Recognizing and managing adverse events in Y-90 radioembolization. *Semin Intervent Radiol*. 2021;38(4):453-459.

    doi: 10.1055/s-0041-1735617

12. Riaz A, Lewandowski RJ, Kulik LM, *et al*. Complications following radioembolization with yttrium-90 microspheres: A comprehensive literature review. *J Vasc Interv Radiol*. 2009;20(9):1121-1130.

    doi: 10.1016/j.jvir.2009.05.030

13. Facciorusso A, Serviddio G, Muscatiello N. Transarterial radioembolization vs chemoembolization for hepatocarcinoma patients: A systematic review and meta-analysis. *World J Hepatol*. 2016;8(18):770-778.

    doi: 10.4254/wjh.v8.i18.770

14. Şener N, Yakupoğlu A. Yttrium-90 transarterial radioembolization and capecitabine in hepatocellular carcinoma with portal vein involvement. *Medicine* (*Baltimore*). 2023;102(35):e34674.

    doi: 10.1097/MD.0000000000034674

15. Salem R, Gordon AC, Mouli S, *et al*. Y90 radioembolization significantly prolongs time to progression compared with chemoembolization in patients with hepatocellular carcinoma. *Gastroenterology*. 2016;151(6):1155-1163.

    doi: 10.1053/j.gastro.2016.08.029

16. Chow PKH, Gandhi M, Tan S, *et al*. SIRveNIB: Selective internal radiation therapy versus sorafenib in Asia-Pacific patients with hepatocellular carcinoma. *J Clin Oncol*. 2018;36(19):1913-1921.

    doi: 10.1200/JCO.2017.76.0892

17. Weber M, Lam M, Chiesa C, *et al*. EANM procedure guideline for the treatment of liver cancer and liver metastases with intra-arterial radioactive compounds. *Eur J Nucl Med Mol Imaging*. 2022;49(5):1682-1699.

    doi: 10.1007/s00259-021-05600-z

18. Schmidt GP, Paprottka P, Jakobs TF, *et al*. FDG-PET-CT and whole-body MRI for triage in patients planned for radioembolisation therapy. *Eur J Radiol*.

2012;81(3):e269-e276.

doi: 10.1016/j.ejrad.2011.02.018

19. Levillain H, Bagni O, Deroose CM, *et al*. International recommendations for personalised selective internal radiation therapy of primary and metastatic liver diseases with yttrium-90 resin microspheres. *Eur J Nucl Med Mol Imaging*. 2021;48(5):1570-1584.

doi: 10.1007/s00259-020-05163-5

20. Lin Y, Gao H, Zheng J, Al-Ibraheem A, Hu P, Shi H. Clinical explorations of [68Ga] Ga-FAPI-04 and [18F] FDG dual-tracer total-body PET/CT and PET/MR imaging. *Semin Nucl Med*. 2024;54(6):904-913.

doi: 10.1053/j.semnuclmed.2024.09.009

21. Miao Y, Feng R, Guo R, *et al*. Utility of [68Ga]FAPI-04 and [18F]FDG dual-tracer PET/CT in the initial evaluation of gastric cancer. *Eur Radiol*. 2023;33(6):4355-4366.

doi: 10.1007/s00330-022-09321-1

22. Sharma A, Muralitharan M, Ramage J, *et al.* Current management of neuroendocrine tumour liver metastases. *Curr Oncol Rep.* 2024;26(9):1070-1084.

doi: 10.1007/s11912-024-01559-w

23. Cao J, Srinivas-Rao S, Mroueh N, *et al*. Cholangiocarcinoma imaging: from diagnosis to response assessment. *Abdom Radiol* (*NY*). 2024;49(5):1699-1715.

doi: 10.1007/s00261-024-04267-y

24. Sänger PW, Freesmeyer M. Early dynamic 68Ga-DOTA-D-Phe1-Tyr3-octreotide PET/CT in patients with hepatic metastases of neuroendocrine tumors. *Clin Nucl Med.* 2016;41(6):447-453.

doi: 10.1097/RLU.0000000000001154

25. Zhou Y, Li L, Wang H, *et al.* Heterogeneous uptake of 68 Ga-DOTATATE and 18 F-FDG in initial diagnosed neuroendocrine tumors patients: Which patients are suitable for dual-tracer PET imaging. *Clin Nucl Med*. 2024;49(6):516-520.

doi: 10.1097/RLU.0000000000005231

26. Chan DL, Pavlakis N, Schembri GP, *et al*. Dual somatostatin receptor/FDG PET/CT imaging in metastatic neuroendocrine tumours: Proposal for a novel grading scheme with prognostic significance. *Theranostics*. 2017;7(5):1149-1158.

doi: 10.7150/thno.18068

27. Shi X, Xing H, Yang X, *et al.* Comparison of PET imaging of activated fibroblasts and 18F-FDG for diagnosis of primary hepatic tumours: A prospective pilot study. *Eur J Nucl Med Mol Imaging*. 2021;48(5):1593-1603.

doi: 10.1007/s00259-020-05070-9

28. Manuppella F, Pisano G, Taralli S, Caldarella C, Calcagni ML. Diagnostic performances of PET/CT using fibroblast activation protein inhibitors in patients with primary and metastatic liver tumors: A comprehensive literature review. *Int J Mol Sci*. 2024;25(13):7197.

doi: 10.3390/ijms25137197

29. Guo W, Pang Y, Yao L, *et al.* Imaging fibroblast activation protein in liver cancer: A single-center post hoc retrospective analysis to compare [68Ga]Ga-FAPI-04 PET/CT versus MRI and [18F]-FDG PET/CT. *Eur J Nucl Med Mol Imaging*. 2021;48(5):1604-1617.

doi: 10.1007/s00259-020-05095-0

30. Kucuk ON, Soydal C, Araz M, Bilgic S, Ibis E. Prognostic importance of 18F-FDG uptake pattern of hepatocellular cancer patients who received SIRT. *Clin Nucl Med*. 2013;38(7):e283-e289.

doi: 10.1097/RLU.0b013e3182867f17

31. Abuodeh Y, Naghavi AO, Ahmed KA, *et al*. Prognostic value of pre-treatment F-18-FDG PET-CT in patients with hepatocellular carcinoma undergoing radioembolization. *World J Gastroenterol*. 2016;22(47):10406-10414.

doi: 10.3748/wjg.v22.i47.10406

32. Kim DY, Lee HW, Kang W, Kim GM, Won JY, Yun M. Metabolic activity assessment by 18 F-fluorodeoxyglucose positron emission tomography in patients with hepatocellular carcinoma undergoing Yttrium-90 transarterial radioembolization. *J Gastroenterol Hepatol*. 2021;36(6):1679-1684.

doi: 10.1111/jgh.15357

33. Boellaard R. Standards for PET image acquisition and quantitative data analysis. *J Nucl Med*. 2009;50 Suppl 1:11S-20S.

doi: 10.2967/jnumed.108.057182

34. Larson SM, Erdi Y, Akhurst T, *et al*. Tumor treatment response based on visual and quantitative changes in global tumor glycolysis using PET-FDG imaging. The visual response score and the change in total lesion glycolysis. *Clin Positron Imaging*. 1999;2(3):159-171.

doi: 10.1016/s1095-0397(99)00016-3

35. Seraj SM, Zadeh MZ, Werner TJ, *et al*. Pretreatment volumetric parameters of FDG-PET predict the survival after Yttrium-90 radio-embolization in metastatic liver disease. *Am J Nucl Med Mol Imaging*. 2019;9(5):248-254.

36. Wong CY, Gates VL, Tang B, *et al*. Fluoro-2-deoxy-D-glucose positron emission tomography/computed tomography predicts extrahepatic metastatic potential of colorectal metastasis: A practical guide for yttrium-90 microsphere liver-directed therapy. *Cancer Biother Radiopharm*. 2010;25(2):233-236.

doi: 10.1089/cbr.2009.0735

37. Piñeiro-Fiel M, Moscoso A, Pubul V, Ruibal Á, Silva-Rodríguez J, Aguiar P. A systematic review of PET textural

analysis and radiomics in cancer. *Diagnostics* (*Basel*). 2021;11(2):380.

doi: 10.3390/diagnostics11020380

38. Blanc-Durand P, Van Der Gucht A, Jreige M, *et al*. Signature of survival: A 18F-FDG PET based whole-liver radiomic analysis predicts survival after 90Y-TARE for hepatocellular carcinoma. *Oncotarget*. 2018;9(4):4549-4558.

doi: 10.18632/oncotarget.23423

39. Ingenerf M, Grawe F, Winkelmann M, *et al*. Neuroendocrine liver metastases treated using transarterial radioembolization: Identification of prognostic parameters at 68Ga-DOTATATE PET/CT. *Diagn Interv Imaging*. 2024;105(1):15-25.

doi: 10.1016/j.diii.2023.06.007

40. Wagemans M, Braat A, van Rooij R, *et al*. Lung mean dose prediction in transarterial radioembolization (TARE): Superiority of [166Ho]-scout over [99mTc]MAA in a prospective cohort study. *Cardiovasc Intervent Radiol*. 2024;47(4):443-450.

doi: 10.1007/s00270-023-03656-y

41. European Association for the Study of the Liver. EASL Clinical Practice Guidelines on the management of hepatocellular carcinoma. *J Hepatol*. 2025;82(2):315-374.

doi: 10.1016/j.jhep.2024.08.028

42. Georgiou MF, Kuker RA, Studenski MT, Ahlman PP, Witte M, Portelance L. Lung shunt fraction calculation using 99mTc-MAA SPECT/CT imaging for 90Y microsphere selective internal radiation therapy of liver tumors. *EJNMMI Res*. 2021;11(1):96.

doi: 10.1186/s13550-021-00837-z

43. Dittmann H, Kopp D, Kupferschlaeger J, *et al*. A prospective study of quantitative SPECT/CT for evaluation of lung shunt fraction before SIRT of liver tumors. *J Nucl Med*. 2018;59(9):1366-1372.

doi: 10.2967/jnumed.117.205203

44. Allred JD, Niedbala J, Mikell JK, Owen D, Frey KA, Dewaraja YK. The value of 99mTc-MAA SPECT/CT for lung shunt estimation in 90Y radioembolization: A phantom and patient study. *EJNMMI Res*. 2018;8(1):50.

doi: 10.1186/s13550-018-0402-8

45. Young S, Flanagan S, D'Souza D, *et al.* Lung shunt fraction calculations before Y-90 transarterial radioembolization: Comparison of accuracy and clinical significance of planar scintigraphy and SPECT/CT. *Diagn Interv Imaging*. 2023;104(4):185-191.

doi: 10.1016/j.diii.2022.12.002

46. Torkian P, Ragulojan R, Woodhead GJ, *et al.* Lung shunt fraction quantification methods in radioembolization: What you need to know. *Br J Radiol*. 2022;95(1139):20220470.

doi: 10.1259/bjr.20220470

47. Stella M, van Rooij R, Lam M, de Jong H, Braat A. Lung dose measured on postradioembolization 90Y PET/CT and incidence of radiation pneumonitis. *J Nucl Med*. 2022;63(7):1075-1080.

doi: 10.2967/jnumed.121.263143

48. Kappadath SC, Lopez BP, Salem R, Lam MGEH. Reassessment of the lung dose limits for radioembolization. *Nucl Med Commun*. 2021;42(10):1064-1075.

doi: 10.1097/MNM.0000000000001439

49. Chiesa C, Sjogreen-Gleisner K, Walrand S, *et al*. EANM dosimetry committee series on standard operational procedures: A unified methodology for 99mTc-MAA pre- and 90Y peri-therapy dosimetry in liver radioembolization with 90Y microspheres. *EJNMMI Phys*. 2021;8(1):77.

doi: 10.1186/s40658-021-00394-3

50. Bastiaannet R, van Roekel C, Kunnen B, Lam M, de Jong H. Is Diffusion-weighted MRI really superior to PET/CT in predicting survival after radioembolization. *Radiology*. 2018;289(1):274-275.

doi: 10.1148/radiol.2018181348

51. Ahmadzadehfar H, Sabet A, Biermann K, *et al*. The significance of 99mTc-MAA SPECT/CT liver perfusion imaging in treatment planning for 90Y-microsphere selective internal radiation treatment. *J Nucl Med*. 2010;51(8):1206-1212.

doi: 10.2967/jnumed.109.074559

52. Ahmadzadehfar H, Duan H, Haug AR, Walrand S, Hoffmann M. The role of SPECT/CT in radioembolization of liver tumours. *Eur J Nucl Med Mol Imaging*. 2014;41 Suppl 1:S115-S124.

doi: 10.1007/s00259-013-2675-5

53. Naymagon S, Warner RR, Patel K, *et al*. Gastroduodenal ulceration associated with radioembolization for the treatment of hepatic tumors: An institutional experience and review of the literature. *Dig Dis Sci*. 2010;55(9):2450-2458.

doi: 10.1007/s10620-010-1156-y

54. Sabet A, Ahmadzadehfar H, Muckle M, *et al*. Significance of oral administration of sodium perchlorate in planning liver-directed radioembolization. *J Nucl Med*. 2011;52(7):1063-1067.

doi: 10.2967/jnumed.110.083626

55. Bailey JJ, Dewaraja Y, Hubers D, Srinivasa RN, Frey KA. Biodistribution of 99mTc-MAA on SPECT/CT performed for 90Y radioembolization therapy planning: A pictorial review. *Clin Transl Imaging*. 2017;5(5):473-485.

doi: 10.1007/s40336-017-0245-8

56. Lenoir L, Edeline J, Rolland Y, *et al*. Usefulness and pitfalls of MAA SPECT/CT in identifying digestive extrahepatic

uptake when planning liver radioembolization. *Eur J Nucl Med Mol Imaging*. 2012;39(5):872-880.

doi: 10.1007/s00259-011-2033-4

57. D'Abadie P, Walrand S, Lhommel R, Hesse M, Jamar F. A Theranostic approach in SIRT: Value of pre-therapy imaging in treatment planning. *J Clin Med*. 2022;11(23):7245.

doi: 10.3390/jcm11237245

58. Garin E, Lenoir L, Rolland Y, *et al*. Dosimetry based on 99mTc-macroaggregated albumin SPECT/CT accurately predicts tumor response and survival in hepatocellular carcinoma patients treated with 90Y-loaded glass microspheres: Preliminary results. *J Nucl Med*. 2012;53(2):255-263.

doi: 10.2967/jnumed.111.094235

59. Hamami ME, Poeppel TD, Müller S, *et al*. SPECT/CT with 99mTc-MAA in radioembolization with 90Y microspheres in patients with hepatocellular cancer. *J Nucl Med*. 2009;50(5):688-692.

doi: 10.2967/jnumed.108.058347

60. Gulec SA, Mesoloras G, Stabin M. Dosimetric techniques in 90Y-microsphere therapy of liver cancer: The MIRD equations for dose calculations. *J Nucl Med*. 2006;47(7):1209-1211.

61. Chiesa C, Mira M, Maccauro M, *et al*. Radioembolization of hepatocarcinoma with (90)Y glass microspheres: Development of an individualized treatment planning strategy based on dosimetry and radiobiology. *Eur J Nucl Med Mol Imaging*. 2015;42(11):1718-1738.

doi: 10.1007/s00259-015-3068-8

62. Salem R, Johnson GE, Kim E, *et al*. Yttrium-90 radioembolization for the treatment of solitary, unresectable HCC: The LEGACY study. *Hepatology*. 2021;74(5):2342-2352.

doi: 10.1002/hep.31819

63. Salem R, Thurston KG. Radioembolization with 90Yttrium microspheres: A state-of-the-art brachytherapy treatment for primary and secondary liver malignancies. Part 1: Technical and methodologic considerations. *J Vasc Interv Radiol*. 2006;17(8):1251-1278.

doi: 10.1097/01.RVI.0000233785.75257.9A

64. Chiesa C, Bardiès M, Zaidi H. Voxel-based dosimetry is superior to mean absorbed dose approach for establishing dose-effect relationship in targeted radionuclide therapy. *Med Phys*. 2019;46(12):5403-5406.

doi: 10.1002/mp.13851

65. Mok GSP, Dewaraja YK. Recent advances in voxel-based targeted radionuclide therapy dosimetry. *Quant Imaging Med Surg*. 2021;11(2):483-489.

doi: 10.21037/qims-20-1006

66. Kappadath SC, Mikell J, Balagopal A, Baladandayuthapani V, Kaseb A, Mahvash A. Hepatocellular carcinoma tumor dose response after 90y-radioembolization with glass microspheres using 90Y-SPECT/CT-based voxel dosimetry. *Int J Radiat Oncol Biol Phys*. 2018;102(2):451-461.

doi: 10.1016/j.ijrobp.2018.05.062

67. Tran-Gia J, Salas-Ramirez M, Lassmann M. What you see is not what you get: On the accuracy of voxel-based dosimetry in molecular radiotherapy. *J Nucl Med*. 2020;61(8):1178-1186.

doi: 10.2967/jnumed.119.231480

68. Elschot M, Vermolen BJ, Lam MG, de Keizer B, van den Bosch MA, de Jong HW. Quantitative comparison of PET and bremsstrahlung SPECT for imaging the *in vivo* yttrium-90 microsphere distribution after liver radioembolization. *PLoS One*. 2013;8(2):e55742.

doi: 10.1371/journal.pone.0055742

69. Tafti BA, Padia SA. Dosimetry of Y-90 microspheres utilizing Tc-99m SPECT and Y-90 PET. *Semin Nucl Med*. 2019;49(3):211-217.

doi: 10.1053/j.semnuclmed.2019.01.005

70. Ahmadzadehfar H, Muckle M, Sabet A, *et al*. The significance of bremsstrahlung SPECT/CT after yttrium-90 radioembolization treatment in the prediction of extrahepatic side effects. *Eur J Nucl Med Mol Imaging*. 2012;39(2):309-315.

doi: 10.1007/s00259-011-1940-8

71. Dewaraja YK, Chun SY, Srinivasa RN, *et al*. Improved quantitative 90 Y bremsstrahlung SPECT/CT reconstruction with Monte Carlo scatter modeling. *Med Phys*. 2017;44(12):6364-6376.

doi: 10.1002/mp.12597

72. Porter CA, Bradley KM, Hippeläinen ET, Walker MD, McGowan DR. Phantom and clinical evaluation of the effect of full Monte Carlo collimator modelling in post-SIRT yttrium-90 Bremsstrahlung SPECT imaging. *EJNMMI Res*. 2018;8(1):7.

doi: 10.1186/s13550-018-0361-0

73. Siman W, Mikell JK, Kappadath SC. Practical reconstruction protocol for quantitative (90)Y bremsstrahlung SPECT/CT. *Med Phys*. 2016;43(9):5093.

doi: 10.1118/1.4960629

74. Jia Y, Li Z, Akhavanallaf A, Fessler JA, Dewaraja YK. 90Y SPECT scatter estimation and voxel dosimetry in radioembolization using a unified deep learning framework. *EJNMMI Phys*. 2023;10(1):82.

doi: 10.1186/s40658-023-00598-9

75. Wright CL, Zhang J, Tweedle MF, Knopp MV, Hall NC. Theranostic imaging of yttrium-90. *Biomed Res Int*. 2015;2015:481279.

doi: 10.1155/2015/481279

76. Dryák P, Šolc J. Measurement of the branching ratio related to the internal pair production of Y-90. *Appl Radiat Isot*. 2020;156:108942.

doi: 10.1016/j.apradiso.2019.108942

77. Werner MK, Brechtel K, Beyer T, Dittmann H, Pfannenberg C, Kupferschläger J. PET/CT for the assessment and quantification of (90)Y biodistribution after selective internal radiotherapy (SIRT) of liver metastases. *Eur J Nucl Med Mol Imaging*. 2010;37(2):407-408.

doi: 10.1007/s00259-009-1317-4

78. Pasciak AS, Bourgeois AC, McKinney JM, *et al*. Radioembolization and the dynamic role of (90)Y PET/CT. *Front Oncol*. 2014;4:38.

doi: 10.3389/fonc.2014.00038

79. Lhommel R, Goffette P, Van den Eynde M, *et al*. Yttrium-90 TOF PET scan demonstrates high-resolution biodistribution after liver SIRT. *Eur J Nucl Med Mol Imaging*. 2009;36(10):1696.

doi: 10.1007/s00259-009-1210-1

80. Costa G, Spencer B, Omidvari N, *et al*. Radioembolization dosimetry with total-body 90Y PET. *J Nucl Med*. 2022;63(7):1101-1107.

doi: 10.2967/jnumed.121.263145

81. Knešaurek K, Martinez RB, Ghesani M. Tumour-to-normal tissue (T/N) dosimetry ratios role in assessment of 90Y selective internal radiation therapy (SIRT). *Br J Radiol*. 2022;95(1129):20210294.

doi: 10.1259/bjr.20210294

82. Vo NH, Malik MS, Tahir MM, *et al*. Prediction of recurrence of hepatocellular carcinoma following radiation segmentectomy with resin microspheres based on underdosed tumor volume on yttrium-90 PET/CT dosimetry. *J Vasc Interv Radiol*. 2025;36(10):1576-1586.

doi: 10.1016/j.jvir.2025.06.018

83. Hesse M, D'Abadie P, Lhommel R, Jamar F, Walrand S. Yttrium-90 TOF-PET-based EUD predicts response post liver radioembolizations using recommended manufacturer FDG reconstruction parameters. *Front Oncol*. 2021;11:592529.

doi: 10.3389/fonc.2021.592529

84. Wei L, Cui C, Xu J, Kaza R, El Naqa I, Dewaraja YK. Tumor response prediction in 90Y radioembolization with PET-based radiomics features and absorbed dose metrics. *EJNMMI Phys*. 2020;7(1):74.

doi: 10.1186/s40658-020-00340-9

85. Busse NC, Al-Ghazi M, Abi-Jaoudeh N, *et al*. AAPM medical physics practice guideline 14.a: Yttrium-90 microsphere radioembolization. *J Appl Clin Med Phys*. 2024;25(2):e14157.

doi: 10.1002/acm2.14157

86. Cherry SR, Jones T, Karp JS, Qi J, Moses WW, Badawi RD. Total-body PET: Maximizing sensitivity to create new opportunities for clinical research and patient care. *J Nucl Med*. 2018;59(1):3-12.

doi: 10.2967/jnumed.116.184028

87. Zhang Y, Hu P, He Y, *et al*. Ultrafast 30-s total-body PET/CT scan: A preliminary study. *Eur J Nucl Med Mol Imaging*. 2022;49(8):2504-2513.

doi: 10.1007/s00259-022-05838-1

88. Zeimpekis KG, Mercolli L, Conti M, *et al*. Phantom-based evaluation of yttrium-90 datasets using biograph vision quadra. *Eur J Nucl Med Mol Imaging*. 2023;50(4):1168-1182.

doi: 10.1007/s00259-022-06074-3

89. Zeimpekis KG, Mercolli L, Conti M, Sari H, Rominger A, Rathke H. 90Y post-radioembolization clinical assessment with whole-body Biograph Vision Quadra PET/CT: Image quality, tumor, liver and lung dosimetry. *Eur J Nucl Med Mol Imaging*. 2024;51(7):2100-2113.

doi: 10.1007/s00259-024-06650-9

90. Zeimpekis KG, Sari H, Gözlügöl N, *et al*. Evaluation of long axial field-of-view (LAFOV) PET/CT for post-treatment dosimetry in Yttrium-90 radioembolization of liver tumors: A comparative study with conventional SPECT imaging. *Eur J Nucl Med Mol Imaging*. 2025;52(4):1460-1471.

doi: 10.1007/s00259-024-07034-9

91. Mercolli L, Zeimpekis K, Prenosil GA, *et al*. Phantom study for 90Y liver radioembolization dosimetry with a long axial field-of-view PET/CT. *Phys Med*. 2024;118:103296.

doi: 10.1016/j.ejmp.2024.103296

92. Kao YH, Steinberg JD, Tay YS, *et al*. Post-radioembolization yttrium-90 PET/CT - part 1: diagnostic reporting. *EJNMMI Res*. 2013;3(1):56.

doi: 10.1186/2191-219X-3-56

93. Woodhead G, Young S. Another hammer, but we need a Wrench, and a screwdriver-positron emission tomography/magnetic resonance imaging represents another tool for post-delivery 90Y dosimetry, but what are we still missing. *J Gastrointest Oncol*. 2024;15(4):2006-2010.

doi: 10.21037/jgo-24-460

94. Demir B, Soydal C, Kucuk NO, *et al*. Voxel-based dosimetry with integrated Y-90 PET/MRI and prediction of response of primary and metastatic liver tumors to radioembolization with Y-90 glass microspheres. *Ann Nucl Med*. 2025;39(1):31-46.

doi: 10.1007/s12149-024-01974-w

95. Demir B, Soydal C, Celebioglu EC, *et al*. Prediction of left lobe hypertrophy with voxel-based dosimetry using

integrated Y-90 PET/MRI after radioembolization of liver tumors with Y-90 microspheres. *Eur J Nucl Med Mol Imaging*. 2025;52(5):1695-1707.

doi: 10.1007/s00259-024-07023-y

96. Calatayud-Jordán J, Carrasco-Vela N, Chimeno-Hernández J, *et al*. Y-90 PET/MR imaging optimization with a Bayesian penalized likelihood reconstruction algorithm. *Phys Eng Sci Med*. 2024;47(4):1397-1413.

doi: 10.1007/s13246-024-01452-7

97. Gurajala R, Partovi S, DiFilippo FP, *et al*. Prospective comparison of positron emission tomography (PET)/magnetic resonance and PET/computed tomography dosimetry in hepatic malignant neoplastic disease after 90Y radioembolization treatment. *J Gastrointest Oncol*. 2024;15(1):356-367.

doi: 10.21037/jgo-23-890

98. Carlier T, Gnesin S, Mikell JK, *et al*. Discordance between 90Y-PET/CT(MR)-estimated activity and dose calibrator measured administered activity: An international study in SIRT patients treated with resin and glass microspheres. *EJNMMI Phys*. 2025;12(1):12.

doi: 10.1186/s40658-025-00725-8

99. Wong CY, Salem R, Raman S, Gates VL, Dworkin HJ. Evaluating 90Y-glass microsphere treatment response of unresectable colorectal liver metastases by [18F]FDG PET: A comparison with CT or MRI. *Eur J Nucl Med Mol Imaging*. 2002;29(6):815-820.

doi: 10.1007/s00259-002-0787-4

100. Zerizer I, Al-Nahhas A, Towey D, *et al*. The role of early ^{18}F-FDG PET/CT in prediction of progression-free survival after ^{90}Y radioembolization: Comparison with RECIST and tumour density criteria. *Eur J Nucl Med Mol Imaging*. 2012;39(9):1391-1399.

doi: 10.1007/s00259-012-2149-1

101. Haug AR, Heinemann V, Bruns CJ, *et al*. 18F-FDG PET independently predicts survival in patients with cholangiocellular carcinoma treated with 90Y microspheres. *Eur J Nucl Med Mol Imaging*. 2011;38(6):1037-1045.

doi: 10.1007/s00259-011-1736-x

102. Shady W, Kishore S, Gavane S, *et al*. Metabolic tumor volume and total lesion glycolysis on FDG-PET/CT can predict overall survival after (90)Y radioembolization of colorectal liver metastases: A comparison with SUVmax, SUVpeak, and RECIST 1.0. *Eur J Radiol*. 2016;85(6):1224-1231.

doi: 10.1016/j.ejrad.2016.03.029

103. Haug AR, Tiega Donfack BP, Trumm C, *et al*. 18F-FDG PET/CT predicts survival after radioembolization of hepatic metastases from breast cancer. *J Nucl Med*. 2012;53(3):371-377.

doi: 10.2967/jnumed.111.096230

104. Bagni O, Filippi L, Schillaci O. 18F-FDG PET-derived parameters as prognostic indices in hepatic malignancies after 90Y radioembolization: Is there a role. *Eur J Nucl Med Mol Imaging*. 2015. 42(3): 367-369.

doi: 10.1007/s00259-014-2966-5

105. Kennedy AS, Ball DS, Cohen SJ, *et al*. Hepatic imaging response to radioembolization with yttrium-90-labeled resin microspheres for tumor progression during systemic chemotherapy in patients with colorectal liver metastases. *J Gastrointest Oncol*. 2015;6(6):594-604.

doi: 10.3978/j.issn.2078-6891.2015.082

106. Szyszko T, Al-Nahhas A, Canelo R, *et al*. Assessment of response to treatment of unresectable liver tumours with 90Y microspheres: Value of FDG PET versus computed tomography. *Nucl Med Commun*. 2007;28(1):15-20.

doi: 10.1097/MNM.0b013e328011453b

107. Sabet A, Meyer C, Aouf A, *et al*. Early post-treatment FDG PET predicts survival after 90Y microsphere radioembolization in liver-dominant metastatic colorectal cancer. *Eur J Nucl Med Mol Imaging*. 2015;42(3):370-376.

doi: 10.1007/s00259-014-2935-z

108. Bagni O, Filippi L, Schillaci O. The role of (18)F-FDG positron emission tomography in the follow-up of liver tumors treated with (90)Yttrium radioembolization. *Am J Nucl Med Mol Imaging*. 2015;5(3):220-232.

109. Michl M, Lehner S, Paprottka PM, *et al*. Use of PERCIST for prediction of progression-free and overall survival after radioembolization for liver metastases from pancreatic cancer. *J Nucl Med*. 2016. 57(3): 355-360.

doi: 10.2967/jnumed.115.165613

110. Barabasch A, Kraemer NA, Ciritsis A, *et al*. Diagnostic accuracy of diffusion-weighted magnetic resonance imaging versus positron emission tomography/computed tomography for early response assessment of liver metastases to Y90-radioembolization. *Invest Radiol*. 2015;50(6):409-415.

doi: 10.1097/RLI.0000000000000144

111. Barabasch A, Heinzel A, Bruners P, Kraemer NA, Kuhl CK. Diffusion-weighted MRI is superior to PET/CT in predicting survival of patients undergoing 90Y radioembolization of hepatic metastases. *Radiology*. 2018;288(3):764-773.

doi: 10.1148/radiol.2018170408

112. Belhocine T, Foidart J, Rigo P, *et al*. Fluorodeoxyglucose positron emission tomography and somatostatin receptor scintigraphy for diagnosing and staging carcinoid tumours: Correlations with the pathological indexes p53 and Ki-67. *Nucl Med Commun*. 2002;23(8):727-734.

doi: 10.1097/00006231-200208000-00005

113. Filippi L, Scopinaro F, Pelle G, *et al*. Molecular response

assessed by (68)Ga-DOTANOC and survival after (90)Y microsphere therapy in patients with liver metastases from neuroendocrine tumours. *Eur J Nucl Med Mol Imaging*. 2016;43(3):432-440.

doi: 10.1007/s00259-015-3178-3

114. Ingenerf M, Kiesl S, Karim S, *et al*. 68Ga-DOTATATE PET/CT and MRI with diffusion-weighted imaging (DWI) in short- and long-term assessment of tumor response of neuroendocrine liver metastases (NELM) following transarterial radioembolization (TARE). *Cancers* (*Basel*). 2021;13(17):4321.

doi: 10.3390/cancers13174321

115. Hartenbach M, Weber S, Albert NL, *et al*. Evaluating treatment response of radioembolization in intermediate-stage hepatocellular carcinoma patients using 18F-fluoroethylcholine PET/CT. *J Nucl Med*. 2015;56(11):1661-1666.

doi: 10.2967/jnumed.115.158758

116. Bertagna F, Bertoli M, Bosio G, *et al*. Diagnostic role of radiolabelled choline PET or PET/CT in hepatocellular carcinoma: A systematic review and meta-analysis. *Hepatol Int*. 2014;8(4):493-500.

doi: 10.1007/s12072-014-9566-0

117. Glunde K, Bhujwalla ZM, Ronen SM. Choline metabolism in malignant transformation. *Nat Rev Cancer*. 2011;11(12):835-848.

doi: 10.1038/nrc3162

118. Filippi L, Bagni O, Notarianni E, Saltarelli A, Ambrogi C, Schillaci O. PET/CT with 18F-choline or 18F-FDG in hepatocellular carcinoma submitted to 90Y-TARE: A real-world study. *Biomedicines*. 2022;10(11):2996.

doi: 10.3390/biomedicines10112996

119. Aujay G, Debordeaux F, Blanc JF, *et al*. 18F-choline PET-computed tomography for the prediction of early treatment responses to transarterial radioembolization in patients with hepatocellular carcinoma. *Nucl Med Commun*. 2021;42(6):633-638.

doi: 10.1097/MNM.0000000000001383

120. Yoshii Y, Waki A, Furukawa T, *et al*. Tumor uptake of radiolabeled acetate reflects the expression of cytosolic acetyl-CoA synthetase: Implications for the mechanism of acetate PET. *Nucl Med Biol*. 2009;36(7):771-777.

doi: 10.1016/j.nucmedbio.2009.05.006

121. Cheung TT, Ho CL, Lo CM, *et al*. 11C-acetate and 18F-FDG PET/CT for clinical staging and selection of patients with hepatocellular carcinoma for liver transplantation on the basis of Milan criteria: Surgeon's perspective. *J Nucl Med*. 2013;54(2):192-200.

doi: 10.2967/jnumed.112.107516

122. Ho CL, Chen S, Cheung SK, *et al*. Radioembolization with 90Y glass microspheres for hepatocellular carcinoma: Significance of pretreatment 11C-acetate and 18F-FDG PET/CT and posttreatment 90Y PET/CT in individualized dose prescription. *Eur J Nucl Med Mol Imaging*. 2018;45(12):2110-2121.

doi: 10.1007/s00259-018-4064-6

ACCSCIENCE PUBLISHING

Advances in Radiotherapy & Nuclear Medicine

REVIEW ARTICLE

Harnessing yttrium-90 selective internal radiation therapy for primary hepatocellular carcinoma: Mechanisms of action and combination strategies

Yue Chai[1†], Danyang Xu[2†], Yang Zha[3†], and Pinchao Fan[4*]

[1]Hepatobiliary Center, The First Affiliated Hospital of Nanjing Medical University, Key Laboratory of Liver Transplantation, Chinese Academy of Medical Sciences, NHC Key Laboratory of Hepatobiliary Cancers, Nanjing, Jiangsu, China

[2]Department of Chemistry, School of Basic Medical Sciences, Ningxia Medical University, Yinchuan, Ningxia, China

[3]Breast Disease Center, The First Affiliated Hospital of Nanjing Medical University, Nanjing, Jiangsu, China

[4]Department of Oncology, The First Affiliated Hospital of Nanjing Medical University, Nanjing, Jiangsu, China

Abstract

Yttrium-90 selective internal radiation therapy (^{90}Y-SIRT) has emerged as a transformative locoregional modality for primary hepatocellular carcinoma (HCC) with distinct radiobiological advantages and favorable safety profiles. ^{90}Y-SIRT is expected to break through the limitations of conventional treatment by combining it with other systemic therapies in the treatment of liver cancer at all stages. This review systematically examines: (i) The four mechanistic foundations of SIRT's therapeutic efficacy, including precise arterial delivery of microspheres, sustained low-dose-rate β-irradiation, tumor-selective high-dose escalation, and modulation of the tumor immune microenvironment; (ii) clinical evidence supporting its dual role in downstaging advanced HCC with portal vein tumor thrombus and enhancing systemic therapy efficacy in intermediate-stage disease; and (iii) comparative studies demonstrating its superiority over transarterial chemoembolization in terms of tumor response, resectability or transplant conversion, and treatment tolerability. In addition, we discuss emerging directions, including the development of cost-effective domestically manufactured microspheres and the integration of biomarker-guided combination regimens to potentiate immunogenic synergy. By integrating mechanistic insights with clinical validation, this review positions ^{90}Y-SIRT as a central pillar in the evolving landscape of precision medicine for primary HCC.

Keywords: Yttrium-90 selective internal radiation therapy; Primary hepatocellular carcinoma; Microsphere embolization; Low-dose-rate irradiation

1. Introduction

Primary hepatocellular carcinoma (HCC) is known as the most common liver malignancy. HCC often exhibits an insidious onset and rapid progression. Consequently,

[†]These authors contributed equally to this work.

***Corresponding author:**
Pinchao Fan
(njmufpc@stu.njmu.edu.cn)

Citation: Chai Y, Xu D, Zha Y, Fan P. Harnessing yttrium-90 selective internal radiation therapy for primary hepatocellular carcinoma: Mechanisms of action and combination strategies. *Adv Radiother Nucl Med*. 2025;3(4):22-37. doi: 10.36922/ARNM025290037

Received: July 20, 2025

Revised: October 12, 2025

Accepted: October 24, 2025

Published online: December 17, 2025

a majority of patients are diagnosed at intermediate or advanced stages and tend to miss the optimal time window for surgical intervention.[1] Due to its increasing morbidity and mortality, HCC has become the sixth most common malignancy and the third leading cause of cancer-related death worldwide in recent years.[2,3] Patients in intermediate and advanced stages face particularly daunting therapeutic challenges: In real-world practice, systemic therapies, mainly immunotherapy and targeted agents, only achieve objective response rates (ORR) of less than 30%, which remains unsatisfactory.[4-6] Conventional external-beam radiotherapy is constrained by the liver's radiation tolerance, and transarterial chemoembolization (TACE) demonstrates waning efficacy against portal vein tumor thrombus (PVTT) and multifocal lesions. Moreover, repeated TACE procedures would cause ischemia and hypoxia in hepatocytes, exacerbating fibrosis and hepatic injury.[7] These limitations highlight the urgent need for novel treatment paradigms that go beyond palliation and for local therapies with improved efficacy.

Radiolabeled microspheres were first introduced in the 1990s, when researchers delivered glass microspheres carrying radionuclides through the hepatic artery to concentrate radiation within the hypervascular tumor microcirculation.[8] More recently, yttrium-90 selective internal radiation therapy (^{90}Y-SIRT) has revolutionized the landscape of precision radiotherapy.[9] Unlike photon-based external-beam approaches, which are limited by the maximum tolerable physical dose, SIRT employs a dynamic vascular targeting mechanism: ^{90}Y-loaded microspheres embolize tumor-feeding arterioles while continuously emitting β-radiation.[10,11] This dual action delivers intratumoral doses exceeding 150 Gy while keeping exposure of normal liver parenchyma below 30 Gy, a radiobiological breakthrough unattainable with conventional techniques.[12,13] The transformative value of SIRT is apparent in two clinical contexts. In advanced HCC, SIRT induces regression of PVTT, facilitates conversion to resectable status, and improves the 3-year overall survival (OS) rate after curative resection.[14,15] In intermediate-stage HCC, SIRT remodels the tumor microenvironment by upregulating programmed cell death ligand 1 (PD-L1) expression and normalizing vasculature, thereby significantly enhancing the delivery and efficacy of systemic agents.[16] SIRT is redefining the standard of care. It surpasses conventional TACE (cTACE) in thrombus penetration, single-session feasibility, and tolerability in Child–Pugh B patients, establishing itself as the optimal local therapy.[17,18] Early combination trials, such as the NASIR-HC trial, which reported an ORR of 41.5%, suggested that SIRT would become a cornerstone of next-generation treatment regimens for HCC.[19] However, a comprehensive analysis of its mechanistic innovations, clinical translation pathways, and multidisciplinary integration strategies is still needed.

This review mainly addresses three key areas: First, the radiobiological mechanisms that enable SIRT's dose escalation; second, a systematic evaluation of its dual clinical benefits in enhancing systemic therapy for intermediate HCC and downstaging advanced HCC; and thirdly, an evidence-based comparison of efficacy and toxicity versus TACE to establish its therapeutic superiority. Beyond, we also explore future developments, including domestically produced microspheres that may reduce costs, and biomarker-guided sequential therapy optimization. Furthermore, it is noteworthy that although the core mechanism of action, selective embolization and sustained beta radiation delivery, remains consistent across different microsphere carrier types, significant distinctions may arise in dosimetry calculation methodologies, recommended activity levels for administration, and the optimal selection for specific clinical scenarios (*e.g.*, tumor size, vascularity, or prior treatments). Currently, clinical guidelines do not establish a definitive preference for one microsphere type over the other. By anchoring SIRT within the paradigm of precision medicine, we aim to accelerate its adoption as a foundational, potentially curative modality for liver cancer.

2. The four mechanistic pillars of SIRT

^{90}Y-SIRT is a form of internal radiotherapy that delivers radioactive microspheres directly into the tumor-feeding arteries through hepatic arterial catherization.[20] This action delivers intratumoral doses exceeding 150 Gy while significantly reducing exposure of normal liver parenchyma to below 30 Gy, a radiobiological breakthrough unattainable with conventional techniques.[21] Its core mechanism leverages the fact that hepatic tumors primarily receive their blood supply from the hepatic artery, allowing for selective targeting of arterial blood flow to achieve high-dose localized radiation within the tumor (with an average tissue penetration of approximately 2.5 mm) while sparing the surrounding normal liver parenchyma.[21] SIRT is administered according to a rigorous, well-defined procedural workflow (Figure 1). Before treatment, comprehensive patient selection and baseline evaluation are required from clinical, imaging, and hepatic functional reserve perspectives. Simulation of ^{90}Y microsphere distribution is performed using ^{99m}Tc-macroaggregated albumin (^{99m}Tc-MAA) single-photon emission computed tomography/computed tomography (SPECT/CT) to assess the lung shunt fraction and the risk of gastrointestinal shunting. Within 2 weeks following the ^{99m}Tc-MAA simulation, TARE treatment is administered, followed by

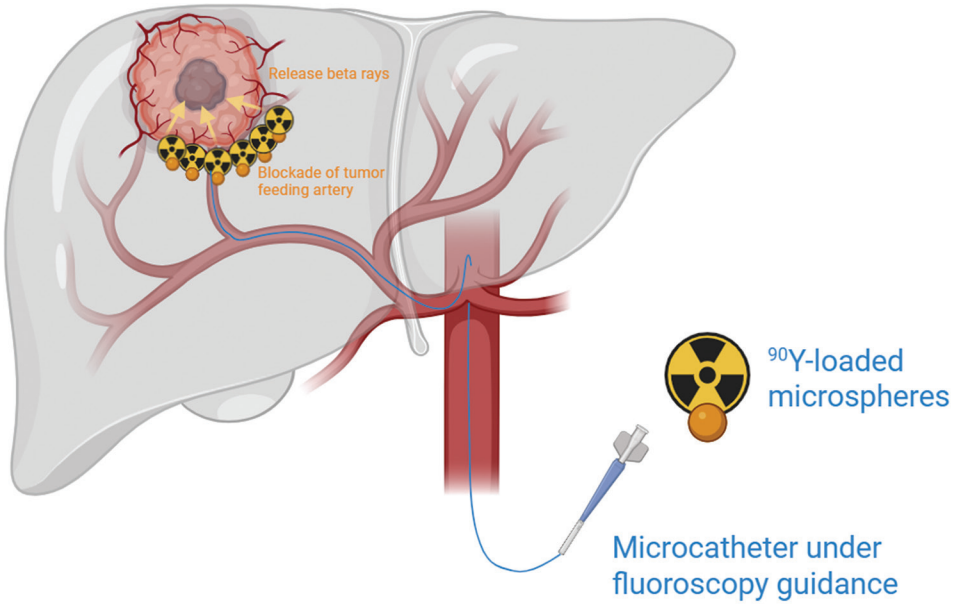

Figure 1. Schematic illustration of selective internal radiation therapy (SIRT) with yttrium-90 (^{90}Y) to treat hepatocellular carcinoma. A microcatheter is advanced under fluoroscopic guidance to selectively deliver ^{90}Y-loaded microspheres into the tumor-feeding hepatic artery. The ^{90}Y-loaded microspheres then lodge within the tumor vasculature, inducing tumor cell death by dual effects: Microembolization of the feeding artery, and localized irradiation via β-rays. Schematic created in BioRender. Yu, N. (2026) https://BioRender.com/mb4bsa8.

positron emission tomography/computed tomography (PET/CT) imaging within 24 h post-procedure to confirm microsphere distribution and absorbed dose. One month after treatment, contrast-enhanced magnetic resonance imaging (MRI) is conducted to evaluate tumor response according to RECIST 1.1 or mRECIST criteria.[22,23] Several mechanisms based on vascular targeting help to explain the advantages of this therapy.

2.1. Vascular-targeted radionuclide delivery

SIRT microspheres, with diameters ranging 20–60 μm, are selectively retained in the tumor vasculature through a size-dependent entrapment mechanism.[24] Administered through hepatic arterial infusion, these microspheres deliver ^{90}Y directly and precisely into the tumor-feeding arteries. Once reaching the tumor microcirculation, they become lodged within the malignant tissue, effectively localizing radionuclide deposition to the tumor site. This process not only disrupts oxygen and nutrient supply to the tumor, but also anchors radioactive particles within the tumor bed, enabling sustained, highly selective irradiation of the lesion core while minimizing damage to the surrounding normal hepatic parenchyma.[25]

Conventional two-dimensional external beam radiotherapy (EBRT) has been largely replaced by emerging technologies in the treatment of HCC. In earlier approaches, whole-liver irradiation with doses of 30–35 Gy frequently resulted in radiation-induced liver disease in 5–10% of patients. However, effective tumor control typically requires doses exceeding 50 Gy, creating an inherent conflict between treatment efficacy and safety. Low-dose whole-liver irradiation yields poor local control rates for HCC, and most early cooperative group trials reported suboptimal tumor responses. As a result, conventional EBRT has been primarily confined to palliative settings in clinical studies and has been nearly abandoned for curative treatment.[26,27] In contrast to EBRT, the principal advantage of SIRT lies in its "inside-out" treatment mechanism. By utilizing interventional techniques to deliver radioactive microspheres directly into the tumor vasculature, SIRT achieves superior dose distribution and coverage, particularly in the treatment of large tumors, multifocal lesions, and HCC complicated by PVTT. This makes it a powerful tool for downstaging and conversion therapy, often enabling initially unresectable cases to become eligible for curative interventions.

At the same time, it is essential to recognize that modern EBRT techniques, particularly SBRT, deliver highly conformal, ablative-dose irradiation per fraction, which induces unique radiobiological effects.[28] These include significant vascular endothelial damage and potent immune activation, potentially eliciting systemic anti-tumor responses such as the abscopal effect.[29] Consequently, SBRT offers irreplaceable value in treating small- to medium-sized tumors in high-risk locations (*e.g.*, adjacent to the gastrointestinal tract or central biliary structures),

where precision is paramount to avoid off-target toxicity. As a result, rather than being competing modalities, SIRT and SBRT represent complementary strategies within the armamentarium of liver-directed radiotherapy. The choice between them should be guided by a multidisciplinary team based on a comprehensive assessment of tumor morphology, anatomic location, hepatic functional reserve, and individual patient profiles, ultimately moving toward a more personalized and optimized treatment paradigm for liver malignancies.

2.2. Sustained low-dose-rate (LDR), high-intensity irradiation

^{90}Y is a high-energy β-emitting radionuclide that delivers sustained radiation from its microsphere carriers once they are lodged in the tumor microvasculature.[30] ^{90}Y can effectively target both the periphery and the deeper zones of solid tumors, making it especially suitable for treating bulky or hypoxic regions that are typically resistant to conventional therapies.[31] Unlike EBRT, which delivers radiation in short, fractionated bursts, ^{90}Y emits continuously over several days, offering a unique LDR irradiation profile with potent radiobiological consequences.[27]

The β-particles released by ^{90}Y have an average energy of 0.94 MeV and a physical half-life of 64.1 h, resulting in continuous therapeutic irradiation for over 72 h.[32] This prolonged exposure induces cumulative sublethal and lethal DNA damage in tumor cells.[33] In particular, the sustained LDR radiation saturates the base excision repair pathway, which is primarily responsible for repairing single-strand DNA breaks.[34] Once saturated, the repair capacity is exceeded, leading to the accumulation of irreparable double-strand DNA breaks, which are highly cytotoxic and often trigger mitotic catastrophe or apoptosis.[35]

Continuous LDR irradiation prolongs the exposure duration, thereby increasing the likelihood of tumor cells being irradiated during the radiosensitive G2/M phase of the cell cycle.[36] In contrast, the intermittent dosing schedule of fractionated EBRT allows tumor cells to repair DNA damage and transition into radioresistant phases between treatments.[37] This temporal discrepancy may limit the therapeutic efficacy of EBRT, particularly in highly proliferative malignancies such as primary HCC.

2.3. Tumor-selective dose escalation

SIRT can maintain radiation exposure to normal liver parenchyma below 30 Gy while delivering a tumor-absorbed dose exceeding 150 Gy, thereby overcoming the dose-escalation barrier imposed on EBRT by whole-liver tolerance thresholds (30–35 Gy). Both clinical and preclinical data have demonstrated a clear dose-response relationship. In the DOSISPHERE-01 phase II randomized trial, intermediate-stage HCC patients receiving a tumor-absorbed dose ≥205 Gy achieved an ORR of 71%, compared with 36% in the standard-dose arm (≥120 Gy); median OS increased 10.7–26.6 months, establishing the dose-dependent efficacy of SIRT in human.[38] *In vitro* assays and murine xenograft models showed that when the local biologically effective dose exceeds 200 Gy, tumor cells accumulate significantly more double-strand DNA breaks and their survival fraction falls below 10%, confirming the cytocidal impact of ultra-high dosing at the cellular level.[31,39] By contrast, conventional EBRT must restrict whole-liver doses to 30–35 Gy or limit partial-volume doses (*e.g.*, 50% hepatic volume) to ≤45 Gy to keep the risk of radiation-induced liver disease within acceptable bounds.[40] As a result, EBRT cannot achieve comparable intratumoral dose deposition. SIRT's microspheres lodge selectively in the terminal arterioles of the tumor microvasculature, confining the bulk of β-radiation to the lesion while diluting exposure to healthy liver, which is called a dose-concentrated, toxicity-dispersed paradigm. Moreover, modern personalized dosimetry techniques, including medical internal radiation dose-based activity planning and post-treatment SPECT/CT or ^{90}Y-PET three-dimensional dose reconstruction, allow clinicians to tailor administered activities for each patient. This approach maximizes intratumoral dosing while ensuring that normal liver exposure remains below 30 Gy, thereby optimizing the efficacy-safety balance.[39,41]

In summary, through highly selective embolization combined with continuous β-radiation delivery, SIRT achieves ultra-high intratumoral doses (>150 Gy) without increasing the risk of injury to normal hepatic tissue. This mechanistic advantage provides robust theoretical and clinical support for intensifying radiotherapeutic regimens, improving local control, and downstaging unresectable liver tumors.

2.4. Modulation of the tumor immune microenvironment

SIRT not only exerts direct cytotoxicity on tumor cells through ionizing radiation, but also remodels the tumor immune microenvironment through multiple mechanisms, thereby creating a more favorable milieu for subsequent immunotherapy and targeted therapies[42] (Figure 2). First, SIRT releases tumor-associated antigens (TAAs) and damage-associated molecular patterns (DAMPs, such as HMGB1 and ATP), which promote dendritic cell maturation and antigen presentation, activating tumor-specific T-cell responses; within an optimal dose range, it also diminishes infiltration of

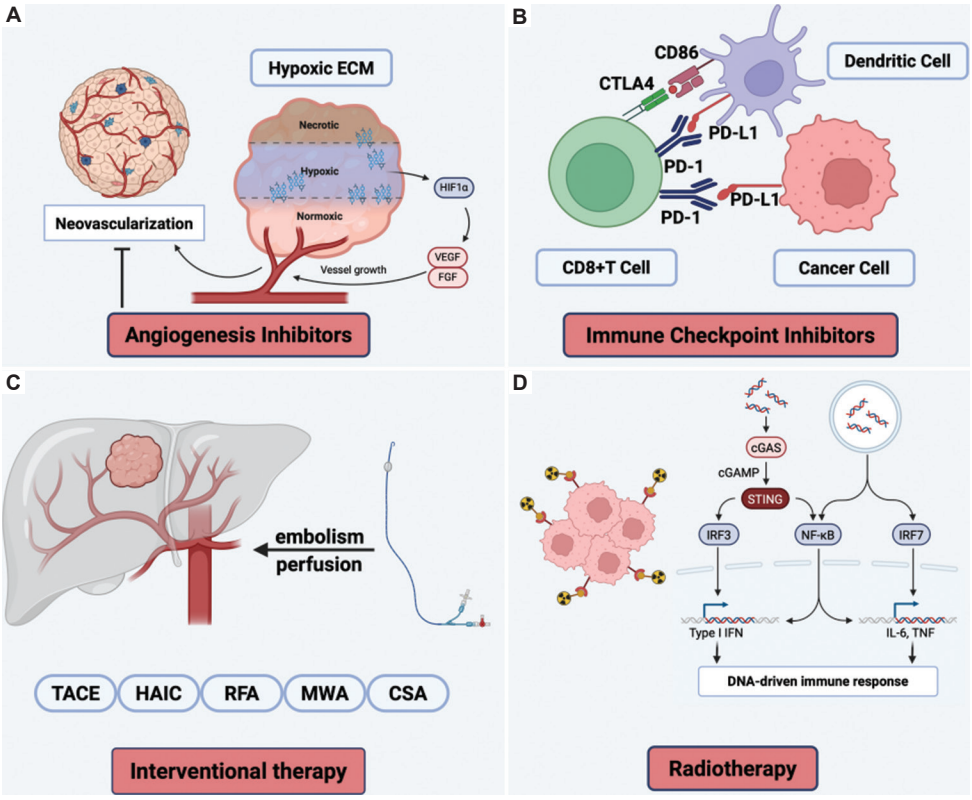

Figure 2. Mechanisms underlying the synergy between SIRT and adjunctive treatment modalities. (A) Combination with anti-angiogenic agents: SIRT delivers β-emitting microspheres selectively to tumor-feeding arterioles, inducing localized vascular injury and hypoxia that activate the HIF-1α pathway. This, in turn, upregulates VEGF and FGF secretion and promotes neovascularization. Co-administration of anti-angiogenic agents (*e.g.*, inhibitors of ECAM, VEGF, or FGF signaling) disrupts this compensatory vascular remodeling, thereby enhancing radiation-induced cytotoxicity and mitigating immune escape. (B) Combination with immune checkpoint inhibitors: In addition to direct tumor cell decimation, SIRT-induced cell death releases tumor-associated antigens (TAAs) and damage-associated molecular patterns (DAMPs), fostering dendritic cell maturation and $CD8^+$ T-cell recruitment, and upregulating PD-L1 expression within the tumor microenvironment. Concurrent blockade of PD-1/PD-L1 or CTLA4 checkpoints relieves T-cell inhibition and amplifies tumor-specific antitumor immunity. (C) Combination with interventional therapies: SIRT can be integrated with other locoregional interventions, such as TACE, HAIC, RFA, MWA, or CSA, to achieve multimodal synergy. The embolic effect of microspheres, when combined with thermal ablation or regional chemotherapy, not only obstructs tumor perfusion but also enables more comprehensive local tumor eradication through sustained thermal or radiative insult. (D) Combination with EBRT and the cGAS-STING-mediated radiogenic immune response: When used alongside EBRT, SIRT-induced DNA damage and the release of fragmented nuclear DNA activate the cGAS-STING axis, triggering downstream IRF3, NF-κB, and IRF7 signaling. This cascade elicits type I IFN production and proinflammatory cytokines (*e.g.*, IL-6, TNF), thereby initiating a systemic, DNA-driven immune response that potentiates both radiotherapeutic and immunotherapeutic efficacy. Schematic created in BioRender. Yu, N. (2026) https://BioRender.com/ck444yw.
Abbreviations: CSA: Cyrosurgical ablation; CTLA4: Cytotoxic T-lymphocyte-associated protein 4; EBRT: External-beam radiation therapy; ECAM: Endothelial cell adhesion molecule; ECM: Extracellular matrix; FGF: Fibroblast growth factor; HAIC: Hepatic arterial infusion chemotherapy; HIF-1α: Hypoxia-inducible factor-1 alpha; IFN: Interferon; IL: Interleukin; IRF: Interferon regulatory factor; MWA: Microwave ablation; NF-κB: Nuclear factor kappa B; PD-L1: Programmed death-ligand 1; PD-1: Programmed cell death protein 1; RFA: Radiofrequency ablation; SIRT: Selective internal radiation therapy; TACE: Transarterial chemoembolization; TNF: Tumor necrosis factor; VEGF: Vascular endothelial growth factor.

regulatory T cells (Tregs) and myeloid-derived suppressor cells, although higher doses or repeated treatments can upregulate immune checkpoints such as PD-L1 and CTLA-4, intensifying immunosuppression, and in rare instances provoke an abscopal effect.[43,44] Second, low-dose SIRT (≤2 Gy) transiently "normalizes" tumor vasculature to improve oxygenation and drug delivery, whereas higher doses (>8 Gy) tend to disrupt vessels and exacerbate hypoxia. Concurrently, SIRT activates cancer-associated fibroblasts (CAFs) to secrete matrix metalloproteinases (MMPs), remodeling the extracellular matrix (ECM) in ways that both facilitate invasion and can form physical barriers to immune cell infiltration.[45,46] Third, radiation induces increased collagen crosslinking, stiffening the ECM and, through activation of transforming growth factor beta and nuclear factor kappa B pathways, enhances deposition of ECM components (*e.g.*, fibronectin and hyaluronan), thereby promoting fibrosis and fortifying an immunosuppressive barrier.[47] Fourth, although the transient vascular normalization phase can alleviate hypoxia, prolonged high-dose SIRT disrupts the microvascular network, leading to regional hypoxia,

hypoxia-inducible factor 1 alpha (HIF-1α) activation, drug resistance and invasiveness; it also drives metabolic reprogramming toward glycolysis (the Warburg effect) and lactate accumulation, which impair effector T-cell function and skew macrophages toward an M2 phenotype.[48-50] Finally, combining SIRT with immune checkpoint inhibitors (ICIs, such as anti-PD-1, anti-PD-L1, or anti-CTLA-4), particularly using hypofractionated low-dose regimens, amplifies immunogenic cell death and systemic antitumor immunity, thereby overcoming "cold" tumor resistance. Moving forward, precise optimization of dose and timing, together with strategic integration of immunotherapy and targeted therapies, will be critical to maximize efficacy and reverse the immunosuppressive microenvironment.[51,52]

3. Comparative advantages of SIRT over other locoregional therapies

Both SIRT and TACE are commonly used locoregional therapies for liver tumors; however, SIRT demonstrates significant advantages over TACE in terms of tumor response and treatment safety. SIRT achieves higher tumor response rates and downstaging potential. The radioactive microspheres used in SIRT emit high-energy β-particles, enabling more precise and concentrated cytotoxic effects on tumor tissue, thereby improving response rates. Another benefit of SIRT over TACE is the potential ability of SIRT to treat larger tumors, while TACE benefit is reduced in tumors >7 cm.[53] For instance, in a randomized controlled trial comparing SIRT and TACE for unresectable HCC,[54] there was a trend that patients treated with radioembolization had a higher response rate than with chemoembolization (49% vs. 36%, p=0.104). Although time-to-progression was longer following radioembolization than chemoembolization (13.3 months vs. 8.4 months, p=0.046), median survival time was not statistically different (17.4 months vs. 20.5 months, p=0.232). SIRT can create more opportunities for subsequent curative treatments, such as liver transplantation or radiofrequency ablation. SIRT is also particularly effective in specific tumor types. For example, in highly vascular liver tumors, especially those resistant or poorly responsive to chemotherapeutic agents, SIRT offers unique therapeutic advantages. In addition, in cases of diffuse intrahepatic tumor spread or major vascular invasion, where TACE is often ineffective or contraindicated, SIRT remains a viable and effective alternative.[55,56]

In addition, comparative studies have evaluated ^{90}Y-SIRT against drug-eluting bead TACE (DEB-TACE) for early- and intermediate-stage HCC. Dhondt *et al.*[57] followed 32 patients treated with ^{90}Y-SIRT and 34 patients treated with DEB-TACE. The TARE group demonstrated significantly longer median time to progression (TTP) and OS, while rates of severe adverse events and 30-day mortality were comparable between the two groups. In conclusion, ^{90}Y-SIRT offers superior tumor control and survival benefits in patients with Barcelona Clinic Liver Cancer (BCLC) Stage A and B HCC, while maintaining a safety profile comparable to that of conventional locoregional therapies.

Meanwhile, SIRT requires fewer treatment sessions compared to TACE. In current clinical practice, SIRT typically involves only one to two treatment sessions, whereas TACE often necessitates four to ten or even more sessions to achieve comparable therapeutic outcomes.[58] This allows patients undergoing SIRT to complete their treatment course more rapidly. SIRT also causes less arterial injury to tumor-feeding vessels. The embolic agents used in TACE can damage the arterial walls supplying the tumor, and repeated TACE procedures may lead to vascular occlusion, thereby limiting future treatment options.[59,60] In contrast, the microspheres used in SIRT are smaller in size and cause relatively minimal vascular injury. This helps maintain the patency of tumor-feeding arteries, preserving the possibility of additional locoregional therapies, such as ablation or repeated intervention, if needed.

SIRT offers greater advantages over TACE in the conversional treatment of liver malignancies complicated by PVTT. PVTT refers to malignant thrombi formed by HCC cells invading the portal venous system and proliferating intravascularly. It is a hallmark of advanced-stage HCC, occurring in approximately 40–60% of patients with late-stage disease.[61] HCC cells infiltrate the main trunk or branches of the portal vein through hepatic sinusoids or small portal venules, forming tumor thrombi characterized by neovascularization, with progressive extension either proximally or distally, sometimes resulting in complete obstruction of the portal vein. Mechanistically, epithelial–mesenchymal transition enhances the migratory capacity of cancer cells, characterized by downregulation of E-cadherin and upregulation of vimentin. Concurrently, MMPs degrade the vascular basement membrane, facilitating the formation and spread of PVTT. The presence of PVTT is a strong negative prognostic factor in HCC. Detached tumor thrombi can lead to multiple intrahepatic metastases, with approximately 80% of PVTT patients showing intrahepatic dissemination.[62] Without treatment, the median survival of PVTT patients is only 2–4 months, significantly lower than that of patients without PVTT (12–18 months).[63] With hepatic resection as monotherapy, the 5-year survival rate and median survival time were reportedly 4–28.5% and 6–14 months, respectively.[64]

Beyond systemic therapies, locoregional treatments play a critical role in the management of PVTT-complicated HCC. TACE is suitable for well-vascularized Vp1 to Vp2 tumor thrombi, but poses a high risk in more advanced cases, where it may cause complete portal vein occlusion. Hepatic arterial infusion chemotherapy (HAIC), commonly using 5-fluorouracil plus platinum-based regimens, has shown superior efficacy and is considered a mainstream approach for PVTT. However, chemotherapy-associated myelosuppression can compromise subsequent treatments.[61] SIRT, by contrast, is applicable across all PVTT types and demonstrates superior efficacy in poorly vascularized tumor thrombi compared to TACE.[65] In a systematic review of 722 HCC patients with portal vein tumor thrombosis treated with ^{90}Y-SIRT, the median complete response (CR) rate was 3.2%, with a partial response (PR) rate of 16.5%, and a median OS of 9.7 months (12.1 months for Child–Pugh A and 6.1 months for B).[66] There is currently a lack of head-to-head phase III randomized controlled trials comparing SIRT with TACE or HAIC. Most available conclusions are derived from retrospective or indirect comparative studies. Some investigations indirectly suggest a pivotal role for SIRT in this therapeutic setting. Hur *et al.*[67] conducted a multicenter clinical trial in Korea involving 216 patients with locally advanced HCC and concurrent PVTT. Their results demonstrated that patients receiving transarterial radioembolization (TARE) achieved a median OS of 28.2 months, significantly superior to the 7.2 months observed in patients treated with tyrosine kinase inhibitors (TKIs) (p<0.001). While progression-free survival (PFS) was similar between the two groups, the TARE group exhibited a trend toward extended survival in the Vp1 or Vp2 PVTT subgroups (p=0.052). The objective response rate was 53.0–56.7% in the TARE group, markedly higher than the 12.3–15.0% in the TKI group. For advanced HCC patients with preserved liver function, TARE may provide superior OS compared to TKI therapy. Further data remain necessary to compare efficacy differences among TACE, HAIC, and SIRT.

4. Applications of ^{90}Y-SIRT in BCLC stage A and B HCC

In the conversion therapy for patients with HCC classified as BCLC stages A and B, ^{90}Y-SIRT demonstrates potential benefits (Table 1). First, as preoperative conversion therapy for hepatectomy: For patients with insufficient future liver remnant (FLR) volume after radical resection, ^{90}Y-SIRT can stimulate rapid hepatic hypertrophy, thereby converting an inadequate FLR to a sufficient FLR that meets the requirements for hepatectomy. For patients who cannot achieve R0 resection or are oncologically ineligible for surgery, ^{90}Y-SIRT may enable tumor downstaging or volume reduction. Second, as preoperative conversion therapy for liver transplantation: In patients exceeding standard liver transplantation criteria, ^{90}Y-SIRT can reduce tumor burden and achieve downstaging, potentially allowing such patients to qualify for transplantation. It has been reported that in conversion therapy for HCC, locally directed therapies combined with systemic regimens exhibit varying success rates. Specifically, the conversion success rate for HAIC combined with systemic therapy ranges 12.8–64.3%, while that for TACE combined with systemic therapy ranges 11.5–57.6%. In contrast, ^{90}Y-SIRT combined with systemic therapy may achieve a significantly higher conversion success rate.[68]

4.1. Conversion downstaging therapy

^{90}Y holds significant value in the conversion therapy of primary HCC. ^{90}Y radiation lobectomy achieves tumor control while simultaneously inducing hypertrophy of the FLR. When the tumor is confined to a unilateral liver lobe, transarterial radiotherapy with ^{90}Y microspheres targeting the affected lobe induces atrophy of the treated lobe and controls the spread of vascular pathology. This process promotes compensatory hypertrophy of the contralateral lobe. The mechanism underlying FLR enlargement involves ^{90}Y-induced hepatic fibrosis and remodeling in the treated region, where radiation and embolic effects on the lobar vasculature cause ipsilateral atrophy. Consequently, the contralateral lobe undergoes compensatory enlargement due to increased blood flow and activation of hepatocyte proliferative signaling pathways.[73,74] Birgin *et al.*[75] systematically analyzed ^{90}Y-SIRT studies published between 2008 and 2020, demonstrating an intrahepatic tumor control rate of 84% following SIRT. Moreover, within 2–3 months post-SIRT, the degree of FLR hypertrophy in most patients had met the requirements for surgical resection.

Radiation lobectomy, which aims to induce hypertrophy of the FLR through targeted irradiation, requires precise dosimetric planning to ensure effective tumor control while stimulating contralateral lobe growth without causing radiation-induced liver disease. Key dose thresholds include ≥88 Gy to non-tumorous parenchyma and ≥205 Gy to tumor for glass microspheres using the partition model, or ≥70 Gy and ≥250 Gy for resin microspheres, respectively. This approach is recommended for Child–Pugh A patients, with FLR volume assessment at 3–6 months post-treatment to evaluate hypertrophy efficacy.[76]

Evidence-based studies involving patients with BCLC Stage A and B HCC have demonstrated that ^{90}Y-SIRT

Table 1. Application of ^{90}Y-SIRT in the treatment of BCLC stage A/B HCC

Clinical setting	Study	Population	Objective	Treatment	Key results	References
Liver transplantation after downstaging for HCC	PREMIERE	BCLC A/B	To compare the therapeutic effect of cTACE and SIRT in patients with HCC.	SIRT versus cTACE	Median TTP: >26 months for ^{90}Y-SIRT versus 6.8 months for cTACE, *P*=0.0012.	69
	UNOS T3 Downstaging	UNOS T3 (mainly BCLC B)	To evaluate TACE and SIRT in the treatment of patients with UNOS T3.	SIRT versus TACE	Downstaging rate (UNOS T3 to T2): 58% for SIRT versus 31% for TACE, *P*=0.023; Significantly better TTP and OS in the SIRT group.	70
Partial hepatectomy after downstaging for HCC	RASER	Measurable lesions ≤3 cm; ECOG PS 0; unresectable and unsuitable for ablation	To evaluate the safety and effectiveness of RS in patients with unresectable HCC and unsuitable for ablation.	High-dose SIRT radiation ablation of hepatic segments	ORR: 100%; Complete remission rate at 6 weeks: 83%.	71
	LEGACY	Unresectable single HCC ≤8 cm	To evaluate the effect of RS in the treatment of unresectable HCC with single tumor≤8 cm.	High-dose SIRT radiation ablation of hepatic segments	Best ORR: 88.3%; 2-year PFS rate for target lesion: 93.9%.	72
	TRACE	BCLC B; BCLC A not suitable for radical treatment; ECOG PS 0-1	To compare the efficacy and safety of SIRT and DEB-TACE in the treatment of unresectable early and middle stage HCC.	SIRT versus DEB-TACE	Median TTP: 17.1 months (SIRT) versus 9.5 months (DEB-TACE), HR 0.36, *P*=0.002; Median OS: 30.2 versus 15.6 months, HR 0.48, *P*=0.006.	57

Abbreviations: BCLC: Barcelona Clinic Liver Cancer; cTACE: Conventional transarterial chemoembolization; DEB-TACE: Drug-eluting bead transarterial chemoembolization; ECOG PS: Eastern Cooperative Oncology Group Performance Status; HCC: Hepatocellular carcinoma; HR: Hazard ratio; ORR: Objective response rate; OS: Overall survival; PFS: Progression-free survival; RS: Radiation segmentectomy; SIRT: Selective internal radiation therapy; TACE: Transarterial chemoembolization; TTP: Time to progression; UNOS: United Network for Organ Sharing.

provides significant benefits in tumor control, prolongation of liver transplant waiting periods, downstaging to meet transplant criteria, and even achieving long-term curative outcomes. Salem *et al.*[69] conducted a phase II prospective randomized controlled trial comparing ^{90}Y-SIRT with cTACE in patients with HCC undergoing downstaging to meet liver transplantation criteria. The median TTP in the ^{90}Y-SIRT group exceeded 26.0 months, substantially longer than the 6.8 months observed in the cTACE group (*p*=0.0012). Another retrospective, single-center, dual-arm study provided preliminary evidence that ^{90}Y-SIRT is significantly more effective than TACE in patients not initially eligible for prioritized liver transplantation, with superior downstaging rates and OS.[70] A multidisciplinary expert consensus from the United States recommended the use of ^{90}Y-SIRT for downstaging to liver transplantation, with key indications including: tumor diameter exceeding 5 cm, presence of PVTT, or multiple small lesions (>3 nodules) within the same hepatic lobe.[77]

4.2. Radiation segmentectomy (RS)

For even earlier-stage HCC, RS has emerged as a potentially curative strategy.[78] RS aims to ablate both the primary tumor and adjacent microscopic satellite lesions, thereby reducing the risk of recurrence. This technique involves delivering a high dose of ^{90}Y-labeled microspheres to one or two hepatic segments in which the tumor is localized, resulting in targeted tumor ablation and segmental atrophy. Kim *et al.*[71] conducted the RASER trial, a prospective study evaluating outcomes in patients with early-stage HCC deemed unsuitable for resection or thermal ablation. In this study, "unfavorable ablation sites" were defined as lesions located within 5 mm of critical structures such as the portal vein, hepatic vein, inferior vena cava, diaphragm, heart, stomach, intestine, liver capsule, gallbladder, or bile duct. The trial reported an ORR of 100% within 6 weeks post-RS, with a median duration of objective response reaching 635 days. Salem *et al.*[72] carried out the LEGACY study, a retrospective analysis of 162 patients with single, unresectable HCC tumors smaller than 8 cm in maximum diameter. In this cohort, RS achieved a regional best ORR of 88.3%, with a 2-year PFS rate of 93.9%. These studies collectively highlight the advantages and indications of ^{90}Y-SIRT-based RS over other ablative methods: It does not require percutaneous puncture, thereby eliminating the risk of needle-track seeding; it is delivered through

a minimally invasive transarterial route, reducing the burden of anesthesia; microspheres naturally follow the tumor's arterial supply and can cover satellite lesions through super-selective catheterization, which may reduce the incidence of microvascular invasion; and digital subtraction angiography enables precise localization of small or occult lesions.[79,80]

5. Synergistic applications of SIRT with immunotherapy and targeted therapy

SIRT-mediated remodeling of the tumor microenvironment and its immunomodulatory synergy have become increasingly recognized. By embolizing tumor-feeding arteries, SIRT reduces aberrant vascular density, thereby improving oxygenation, inhibiting the HIF-1α pathway, and alleviating immunosuppression. The high-dose radiation delivered by SIRT induces tumor cells to release DAMPs and neoantigens, which promote dendritic cell maturation and $CD8^+$ T-cell priming, thereby "fueling" subsequent immunotherapy. The triplet regimen of radiotherapy, immunotherapy, and targeted therapy holds significant translational potential: SIRT liberates neoantigens, ICIs activate T cells, and TKIs suppress tumor angiogenesis and immune escape, collectively forming a closed-loop

Table 2. Clinical trials of ^{90}Y-SIRT combined with ICIs, TKIs, or both in HCC

Combination	Study	Population	Treatment	Scale	Key results	References
Combined with ICIs	CA 209-678	Child–Pugh A cirrhosis and advanced HCC are not suitable for curative surgery.	SIRT+Nivo	36	ORR: 30.6% mPFS: 5.6 months mOS: 16.9 months	52
	Lee *et al.*	Child–Pugh score ≤7 and locally advanced HCC, defined as BCLC stage B HCC or BCLC-C disease without extrahepatic metastases.	SIRT+Durva	24	mTTP: 15.2 months ORR: 83% mPFS: 6.9 months	83
	Yu *et al.*	Eligible patients had poor prognosis, localized HCC defined as having PVT, multifocal disease, and/or diffuse disease that were not eligible for liver transplant or surgical resection.	SIRT+Pembro	29	ORR: 30.8% mPFS: 9.95 months mOS: 27.3 months	84
	Zhan *et al.*	Patients had preserved liver function (Child–Pugh scores A-B7) and either advanced HCC due to macrovascular invasion or limited extrahepatic disease or aggressive intermediate stage HCC.	SIRT+Nivo	26	ORR: 24% TTP: 5.7 months mOS: 17.2 months	85
	NASIR-HCC	BCLC B2 substage (single or multiple tumors beyond the up-to-7 rule), or unilobar tumors with segmental or lobar PVI; no extrahepatic spread; and preserved liver function.	SIRT+Nivo	42	ORR: 41.5% mTTP: 8.8 months mOS: 20.9 months	19
Combined with TKIs	SORAMIC	BCLC B/C	SIRT+Sora	424	mOS: 12.1 months	81
	NCT0071279	BCLC B/C	SIRT+Sora	29	ORR: 25% mPFS: 15.2 months mOS: 20.3 months	86
	Salman *et al.*	Eligible patients with unresectable HCC and a life expectancy of at least 12 weeks.	SIRT+Sora	29	ORR: 31% mOS: 12.4 months	87
Combined with both ICIs and anti-angiogenic agents	Villalobos *et al.*	HCC with T+A or Nivo received within 3 months before and after ^{90}Y-RE	^{90}Y: liver segment ≥150 Gy, liver lobe >120 Gy plus T+A or Nivo	19	ORR: 60% versus 56% mOS: 10.7 months versus 16.4 months	88
	Mejait *et al.*	Child-Pugh A HCC treated with SIRT	SIRT+T+A or not	35	ORR: 87% versus 60% mPFS: 11.3 months versus 5.8 months	89

Abbreviations: BCLC: Barcelona Clinic Liver Cancer; DCR: Disease control rate; Durva: Durvalumab; HCC: Hepatocellular carcinoma; ICIs: Immune checkpoint inhibitors; mOS: Median overall survival; mPFS: Median progression-free survival; Nivo: Nivolumab; ORR: Objective response rate; Pembro: Pembrolizumab; PVI: Portal vein invasion; PVT: Portal vein thrombus; RE: Radioembolization; Sora: Sorafenib; T+A: Atezolizumab+Bevacizumab; TKIs: Tyrosine kinase inhibitors; TTP: Time to progression.

antitumor therapeutic circuit. This novel combination strategy represents a breakthrough that transcends traditional monotherapy approaches. Since 1998, a series of clinical trials have investigated the therapeutic strategies of ^{90}Y-SIRT, ranging from monotherapy to combination with either targeted therapy or immunotherapy, and even dual combination with both (Table 2). The SORAMIC trial indicated that although SIRT combined with sorafenib did not significantly improve OS in the experimental group, it substantially enhanced local tumor control.[81] Moreover, certain subgroups, such as patients without cirrhosis, younger patients, and those with non-alcoholic fatty liver disease-related HCC, may derive potential benefit. However, limitations of the trial included the lack of effective second-line therapy after disease progression, which may have diminished the synergistic effect and potential benefits of ^{90}Y-SIRT. Craciun *et al.*[82] found that ^{90}Y-SIRT, compared with TACE or no preoperative therapy, significantly enhanced the recruitment and activation of intratumoral effector immune cells. These findings suggest that ^{90}Y-SIRT may be a superior candidate to TACE when used in combination with immunotherapy strategies. Consequently, prospective studies are needed to further determine the optimal radiation dose of ^{90}Y-SIRT for inducing immunogenic effects and to identify the most effective types of immune checkpoint inhibitors for combination. Regarding the optimal sequencing of therapies, some investigators recommend administering SIRT first, followed by immunotherapy after an interval of 1–2 weeks, to avoid potential lymphocyte depletion associated with concurrent treatment. Studies have explored the combination of ^{90}Y-SIRT and nivolumab in unresectable HCC.[19,52]

A retrospective study by Yeo *et al.*[90] included 1,664 patients with advanced HCC (TNM stage III/IV) who received either first-line ^{90}Y-SIRT plus immunotherapy or immunotherapy alone. Subgroup analysis demonstrated a significantly longer median OS in the combination group (24.4 months vs. 12.7 months, $p<0.001$). Another retrospective study compared patients treated with ^{90}Y-SIRT plus TKIs versus those treated with ^{90}Y-SIRT plus ICIs.[91] The latter group exhibited an ORR of 89%, significantly higher than the former, with more pronounced radiological tumor regression. This suggests that tumor destruction by ^{90}Y-SIRT may lead to robust release of immunogenic antigens, resulting in a synergistic interaction with ICIs and offering greater therapeutic benefit when combined with immunotherapy. Collectively, these studies report ORRs ranging 30.8–83% for patients treated with ^{90}Y-SIRT in combination with ICIs. In recent years, several clinical trials have been launched evaluating ^{90}Y-SIRT followed by combinations of targeted and immunotherapy agents, such as atezolizumab plus bevacizumab. Results from these studies are expected to further inform the clinical integration of ^{90}Y-SIRT in the management of HCC. Meanwhile, additional clinical evidence that can enhance efficient patient selection warrants close attention, including biomarker-guided precision therapies, more refined applications of molecular subtyping, and the exploitation of the abscopal effect in radiotherapy.

6. Conclusion

^{90}Y-SIRT has firmly established itself as a transformative locoregional modality for HCC, yet several challenges temper its broad adoption. Despite robust data demonstrating its ability to deliver ultrahigh intratumoral doses (>150 Gy) with sparing of normal liver tissue, standardization of dosimetry remains a critical hurdle. The DOSISPHERE-01 trial highlighted that personalized, multicompartment dosimetry significantly improves objective response rates compared with standard approaches, underscoring the need for consensus on treatment planning and dose-reporting standards.

Clinically, while SIRT outperforms TACE in downstaging advanced tumors and synergizing with systemic agents to enhance response, real-world implementation is constrained by high procedural costs, limited access to microsphere technology, and variability in operator expertise. Ongoing efforts to develop domestically manufactured microspheres aim to reduce economic barriers and streamline supply chains, potentially broadening availability across diverse healthcare settings. Another pressing dilemma is the dichotomous immunologic effect of radiation: low-dose SIRT can transiently normalize vasculature and prime antitumor immunity, whereas excessive dosing risks exacerbating hypoxia, fibrosis, and immunosuppression via TGF-β and HIF-1α–mediated pathways. This underscores the imperative for biomarker-guided patient selection and precise optimization of dose-fractionation schedules. Early-phase studies combining SIRT with ICIs report higher ORRs, yet prospective trials must define the ideal sequencing and identify predictive biomarkers of synergy.

It is particularly important to discuss the place of ^{90}Y-SIRT in the modern multidisciplinary treatment decision tree for HCC. ^{90}Y-SIRT has evolved from a mere palliative approach to a core pillar treatment option and a key bridge therapy throughout early, intermediate, and advanced diseases. For unresectable HCC, hyperselective RS can be used as a radical alternative, with the advantage of a non-puncture pathway that effectively avoids implant metastasis and provides a local control rate comparable to

surgery. For borderline resectable intermediate-stage HCC, radiation lobectomy has achieved the dual goals of tumor downstaging and increasing future liver residual volume by inducing compensatory hyperplasia of the contralateral liver lobe, successfully creating transformational conditions for liver transplantation or radical resection. For advanced HCC with PVTT, ^{90}Y-SIRT not only provides local control and survival benefits better than cTACE by virtue of its non-embolism-dominated mechanism and unique immune microenvironment regulation ability, but also acts as a synergist to synergize with immune checkpoint inhibitors and targeted drugs, transforming uncontrollable advanced diseases into potentially controllable states and reshaping the advanced treatment pattern. Therefore, its decision-making logic is anchored based on liver function and tumor burden, and ^{90}Y-SIRT is regarded as a strategic choice to achieve the trinity of local control, downstaging transformation, and system synergy, and is a key link connecting local treatment and systemic treatment.

In addition to ^{90}Y, other nuclides that can be used in tumor treatment are also under development. ^{213}Bi is an α-particle emitter whose radiobiological advantages stem from high linear energy transfer and short tissue range. Compared with ^{90}Y, ^{213}Bi is mechanistically and applicably complementary.[85] ^{90}Y relies on cross-fire effects to cover large tumor volumes (range 2.5 mm), but is limited by normal tissue dose constraints (hepatic tolerance <30 Gy). ^{213}Bi achieves cell-level precision killing with high linear energy transfer, especially suitable for diffuse lesions or ^{90}Y drug resistance. Clinical selection should be based on tumor size, hypoxic status, and target expression level, and the synergistic use of different nuclides can optimize the treatment window, such as ^{90}Y first tumor reduction and ^{213}Bi removal of residues. ^{177}Lu has both therapeutic and diagnostic capabilities and has become the core of neuroendocrine tumor diagnosis and treatment. ^{225}Ac, as the ^{213}Bi parent, can release multiple sets of α-particles, but the risk of daughter nuclide redistribution needs to be considered. The future direction focuses on combination therapy and vector innovation. Individualized multinuclide selection marks the entry of liver cancer treatment into the era of precision radiotherapy.

Looking ahead, the integration of SIRT into precision-medicine paradigms hinges on four pillars: (i) Rigorous standardization of personalized dosimetry; (ii) expanded cost-effective microsphere manufacturing; (iii) biomarker-driven combination regimens that exploit the abscopal effect; and (iv) large, multicenter randomized trials to validate long-term survival and quality-of-life benefits. By addressing these challenges through multidisciplinary collaboration and technological innovation, ^{90}Y-SIRT is poised not merely as a second-line rescue therapy but as a cornerstone curative strategy in the modern management of primary HCC.

Acknowledgments

None.

Funding

None.

Conflict of interest

The authors declare they have no competing interests.

Author contributions

Conceptualization: Pinchao Fan, Yue Chai
Visualization: Yang Zha, Yue Chai
Writing–original draft: Yue Chai, Danyang Xu, Yang Zha
Writing–review & editing: Pinchao Fan

Ethics approval and consent to participate

Not applicable.

Consent for publication

Not applicable.

Availability of data

Not applicable.

References

1. Singal AG, Kanwal F, Llovet JM. Global trends in hepatocellular carcinoma epidemiology: Implications for screening, prevention and therapy. *Nat Rev Clin Oncol*. 2023;20(12):864-884.

   doi: 10.1038/s41571-023-00825-3

2. Forner A, Reig M, Bruix J. Hepatocellular carcinoma. *Lancet*. 2018;391(10127):1301-1314.

   doi: 10.1016/s0140-6736(18)30010-2

3. Sung H, Ferlay J, Siegel RL, *et al*. Global cancer statistics 2020: GLOBOCAN estimates of incidence and mortality worldwide for 36 cancers in 185 countries. *CA Cancer J Clin*. 2021;71(3):209-249.

   doi: 10.3322/caac.21660

4. Finn RS, Qin S, Ikeda M, *et al*. Atezolizumab plus bevacizumab in unresectable hepatocellular carcinoma. *N Engl J Med*. 2020;382(20):1894-1905.

   doi: 10.1056/NEJMoa1915745

5. Yau T, Park JW, Finn RS, *et al*. Nivolumab versus sorafenib in advanced hepatocellular carcinoma (CheckMate 459): A randomised, multicentre, open-label, phase 3 trial. *Lancet*

Oncol. 2022;23(1):77-90.

doi: 10.1016/s1470-2045(21)00604-5

6. Yau T, Kang YK, Kim TY, *et al*. Efficacy and safety of nivolumab plus ipilimumab in patients with advanced hepatocellular carcinoma previously treated with sorafenib: The checkMate 040 randomized clinical trial. *JAMA Oncol*. 2020;6(11):e204564.

   doi: 10.1001/jamaoncol.2020.4564

7. Qu K, Yan Z, Wu Y, *et al*. Transarterial chemoembolization aggravated peritumoral fibrosis via hypoxia-inducible factor-1α dependent pathway in hepatocellular carcinoma. *J Gastroenterol Hepatol*. 2015;30(5):925-32.

   doi: 10.1111/jgh.12873

8. Liu L, Teng G, Zhang D, *et al*. Toxicology of intrahepatic arterial administration of interventional phosphorus-32 glass microspheres to domestic pigs. *Chin Med J (Engl)*. 1999;112(7):632-636.

9. Hamad A, Aziz H, Kamel IR, Diaz DA, Pawlik TM. Yttrium-90 Radioembolization: Current indications and outcomes. *J Gastrointest Surg*. 2023;27(3):604-614.

   doi: 10.1007/s11605-022-05559-8

10. D'Abadie P, Walrand S, Lhommel R, Hesse M, Borbath I, Jamar F. Optimization of the clinical effectiveness of radioembolization in hepatocellular carcinoma with dosimetry and patient-selection criteria. *Curr Oncol*. 2022;29(4):2422-2434.

    doi: 10.3390/curroncol29040196

11. Mansur A, Habibollahi P, Fang A, *et al*. New frontiers in radioembolization. *Ther Adv Med Oncol*. 2024;16:17588359241280692.

    doi: 10.1177/17588359241280692

12. Cremonesi M, Chiesa C, Strigari L, *et al*. Radioembolization of hepatic lesions from a radiobiology and dosimetric perspective. *Front Oncol*. 2014;4:210.

    doi: 10.3389/fonc.2014.00210

13. Ibrahim SM, Lewandowski RJ, Sato KT, *et al*. Radioembolization for the treatment of unresectable hepatocellular carcinoma: A clinical review. *World J Gastroenterol*. 2008;14(11):1664-1669.

    doi: 10.3748/wjg.14.1664

14. Mosconi C, Cappelli A, Pettinato C, Golfieri R. Radioembolization with Yttrium-90 microspheres in hepatocellular carcinoma: Role and perspectives. *World J Hepatol*. 2015;7(5):738-752.

    doi: 10.4254/wjh.v7.i5.738

15. Chen ZH, Zhang XP, Lu YG, *et al*. Actual long-term survival in HCC patients with portal vein tumor thrombus after liver resection: A nationwide study. *Hepatol Int*. 2020;14(5): 754-764.

    doi: 10.1007/s12072-020-10032-2

16. Choi C, Yoo GS, Cho WK, Park HC. Optimizing radiotherapy with immune checkpoint blockade in hepatocellular carcinoma. *World J Gastroenterol*. 2019;25(20):2416-2429.

    doi: 10.3748/wjg.v25.i20.2416

17. Choi JW, Kim HC. Radioembolization for hepatocellular carcinoma: What clinicians need to know. *J Liver Cancer*. 2022;22(1):4-13.

    doi: 10.17998/jlc.2022.01.16

18. Fidelman N, Kerlan RK, Jr. Transarterial chemoembolization and (90)Y radioembolization for hepatocellular carcinoma: Review of current applications beyond intermediate-stage disease. *AJR Am J Roentgenol*. 2015;205(4):742-752.

    doi: 10.2214/ajr.15.14802

19. De La Torre-Aláez M, Matilla A, Varela M, *et al*. Nivolumab after selective internal radiation therapy for the treatment of hepatocellular carcinoma: A phase 2, single-arm study. *J Immunother Cancer*. 2022;10(11):e005457.

    doi: 10.1136/jitc-2022-005457

20. Liu DM, Leung TW, Chow PK, *et al*. Clinical consensus statement: Selective internal radiation therapy with yttrium 90 resin microspheres for hepatocellular carcinoma in Asia. *Int J Surg*. 2022;102:106094.

    doi: 10.1016/j.ijsu.2021.106094

21. Lewandowski RJ, Salem R. Yttrium-90 radioembolization of hepatocellular carcinoma and metastatic disease to the liver. *Semin Intervent Radiol*. 2006;23(1):64-72.

    doi: 10.1055/s-2006-939842

22. Kim SP, Cohalan C, Kopek N, Enger SA. A guide to ^{90}Y radioembolization and its dosimetry. *Phys Med*. 2019;68: 132-145.

    doi: 10.1016/j.ejmp.2019.09.236

23. Singh P, Anil G. Yttrium-90 radioembolization of liver tumors: What do the images tell us? *Cancer Imaging*. 2014;13(4):645-657.

    doi: 10.1102/1470-7330.2013.0057

24. Molvar C, Lewandowski R. Yttrium-90 radioembolization of hepatocellular carcinoma-performance, technical advances, and future concepts. *Semin Intervent Radiol*. 2015;32(4):388-397.

    doi: 10.1055/s-0035-1564704

25. Anbari Y, Veerman FE, Keane G, *et al*. Current status of yttrium-90 microspheres radioembolization in primary and metastatic liver cancer. *J Interv Med*. 2023;6(4):153-159.

    doi: 10.1016/j.jimed.2023.09.001

26. Choi SH, Seong J. Strategic application of radiotherapy for hepatocellular carcinoma. *Clin Mol Hepatol*. 2018;24(2):

114-134.

doi: 10.3350/cmh.2017.0073

27. Fuss M, Salter BJ, Herman TS, Thomas CR Jr. External beam radiation therapy for hepatocellular carcinoma: Potential of intensity-modulated and image-guided radiation therapy. *Gastroenterology*. 2004;127(5 Suppl 1):S206-S217.

doi: 10.1053/j.gastro.2004.09.035

28. Dudzinski SO, Newman NB, McIntyre J, *et al*. Emerging evidence-based role for external-beam radiation therapy in hepatocellular carcinoma. *Lancet Gastroenterol Hepatol*. 2025;10(4):387-398.

doi: 10.1016/s2468-1253(24)00267-x

29. Song CW, Glatstein E, Marks LB, *et al*. Biological principles of stereotactic body radiation therapy (SBRT) and stereotactic radiation surgery (SRS): Indirect cell death. *Int J Radiat Oncol Biol Phys*. 2021;110(1):21-34.

doi: 10.1016/j.ijrobp.2019.02.047

30. Salem R, Mazzaferro V, Sangro B. Yttrium 90 radioembolization for the treatment of hepatocellular carcinoma: Biological lessons, current challenges, and clinical perspectives. *Hepatology*. 2013;58(6):2188-2197.

doi: 10.1002/hep.26382

31. De La Garza-Ramos C, Toskich BB. Radioembolization for the treatment of hepatocellular carcinoma: The road to personalized dosimetry and ablative practice. *Semin Intervent Radiol*. 2021;38(4):466-471.

doi: 10.1055/s-0041-1735571

32. Wright CL, Zhang J, Tweedle MF, Knopp MV, Hall NC. Theranostic imaging of yttrium-90. *Biomed Res Int*. 2015;2015:481279.

doi: 10.1155/2015/481279

33. Piron B, Paillas S, Boudousq V, *et al*. DNA damage-centered signaling pathways are effectively activated during low dose-rate Auger radioimmunotherapy. *Nucl Med Biol*. 2014;41 Suppl: e75-e83.

doi: 10.1016/j.nucmedbio.2014.01.012

34. Melia E, Parsons JL. DNA damage and repair dependencies of ionising radiation modalities. *Biosci Rep*. 2023;43(10):BSR20222586.

doi: 10.1042/bsr20222586

35. Thoms J, Bristow RG. DNA repair targeting and radiotherapy: A focus on the therapeutic ratio. *Semin Radiat Oncol*. 2010;20(4):217-222.

doi: 10.1016/j.semradonc.2010.06.003

36. Tauchi H, Nakamura N, Komatsu K, Sawada S. Accumulation of cells at G2/M stage by low dose-rate irradiation renders the cell population more susceptible to the subsequent induction of 6-thioguanine-resistant mutations by 252Cf fission neutrons. *J Radiat Res*. 1996;37(1):49-57.

doi: 10.1269/jrr.37.49

37. Hami R, Apeke S, Redou P, *et al*. Predicting the tumour response to radiation by modelling the five Rs of radiotherapy using PET images. *J Imaging*. 2023;9(6):124.

doi: 10.3390/jimaging9060124

38. Garin E, Tselikas L, Guiu B, *et al*. Personalised versus standard dosimetry approach of selective internal radiation therapy in patients with locally advanced hepatocellular carcinoma (DOSISPHERE-01): A randomised, multicentre, open-label phase 2 trial. *Lancet Gastroenterol Hepatol*. 2021;6(1):17-29.

doi: 10.1016/s2468-1253(20)30290-9

39. Lee BQ, Abbott EM, Able S, *et al*. Radiosensitivity of colorectal cancer to ^{90}Y and the radiobiological implications for radioembolisation therapy. *Phys Med Biol*. 2019;64(13):135018.

doi: 10.1088/1361-6560/ab23c4

40. Tanguturi SK, Wo JY, Zhu AX, Dawson LA, Hong TS. Radiation therapy for liver tumors: Ready for inclusion in guidelines? *Oncologist*. 2014;19(8):868-879.

doi: 10.1634/theoncologist.2014-0097

41. Boughdad S, Duran R, Prior JO, *et al*. Measure of ^{90}Y-glass microspheres residue post-TARE using PET/CT and potential impact on tumor absorbed dose in comparison $^{99]}$mTc-MAA SPECT/CT dosimetry. *EJNMMI Rep*. 2024;8(1):26.

doi: 10.1186/s41824-024-00214-8

42. Torkian P, Haghshomar M, Farsad K, Wallace S, Golzarian J, Young SJ. Cancer immunology: Impact of radioembolization of hepatocellular carcinoma on immune response modulation. *AJR Am J Roentgenol*. 2023;220(6):863-872.

doi: 10.2214/ajr.22.28800

43. Wang X, Zhang H, Zhang X, Liu Y. Abscopal effect: From a rare phenomenon to a new frontier in cancer therapy. *Biomark Res*. 2024;12(1):98.

doi: 10.1186/s40364-024-00628-3

44. Liu Y, Dong Y, Kong L, Shi F, Zhu H, Yu J. Abscopal effect of radiotherapy combined with immune checkpoint inhibitors. *J Hematol Oncol*. 2018;11(1):104.

doi: 10.1186/s13045-018-0647-8

45. D'Alonzo RA, Keam S, Gill S, *et al*. Fractionated low-dose radiotherapy primes the tumor microenvironment for immunotherapy in a murine mesothelioma model. *Cancer Immunol Immunother*. 2025;74(2):44.

doi: 10.1007/s00262-024-03889-x

46. Virani NA, Kelada OJ, Kunjachan S, *et al*. Noninvasive imaging of tumor hypoxia after nanoparticle-mediated

tumor vascular disruption. *PLoS One*. 2020;15(7):e0236245.

doi: 10.1371/journal.pone.0236245

47. Vallée A, Lecarpentier Y, Guillevin R, Vallée JN. Interactions between TGF-β1, canonical WNT/β-catenin pathway and PPAR γ in radiation-induced fibrosis. *Oncotarget*. 2017;8(52):90579-90604.

doi: 10.18632/oncotarget.21234

48. Chen J, Wang S, Ding Y, Xu D, Zheng S. Radiotherapy-induced alterations in tumor microenvironment: Metabolism and immunity. *Front Cell Dev Biol*. 2025;13:1568634.

doi: 10.3389/fcell.2025.1568634

49. Liu S, Wang W, Hu S, *et al*. Radiotherapy remodels the tumor microenvironment for enhancing immunotherapeutic sensitivity. *Cell Death Dis*. 2023;14(10):679.

doi: 10.1038/s41419-023-06211-2

50. Belisario DC, Kopecka J, Pasino M, *et al*. Hypoxia dictates metabolic rewiring of tumors: Implications for chemoresistance. *Cells*. 2020;9(12):2598.

doi: 10.3390/cells9122598

51. Li M, Liu D, Lee D, *et al*. Targeted alpha-particle radiotherapy and immune checkpoint inhibitors induces cooperative inhibition on tumor growth of malignant melanoma. *Cancers (Basel)*. 2021;13(15):3676.

doi: 10.3390/cancers13153676

52. Tai D, Loke K, Gogna A, *et al*. Radioembolisation with Y90-resin microspheres followed by nivolumab for advanced hepatocellular carcinoma (CA 209-678): A single arm, single centre, phase 2 trial. *Lancet Gastroenterol Hepatol*. 2021;6(12):1025-1035.

doi: 10.1016/s2468-1253(21)00305-8

53. Kadalayil L, Benini R, Pallan L, *et al*. A simple prognostic scoring system for patients receiving transarterial embolisation for hepatocellular cancer. *Ann Oncol*. 2013;24(10):2565-2570.

doi: 10.1093/annonc/mdt247

54. Salem R, Lewandowski RJ, Kulik L, *et al*. Radioembolization results in longer time-to-progression and reduced toxicity compared with chemoembolization in patients with hepatocellular carcinoma. *Gastroenterology*. 2011;140(2):497-507.e2.

doi: 10.1053/j.gastro.2010.10.049

55. Reig M, Forner A, Rimola J, *et al*. BCLC strategy for prognosis prediction and treatment recommendation: The 2022 update. *J Hepatol*. 2022;76(3):681-693.

doi: 10.1016/j.jhep.2021.11.018

56. Brown AM, Kassab I, Massani M, *et al*. TACE versus TARE for patients with hepatocellular carcinoma: Overall and individual patient level meta analysis. *Cancer Med*. 2023;12(3):2590-2599.

doi: 10.1002/cam4.5125

57. Dhondt E, Lambert B, Hermie L, *et al*. ^{90}Y radioembolization versus drug-eluting bead chemoembolization for unresectable hepatocellular carcinoma: Results from the TRACE phase II randomized controlled trial. *Radiology*. 2022;303(3):699-710.

doi: 10.1148/radiol.211806

58. Patel KR, Menon H, Patel RR, Huang EP, Verma V, Escorcia FE. Locoregional therapies for hepatocellular carcinoma: A systematic review and meta-analysis. *JAMA Netw Open*. 2024;7(11):e2447995.

doi: 10.1001/jamanetworkopen.2024.47995

59. Hao K, Paik AJ, Han LH, Makary MS. Yttrium-90 radioembolization treatment strategies for management of hepatocellular carcinoma. *World J Radiol*. 2024;16(10): 512-527.

doi: 10.4329/wjr.v16.i10.512

60. Lu H, Liang B, Xia X, Zheng C. Predictors and risk factors of bile duct injury after transcatheter arterial chemoembolization for hepatocellular carcinoma. *BMC Cancer*. 2024;24(1):1085.

doi: 10.1186/s12885-024-12864-9

61. Yuan Y, He W, Yang Z, *et al*. TACE-HAIC combined with targeted therapy and immunotherapy versus TACE alone for hepatocellular carcinoma with portal vein tumour thrombus: A propensity score matching study. *Int J Surg*. 2023;109(5):1222-1230.

doi: 10.1097/js9.0000000000000256

62. Lee SM, Choi JH, Yoon JH, *et al*. Efficacy and safety of image-guided hypofractionated radiotherapy for hepatocellular carcinoma with portal vein tumor thrombosis: A retrospective, multicenter study. *BMC Cancer*. 2025;25(1):736.

doi: 10.1186/s12885-025-13739-3

63. Jiang JF, Lao YC, Yuan BH, *et al*. Treatment of hepatocellular carcinoma with portal vein tumor thrombus: Advances and challenges. *Oncotarget*. 2017;8(20):33911-33921.

doi: 10.18632/oncotarget.15411

64. Minagawa M, Makuuchi M. Treatment of hepatocellular carcinoma accompanied by portal vein tumor thrombus. *World J Gastroenterol*. 2006;12(47):7561-7567.

doi: 10.3748/wjg.v12.i47.7561

65. Ormiston W, Samuelson S, Van Wyk M, *et al*. Safety and efficacy of selective internal radiation therapy for portal vein tumour thrombus in advanced hepatocellular carcinoma: A single-centre experience in Australia. *J Med Imaging Radiat Oncol*. 2025;69(2):244-250.

doi: 10.1111/1754-9485.13837

66. Jia Z, Jiang G, Tian F, Zhu C, Qin X. A systematic review on the safety and effectiveness of yttrium-90 radioembolization for hepatocellular carcinoma with portal vein tumor thrombosis. *Saudi J Gastroenterol*. 2016;22(5):353-359.

doi: 10.4103/1319-3767.191139

67. Hur MH, Cho Y, Kim DY, *et al*. Transarterial radioembolization versus tyrosine kinase inhibitor in hepatocellular carcinoma with portal vein thrombosis. *Clin Mol Hepatol*. 2023;29(3):763-778.

doi: 10.3350/cmh.2023.0076

68. Ma YN, Jiang X, Liu H, Song P, Tang W. Conversion therapy for initially unresectable hepatocellular carcinoma: Current status and prospects. *Biosci Trends*. 2024;17(6):415-426.

doi: 10.5582/bst.2023.01322

69. Salem R, Gordon AC, Mouli S, *et al*. Y90 Radioembolization significantly prolongs time to progression compared with chemoembolization in patients with hepatocellular carcinoma. *Gastroenterology*. 2016;151(6):1155-1163.e2.

doi: 10.1053/j.gastro.2016.08.029

70. Lewandowski RJ, Kulik LM, Riaz A, *et al*. A comparative analysis of transarterial downstaging for hepatocellular carcinoma: Chemoembolization versus radioembolization. *Am J Transplant*. 2009;9(8):1920-1928.

doi: 10.1111/j.1600-6143.2009.02695.x

71. Kim E, Sher A, Abboud G, *et al*. Radiation segmentectomy for curative intent of unresectable very early to early stage hepatocellular carcinoma (RASER): A single-centre, single-arm study. *Lancet Gastroenterol Hepatol*. 2022;7(9):843-850.

doi: 10.1016/s2468-1253(22)00091-7

72. Salem R, Johnson GE, Kim E, *et al*. Yttrium-90 radioembolization for the treatment of solitary, unresectable HCC: The LEGACY study. *Hepatology*. 2021;74(5):2342-2352.

doi: 10.1002/hep.31819

73. Salem R, Padia SA, Lam M, *et al*. Clinical and dosimetric considerations for Y90: Recommendations from an international multidisciplinary working group. *Eur J Nucl Med Mol Imaging*. 2019;46(8):1695-1704.

doi: 10.1007/s00259-019-04340-5

74. Entezari P, Gabr A, Kennedy K, Salem R, Lewandowski RJ. Radiation lobectomy: An overview of concept and applications, technical considerations, outcomes. *Semin Intervent Radiol*. 2021;38(4):419-424.

doi: 10.1055/s-0041-1735530

75. Birgin E, Rasbach E, Seyfried S, *et al*. Contralateral liver hypertrophy and oncological outcome following radioembolization with ^{90}Y-microspheres: A systematic review. *Cancers (Basel)*. 2020;12(2):294.

doi: 10.3390/cancers12020294

76. Villalobos A, Pisanie JLD, Gandhi RT, Kokabi N. Yttrium-90 radioembolization dosimetry: Dose considerations, optimization, and tips. *Semin Intervent Radiol*. 2024;41(1): 63-78.

doi: 10.1055/s-0044-1779715

77. Baker T, Tabrizian P, Zendejas I, *et al*. Conversion to resection post radioembolization in patients with HCC: Recommendations from a multidisciplinary working group. *HPB (Oxford)*. 2022;24(7):1007-1018.

doi: 10.1016/j.hpb.2021.12.013

78. Jia Z, Wang C, Paz-Fumagalli R, Wang W. Radiation segmentectomy for hepatic malignancies: Indications, devices, dosimetry, procedure, clinical outcomes, and toxicity of yttrium-90 microspheres. *J Interv Med*. 2019;2(1):1-4.

doi: 10.1016/j.jimed.2019.05.001

79. Mourad SN, De La Garza-Ramos C, Toskich BB. Radiation segmentectomy for the treatment of hepatocellular carcinoma: A practical review of evidence. *Cancers (Basel)*. 2024;16(3):669.

doi: 10.3390/cancers16030669

80. Prachanronarong K, Kim E. Radiation segmentectomy. *Semin Intervent Radiol*. 2021;38(4):425-431.

doi: 10.1055/s-0041-1735529

81. Ricke J, Klümpen HJ, Amthauer H, *et al*. Impact of combined selective internal radiation therapy and sorafenib on survival in advanced hepatocellular carcinoma. *J Hepatol*. 2019;71(6):1164-1174.

doi: 10.1016/j.jhep.2019.08.006

82. Craciun L, De Wind R, Demetter P, *et al*. Retrospective analysis of the immunogenic effects of intra-arterial locoregional therapies in hepatocellular carcinoma: A rationale for combining selective internal radiation therapy (SIRT) and immunotherapy. *BMC Cancer*. 2020;20(1):135.

doi: 10.1186/s12885-020-6613-1

83. Lee YB, Nam JY, Cho EJ, *et al*. A phase I/IIa trial of yttrium-90 radioembolization in combination with durvalumab for locally advanced unresectable hepatocellular carcinoma. *Clin Cancer Res*. 2023;29(18):3650-3658.

doi: 10.1158/1078-0432.Ccr-23-0581

84. Yu S, Yu M, Keane B, *et al*. A pilot study of pembrolizumab in combination with Y90 radioembolization in subjects with poor prognosis hepatocellular carcinoma. *Oncologist*. 2024;29(3):270-e413.

doi: 10.1093/oncolo/oyad331

85. Zhan C, Ruohoniemi D, Shanbhogue KP, *et al*. Safety of combined yttrium-90 radioembolization and immune

checkpoint inhibitor immunotherapy for hepatocellular carcinoma. *J Vasc Interv Radiol*. 2020;31(1):25-34.

doi: 10.1016/j.jvir.2019.05.023

86. Chow PK, Poon DY, Khin MW, *et al*. Multicenter phase II study of sequential radioembolization-sorafenib therapy for inoperable hepatocellular carcinoma. *PLoS One*. 2014;9(3):e90909.

doi: 10.1371/journal.pone.0090909

87. Salman A, Simoneau E, Hassanain M, *et al*. Combined sorafenib and yttrium-90 radioembolization for the treatment of advanced hepatocellular carcinoma. *Curr Oncol*. 2016;23(5):e472-e480.

doi: 10.3747/co.23.2827

88. Villalobos A, Dabbous HH, Little O, *et al*. Safety and efficacy of concurrent atezolizumab/bevacizumab or nivolumab combination therapy with yttrium-90 radioembolization of advanced unresectable hepatocellular carcinoma. *Curr Oncol*. 2023;30(12):10100-10110.

doi: 10.3390/curroncol30120734

89. Mejait A, Roux C, Soret M, *et al*. Enhanced therapeutic outcomes with atezolizumab-bevacizumab and SIRT combination compared to SIRT alone in unresectable HCC: A promising approach for improved survival. *Clin Res Hepatol Gastroenterol*. 2024;48(2):102282.

doi: 10.1016/j.clinre.2024.102282

90. Yeo YH, Liang J, Lauzon M, *et al*. Immunotherapy and transarterial radioembolization combination treatment for advanced hepatocellular carcinoma. *Am J Gastroenterol*. 2023;118(12):2201-2211.

doi: 10.14309/ajg.0000000000002467

91. Garcia-Reyes K, Gottlieb RA, Menon KM, *et al*. Radioembolization plus immune checkpoint inhibitor therapy compared with radioembolization plus tyrosine kinase inhibitor therapy for the treatment of hepatocellular carcinoma. *J Vasc Interv Radiol*. 2024;35(5):722-730.e1.

doi: 10.1016/j.jvir.2024.02.004

ACCSCIENCE PUBLISHING

Advances in Radiotherapy & Nuclear Medicine

ORIGINAL RESEARCH ARTICLE

3D-printed personalized bolus designed through structured-light scanning for adaptive radiotherapy

Faycal Kharfi[1]*, Moufida Belatar[1], and Karim Benkahila[2]

[1]Laboratory of Dosing, Analysis, and Characterization with High Resolution, Department of Physics, Faculty of Sciences, Sétif 1 University Ferhat Abbas, Sétif, Algeria

[2]Department of Radiotherapy, Anti-Cancer Center of Setif, Sétif, Algeria

Abstract

Conformal dose delivery in external beam radiotherapy often requires a tissue-equivalent bolus to compensate for surface irregularities and increase skin dose. However, traditional bolus fabrication methods are time-consuming, imprecise, and poorly adaptable to patient anatomy. This study presents an alternative, innovative workflow that integrates three-dimensional (3D) structured-light scanning (SLS), computer-aided design, and 3D printing to rapidly and accurately fabricate patient-specific boluses. First, a chin bolus was generated within the treatment planning system using a Rando anthropomorphic phantom as a reference. The generated bolus was then processed, 3D-printed, and tested. To avoid additional computed tomography scans and unnecessary X-ray exposure, a high-resolution, inoffensive SLS scanner was used to capture the treatment surface. The resulting point-cloud data were imported into 3D modeling software to design a custom bolus geometry that conforms exactly to the patient's skin contour. The workflow also incorporated a rapid rescanning and reprinting loop, enabling intra-fractional and inter-fractional modifications in response to anatomical changes. The 3D-printed bolus demonstrated excellent conformity to the phantom surface. The entire process, from scanning to bolus deployment, was completed within a reasonable timeframe, substantially reducing patient waiting time compared with conventional methods. Overall, the proposed 3D printing-based workflow offers a rapid, accurate, and patient-specific alternative to conventional bolus fabrication. By leveraging SLS and digital modeling, this approach enhances conformity, improves dosimetric accuracy, and allows agile modifications to accommodate anatomical changes, thereby optimizing radiotherapy treatment delivery.

Keywords: Radiotherapy; Patient-specific bolus; 3D printing; Structured-light scanning; 3D modeling; Rapid fabrication and modification

***Corresponding author:**
Faycal Kharfi
(kharfifaycal@univ-setif.dz)

Citation: Kharfi F, Belatar M, Benkahila K. 3D-printed personalized bolus designed through structured-light scanning for adaptive radiotherapy. *Adv Radiother Nucl Med*. 2025;3(4):38-48. doi: 10.36922/ARNM025250032

Received: June 19, 2025

Revised: August 30, 2025

Accepted: September 22, 2025

Published online: October 16, 2025

1. Introduction

Bolus materials are routinely used in external beam radiotherapy to increase surface dose and optimize dose homogeneity for superficial tumors (e.g., breast, head, neck, and skin cancers).[1-3] Even with advanced techniques such as intensity-modulated radiation therapy (IMRT) or electron therapy, a customized bolus remains critical for

achieving conformal dose coverage near the skin surface.[1] In practice, each patient's anatomy is unique and may change over the treatment course (due to, e.g., weight loss or tumor regression), highlighting a significant clinical need for patient-specific and adaptable bolus solutions. An ideal bolus can closely match the patient's external contour and can be rapidly modified or replaced as needed during a course of adaptive therapy.

Conventional bolus materials (e.g., flat gel sheets, rubber/wax moulage, and moldable compounds) have well-known limitations, for example:

- Poor fit on complex anatomy: Flat or generic bolus sheets cannot match curved/irregular skin surfaces, causing air gaps that degrade dose accuracy.[4]
- Labor-intensive fabrication: Manual molding or cutting of bolus on the day of treatment is time-consuming and prone to error.
- Inconsistent reproducibility: Conventional bolus is not easily replicated, and repositioning can vary between fractions.
- Limited adaptability: Once made, a conventional bolus cannot be rapidly modified to adapt to changes in patient anatomy, thus requiring the fabrication of a new bolus.

These boluses cannot easily conform to irregular surfaces, resulting in significant air gaps and dose uncertainties in complex regions such as the nose, ear, and scalp.[4] Manual shaping of bolus is labor-intensive, time-consuming, and varies across staff, compromising reproducibility and efficiency. In many clinics, bolus placement requires trial-and-error adjustments for each fraction, adding to patient discomfort and workflow burden. These factors motivate automated fabrication methods to produce snug, reproducible bolus shapes for each individual.

By contrast, additive manufacturing (e.g., 3D printing) enables truly patient-specific bolus design. Using 3D printing, bolus geometry can be generated directly from a patient's surface model (e.g., derived from computed tomography [CT] scans or optical scans), yielding a form-fitting device. Recent studies have demonstrated several clear advantages: 3D-printed boluses show superior conformity and homogeneity, significantly reducing hot/cold spots compared with manually fabricated boluses.[4-6] For example, Bochyńska *et al.*[5(p100)] reported that customized 3D-printed boluses produced "improved dose distribution, better bolus conformity, and reduced setup times" relative to traditional methods. Likewise, Gugliandolo *et al.*[4] noted that 3D-printed boluses provided excellent anatomical conformity, rapid fabrication, and high reproducibility. In practice, these improvements translate to fewer air gaps, more accurate skin dose delivery, and more streamlined workflows. Additional benefits include the ability to tailor bolus thickness or density (through printer infill settings) to modulate dose gradients, as well as the option to fabricate soft or flexible materials to improve patient comfort. A summarized overview of the main advantages of 3D printing and modeling technologies in dose-bolus fabrication is as follows:

- Precise anatomical fit: Customized bolus fits the patient's skin, minimizing air gaps.[4,5]
- Improved dosimetry: 3D-printed boluses yield more uniform surface dose coverage, enhancing target coverage.[5]
- High reproducibility: Digital workflows eliminate manual variability, ensuring one-to-one replication of the bolus design.[4,7]
- High workflow efficiency: Automated fabrication can reduce preparation time. A study found that 3D printing improved fabrication efficiency and reduced overall treatment time compared with manually fabricated boluses.[5]

A key enabler of this paradigm is 3D surface scanning and modeling. Optical scanning technologies—such as structured-light scanning (SLS), 3D depth sensing, and even smartphone photogrammetry—can capture a patient's external contour with high spatial resolution and without ionizing radiation.[8,9] For example, Douglass[8(p141)] emphasized that SLS and other optical scanners "have been shown to be useful for 3D printing applications due to their higher spatial resolution, non-ionizing imaging." Recent work showed that modern smartphone-based photogrammetry or light detection and ranging (LiDAR) apps can produce surface meshes sufficient for bolus design.[9] These methods allow rapid capture of the treatment area before or even during a session, potentially enabling on-the-fly bolus generation or modification. Optical scanners thus supplement or replace the need for additional CT scans to obtain surface geometry, saving time and radiation dose. The benefits of SLS and 3D modeling include:

- High-resolution contour capture: Devices such as handheld SLS scanners can record sub-millimeter details on skin surfaces.[8]
- Non-ionizing imaging: Surface acquisition through photogrammetry/LiDAR avoids additional CT dose.[9]
- Rapid digital workflow: Captured models can be edited in 3D software (e.g., adding bolus thickness) and exported for printing before or during patient treatment.[9]
- High accessibility: Even consumer devices (e.g., tablets and phones) can generate viable models for bolus design, making the approach feasible in clinics.[9]

Implementation feasibility has been demonstrated in recent clinical experiences. Basaula *et al.*[1] reported a 4-year experience at a large cancer center, during which over 2,000 patient-specific boluses were 3D printed using polylactic acid (PLA) filament. Their workflow achieved a turnaround of 3 days from plan design to bolus delivery. The authors noted that fused deposition modeling (FDM) printing yielded "smooth and reproducible boluses," and that once established, the associated quality assurance processes were streamlined. In addition, the availability of low-cost, open-source software and commercial services (e.g., specialized bolus-design tools) further reduces barriers to adoption. Overall, current evidence suggests that clinics can realistically integrate 3D-printed bolus workflows without significant cost and delay.[1,5]

In summary, the integration of 3D scanning, modeling, and printing offers a powerful alternative to conventional bolus fabrication. By capturing patient anatomy through SLS or photogrammetric methods and then 3D printing a customized bolus, this approach minimizes air gaps, enhances dose conformity, and accelerates production.[5] Such personalized boluses can improve patient comfort (by avoiding the need for tight, manually shaped molds) and support adaptive radiotherapy through rapid, on-treatment modifications. Recent global studies further underscore the technical viability and clinical potential of this strategy, paving the way for the routine implementation of patient-specific, adaptable bolus solutions in modern radiotherapy practice.[1,5]

2. Materials and methods

2.1. Virtual bolus generation and extraction from the treatment planning system (TPS)

The integration of a virtual bolus within the radiotherapy treatment planning workflow is essential for ensuring adequate dose build-up in regions close to the skin or in anatomically irregular areas. In the Eclipse™ TPS (11.0.31 Varian Medical Systems, California, United States [US]), virtual boluses were routinely generated during the contouring and planning stages to simulate the effect of a physical bolus and ensure proper dose coverage at or near the surface of the body.

In Eclipse, the virtual bolus was typically as a structure with a predefined thickness, such as 5 mm or 10 mm, overlying the patient's external contour. This was accomplished through Boolean operations or dedicated tools within the Structure Set module. The planner defined the extent of the bolus by expanding the patient surface (external contour) outward using the "Structure Expansion" function or by manually drawing a volume over the area of interest. Material properties were then assigned to the virtual bolus, commonly using a tissue-equivalent electron density (e.g., 1.0 g/cm^3) to replicate the attenuation characteristics of a standard tissue-equivalent material, such as Superflab.

Once incorporated into the planning CT and dose calculation, the virtual bolus allowed the TPS to simulate surface dose build-up and optimize beam fluence accordingly. This is particularly relevant in techniques such as IMRT or volumetric-modulated arc therapy, where modulation relies on accurate modeling of the entire treatment geometry, including the presence of a bolus. Dose calculation algorithms, such as anisotropic analytical algorithm and Acuros XB, took the virtual bolus into account, allowing for the precise modeling of scattering and attenuation effects at the tissue–bolus interface.

After treatment planning and optimization, the virtual bolus structure was exported in digital imaging and communications in medicine (DICOM) radiation therapy (RT) structure (RT structure set) along with the CT dataset and other plan components (e.g., RT plan and RT dose). The structure corresponding to the bolus, converted to a 3D volumetric object in STL format, was then used for 3D printing. The extraction process involved:

(i) Exporting the DICOM radiotherapy structures set from Eclipse, including the bolus contour.
(ii) Importing the DICOM dataset into "3D Slicer," which is an open-source 3D medical image processing software.
(iii) Segmenting and converting the bolus structure into a surface mesh (e.g., STL or OBJ format) suitable for 3D printing.
(iv) Optionally, smoothing and editing the mesh (e.g., adding flexibility zones or attachment features) to improve printability or comfort with a computer-aided design (CAD) software, such as MeshLab.
(v) Sending the final mesh to a 3D printer using the Bambu Studio software (V2.0.3.54, Bambu Lab, France).

This process enabled a seamless transition from virtual bolus planning to physical bolus fabrication, ensuring high fidelity between the planned dose distribution and the delivered treatment. It also facilitated iterative or adaptive approaches, where new bolus designs were rapidly generated and printed in response to patient anatomical changes during the treatment course.

Recent studies have demonstrated the robustness of this approach. For example, Basaula *et al.*[1] leveraged Eclipse-generated virtual bolus contours to fabricate patient-specific boluses using low-cost FDM 3D printing technologies, showing strong dosimetric agreement between planned and delivered doses. This underlines the feasibility of incorporating virtual-to-physical bolus workflows directly into clinical radiotherapy practice.

In this work, instead of a real patient, a chin-surface bolus was designed based on a real radiotherapy treatment case reproduced using Rando phantom CT data. The Rando anthropomorphic phantom (often known as the Alderson Rando phantom or simply Rando phantom) is a widely used tissue-equivalent phantom designed to simulate the human body for applications in medical physics, radiotherapy, radiation dosimetry, and imaging research. This physical phantom was suitable for our study because it allowed repeated scanning and bolus placement operations without any constraints associated with real patients. PLA was used as the printing material due to its well-characterized properties, previously reported in the literature (mass density: 1.22 ± 0.05 g/cm^3, Hounsfield units: 122 ± 10).[10]

2.2. 3D printing of bolus

The fabrication of patient-specific boluses through 3D printing offers an efficient and precise approach for reproducing complex anatomical surfaces. In this study, a flexible bolus was fabricated using the Bambu Lab P1S 3D printer (Bambu Lab, France) with basic PLA filament. PLA is a thermoplastic polyester known for its biodegradability and eco-friendliness. It is a rigid, biocompatible material that offers acceptable conformity and patient comfort. Its mechanical properties make it particularly suitable for applications involving skin contact and anatomical adaptability. The printer and material parameters are summarized in Table 1, and the optimal printing conditions are in Table 2.

Table 1. 3D printer parameters

Characteristic	Description
Printer model	Bambu Lab P1S
Extrusion type	Direct drive
Build volume (in mm^3)	256×256×256
Nozzle diameter (mm)	0.4
Filament material	Basic polylactic acid (diameter 1.75 mm)

Table 2. 3D printing conditions

Parameter	Value
Nozzle temperature (°C)	220
Bed temperature (°C)	60
Printing speed	First layers: +50 mm/d; other layers: +200 mm/s
Travel speed (mm/s)	500
Layer height (mm)	0.2
Infill density	100% (solid bolus)

2.3. SLS of the surface receiving bolus

Accurate acquisition of the patient's external surface is critical in designing personalized radiotherapy boluses. SLS offers a high-resolution, non-ionizing method to capture detailed 3D geometry of anatomical surfaces, especially in cases where CT imaging may be limited or not ideal for surface modeling. In this study, the EinScan Pro + SLS scanner (Shining 3D, China) was used to scan the body region receiving the bolus, producing precise surface meshes that served as the basis for virtual bolus design and 3D printing.

The EinScan Pro+ is a handheld SLS scanner with an accuracy of up to 0.05 mm, making it suitable for capturing fine anatomical details necessary for bolus conformity. The following steps outline the workflow for SLS and data processing:

(i) Step 1: Patient or phantom preparation

- Positioning: The patient (or anatomical phantom) was placed in a stable, treatment-like position using immobilization devices when needed (e.g., thermoplastic mask and breast board).
- Surface preparation: Reflective or shiny surfaces (e.g., oily skin and certain phantom materials) were matted using a scanning spray (e.g., AESUB) to enhance light pattern capture.
- Landmark markers: Optional registration targets were placed on anatomical reference points to aid in surface alignment or repeated scans.

(ii) Step 2: Scanner setting and calibration

- Mode selection: The Handheld HD Scan mode was used to balance high resolution and ease of mobility.
- Calibration: A built-in calibration panel was used to calibrate the scanner before each session to ensure geometric fidelity.
- Working distance: The optimal scanner-to-surface distance of 400–600 mm was maintained to maximize accuracy and minimize distortion.

(iii) Step 3: Surface scanning procedure

- The scanning was performed by moving the EinScan Pro+ scanner around the treatment area in smooth, overlapping passes to ensure full surface coverage.
- Real-time feedback provided by the EXScan Pro software (3.1.0.2 Shining 3D, China) helped verify complete coverage and avoid holes or voids.
- The scanner projected a series of light patterns (structured stripes) onto the surface, and two onboard cameras recorded the resulting deformations to calculate 3D geometry.

(iv) Step 4: Mesh generation and processing
- The raw point cloud data were automatically converted into a watertight 3D mesh using the EXScan Pro software.
- Post-processing steps included:
  - Hole filling (for incomplete data in occluded regions)
  - Mesh smoothing (to reduce noise and scanning artifacts)
  - Decimation (to reduce polygon count while preserving shape fidelity)
  - Exporting the mesh as a 3D object (OBJ) file for bolus design

(v) Step 5: Bolus design integration
- The OBJ surface model was imported into the 3D Photoshop software (25.0.0 Adobe Inc., US).
- A virtual bolus was then designed over the target surface with a predefined thickness (5 mm), accounting for treatment margins and anatomical landmarks.
- The digital bolus was extracted as separate STL and OBJ files for 3D printing.

The advantages of the used EinScan Pro+ SLS scanner are as follows:
- High accuracy (<100 μm): Enables tight bolus conformity with minimal air gaps
- Non-ionizing and contactless: Safe for repeated use and comfortable for patients
- Rapid acquisition (~2–3 min/region): Suitable for clinical workflows
- Color texture capture (optional): Useful for anatomical annotation or surface matching
- Compatibility with standard CAD tools: Ensures seamless integration into the bolus design pipeline

The use of the EinScan Pro+ significantly enhances the precision and adaptability of surface-based bolus design. Its ability to generate anatomically accurate 3D meshes enables the production of personalized boluses that closely conform to complex regions such as the face, scalp, and breast, improving dose delivery while minimizing setup variability. The SLS workflow also allows for adaptive rescanning during the treatment course, enabling dynamic bolus redesign in response to anatomical changes.

3. Results

Figure 1 presents the initial bolus design and fabrication. It shows the end-to-end creation of a patient-specific bolus during the first (non-adaptive) phase. Figure 1A is the TPS: the patient (Rando phantom) CT is displayed with the contoured target volume and an overlaid virtual bolus structure designed to encompass the superficial target. This virtual bolus was generated from the planning target volume and mapped onto the surface in TPS. Figure 1B depicts the digital and physical manifestation of the design: a computer-generated 3D model of the bolus (reconstructed from the TPS data) and the actual 3D-printed bolus device. Finally, Figure 1C shows the 3D-printed bolus fitted onto the Rando head phantom at the treatment setup. This confirmed that the customized device conforms to the phantom's surface. By matching the patient's anatomy, the bolus minimizes air gaps, which are known to degrade surface dose delivery. Indeed, earlier studies reported that a properly fitted 3D-printed bolus increased the skin dose to nearly 100% of the prescription (vs. only 10–40% without bolus) for a 6 MV beam, thus achieving the intended surface coverage.[11-14] In summary, Figure 1 conveys that the virtual bolus design in TPS was faithfully translated into a physical device and correctly placed on the patient-equivalent phantom, a critical step that underpins accurate dose delivery to a superficial target.

Figure 2 presents the adaptive bolus designed through SLS, illustrating the adaptive phase where the bolus was updated based on an optical surface scan. Figure 2A presents a 3D surface mesh of the Rando head acquired using an SLS scanner. This non-ionizing scan captures the exact external contour of the phantom's anatomy without additional CT imaging. From these scan data, a new adaptive bolus was digitally generated (Figure 2B) to match the updated surface geometry. Figure 2C displays the resulting 3D-printed adaptive bolus fitted onto the Rando phantom's head, confirming that the bolus matched the scanned anatomy and achieved minimal air gaps. Prior work has shown that boluses generated from surface scans achieved mean fitting gaps of 1–2 mm (e.g., 1.4 mm), significantly better than manually contoured boluses.[11-15] By using SLS for adaptation, one can modify the bolus to reflect any anatomical changes (e.g., patient weight loss or tumor shrinkage) without repeating a CT scan. Clinically, this adaptive workflow ensures the bolus continues to conform tightly to the patient's evolving surface, preserving dose accuracy and coverage while avoiding additional imaging and exposure to X-rays.

Dose delivery with a tissue-equivalent bolus is a critical parameter for verifying if dosimetric objectives are achieved. The longitudinal dose profiles with and without the customized bolus are presented in Figure 3, comparing the depth–dose distribution along the beam's central (longitudinal) axis. Without the bolus, the beam's skin-sparing effect resulted in a low surface dose and a build-up region located a few millimeters beneath the skin. Adding the bolus shifted this build-up region outward

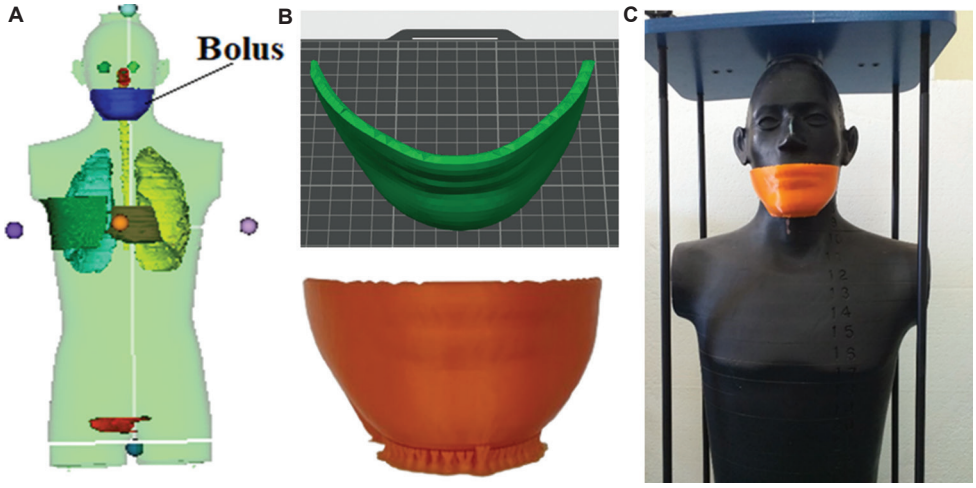

Figure 1. Designed and 3D-printed dose bolus. (A) Virtual bolus generated in the treatment planning system. (B) 3D-modeled (top) and 3D-printed (bottom) bolus during the first treatment phase. (C) 3D-printed bolus on the Rando phantom.

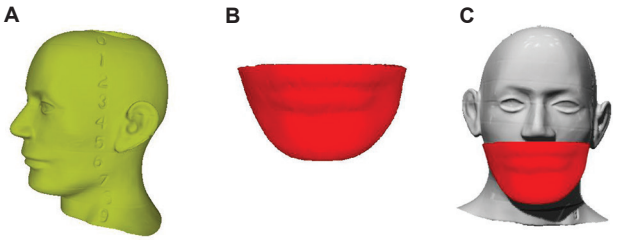

Figure 2. Structured-light scanning 3D model of the Rando phantom head and the related generated bolus. (A) Structured-light scanning model of the Rando phantom head. (B) 3D model of the adaptive bolus during the adaptive phase. (C) 3D-printed adaptive bolus on the Rando head.

and markedly increased the surface dose. In effect, the bolus elevated the superficial dose, ensuring that the prescribed dose reaches the skin surface and minimizing epidermal underdosing. Figure 3B visually demonstrates this dosimetric advantage: the with-bolus curve displays a much higher dose at zero depth. Consistent with previously published results, we observed that the bolus increased the surface dose from 1–5% to approximately 25% of the prescription dose. In summary, Figure 3 confirms that adding a customized bolus leads to a significantly higher and earlier dose deposition within the target, improving surface coverage in accordance with the treatment plan.

The transverse dose profiles across the treatment volume for plans with and without bolus are presented in Figure 4. The with-bolus profile is flatter and higher across the target region compared with the without-bolus profile. The use of the bolus resulted in a more uniform high-dose region at the surface and reduced dose falloff at the field edges, ensuring that the entire width of the superficial target received an adequate dose. In practical terms, this results in closer agreement between the planned and delivered doses across the target cross-section. The observed improvement in dose uniformity and target coverage suggests enhanced local target control without increasing the dose to adjacent tissues. Overall, Figure 4 confirms that the application of a customized bolus yields a superior transverse dose distribution, thereby improving treatment accuracy.

4. Discussion

4.1. Bolus design and fit

The planned (TPS-generated) bolus was successfully 3D-printed and placed on the Rando head phantom (Figure 1), and a second adaptive bolus was generated through the high-resolution SLS of the Rando phantom (Figure 2). Qualitatively, both boluses conformed closely to the phantom surface, but the SLS-derived bolus more closely matched the fine facial contours. The results are consistent with prior phantom studies showing that surface-scanner–based boluses produce smaller air gaps than CT-based designs.[15,16] For example, Dipasquale *et al.*[15] reported maximum bolus-to-skin gaps of 1–2 mm for CT-derived boluses, compared with <0.6 mm for boluses generated from high-resolution surface scans. In volunteer tests, they acquired scans in 0.6–7.0 min, and the printed boluses required no manual reshaping. Similarly, Sasaki *et al.*[17] achieved an average shape error of <0.5 mm in 9 of 10 patient cases, with no fit or comfort issues. Our results align with these observations: the SLS-based adaptive bolus fits the Rando phantom with negligible gaps, illustrating excellent anatomical conformity. Quantitative evaluation confirmed that, without applying any mechanical pressure during placement, the air gap between the bolus and phantom surface did not exceed 0.6 mm even in the worst

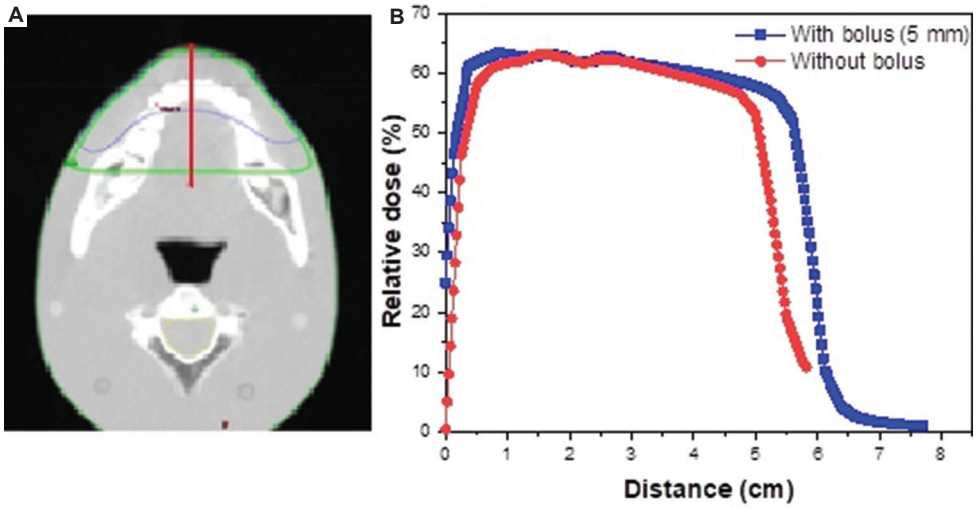

Figure 3. Longitudinal dose profiles showing the role and advantage of a customized bolus. (A) Computed tomography image showing the selected axial longitudinal line for dose profiles plotting; (B) Dose profiles with and without bolus.

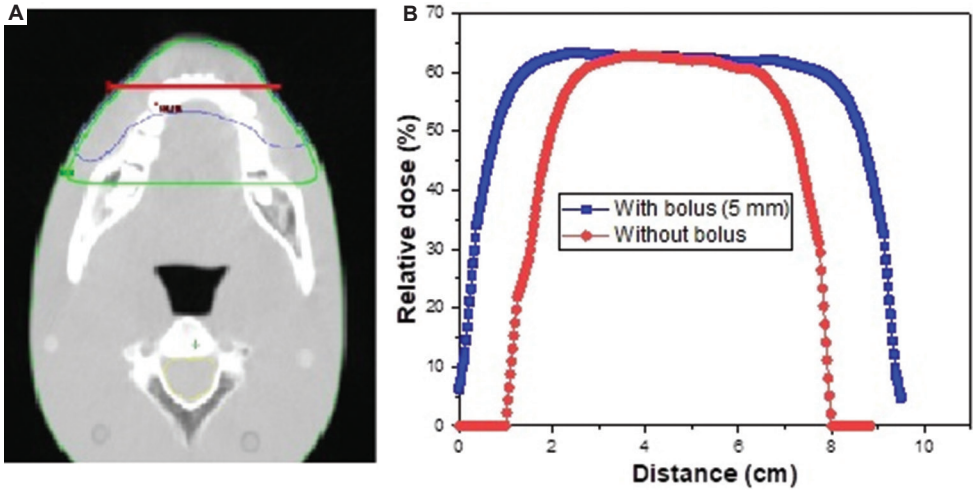

Figure 4. Transverse dose profiles showing the role and advantage of a customized bolus. (A) Computed tomography image showing the selected transverse line for dose profiles plotting. (B) Dose profiles with and without bolus.

case. In addition, the air gap only existed in <15% of the total covered surface (as measured from scanning data). This minimal air gap had no significant impact on the dose profile and delivery.

Overall, these findings demonstrate the feasibility of the optical-scanning workflow for fabricating patient-specific boluses, replacing laborious manual or secondary CT-based methods. In contrast, conventional bolus fabrication (e.g., wax and gel sheets) is time-consuming and often yields poor surface conformity.[15] By comparison, 3D-printed boluses derived from SLS data overcome these limitations. The high scanning resolution (0.05 mm) ensures precise surface modeling without additional radiation exposure. In addition, Crowe *et al.*[18] emphasized that SLS achieves submillimeter accuracy, is cost-effective, and allows on-table adaptive bolus generation.

4.2. Dosimetric impact

Figures 3 and 4 compare longitudinal and transverse dose profiles with and without the printed bolus. In both cases, the bolus significantly elevated the surface dose and shifted the build-up regions closer to the surface. Specifically, the longitudinal profile (Figure 3) showed that, with the bolus, the relative surface dose (0 cm) increased to a substantial fraction of the prescription level (rather than near-zero), and 55–60% of the build-up region was shifted upward by several centimeters. This clearly demonstrates the typical bolus effect of bringing the dose build-up region

closer to the skin surface. Quantitatively, the with-bolus curve reached >60% of the nominal dose at 1–2 cm depth. These findings align well with prior reports. Robar *et al.*[19] found that a custom 3D-printed chest-wall bolus delivered skin doses within 3% of planned values compared with standard boluses. Likewise, Ciobanu *et al.*[20] and Wang *et al.*[21] observed measured surface doses within 1% of TPS predictions when using 3D-printed boluses. In our study, the measured profiles likewise confirmed that the 3D-printed PLA bolus restored the full prescription dose at the surface, as intended. Owing to the excellent conformity of the printed boluses, planning target volume coverage was preserved. This agrees with literature demonstrating that custom boluses reproduce target dose–volume histogram parameters nearly identical to those defined in the TPS: the PLA bolus achieved virtually identical target coverage and homogeneity to the TPS-defined bolus. Previous studies have also reported excellent dosimetric fidelity. Zhang *et al.*[22] showed deviations below 3% in percentage–depth–dose curves for PLA/thermoplastic polyether urethane (TPU) boluses versus water. Our results echoed that 3D-printed boluses accurately reproduce the planned dose distribution.[22] Furthermore, a previous study further confirmed these advantages.[23] In summary, the dose-profile data confirm that the 3D-printed bolus effectively boosts surface dose without compromising homogeneity and target coverage.

4.3. Clinical implementation

Our findings support the growing evidence that patient-specific 3D-printed boluses are clinically feasible and highly conformal. Multiple groups have demonstrated successful use of 3D-printed boluses in patients with irregular anatomical surfaces. For example, Malone *et al.*[24] retrospectively evaluated 60 patients (627 fractions) treated with TPU boluses, reporting that 75% of fractions were rated "good" or "excellent" fit—particularly for head, neck, scalp, and extremities. Importantly, fit quality remained stable throughout the treatment course, demonstrating the reproducibility of printed boluses. Similarly, Sasaki *et al.*[17] used 3D surface scanning and reported no issues with fit or patient comfort across their initial 10 case. Our phantom study concurs with these findings: both the original and adaptive boluses were placed reproducibly on the anthropomorphic head with minimal inter-setup variation. The inherent rigidity of 3D-printed boluses provides excellent daily reproducibility, as they naturally align with the patient's anatomy. In a clinical trial, Robar *et al.*[19] noted that a 3D-printed chest-wall bolus reduced large air gaps (≥5 mm) from 30% with sheet boluses to 13% with 3D-printed boluses, indicating their superior placement consistency. Collectively, these data highlight that customized boluses conform closely and reproducibly to patient anatomy, thereby promoting reliable dose delivery across fractions.

4.4. Workflow efficiency and adaptability

A key benefit of the SLS–3D-printing workflow is its efficiency and adaptability. Because the bolus is derived from optical scans, no additional CT imaging is required, saving time and avoiding additional radiation exposure.[8,11] In our study, the phantom surface was scanned within minutes and generated a mesh for bolus design—comparable to clinical reports, where Dipasquale *et al.*[15] used a surface scanner to acquire volunteer models in 0.6–7 min. Once segmented, the bolus can be rapidly designed and sent for printing. Ehler *et al.*[25] found that segmentation and print preparation averaged 5–6 h, with printing requiring several additional hours but minimal staff intervention. Similarly, Robar *et al.*[19] noted that patient setup time reduced (from 104 s to 76 s on average) when using 3D-printed boluses, although their total lead time included 12.6 h of offline printing.

Thus, the workflow replaces manual bolus shaping and repeat CT imaging with primarily CAD and automated fabrication. In practice, once printing begins, therapists are free to attend to other tasks. The SLS step requires no consumables or ionizing dose and can be repeated as needed, enabling true "CT-free" adaptation. If a patient's anatomy changes (due to, e.g., weight loss or swelling), a new surface scan and bolus can be generated rapidly, something impractical with traditional methods. Moreover, digital fabrication reduces human error and streamlines record-keeping. Overall, our experience echoes other reports that modernizing bolus fabrication through 3D printing can modernize the mold room, improving efficiency without sacrificing accuracy.[17,25] In terms of time consumption, the total workflow duration for the considered case was approximately 14 h.

4.5. Clinical implications and multi-fraction adaptation

The combination of improved dose delivery and workflow flexibility has clear clinical advantages. For superficial tumors (e.g., those in skin, chest wall, nose, and ear), the enhanced surface dose achieved with a well-fitted bolus can improve tumor control. In multi-fraction regimens, anatomical changes (e.g., tumor regression and edema) are common. Because our method relies on a simple surface capture, the bolus can be refabricated mid-treatment if needed. For example, if a patient experiences weight loss or tissue subsidence under the mask, a new surface scan and 3D print can promptly generate an updated bolus that conforms to the modified anatomy—something not readily achievable with manually fabricated boluses. Malone *et al.*[24]

found that bolus conformity remained stable throughout most treatment courses, with changes observed mainly in pelvic cases, where an SLS approach could enable adaptive compensation.[26] Similarly, Sasaki *et al.*[17] noted that patients reported no discomfort with printed boluses. In addition, material selection plays a key role in patient comfort: flexible, shape-retaining filaments can conform closely to skin contours while avoiding the wrinkles sometimes seen with standard gel sheets.

In summary, our results demonstrate that SLS-guided, 3D-printed boluses can reliably increase surface dose and maintain target coverage, consistent with published evidence. The results also showed improved fit and dosimetric performance of 3D-printed boluses. The workflow is feasible and efficient: high-resolution optical scanning eliminates the need for additional CT imaging, and CAD-based printing integrates smoothly into clinical routines without undue burden. It is therefore concluded that patient-specific, 3D-printed boluses offer tangible improvements in superficial dose delivery and treatment adaptability, making them a practical option for multi-fraction radiotherapy involving irregular surfaces.

5. Conclusion

This study demonstrated the clinical feasibility, dosimetric reliability, and workflow efficiency of using SLS combined with 3D printing to generate personalized boluses for adaptive radiotherapy. The integration of high-resolution surface scanning enables precise anatomical modeling without additional radiation exposure, while 3D printing ensures reproducible fabrication of conformal boluses that minimize air gaps and maintain target coverage. The dosimetric results confirmed that the boluses significantly enhanced superficial dose delivery, shifted the build-up region outward, and improved longitudinal and transverse dose uniformity. Compared with conventional fabrication methods, the patient-specific designs provided superior conformity and reproducibility, closely matching planned treatment objectives. Furthermore, the workflow allowed rapid adaptation of the bolus during treatment courses without repeat CT imaging, offering a clinically practical strategy for managing anatomical changes across multiple fractions. Taken together, these findings support the adoption of digitally designed and 3D-printed boluses as a robust and scalable solution for modern radiotherapy, particularly in cases requiring high surface-dose precision and anatomical flexibility.[27-33]

Acknowledgments

The authors of this article would like to thank Prof. K. Boudadoud, head of the radiotherapy department at the Fighting Against Cancer Medical Center of Sétif for facilitating access to the department for the use of necessary materials.

Funding

The research received funding from the Thematic Research Agency in Health and Life Sciences and the General Direction of Scientific Research and Technological Development, Algerian Higher Education and Scientific Research Ministry, within the framework of the national research project, under Grant Agreement No. 03/18/DFPR/ATRSSV/22 of 01/03/2022.

Conflict of interest

The authors declare that they have no competing interests.

Author contributions

Conceptualization: Faycal Kharfi
Investigation: All authors
Methodology: Faycal Kharfi
Writing–original draft: Faycal Kharfi
Writing–review & editing: Faycal Kharfi

Ethics approval and consent to participate

Not applicable.

Consent for publication

Not applicable.

Availability of data

Data used in this work is available from the corresponding author upon reasonable request.

References

1. Basaula D, Hay B, Wright M, *et al.* Additive manufacturing of patient specific bolus for radiotherapy: Large scale production and quality assurance. *Phys Eng Sci Med.* 2024;47(2):551-561.

   doi: 10.1007/s13246-024-01385-1

2. McCallum S, Maresse S, Fearns P. Evaluating 3D-printed bolus compared to conventional bolus types used in external beam radiation therapy. *Curr Med Imaging.* 2021;17(7): 820-831.

   doi: 10.2174/1573405617666210202114336

3. Lu Y, Song J, Yao X, An M, Shi Q, Huang X. 3D printing polymer-based bolus used for radiotherapy. *Int J Bioprint.* 2021;7(4):414.

   doi: 10.18063/ijb.v7i4.414

4. Gugliandolo SG, Pillai SP, Rajendran S, *et al.* 3D-printed

boluses for radiotherapy: Influence of geometrical and printing parameters on dosimetric characterization and air gap evaluation. *Radiol Phys Technol*. 2024;17(2):347-359.

doi: 10.1007/s12194-024-00782-1

5. Bochyńska A, Zawadzka A, Kukołowicz P, Spałek MJ. Application of 3D printing for personalized boluses in radiotherapy: A systematic review. *Rep Pract Oncol Radiother*. 2025;30(1):100-113.

doi: 10.5603/rpor.104014

6. Rooney MK, Rosenberg DM, Braunstein S, *et al*. Three-dimensional printing in radiation oncology: A systematic review of the literature. *J Appl Clin Med Phys*. 2020;21(8):15-26.

doi: 10.1002/acm2.12907

7. Sands G, Clark CH, McGarry CK. A review of 3D printing utilisation in radiotherapy in the United Kingdom and Republic of Ireland. *Phys Med*. 2023;115:103143.

doi: 10.1016/j.ejmp.2023.103143

8. Douglass MJJ. Can optical scanning technologies replace CT for 3D printed medical devices in radiation oncology? *J Med Radiat Sci*. 2022;69(2):139-142.

doi: 10.1002/jmrs.579

9. Bridger CA, Caraça Santos AM, Reich PD, Douglass MJJ. An evaluation of consumer smartphones for generating bolus and surface mould applicators for radiation oncology. *Med Phys*. 2024;51(6):4447-4457.

doi: 10.1002/mp.17103

10. Kharfi F, Benkahila K, Boulkhessaim F, *et al*. Implementation of 3D printing and modeling technologies for the fabrication of dose boluses for external radiotherapy at the CLCC of Sétif, Algeria. *Technol Cancer Res Treat*. 2024;23:15330338241266479.

doi: 10.1177/15330338241266479

11. Weerasinghe C, Estoesta P, Cullen A, Claridge Mackonis E. Three-dimensional printing in breast radiation therapy: A scoping review of the literature. *J Med Radiat Sci*. 2025;72(3):297-307.

doi: 10.1002/jmrs.70000

12. Takanen S, Ianiro A, Pinnarò P, *et al*. A customized 3D-printed bolus for high-risk breast cancer with skin infiltration: A pilot study. *Curr Oncol*. 2024;31(9):5224-5232.

doi: 10.3390/curroncol31090386

13. Yu S, Ahn SH, Choi SH, Ahn WS, Jung IH. Clinical application of a customized 3D-printed bolus in radiation therapy for distal extremities. *Life (Basel)*. 2023;13(2):362.

doi: 10.3390/life13020362

14. Canters RA, Lips IM, Wendling M, *et al*. Clinical implementation of 3D printing in the construction of patient specific bolus for electron beam radiotherapy for non-melanoma skin cancer. *Radiother Oncol*. 2016;121(1):148-153.

doi: 10.1016/j.radonc.2016.07.011

15. Dipasquale G, Poirier A, Sprunger Y, Uiterwijk JWE, Miralbell R. Improving 3D-printing of megavoltage X-rays radiotherapy bolus with surface-scanner. *Radiat Oncol*. 2018;13:203.

doi: 10.1186/s13014-018-1148-1

16. Hobbis D, Michael DA, Samir HP, Tegtmeier RC, Laughlin BS, Chitsazzadeh S. Comprehensive clinical implementation, workflow, and FMEA of bespoke silicone bolus cast from 3D printed molds using open-source resources. *J Appl Clin Med Phys*. 2024;25(11):e14498.

doi: 10.1002/acm2.14498

17. Sasaki DK, McGeachy P, Alpuche Aviles JE, McCurdy B, Koul R, Dubey A. A modern mold room: Meshing 3D surface scanning, digital design, and 3D printing with bolus fabrication. *J Appl Clin Med Phys*. 2019;20(9):78-85.

doi: 10.1002/acm2.12703

18. Crowe S, Luscombe J, Maxwell S, *et al*. Evaluation of optical 3D scanning system for radiotherapy use. *J Med Radiat Sci*. 2022;69:218-226.

doi: 10.1002/jmrs.562

19. Robar JL, Moran K, Allan J, *et al*. Intrapatient study comparing 3D printed bolus versus standard vinyl gel sheet bolus for postmastectomy chest wall radiation therapy. *Pract Radiat Oncol*. 2018;8(4):221-229.

doi: 10.1016/j.prro.2017.12.008

20. Ciobanu AC, Petcu LC, Jarai-Szabo F, Balint Z. Validation of a 3D printed bolus for radiotherapy: A proof-of-concept study. B*iomed Phys Eng Express*. 2025;11(2):025033.

doi: 10.1088/2057-1976/adb15d

21. Wang X, Wang X, Xiang Z, *et al*. The clinical application of 3D-printed boluses in superficial tumor radiotherapy. *Front Oncol*. 2021;11:698773.

doi: 10.3389/fonc.2021.698773

22. Zhang C, Lewin W, Cullen A, Thommen D, Hill R. Evaluation of 3D printed bolus for radiotherapy using megavoltage X-ray beams. *Radiol Phys Technol*. 2023;16(3):414-421.

doi: 10.1007/s12194-023-00727-0

23. Ghediri N, Kharfi F, Benkahila K, *et al*. Dosimetric validation and surface fit evaluation of 3D-printed dose boluses for radiation therapy applications. *Int J Cancer Manag*. 2025;18(1):e159515.

doi: 10.5812/ijcm-159515

24. Malone C, Gill E, Lott T, *et al*. Evaluation of the quality

of fit of flexible bolus material created using 3D printing technology. *J Appl Clin Med Phys.* 2022;23(3):e13490.

doi: 10.1002/acm2.13490

25. Ehler E, Sterling D, Dusenbery K, Lawrence J. Workload implications for clinic workflow with implementation of three-dimensional printed customized bolus for radiation therapy: A pilot study. *PLoS One.* 2018;13(10):e0204944.

doi: 10.1371/journal.pone.0204944

26. Kang D, Wang B, Peng Y, Liu X, Deng X. Low-cost iphone-assisted processing to obtain radiotherapy bolus using optical surface reconstruction and 3D-printing. *Sci Rep* 2020;10(1):8016.

doi: 10.1038/s41598-020-64967-5

27. Spałek MJ, Bochyńska A, Borkowska A, Mroczkowski P, Szostakowski B. Challenges and solutions in 3D printing for oncology: A narrative review. *Chin Clin Oncol*. 2024;13(4):49.

doi: 10.21037/cco-24-4

28. Lizondo M, Lorenzo A, Adell-Gómez N, *et al*. Comparative study of flexible 3D printing materials for clinical application as boluses in radiotherapy. *Phys Med*. 2025;134:104987.

doi: 10.1016/j.ejmp.2025.104987

29. Park JM, Son J, An HJ, Kim JH, Wu HG, Kim JI. Bio-compatible patient-specific elastic bolus for clinical implementation. *Phys Med Biol.* 2019;64(10):105006.

doi: 10.1088/1361-6560/ab1c93

30. Kong Y, Yan T, Sun Y, *et al*. A dosimetric study on the use of 3D-printed customized boluses in photon therapy: A hydrogel and silica gel study. *J Appl Clin Med Phys*. 2019;20(1):348-55.

doi: 10.1002/acm2.12489

31. Su S, Moran K, Robar JL. Design and production of 3D printed bolus for electron radiation therapy. *J Appl Clin Med Phys.* 2014;15(4):4831.

doi: 10.1120/jacmp.v15i4.4831

32. Kim SW, Shin HJ, Kay CS, Son SH. A customized bolus produced using a 3-dimensional printer for radiotherapy. *PloS One.* 2014;9(10):e110746.

doi: 10.1371/journal.pone.0110746

33. Zhao Y, Moran K, Yewondwossen M, *et al*. Clinical applications of 3-dimensional printing in radiation therapy. *Med Dosim*. 2017;42(2):150-155.

doi: 10.1016/j.meddos.2017.03.001

ACCSCIENCE PUBLISHING

Advances in Radiotherapy & Nuclear Medicine

ORIGINAL RESEARCH ARTICLE

Strategies to minimize X-ray exposure and enhance dosimetric quality in pediatric nephroblastoma

Fatna Assaoui[1,2,3]*

[1]Laboratory of Health Sciences and Techniques, Environment and Care, Higher Institute of Nursing Professions and Health Techniques, Ministry of Health and Social Protection, Rabat, Morocco

[2]Medical Physics Section, Abdus Salam International Center for Theoretical Physics, Trieste, Italy

[3]Department of Radiotherapy, National Institute of Oncology, Mohamed V University, Rabat, Morocco

Abstract

Pediatric nephroblastoma is a rare kidney cancer occurring in children. This study investigates the impact of kidney shielding using a multileaf collimator compared with individual block techniques on dose–volume histograms (DVHs) of organs at risk (OARs) and on planning target volume (PTV) coverage during whole-abdominal irradiation with 6 MV beams in children with nephroblastoma. A computed tomography scan was performed in the supine position for five children with nephroblastoma. Treatment plans for both techniques—the conformal block technique (CFBT) and the conventional block technique (CVBT)—were created using the three-dimensional treatment planning system XIO version 4.8. Plans were compared based on dose conformity, homogeneity, and DVHs of OARs. Statistical analysis was performed using the *t*-test. The mean PTV conformity and homogeneity indices were 0.99 and 1.13 for CFBT, and 0.95 and 1.08 for CVBT, respectively. CFBT demonstrated superior target coverage, achieving 95% of the prescribed dose on 99.2% of the PTV compared to 95.0% for CVBT, which showed greater dose heterogeneity due to conventional kidney shielding and underdosing of adjacent abdominal regions. The average mean dose to the healthy kidney was 11.65 Gy (11.27–12.05) for CFBT and 11.44 Gy (11.09–11.75) for CVBT, with no significant differences in other OARs ($p>0.05$). CFBT represents an important advancement in three-dimensional conformal radiotherapy for children in developing countries, providing improved PTV homogeneity, enhanced treatment quality assurance, and a reduced potential for human error compared to CVBT. After the initial 10.5 Gy, the abdominal cavity was treated uniformly with CFBT.

Keywords: X-ray exposure; Nephroblastoma; Dose homogeneity; Dose volume histograms of organs at risk

***Corresponding author:**
Fatna Assaoui
(Assaoui2003@yahoo.fr)

Citation: Assaoui F. Strategies to minimize X-ray exposure and enhance dosimetric quality in pediatric nephroblastoma. *Adv Radiother Nucl Med*. 2025;3(4):49-58. doi: 10.36922/ARNM025290036

Received: July 20, 2025

Revised: September 2, 2025

Accepted: September 23, 2025

Published online: October 28, 2025

1. Introduction

Cancer is the second most common cause of pediatric death in developed countries.[1] However, over the past three decades, there has been a substantial and continuous improvement in the survival rates of children diagnosed with renal cell carcinoma. This progress is primarily due to the adoption of risk-adapted treatment stratification, a strategy

in which therapeutic protocols are carefully selected and personalized based on both the tumor's clinical stage and its underlying histological subtype. Such an approach has allowed clinicians to balance treatment intensity with disease aggressiveness, thereby avoiding both undertreatment and unnecessary toxicity. At the same time, the likelihood of achieving a long-term cure has steadily increased in recent years, a trend that has been strongly reinforced by the availability of highly specific, modern diagnostic techniques. These advanced imaging modalities and histopathological procedures enable more accurate disease detection, precise staging, and refined prognostication, all of which contribute to improved clinical outcomes.[2]

For patients with advanced neuroblastoma, the current international standards of care emphasize a multimodal therapeutic strategy. This combined approach usually integrates surgical intervention in the form of nephrectomy, targeted local control through radiotherapy, and systemic disease management with multiagent chemotherapy regimens. Each component of this strategy plays a complementary role: Surgery eliminates the primary tumor mass, radiotherapy reduces the risk of local recurrence, and chemotherapy addresses micrometastatic or disseminated disease, thereby improving overall survival.[3-5]

In contrast, children diagnosed with Wilms' tumor, that is either unresectable at presentation or already metastatic at the time of diagnosis, face a less favorable prognosis compared to those with localized, resectable disease. To overcome this challenge, pre-operative chemotherapy has been established as the standard treatment modality in trials conducted by the International Society of Pediatric Oncology. The rationale for this approach is that administering chemotherapy before surgical intervention often leads to a significant reduction in tumor size. This not only makes surgical resection technically more feasible but also decreases the risk of intraoperative complications, particularly in cases where the tumor initially encases or abuts vital anatomical structures such as major blood vessels or adjacent organs. Consequently, the integration of pre-operative chemotherapy has become a cornerstone in the management of complex and advanced presentations of Wilms' tumor.[6,7] Children's tissues are radiosensitive as they are still developing, raising concerns about the radiation treatment of neuroblastoma. Given that cancers in children are always chemosensitive, recent therapeutic protocols have attempted to decrease the use of radiotherapy in different ways.[8-11]

In contemporary pediatric and adult oncology, the surgical approach to renal tumors has undergone substantial refinement, with partial nephrectomy now being strongly recommended by recently published clinical guidelines as the standard treatment for patients with stage T1a and T1b tumors.[12] This shift away from routine radical nephrectomy reflects the growing recognition of the critical importance of preserving functional renal parenchyma, which plays a central role in preventing long-term renal impairment. Preserving kidney tissue is particularly relevant in specific patient groups such as individuals with a solitary kidney, those presenting with bilateral renal tumors, or patients with pre-existing renal insufficiency. For these populations, nephron-sparing surgery, whenever technically achievable, offers an optimal balance between maintaining oncological control and safeguarding renal function, thereby minimizing the lifelong risks of chronic kidney disease and its associated systemic complications.[12,13] While advances in surgical techniques have considerably improved outcomes, attention has increasingly turned to the long-term sequelae of cancer therapies, particularly the after-effects associated with radiotherapy. Unlike acute toxicities, which present during or shortly after treatment, after-effects often emerge insidiously, developing over several months or even years following therapy. These complications are of major clinical significance as they may negatively influence not only survival but also quality of life. Of particular concern is the heightened risk of secondary primary malignancies, which can occur within the irradiated field or in tissues exposed to even relatively low radiation doses. Moreover, survivors may experience growth disturbances, organ dysfunction, and a range of functional impairments, further underlining the need for continued surveillance and the ongoing refinement of therapeutic strategies to reduce long-term toxicity while preserving high cure rates.[14-16] Intensity-modulated radiotherapy (IMRT) improves the dose in the tumor volume and decreases the highest doses in normal tissues, but increases the irradiated volumes at low doses. In recent years, the introduction of advanced radiotherapy modalities, such as IMRT, has significantly changed the landscape of cancer treatment. However, its application within the pediatric population has been approached with considerable caution and careful evaluation.[17] The primary reason for this prudence is the heightened sensitivity of children to radiation-induced toxicities, coupled with their longer life expectancy, which substantially increases the window of risk for developing late complications. Several investigators have raised concerns that the more complex dose distributions associated with IMRT—although effective in improving target conformity—may inadvertently expose a larger volume of normal tissues to low or intermediate doses of radiation. As a consequence, some authors have estimated that the probability of radiation-induced secondary malignancies in children treated with IMRT could be two-fold higher compared to conventional techniques.[18-20]

In this context, proton beam therapy has emerged as a potentially superior alternative, particularly when the overarching goal is to minimize the incidence of secondary cancers and to achieve optimal sparing of surrounding healthy tissues. The fundamental physical property of protons, namely the Bragg peak, enables the delivery of a highly conformal dose to the tumor while significantly reducing radiation exposure beyond the target volume. This characteristic is especially advantageous in pediatric oncology, where minimizing unnecessary irradiation to critical structures is crucial for reducing the long-term burden of treatment-related morbidity. Consequently, proton therapy is increasingly regarded as a treatment modality that may offer significant benefits over photon-based IMRT, particularly in terms of reducing late toxicities and improving quality of life.

The current study involved five children with nephroblastoma who underwent radiotherapy following radical homolateral nephrectomy. It aimed to analyze the safety and feasibility of the conformal block using a multileaf collimator (MLC) (conformal block technique [CFBT]) and its impact on controlling the tumor and dose volume of organs at risk (OARs) compared to the traditional block (conventional block technique [CVBT]). Beyond ensuring the precise reproduction of the kidney block's spatial position, this approach also reduces room time by minimizing the need for intra-fraction therapist intervention, which is required in the conventional technique.

2. Materials and methods

This retrospective study included five pediatric patients diagnosed with nephroblastoma; three with stage T3 M_0 and two with stage T2 M_0 disease, with ages ranging from 2 to 10 years (median age 5.4 years). Staging procedures for all patients included abdominal and thoracic computed tomography (CT) scans.

Following initial chemotherapy, all patients underwent planned surgical resection. Three children received right-sided nephrectomy, whereas two underwent left-sided nephrectomy. In all cases, surgical resection was deemed microscopically complete. Subsequently, all patients received three-dimensional conformal radiotherapy (3D-RT).

2.1. Positioning and target delineation

The patients underwent CT scanning in the supine position, with a 5 mm slice thickness and no contrast injection (in vacuum cradles for immobilization). The clinical target volume (CTV) and OARs (heart, healthy kidney, spinal cord, femoral heads, lung, liver, spleen, and stomach) were delineated using the Focal software (version 4.62, Computerized Medical System, United States). The CTV corresponded to the initial tumor site and was contoured according to the initial diagnostic CT scan (Figure 1). The planning target volume (PTV) was automatically generated by expanding the CTV with a uniform 5 mm 3D margin.

2.2. Treatment equipment and methods

The dosimetries of both techniques were performed using the treatment planning system XIO (version 4.8), with comparisons made using *t*-tests. The irradiation therapy was delivered at 15 Gy in 10 fractions over 5 times a week. The PTV was designed to receive at least 95% of the prescribed dose.

The treatment plans were delivered using anteroposterior (AP) 6 MV photon fields in two phases, each employing a different technique:

(i) CFBT. First course: 10.5 Gy, AP opens fields (Figure 2A and B), and second course: 4.5 Gy AP (Figure 2C and D) with kidney shielding (MLC block) and two segments AP fields (Figure 2E and F).

(ii) CVBT. First course: 10.5 Gy, AP opens fields (Figure 3A and B); and second course: 4.5 Gy AP (Figure 3C and D) with kidney shielding (traditional block).

A uniform dose into all the vertebrae proximal to the CTV was required to prevent a lack of homogeneity in vertebral growth. The volume of the contralateral kidney receiving 12 Gy (V_{12}) was limited to 20%. No dose constraint was applied to the liver, as the prescribed dose was 15 Gy, and a mean dose of 25 Gy to the entire organ was considered acceptable.[21]

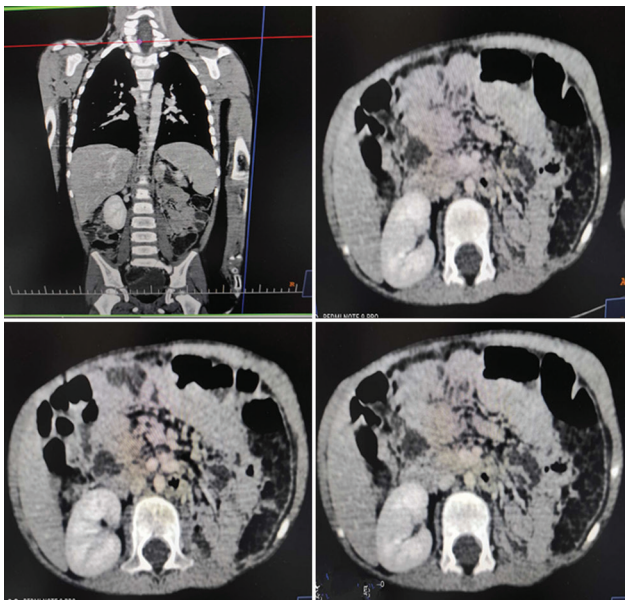

Figure 1. Computed tomography imaging prior to left nephrectomy

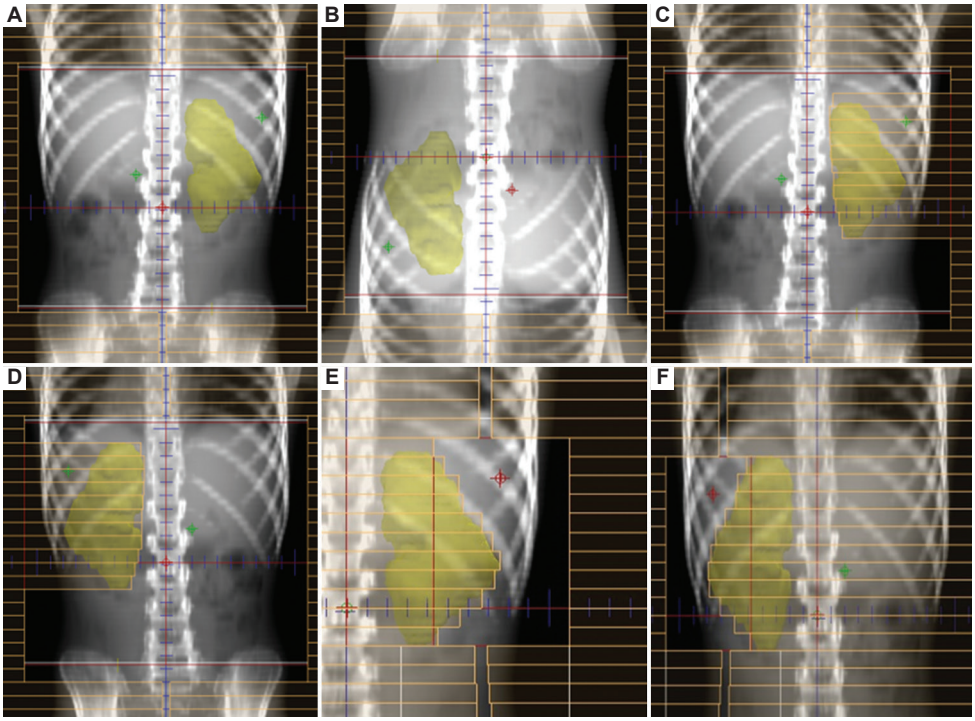

Figure 2. The six anteroposterior fields with and without a multileaf collimator block for the conformational block technique. (A) Ant 1, (B) Post 2, (C) Ant 3, (D) Post 4, (E) Ant 5, and (F) Post 6.
Abbreviations: Ant: Anterior; Post: Posterior.

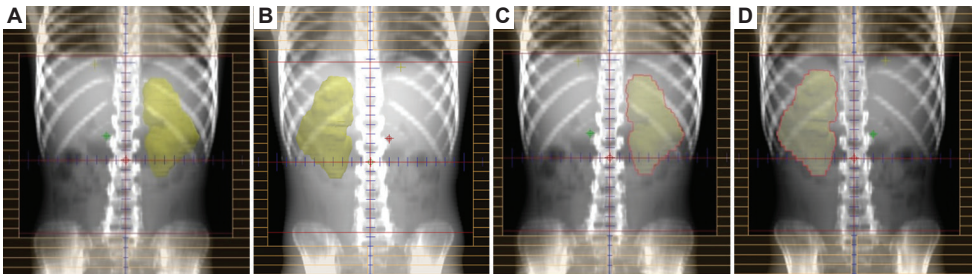

Figure 3. The four anteroposterior fields with and without a traditional block for the conventional block technique. (A) Ant 1, (B) Post 2, (C) Ant 3, and (D) Post 4.
Abbreviations: Ant: Anterior; Post: Posterior.

2.3. Statistical analysis

The dose–volume histograms (DVHs) were calculated for all OARs, and their average doses were compared. The conformity index (CI) and the homogeneity index (HI) were computed and compared for both techniques. A *t*-test was performed using Microsoft Excel 2010 "*t*-student program." $p \leq 0.05$ was considered statistically significant.

3. Results

3.1. The PTV

The average values of the $PTV_{95\%}$ (defined as the percentage of the PTV receiving at least 95% of the prescribed dose according to the International Commission on Radiation Units and Measurements Report 50) were 99.2% (range: 98–100%) and 95.0% (range: 94–96%) for CFBT and CVBT, respectively. The mean conformity and homogeneity indices for CFBT were 0.98 and 1.13, respectively, whereas for CVBT, they were 0.95 and 1.08, respectively. The differences were statistically significant for $PTV_{95\%}$ ($p=3.93\times10^{-5}$) and for the CI ($p=3.03\times10^{-5}$) but not significantly different for the HI ($p=0.06$) (Table 1, Figure 4).

3.2. Organs at risk

The mean dose to the healthy kidney was 11.65 Gy for CFBT and 11.44 Gy for CVBT ($p=0.018$). The V_{12} (which corresponds to the volume of the healthy kidney receiving

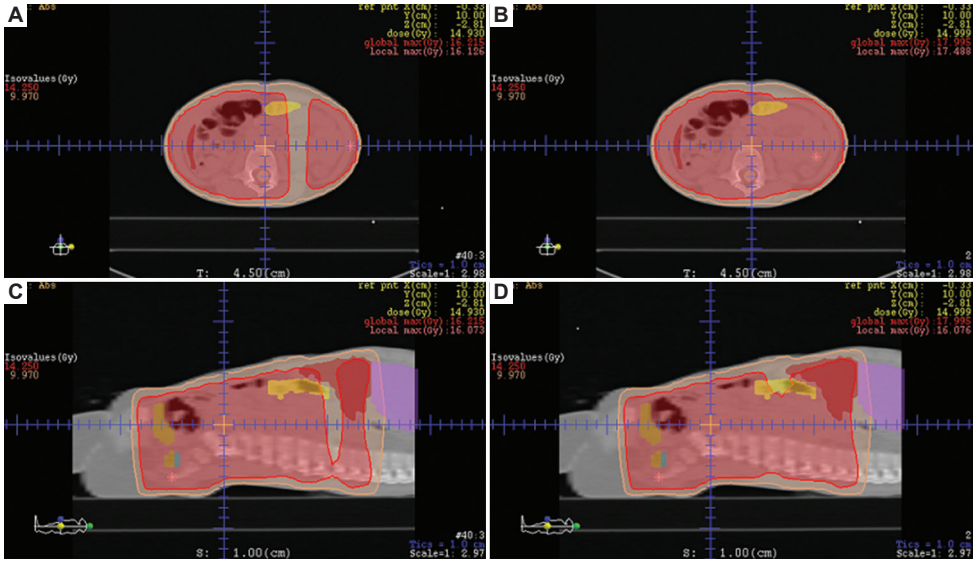

Figure 4. The transversal and sagittal dose distribution. Transversal dose distribution of the (A) conventional block technique and (B) the conformational block technique. (C) Sagittal dose distribution of the conventional block technique and (D) the conformational block technique. The brown and red isodose correspond to 95% of the prescribed dose, 10.5 Gy and 15.0 Gy, respectively.

Table 1. Dosimetric comparison of conformational and conventional block techniques

Parameters	CFBT	CVBT	*p*-value
Mean $PTV_{95\%}$	99.2%	95.0%	$3.93\ 10^{-5}$
Mean CI	0.98	0.95	$3.03\ 10^{-5}$
Mean HI	1.13	1.08	0.06

Abbreviations: CFBT: Conformational block technique; CI: Conformity index; CVBT: Conventional block technique; HI: Homogeneity index; PTV: Planning target volume.

Table 2. Average contralateral kidney mean dose and V_{12}

Parameters	Mean dose (Gy)		V_{12} (%)	
	CFBT	CVBT	CFBT	CVBT
Average	11.65	11.44	21.44%	18.27%
p-value	0.018		0.25	

Abbreviations: CFBT: Conformational block technique; CVBT: Conventional block technique.

Table 3. Average doses of the organs at risk for conformational and conventional block techniques

Doses	Spleen (Gy)		Liver (Gy)		Stomach (Gy)	
	CFBT	CVBT	CFBT	CVBT	CFBT	CVBT
$D_{20\%}$	15.56	14.6	15.08	15.00	14.7	14.69
	p=0.19		*p*=0.53		*p*=0.87	
$D_{40\%}$	15.39	15.00	14.78	14.82	13.24	13.22
	p=0.008		*p*=0.62		*p*=0.5	
$D_{60\%}$	14.83	14.72	14.66	14.64	12.11	12.00
	p=0.36		*p*=0.79		*p*=0.31	
$D_{72\%}$	14.35	14.35	-		-	
	p=1					
$D_{80\%}$	-		14.48	14.63	11.40	11.23
			p=0.5		*p*=0.10	

Abbreviations: CFBT: Conformational block technique; CVBT: Conventional block technique.

12 Gy) was 21.44% (range: 13–37) for CFBT and 18.27% (range: 17–25.8) for CVBT (*p*=0.25) (Table 2). The V_{12} constraint was met in four out of five patients with both techniques and exceeded in one case.

The doses in the spinal cord and the femoral heads were the same for both approaches (Figure 5). The average doses in 20% and 60% of the spleen (*p*=0.19; *p*=0.36), stomach (*p*=0.87; *p*=0.31), and liver (*p*=0.53; *p*=0.79) were not statistically significant. The spleen dose in 40% was significantly lower (*p*=0.008) with the CVBT. In contrast, dose differences for the stomach and liver were not statistically significant, with p-values of 0.5 and 0.62 at 40%, and 0.1 and 0.5 at 80%, respectively. The average dose in 72% of the spleen was 14.35 Gy for both techniques (Table 3). The curves intersect at an average dose of 14.70 Gy (spleen), 10.77 Gy stomach and 9.53 Gy (liver).

4. Discussion

Patients with renal cancer are at a high risk of developing chronic kidney disease complications, including cardiovascular diseases, renal failure, and mortality.[22] In the study of Siva *et al.*[23] involving 23 patients with renal cell carcinoma and normal kidney function, the crude local

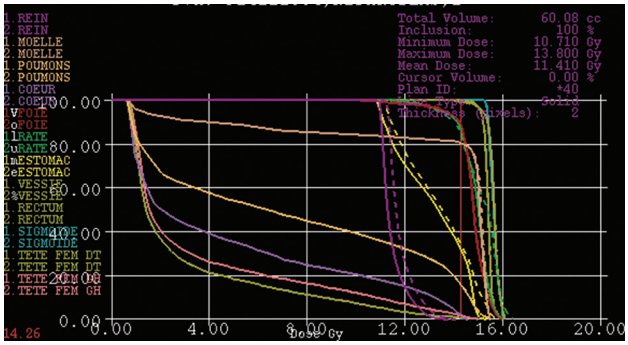

Figure 5. The dose–volume histograms of the organs at risk for the conventional block technique (solid lines) and the conformational block technique (dashed lines)

control rate and the estimated 2-year local control rate following stereotactic ablative radiotherapy (SABR) using the CyberKnife system were reported to range between 84–100% and 86–100%, respectively.[23] Lo *et al.*[24] analyzed the efficiency of SABR in patients with chronic kidney disease and renal cell carcinoma by presenting preliminary findings on local control, side effects, and renal function status following SABR using CyberKnife.[24] Therefore, SABR may be an acceptable alternative treatment option for patients with contraindicated nephron-sparing surgery.[24]

At the National Cancer Institute–Centro di Riferimento Oncologico, Aviano, Italy, low-dose regimens of 21 Gy in 14 fractions and 14.4 Gy in eight fractions were used to treat the flank in neuroblastoma and Wilms' tumor, respectively.[25] However, using high doses of radiation can result in scoliosis of the vertebral bone irradiation in young children. Traditionally, the conventional radiotherapy approach for the management of abdominal malignancies such as neuroblastoma and Wilms' tumor has involved the irradiation of relatively large treatment volumes. The standard clinical practice has typically encompassed not only the tumor bed itself but also the addition of margins of approximately 2 cm in all directions to account for microscopic disease spread and potential uncertainties in target delineation. Furthermore, these fields have historically included the entire width of the vertebral body and the para-aortic lymph nodes, which were encompassed within broad AP radiation fields to ensure adequate regional disease control. While this approach was successful in reducing the risk of locoregional recurrence, it also resulted in a considerable amount of normal tissue being exposed to therapeutic doses of radiation.

Evidence of the long-term musculoskeletal complications associated with this conventional strategy was highlighted in a clinical series reported by the University of Iowa, which investigated the incidence of radiation-induced scoliosis among pediatric patients treated for Wilms' tumor. In their cohort of 55 children, the investigators observed a clear dose–response relationship between the amount of radiation delivered to the spine and the subsequent development of spinal deformities. Specifically, the incidence of scoliosis was reported at 8% in patients who received relatively low radiation doses in the range of 10–12 Gy, rising dramatically to 46% among those treated with intermediate doses of 12.1–23.9 Gy, and reaching as high as 63% in patients who had received higher cumulative doses between 24 and 40 Gy.[26] These findings underscore the significant vulnerability of the developing pediatric skeleton to even moderate levels of irradiation and the importance of modern treatment approaches that aim to minimize long-term musculoskeletal toxicity while maintaining effective tumor control. The helical tomotherapy (HT) improved the homogeneity of the doses along the vertebral body to avoid abnormalities in bone growth, decreased the small bowel dose, and spared the healthy kidney to less than 40% of the prescribed dose,[25] with a better control of the PTV and a greater homogeneity in whole abdominal irradiation compared to the 3D-RT.[25,27,28] On the contrary, the increase in secondary malignancies due to low doses to normal tissues and the integral dose 30 years after treatment results in an incidence of around 10–20%.[18] Although the introduction and widespread adoption of highly conformal radiotherapy techniques in the management of pediatric malignancies have made it possible to substantially reduce treatment-related toxicities—particularly those arising from excessive radiation exposure to nearby OARs—a high degree of caution continues to be warranted in this vulnerable patient population. The pediatric setting presents unique challenges, as children not only exhibit greater biological sensitivity to ionizing radiation but also have a longer life expectancy, thereby creating an extended window of risk for the emergence of late effects. For this reason, whenever a new technology or radiotherapy modality is incorporated into clinical practice, careful and systematic consideration of both its benefits and potential long-term risks is essential. One of the most pressing concerns in this context is the occurrence of radiation-induced secondary malignancies, which, in many survivors, have emerged as a dominant late complication of treatment.

An illustrative example can be found in the relationship between radiation dose and the risk of thyroid cancer. Epidemiological and modeling studies have shown a paradoxical dose–response curve: the relative risk of developing thyroid cancer appears to increase following exposure to low doses of radiation, whereas at higher dose levels, the risk subsequently declines, presumably due to cell-killing effects that prevent malignant transformation.[20] However, this theoretical outcome does not fully align

with observations in clinical practice. In real-world settings, most radiation-induced secondary tumors tend to arise not exclusively in low-dose regions but rather within or adjacent to the high-dose treatment volumes, where tissues are exposed to substantial irradiation.[29] This discrepancy highlights the complexity of carcinogenesis following therapeutic radiation exposure and underscores the need for ongoing clinical surveillance and continuous refinement of dose-delivery strategies to mitigate the incidence of secondary malignancies in pediatric cancer survivors. Previous studies[16,25,30,31] analyzed the treatment of neuroblastoma using IMRT and 3D-RT, with IMRT techniques improving the CI. In cases where the ipsilateral kidney has been removed, strict shielding of the contralateral kidney is required. In a comparative dosimetric analysis, Beneyton *et al.*[30] investigated the differences in OARs exposure between HT and 3D-RT. Their results demonstrated that, overall, the recorded dose values for both techniques remained very low and consistently below the generally accepted tolerance thresholds for critical organs, thereby supporting the safety of both approaches. Furthermore, the investigators did not observe any statistically significant differences when comparing the mean doses or the V_{12} Gy values delivered by HT and 3D-RT across most evaluated structures, suggesting that the two modalities provided comparable dosimetric protection in most regions at risk.

However, a notable distinction was identified in the evaluation of the kidney ipsilateral to the tumor, which is often one of the most vulnerable organs in abdominal radiotherapy. In this specific case, the application of HT yielded a measurable improvement in dose sparing compared to 3D-RT. More precisely, HT achieved a 17% reduction in the mean average dose and a more substantial 43% decrease in the mean V_{12} Gy to the ipsilateral kidney relative to conventional 3D-RT.[30] These findings highlight the potential of HT to provide enhanced renal protection while maintaining adequate target coverage, which is particularly important in pediatric patients, where long-term preservation of renal function remains a critical objective of treatment. On the other hand, avoiding inhomogeneous growth of the bone requires irradiation of the vertebrae at higher doses, which results in an increased dose to the contralateral kidney, even with HT. Furthermore, the beam's cranio-caudal size is relatively higher with HT than with 3D-RT due to technical reasons related to the tomotherapy system.[30] 3D-RT plays an integral part in radiotherapy and may serve as a practical option for pediatric and young patients in developing countries. It is particularly beneficial for centers in the early stages of adopting modern radiotherapy practices, those still using conventional techniques, or those experienced in 3D-RT but without access to advanced modalities such as IMRT, VMAT, and Gamma Knife.

In the context of the present investigation, we sought to illustrate the clinical application of 3D-RT by presenting several representative treatment examples. Through this work, our preliminary institutional experience has provided valuable insights into the comparative performance of different planning approaches. Specifically, the analysis indicated that the use of the CFBT resulted in notable dosimetric advantages when assessed against the more traditional CVBT. The benefits observed with CFBT were twofold: there was evidence of improved sparing of surrounding critical normal structures, thereby reducing the risk of unnecessary irradiation to healthy OARs; and treatment plans generated with CFBT demonstrated superior homogeneity within the PTV, which is an essential parameter for ensuring consistent and effective tumor dose coverage. These preliminary findings suggest that, in clinical practice, CFBT has the potential to enhance the overall quality of 3D-RT planning by achieving a more favorable balance between tumor control and normal tissue protection compared with CVBT, as well as with regimens prescribing 12 Gy in eight fractions followed by 3 Gy in two fractions, instead of 10.5 Gy in seven fractions followed by 4.5 Gy in three fractions for the first course, and 4.5 Gy in three fractions for the second course. The dose conformity advantages of CFBT are significant to selectively recommend its use in the pediatric population. The use of the conventional block requires more time than the MLC block, significantly impacting verification and setup correction, particularly for the posterior field. This is true for all patients, but especially for younger ones, where treatment compliance is not always adequate.

In our study, we did not report detailed dose–volume data for the intestines, since the prescribed dose was relatively low (15 Gy in 1.5 Gy fractions). According to international pediatric radiotherapy protocols of the Oncology Pediatric International Society and the Children's Oncology Group, intestinal dose constraints are not explicitly defined at these dose levels. In contrast, constraints are mandatory for the kidneys and liver.[32] Recent reviews from the Pediatric Normal Tissue Effects in the Clinic initiative also highlighted that pediatric dose–volume data for the bowel remain limited, and clinically significant intestinal toxicities are usually observed at higher doses (>30–40 Gy), often in association with surgery.[33-35] At low abdominal doses such as 15 Gy, the risk of late enteritis is considered minimal, and current practice therefore emphasizes dose uniformity and the ALARA principle rather than strict bowel dose constraints.

5. Conclusion

This study highlighted the significance of the CFBT in the development of 3D-RT for children in developing countries. The CFBT achieved better PTV homogeneity and improved quality control of treatment planning by reducing potential human errors. After the first 10.5 Gy, the abdominal cavity was treated more uniformly with the CFBT compared to the CVBT, where individual kidney blocks reduced dose uniformity. In addition, the block setup required in the CVBT prolonged treatment time and increased the probability of inter- and intra-fractional (inter-fields) errors. Therefore, the CFBT appears to be the more acceptable approach for pediatric abdominal irradiation in this setting.

Acknowledgments

The author would like to thank the Head of the ICTP Medical Physics Section, Professor Luciano Bertocchi, and the Director of the ICTP, Professor Fernando Quevedo, the International Atomic Energy Agency, the Italian Government, and UNESCO for their hospitality at the Abdus Salam International Centre for Theoretical Physics (ICTP), Trieste, Italy.

Funding

None.

Conflict of interest

The author declares no conflict of interest.

Author contributions

This is a single-authored article.

Ethics approval and consent to participate

This study was retrospective in nature, and all data were anonymized before analysis. The study analyzed previously collected data, with no direct contact with the patients during the research. Additionally, the study does not involve sensitive information or experimental procedures.

Consent for publication

Not applicable.

Availability of data

The data analyzed in this study are available from the corresponding author upon reasonable request.

References

1. Kaatsch P. Epidemiology of childhood cancer. *Cancer Treat Rev*. 2010;36:277-285.

   doi: 10.1016/j.ctrv.2010.02.003

2. Sun M, Thuret R, Abdollah F, *et al*. Age-adjusted incidence, mortality, and survival rates of stage-specific renal cell carcinoma in North America: A trend analysis. *Eur Urol*. 2011;59:135-141.

   doi: 10.1016/j.eururo.2014.10.002

3. Green DM. The treatment of stages I-IV favorable histology Wilms' tumor. *J Clin Oncol* 2004;22(8):1366-1372.

   doi: 10.1200/jco.2004.08.008

4. Dome JS, Cotton CA, Perlman EJ, *et al*. Treatment of anaplastic histology wilms' tumor: Results from the fifth national wilms' tumor study. *J Clin Oncol*. 2006;24(15):2352-2358.

   doi: 10.1200/jco.2005.04.7852

5. Tournade MF, Com-Nougue C, De Kraker J, *et al*. Optimal duration of preoperative therapy in unilateral and nonmetastatic Wilms' tumor in children older than 6 months: Results of the ninth international society of pediatric oncology wilms' tumor trial and study. *J Clin Oncol*. 2001;19(2):488-500.

   doi: 10.1200/jco.2001.19.2.488

6. Lemerle J, Voute PA, Tournade MF, *et al*. Effectiveness of preoperative chemotherapy in Wilms' tumor: Results of an international society of paediatric oncology (SIOP) clinical trial. *J Clin Oncol*. 1983;1(10):604-609.

   doi: 10.1200/jco.1983.1.10.604

7. Tournade MF, Com-Nougue C, Voute PA, *et al*. Results of the sixth international society of pediatric oncology wilms' tumor trial and study: A risk-adapted therapeutic approach in Wilms' tumor. *J Clin Oncol*. 1993;11(6):1014-1023.

   doi: 10.1200/jco.1993.11.6.1014

8. Geyer JR, Sposto R, Jennings M, *et al*. Multiagent chemotherapy and deferred radiotherapy in infants with malignant brain tumors: A report from the Children's Cancer Group. *J Clin Oncol*. 2005;23(30):762-7631.

   doi: 10.1200/jco.2005.09.095

9. Grill J, Le Deley MC, Gambarelli D, *et al*. Postoperative chemotherapy without irradiation for ependymoma in children under 5 years of age: A multicenter trial of the French society of pediatric oncology. *J Clin Oncol*. 2001;19(5):1288-1296.

   doi: 10.1200/jco.2001.19.5.1288

10. Grundy RG, Wilne SA, Weston CL, *et al*. Primary postoperative chemotherapy without radiotherapy for intracranial ependymoma in children: The UKCCSG/SIOP prospective study. *Lancet Oncol*. 2007;8(8):696-705.

    doi: 10.1016/S1470-2045(07)70208-5

11. Tai BC, Grundy RG, Machin D. On the importance of accounting for competing risks in pediatric cancer trials designed to delay

or avoid radiotherapy: I. Basic concepts and first analyses. *Int J Radiat Oncol Biol Phys*. 2010;76(5):1493-1499.

doi: 10.1016/j.ijrobp.2009.03.035

12. Campbell SC, Novick AC, Belldegrun A, *et al*. Guideline for management of the clinical T1 renal mass. *J Urol*. 2009;182:1271-1279.

doi: 10.1016/j.juro.2009.07.004

13. Huang WC, Levey AS, Serio AM, *et al*. Chronic kidney disease after nephrectomy in patients with renal cortical tumours: A retrospective cohort study. *Lancet Oncol*. 2006;7:735-740.

doi: 10.1016/S1470-2045(06)70803-8

14. Feuvret L, Noel J, Mazeronn JJ, Bey P. Conformity index: A review. *Int J Radiat Oncol Biol Phys*. 2006;64(2):333-342.

doi: 10.1016/j.ijrobp.2005.09.028

15. Shaw E, Scott C, Souhami L, *et al*. Single dose radiosurgical treatment of recurrent previously irradiated primary brain tumors and brain metastases: Final report of RTOG protocol 90-05. *Int J Radiat Oncol Biol Phys*. 2000;47(2):291-298.

doi: 1016/s0360-3016(99)00507-6.

16. Paulino AC, Ferenci MS, Chiang KY, *et al*. Comparison of conventional to intensity modulated radiation therapy for abdominal neuroblastoma. *Pediatr Blood Cancer*. 2006;46(7):739-744.

doi: 10.1002/pbc.20456

17. Sterzing F, Stoiber EM, Nill S, *et al*. Intensity modulated radiotherapy (IMRT) in the treatment of children and adolescents--a single institution's experience and a review of the literature. *Radiat Oncol*. 2009;4:37.

doi: 10.1186/1748-717x-4-37

18. Armstrong GT, Liu Q, Yasui Y, *et al*. Late mortality among 5-year survivors of childhood cancer: A summary from the childhood cancer survivor study. *J Clin Oncol*. 2009;27: 2328-2338.

doi: 10.1200/jco.2008.21.1425

19. Hall EJ. Intensity-modulated radiation therapy, protons, and the risk of second cancers. *Int J Radiat Oncol Biol Phys*. 2006;65:1-7.

doi: 10.1016/j.ijrobp.2006.06.058

20. Bhatti P, Veiga LH, Ronckers CM, *et al*. Risk of second primary thyroid cancer after radiotherapy for a childhood cancer in a large cohort study: An update from the childhood cancer survivor study. *Radiat Res*. 2010;174:741-752.

doi: 10.1667/RR2240.1

21. Dowson LA, En Haken RK, Lawrence TS. Partial irradiation of the liver. *Semin Radiat Oncol*. 2001;11(3):240-246.

doi: 10.1053/srao.2001.23485

22. Go AS, Chertow GM, Fan D, McCulloch CE, Hsu CY. Chronic kidney disease and the risks of death, cardiovascular events, and hospitalization. *N Engl J Med*. 2004;351: 1296-1305.

doi: 10.1056/nejmoa04103

23. Siva S, Pham D, Gill S, Corcoran NM, Foroudi F. A systematic review of stereotactic radiotherapy ablation for primary renal cell carcinoma. *BJU Int*. 2012;110:E737-E743.

doi: 10.1111/j.1464-410X.2012.11550.x

24. Cheng-Hsiang Lo, Wen-Yen Huang, Hsing-Lung Chao, *et al*. Novel application of stereotactic ablative radiotherapy using CyberKnife® for early-stage renal cell carcinoma in patients with pre-existing chronic kidney disease: Initial clinical experiences. *Oncol Lett*. 2014;8:355-360.

doi: 10.3892/ol.2014.2129

25. Mascarin M, Giugliano FM, Coassin E, *et al*. Helical tomotherapy in children and adolescents: Dosimetric comparisons, opportunities and issues. *Cancers (Basel)*. 201;3:3972-3990.

doi: 10.3390/cancers3043972

26. Paulino AC, Wen BC, Brown CK, *et al*. Late effects in children treated with radiation therapy for Wilms' tumor. *Int J Radiat Oncol Biol Phys*. 2000;46:1239-1246.

doi: 10.1016/S0360-3016(99)00534-9

27. Rochet N, Sterzing F, Jensen A, *et al*. Helical tomotherapy as a new treatment technique for whole abdominal irradiation. *Strahlenther Onkol*. 2008;184:145-149.

doi: 10.1007/s00066-008-1772-z

28. Plowman PN, Cooke K, Walsh N. Indications for tomotherapy/intensity-modulated radiation therapy in paediatric radiotherapy: Extracranial disease. *Br J Radiol*. 2008;81:872-880.

doi: 10.1259/bjr/14878999

29. Newhauser WD, Durante M. Assessing the risk of second malignancies after modern radiotherapy. *Nat Rev Cancer*. 2011;11:438-448.

doi: 10.1038/nrc3069

30. Beneyton V, Niederst C, Vigneron C, *et al*. Comparison of the dosimetries of 3-dimentions radiotherapy (3D-RT) with linear accelerator and intensity modulated radiotherapy (IMRT) with helical tomotherapy in children irradiated for neuroblastoma. *BMC Med Phys*. 2012;12:2.

doi: 10.1186/1756-6649-12-2

31. Shaffer R, Vollans E, Vellani R, *et al*. A radiotherapy planning study of RapidArc, intensity modulated radiotherapy, three-dimentional conformal radiotherapy, and parallel opposed beams in the treatment of pediatric retroperitoneal tumors. *Pediatr Blood Cancer*. 2011;56(1):16-23.

doi: 10.1002/pbc.22649

32. Dome JS, Graf N, Geller JI, *et al*. Advances in Wilms tumor treatment and biology: Progress through international collaboration. *J Clin Oncol*. 2015;33(27):2999-3007.

doi: 10.1200/jco.2015.62.1888

33. Constine LS, Ronckers CM, Hua CH, *et al*. Pediatric Normal Tissue Effects in the Clinic (PENTEC): An international collaborative review of late effects from radiation therapy for childhood cancer. *Int J Radiat Oncol Biol Phys*. 2023;115(2):381-400.

doi: 10.1016/j.ijrobp.2023.06.037

34. Merchant, TE, Farr, JB, Sabin, ND, *et al*. Late effects of abdominal and pelvic radiotherapy in childhood cancer survivors: Dose-volume considerations. *Pediatr Blood Cancer*. 2022;69:e29645.

35. Teh BS, Amos RA, Paulino AC, *et al*. Radiation-induced bowel injury in pediatric oncology: Evidence and clinical considerations. *Pediatr Radiat Oncol Rev*. 2021;10(1):45-56.

ACCSCIENCE PUBLISHING

Advances in Radiotherapy & Nuclear Medicine

ORIGINAL RESEARCH ARTICLE

^{68}Ga-radiolabeled triphenylphosphonium positron emission tomography tracers for rhabdomyosarcoma tumor targeting

Chang-Tong Yang[1,2]*, Bin Xia[3], Tao He[3], Zhao Liu[2], David Chee Eng Ng[1,2], Amos Hong Pheng Loh[2,4], and Yiu Ming Khor[1,2]

[1]Department of Nuclear Medicine and Molecular Imaging, Radiological Sciences Division, Singapore General Hospital, Singapore

[2]Duke–NUS Medical School, Singapore

[3]School of Chemistry and Chemical Engineering, Hefei University of Technology, Hefei, Anhui, China

[4]VIVA-KKH Paediatric Brain and Solid Tumour Programme, Children's Blood and Cancer Centre, KK Women's and Children's Hospital, Singapore

(This article belongs to the *Special Issue: Recent Developments in Radiopharmaceuticals*)

Abstract

The proper functioning of mitochondria requires preserving the membrane potential (ΔΨm) within a narrow window. Significant deviation from the membrane potential of mitochondria is a well-established indicator of mitochondrial dysfunction. Various pathological conditions, such as cancer, diabetes, and cardiotoxicity, have been linked to mitochondrial dysfunction, highlighting the need for reliable methods to assess membrane potential *in vivo*. Hence, there is a need to explore radiolabeled lipophilic cations that accumulate within mitochondria in proportion to the potential gradient. The lipophilic organic cation triphenylphosphonium (TPP) has gained attention as a promising tracer for non-invasive imaging of mitochondrial function. It has been labeled with various radioisotopes, such as F-18, for imaging mitochondrial membrane potential in cancer through positron emission tomography (PET). The first attempt to quantify membrane potential in living organisms by examining the biodistribution of the ^{11}C-labeled TPP derivative was reported more than 30 years ago. Herein, a series of TPP derivatives, together with TPP, have been radiolabeled with ^{64}Cu for imaging gliomas, which are characterized by high mitochondrial content. 2-(diphenylphosphoryl)-ethyldiphenylphosphonium (TPEP) has demonstrated superior tumor uptake and favorable tumor-to-background ratios, leading to its selection for further assessment as a magnetic resonance imaging contrast agent. Building on these findings, we developed ^{68}Ga-labeled TPP and TPEP as novel PET tracers for rhabdomyosarcoma. To assess how the choice of targeting moiety and bifunctional chelator influences tracer performance, biodistribution studies were conducted in mitochondrial-rich rhabdomyosarcoma patient-derived xenografts. These results support further development of ^{68}Ga-TPP-based agents for mitochondrial-targeted oncologic imaging applications.

Keywords: ^{68}Ga-radiolabeled tracers; Triphenylphosphonium cation; Tumor targeting; Positron emission tomography radiotracer; Rhabdomyosarcoma

***Corresponding author:**
Chang-Tong Yang
(yang.changtong@sgh.com.sg)

Citation: Yang C, Xia B, He T, *et al*. ^{68}Ga-radiolabeled triphenylphosphonium positron emission tomography tracers for rhabdomyosarcoma tumor targeting. *Adv Radiother Nucl Med*. 2025;3(4):59-71. doi: 10.36922/ARNM025310040

Received: August 2, 2025

Revised: September 24, 2025

Accepted: October 28, 2025

Published online: November 14, 2025

1. Introduction

The proper functioning of mitochondria requires preserving the membrane potential (ΔΨm) within a narrow window. Any significant deviation from this membrane potential can impair oxidative phosphorylation, ATP synthesis, and overall cellular homeostasis. Therefore, alterations in mitochondrial membrane potential have become an important indicator of mitochondrial dysfunction. Several pathological conditions, including cancer,[1] diabetes,[2] and cardiotoxicity,[3] have been linked to disturbances in mitochondrial activity, highlighting the need for reliable methods to assess membrane potential *in vivo*. Lipophilic cationic molecules can be used to estimate mitochondrial membrane potential, which is a key biomarker of mitochondrial dysfunction.[4-6] Hence, there is a need to explore lipophilic cations that accumulate within mitochondria in proportion to the potential gradient. As membrane potential is negative (~180 mV), cations, such as triphenylphosphonium (TPP^+) and its derivatives, are electrophoretically driven across mitochondrial membranes, leading to their selective accumulation within the organelle.[7] These properties enable their use as indicators for mitochondrial targeting anti-tumor activity.[8-10]

Radiolabeled lipophilic cation complexes have been explored as mitochondria-targeted radiotracers for their therapeutic and diagnostic applications.[11] [^{3}H]-labeled tetraphenyl-phosphonium has been reported as a tracer for tumor imaging and staging due to its accumulation in certain types of tumors, despite its considerable heart and kidney uptake.[12] Due to their strong voltage dependence, TPP derivatives have been developed as radiotracers for detecting mitochondrial dysfunction in cancers and other diseases. Among them, 4-([^{18}F]fluorobenzyl)-TPP has attracted particular attention due to its sensitivity to deviation in membrane potential. It has been applied in non-small-cell lung cancer models to quantify membrane potential *in vivo* and to visualize both physiological and pathological processes where mitochondrial activity is disrupted.[13] Beyond lung cancer, radiolabeled TPP cations have shown selective accumulation in tumors with high mitochondrial content, such as gliomas, as well as prolonged retention in brain malignancies, supporting their potential as molecular probes for oncology imaging.[14] These findings underscore the value of TPP-based tracers for non-invasive assessment of mitochondrial bioenergetics in tumor biology.

The cardiovascular field has also benefited from the development of TPP-based positron emission tomography (PET) tracers. More than three decades ago, the first *in vivo* study of mitochondrial membrane potential was reported using the biodistribution of ^{11}C-triphenylmethylphosphonium (^{11}C-TPMP).[15] ^{11}C-TPMP has been validated as a PET tracer for assessing myocardial perfusion.[16] Recognizing the limitations of the short half-life of carbon-11, several ^{18}F-labeled analogs have been synthesized with tailored linker polarity to optimize their biodistribution. Furthermore, 4-[^{18}F]fluorobenzyl-TPP and 4-[^{18}F]fluorophenyl-TPP have been evaluated as agents for myocardial perfusion and blood flow imaging, demonstrating favorable uptake characteristics and improved tracer kinetics.[17-23] Collectively, these studies highlight the versatility of TPP-derived cations as radiopharmaceuticals across both oncology and cardiology applications.

We previously developed various ^{64}Cu-labeled TPP and related cationic tracers to evaluate their potential for PET imaging of selective tumors.[24-27] These studies systematically examined the effects of structural features, including the length and lipophilicity of linkers, targeting groups, bifunctional chelators, and overall molecular charge, on tumor uptake and biodistribution. Among the TPP derivatives investigated, ^{64}Cu-labeled conjugates incorporating 2-(diphenylphosphoryl)-ethyldiphenylphosphonium (TPEP) demonstrated markedly improved tumor uptake, attributed to the increased hydrophilicity and favorable structural properties of the diphenylphosphoryl group. This finding established TPEP as a lead candidate for further bimodal imaging applications.

Encouraged by the PET results, TPEP was further developed as a platform for magnetic resonance imaging (MRI) through chelation with a DO3A-based Gd^{3+} complex, yielding a novel lipophilic cationic contrast agent.[28] This agent combines the mitochondrial-targeting properties of TPEP with the paramagnetic features of Gd^{3+}, enabling high-resolution tumor imaging while retaining selectivity for cells with elevated mitochondrial membrane potential. *In vitro* cytotoxicity assessment across normal and tumor cell lines, including HEK293, HeLa, A498, HT1080, and HK2, demonstrated low toxicity, with half-maximal inhibitory concentration values in the low millimolar range. In addition, *in vivo* studies in C57BL/6 mice indicated prolonged retention in the liver and kidney, consistent with membrane binding and intracellular accumulation. MRI of SCID mice bearing A498 renal carcinoma xenografts showed significant signal enhancement in tumor tissues, validating effective mitochondrial targeting *in vivo*. Alongside other reports of DO3A-TPP-based Gd^{3+} complexes with selective tumor accumulation,[29,30] these findings highlight the potential of mitochondria-targeted cationic scaffolds as versatile platforms for both PET and

MRI, offering a translational route for multimodal cancer imaging and future theranostic applications.

Mitochondrial function plays a critical role in the biology of human rhabdomyosarcoma, where enhanced oxidative metabolism supports redox balance, promotes survival under stress, and protects cells from apoptosis.[31] This metabolic adaptation highlights the organelle as a potential therapeutic target in this tumor type. One example is SkQ1, a mitochondria-targeted antioxidant engineered as a conjugate of the lipophilic decyl-TPP cation with plastoquinone. By directing the antioxidant moiety specifically to mitochondria, SkQ1 effectively neutralizes reactive oxygen species at their primary site of generation. In pre-clinical studies, SkQ1 suppressed the proliferation of rhabdomyosarcomas *in vitro* and significantly reduced tumor burden in xenograft models in nude mice.[32,33] These findings not only demonstrate the critical role of mitochondria in maintaining the malignant phenotype of rhabdomyosarcoma but also emphasize the therapeutic potential of mitochondria-targeted agents. Such strategies may provide dual benefits by both disrupting tumor cell metabolism and sensitizing cells to stress-induced apoptosis, thereby complementing existing treatment modalities.

Previous studies reported that Gd^{3+} complexes incorporating bifunctional chelators conjugated to arylphosphonium cations were designed as the first tumor-selective mitochondrial agents for potential use in dual-modality cancer therapy.[34] We herein chose rhabdomyosarcoma patient-derived xenograft (PDX) models to perform *in vivo* biodistribution studies using ^{68}Ga-labeled triphenyl(4-((4,7,10-tris(carboxymethyl)-1,4,7,10-tetraazacyclododecan-1-yl) methyl)benzyl)-phosphonium acetate (TPP-xy-DO3A), triphenyl(4-((3-(4-((1,4,7-tris(carboxymethyl)-1,4,7-triazonan-2-yl)methyl)phenyl)thioureido)methyl) benzyl)-phosphonium acetate (TPP-xy-Bn-NOTA), (2-(diphenylphosphoryl)ethyl)diphenyl(4-((4,7,10-tris(carboxymethyl)-1,4,7,10-tetraazacyclododecan-1-yl) methyl)benzyl)-phosphonium acetate (TPEP-xy-DO3A), and (2-(diphenylphosphoryl)-ethyl)diphenyl(4-((4,7,10-tris(carboxymethyl)-1,4,7-triazonan-2-yl)methyl)-phenyl)thioureido)methyl)benzyl)-phosphonium acetate (TPEP-xy-Bn-NOTA) tracers (Figure 1). The choice of ^{68}Ga was based on its generator availability, favorable half-life for small-molecule pharmacokinetics, and efficient labeling chemistry. TPP and TPEP cations have been extensively investigated as targeting vectors for mitochondria to selectively deliver ^{68}Ga into tumor cells, which characteristically maintain a higher mitochondrial membrane potential relative to normal cells. NOTA-based chelators conjugated with TPP and TPEP were synthesized, and their radiolabeling properties with ^{68}Ga were systematically compared to those of the widely used DO3A chelator conjugates through biodistribution and excretion studies. The smaller macrocyclic cavity of NOTA is optimally suited to accommodate the Ga^{3+} ion, thereby affording thermodynamically more stable complexes than those formed with the 12-membered DOTA framework.[34-36]

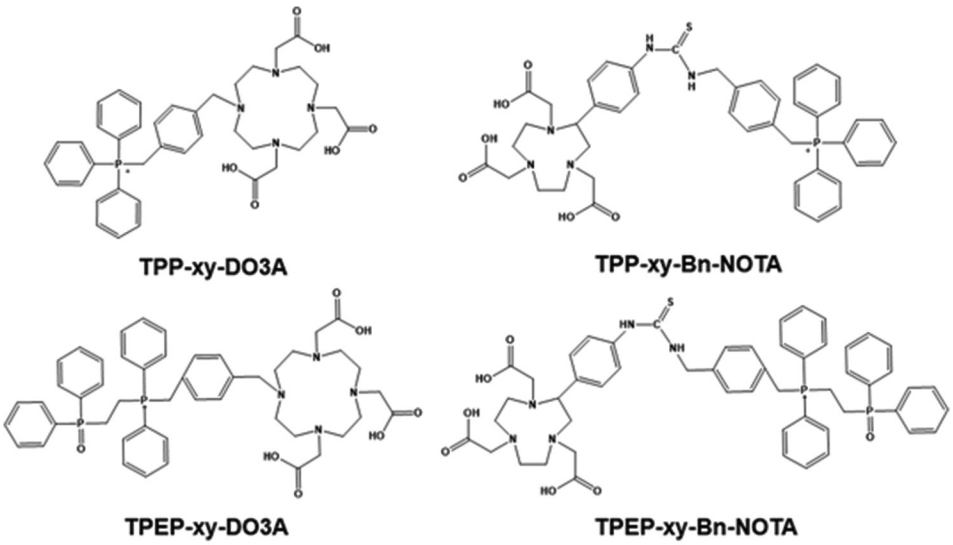

Figure 1. Molecular structures of the four ligands: ^{68}Ga-labeled triphenyl(4-((4,7,10-tris(carboxymethyl)-1,4,7,10-tetraazacyclododecan-1-yl)methyl) benzyl)-phosphonium acetate, triphenyl(4-((3-(4-((1,4,7-tris(carboxymethyl)-1,4,7-triazonan-2-yl)methyl)phenyl)thioureido)methyl)benzyl)-phosphonium acetate, (2-(diphenylphosphoryl)ethyl)diphenyl(4-((4,7,10-tris(carboxymethyl)-1,4,7,10-tetraazacyclododecan-1-yl)methyl)benzyl)-phosphonium acetate, and (2-(diphenylphosphoryl)-ethyl)diphenyl(4-((4,7,10-tris(carboxymethyl)-1,4,7-triazonan-2-yl)methyl)-phenyl)thioureido) methyl)benzyl)-phosphonium acetate.

2. Materials and methods

2.1. Materials

Chemicals and reagents were purchased from Sigma/Aldrich (United States [US]) and used as received unless stated otherwise. *p*-SCN-Bn-DOTA(2-(4-isothiocyanatobenzyl)-1,4,7,10-tetraazacyclododecane-1,4,7,10-tetraacetic acid) and *p*-SCN-Bn-NOTA(2-(4-isothiocyanatobenzyl)-1,4,7-triazacyclononane-1,4,7-triacetic acid) were purchased from Macrocyclics Inc. (US). ^{1}H nuclear magnetic resonance (NMR) spectra were obtained using the VNMRS 600 MHz NMR spectrometer (Agilent/Varian, US). Chemical shifts were reported as δ in ppm relative to tetramethylsilane. Electrospray ionization (ESI)-mass spectral data were collected using positive mode on the Finnigan LCQ Classic mass spectrometer (MS; Thermo Fisher Scientific, US) at Metabolomics in Duke-National University of Singapore Medical School.

2.2. Synthesis of compounds

2.2.1. TPP-xy-DO3A and TPP-xy-Bn-NOTA

To synthesize (4-bromobutyl)TPP bromide (TPP-xy-Br), 1,2-triphenylphosphane (1.31 g, 5 mmol) was dissolved in toluene (50 mL), and then the hot solution of α,α'-dibromo-*p*-xylene (1.18 g, 5 mmol, in 20 mL of toluene) was added dropwise into the mixture. The mixture was stirred and refluxed for 20 h. The white solid was filtered and washed with toluene and diethyl ether. Then, TPP-xy-Br was obtained after vacuum drying for 12 h as a white solid (2.15 g, yield 86.3%; ^{1}H NMR: $CDCl_3$, 4.33 [s, 2H, CH2Br], 5.33 [d, 2H, PCH2], 7.05 [m, 4H, C6H4], 7.59–7.71 [m, 15H, C6H5]).

To synthesize 4-aminomethylbenzyltris(phenyl) phosphonium bromide (TPP-xy-NH_2), TPP-xy-Br (526 mg, 1 mmol) and potassium phthalimide (220 mg, 1.2 mmol) were added to 30 mL of acetonitrile and refluxed for 24 h. The resulting intermediate was dissolved in ethanol (30 mL), followed by the addition of aqueous hydrazine (55%, 2 mL), and the mixture was refluxed for a further 24 h. After removal of volatiles under vacuum conditions, the residue was dissolved in dichloromethane (20 mL) and filtered to remove insoluble by-products. Evaporation of the solvent afforded TPP-xy-NH_2 as a yellow solid (364 mg, yield 78.8%).

To synthesize TPP-xy-DO3A, TPP-xy-Br (92 mg, 0.2 mmol) and DO3A-tBu (103 mg, 0.2 mmol) were dissolved in 10 mL of N,N-dimethylformamide (DMF), followed by the addition of 0.5 g K_2CO_3. The mixture was stirred at 50°C for 12 h. After removing the solid through filtration, the solvent was evaporated, and the residue was dissolved in trifluoroacetic acid (10 mL). The mixture was stirred at room temperature for 4 h. Then, the residue was dissolved in 5 mL of water and dialyzed (500 Da cutoff) in deionized water for 48 h. TPP-xy-DO3A was obtained after vacuum drying as a yellow solid (121 mg, yield 85%; ESI-MS: m/z = 711.3 for M^+ [calcd 710.3 for $[C_{40}H_{47}N_4O_6P]^+$]).

To synthesize TPP-xy-Bn-NOTA, TPP-xy-NH_2 (37 mg, 0.08 mmol) and *p*-SCN-Bn-NOTA (37 mg, 0.08 mmol) were dissolved in DMF (5 mL), followed by the addition of NaOH solution to adjust the pH to 8.5. The mixture was stirred at room temperature for 12 h. Then, the mixture was dialyzed (500 Da cutoff) in deionized water for 48 h. TPP-xy-Bn-NOTA was obtained after vacuum drying as a yellow solid (53 mg, yield 72%; ESI-MS: m/z = 832.3 for M^+ [calcd 831.3 for $[C_{46}H_{50}N_5O_6PS]^+$]).

2.2.2. TPEP-xy-DO3A and TPEP-xy-Bn-NOTA

To synthesize (4-bromobutyl)TPEP bromide (TPEP-xy-Br), a stirred solution of 1,2-bis(diphenylphosphino) ethane monoxide (2.07 g, 5 mmol) in toluene (50 mL) was added dropwise to a pre-heated solution of α,α'-dibromo-*p*-xylene (1.18 g, 5 mmol) in toluene (20 mL). The reaction mixture was then heated under reflux with stirring for 20 h. Upon completion, the white solid product was isolated through filtration, thoroughly washed with toluene followed by diethyl ether, and dried under vacuum for 12 h to yield TPEP-xy-Br as a white solid (3.01 g, 92.6%; 1H NMR [DMSO-d6]: 2.64 [m, 2H, O=PCH2); 3.00 [m, 2H, PCH2]; 4.65 [s, 2H, CH2Br]; 4.88 [d, 2H, PCH2]; 6.85 [d, 4H, C6H4]; 7.17–7.85 [m, 20H, C6H5]).

To synthesize (4-(aminomethyl)benzyl) (2-(diphenylphosphoryl)ethyl)diphenylphosphonium (TPEP-xy-NH_2), a mixture of TPEP-xy-Br (680 mg, 1 mmol) and potassium phthalimide (220 mg, 1.2 mmol) in acetonitrile (30 mL) was refluxed for 24 h. The resulting yellow precipitate was isolated through filtration and dried. This intermediate and aqueous hydrazine (55%, 2 mL) were then dissolved in ethanol (30 mL), and the solution was refluxed for an additional 24 h. Following the removal of volatiles under reduced pressure, the residue was dissolved in dichloromethane (20 mL) and filtered. Concentration of the filtrate *in vacuo* afforded the target compound (TPEP-xy-NH_2) as a yellow solid (440 mg, 82.3% yield).

To synthesize TPEP-xy-DO3A, a solution of TPEP-xy-Br (135.6 mg, 0.2 mmol) and DO3A-tBu (103 mg, 0.2 mmol) in anhydrous DMF (10 mL) was prepared. Potassium carbonate (K_2CO_3, 0.5 g) was introduced, and the reaction mixture was stirred at 50°C for 12 h. Upon completion, solids were removed through filtration, and the solvent was evaporated under reduced pressure. The resulting residue was treated with trifluoroacetic acid (10 mL) and stirred at ambient temperature for 4 h. The crude product was

then dissolved in water (5 mL) and subjected to dialysis against deionized water using a 500-Da molecular-weight-cutoff membrane for 48 h. Final purification via vacuum drying afforded the target compound, TPEP-xy-DO3A, as a yellow solid (143 mg, 83% yield; ESI-MS: m/z = 863.4 for M^+ [calcd 864.4 for $[C_{48}H_{56}N_4O_7P_2]^+$]).

To synthesize TPEP-xy-Bn-NOTA, TPEP-xy-NH_2 (50 mg, 0.08 mmol) and *p*-SCN-Bn-NOTA (37 mg, 0.08 mmol) were dissolved in anhydrous DMF (5 mL). The pH of the reaction mixture was then adjusted to 8.5 using a NaOH solution. Conjugation was allowed to proceed under constant stirring at ambient temperature for 12 h. The crude product was purified through dialysis against deionized water using a membrane (500 Da molecular weight cutoff) for 48 h. Subsequent lyophilization afforded the target compound, TPEP-xy-Bn-NOTA, as a yellow solid in 71% yield (62 mg; ESI-MS: m/z = 984.4 for M^+ [calcd 983.4 for $[C_{54}H_{59}N_5O_7P_2S]^+$]).

2.3. ^{68}Ga radiolabeling

^{68}Ga has a half-life of 68 min and decays predominantly through β^+ emission (E_{max} = 1.92 MeV, 90%), with the remaining 10% through electron capture. All procedures involving radioisotopes were conducted in laboratories approved by the National Environment Agency, Singapore, in compliance with the Radiation Protection and Nuclear Sciences Department guidelines for radiation safety and contamination control. Radioactivity of ^{68}Ga was measured using the AtomLab™ 500 dose calibrator (Biodex Medical Systems, Inc., US). For quality control, thin-layer chromatography (TLC) was performed on silica gel (SG) 60 F254 aluminum sheets (20 × 20 cm; Merck KGaA, Germany), cut into 2 × 10 cm strips. Instant TLC (iTLC) was analyzed on the Bioscan AR-2000 system (US) equipped with a P10 cylinder containing methane/argon gas. High-performance liquid chromatography (HPLC) was carried out using the Agilent 1260 system (Agilent Technologies, US) with a UV-vis detector (λ = 220 nm), a one-inch NaI/PMT flow-ram detector (LabLogic Systems Ltd., United Kingdom), and a Zorbax Rx-C18 column (4.6 × 150 mm, 300 Å). The mobile phase consisted of solvent A (10 mM ammonium acetate) and solvent B (acetonitrile), delivered at 1 mL/min under isocratic conditions (80:20, A: B) for 0–5 min, followed by a linear gradient from 20% to 60% B over 5–15 min.

Radiolabeling of ^{68}Ga to the ligands was performed by reacting $^{68}GaCl_3$ solution (2.0–3.0 mCi) in 0.05 N HCl, obtained from a ^{68}Ge/^{68}Ga generator (ITM Medical Isotopes GmbH, ITM Isotope Technologies Munich SE, Germany), with the ligands in 0.1 M NH_4OAc buffer (pH = 4.5–5.0) at 90–95°C for 25–30 min. The mixture was then cooled to room temperature, and the resulting solution was analyzed by radio-TLC using a glass microfiber impregnated with SG (iTLC–SG) plate with 10 mM NH_4OAc/MeCN (9:1) as the mobile phase. The ^{68}Ga-labeled tracer was purified by passing the reaction mixture through a conditioned Sep-Pak@Plus short C-18 cartridge (Waters). The C-18 cartridge was conditioned sequentially with 10 mL of ethanol, followed by 10 mL of sterile water. The ^{68}Ga-labeled tracer was trapped on the cartridge and subsequently eluted using 1 mL of 70% ethanol delivered through a 1 mL syringe. The radioactivity of the eluate was measured, and quality control was performed by radio-HPLC analysis of the purified compounds: ^{68}Ga(TPP-xy-DO3A) (Tracer 1), ^{68}Ga(TPP-xy-Bn-NOTA) (Tracer 2), ^{68}Ga(TPEP-xy-DO3A) (Tracer 3), and ^{68}Ga(TPEP-xy-Bn-NOTA) (Tracer 4).

2.4. Animal model

A PDX model was generated from metastatic alveolar rhabdomyosarcomas harboring the *PAX7–FKHR* fusion (t(1;13) translocation), obtained following written parental consent under SingHealth Duke-NUS CIRB protocol 2014/2079 (Modeling, Analysis, and Translational Therapeutics for Tumors of Childhood; Case ID: RHB24-0521). The use of rhabdomyosarcoma PDX models provides a high degree of translational relevance. Unlike conventional cell-line xenografts, PDX tumors retain the histological architecture, genetic heterogeneity, and metabolic features of the patient's tumor, including mitochondrial density and microenvironmental interactions.

The tumor specimen was finely minced under sterile conditions, and 0.1 mL of tumor slurry was combined with Matrigel™ basement membrane matrix (BD Biosciences, Cat#354234, US) in a 5:1 ratio to enhance engraftment and support tumor cell viability. The mixture was orthotopically implanted into the intramuscular space of NOD scid gamma (NSG; NOD.Cg-*Prkdc*^{scid} *Il2rg*^{tm1Wjl}/SzJ) mice under inhalational anesthesia with pharmaceutical-grade isoflurane that complies with US Pharmacopeia specifications (<5%), ensuring minimal animal distress. Upon successful initial engraftment, tumors were serially passaged into NOD scid (NOD.CB17-*Prkdc*^{scid}/J) mice using the same orthotopic implantation procedure to expand the PDX cohort. At each passage, xenograft tumors were assessed histologically to confirm that the morphological features of the original patient tumor were preserved, including the cellular architecture and characteristic markers of alveolar rhabdomyosarcoma (Figure 2).

A total of 48 8-week-old female mice were used in the study. Animals were housed in a temperature-controlled, specific pathogen-free facility within a microisolator or

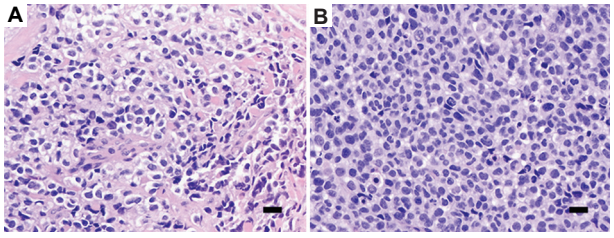

Figure 2. Representative photomicrographs of alveolar rhabdomyosarcoma histological sections from (A) patient and (B) patient-derived xenograft model, demonstrating recapitulation of small blue round cell tumor morphology and characteristic rhabdoid cell features (hematoxylin and eosin staining; magnification: 40×, scale bar: 40 μm)

pressurized individually ventilated cages under maximum barrier conditions. Water was supplemented with antibiotics and acidified (pH 2.5–3.0) to prevent infection, and mice were fed a standard diet *ad libitum*. Tumor growth was monitored at least weekly by measuring ipsilateral thigh circumference, and animals were randomized into four study groups when tumors reached a target weight of 0.3–0.6 g. All experimental procedures were conducted in strict accordance with institutional ethical guidelines and were approved by the Institutional Animal Care and Use Committee (IACUC No. 2016/SHS/1468). Measures were taken to minimize animal discomfort and ensure humane endpoints, in line with best practices for PDX modeling of pediatric sarcomas.

2.5. Biodistribution study

The ^{68}Ga radiotracers (~3 MBq) were administered to tumor-bearing mice through the tail vein. At 15, 30, 60, and 90 mins after injection, the mice (n = 3/time point) were sacrificed. Tumors and selected organs (the liver, kidneys, heart, lungs, blood, and muscle) were excised, weighed, and counted using a γ-counter (1480 WIZARD, PerkinElmer, Inc., US). Uptake was expressed as a percentage of injected dose per gram of tissue (%ID/g). The biodistribution data and target-to-background ratios are reported as mean ± standard deviation. Statistical analyses were performed through Student's t-test and one-way analysis of variance using Python 3.10 (Python Software Foundation, US). The level of significance was set at $p<0.05$.

3. Results and discussion

Four tracers were synthesized following previously published procedures with minor modifications[24] and subsequently characterized using high-resolution ESI-MS (details provided in Figure A1) to confirm their molecular integrity and purity. For radiolabeling, $^{68}GaCl_3$ was obtained from a ^{68}Ge–^{68}Ga generator through elution using 0.05 N HCl delivered through a 10-mL syringe. The initial elution fraction (~0.5 mL) was discarded into a waste vial to remove impurities and residual long-lived ^{68}Ge. The subsequent 1 mL fraction, corresponding to a sudden increase in activity as detected via a dose calibrator placed adjacent to the generator, was collected and designated for radiolabeling. Any additional elution beyond this point was discarded to minimize contamination.

The total activity of the collected eluate ranged from 9 to 10 mCi, of which approximately 0.6 mL of high-purity $^{68}GaCl_3$ (approximately 5 mCi) was withdrawn for immediate use in subsequent labeling reactions. Notably, the pH of the eluted $^{68}GaCl_3$ was not adjusted before labeling, simplifying the preparation process and minimizing the potential loss of radioactivity during pH adjustment. This approach ensured a reproducible and high-activity source of ^{68}Ga suitable for efficient ligand labeling, while adhering to radiation safety protocols for handling short-lived positron-emitting isotopes.

Both DO3A and NOTA were selected as the bifunctional chelators in this study because they can effectively form highly stable chelates with clinically relevant radionuclides, such as ^{64}Cu and ^{111}In. They belong to the family of macrocyclic chelators, which are favored in nuclear medicine for their strong kinetic inertness and thermodynamic stability.[37] NOTA has demonstrated superior performance with ^{68}Ga, a positron-emitting radionuclide commonly used in PET imaging due to its convenient generator availability. This is evident in the reported stability constants, where NOTA forms a highly stable complex with Ga^{3+} (K_ML = 31.10), markedly higher compared to DOTA (K_ML = 21.3).[38,39] The increased stability of NOTA–Ga complexes reduces the risk of *in vivo* dissociation or transchelation to serum proteins, thereby ensuring reliable imaging contrast and minimizing non-specific background uptake. Structurally, NOTA is a hexadentate N_3O_3 macrocycle, which coordinates with Ga^{3+} to yield a neutral Ga–NOTA complex.[34] This neutrality is advantageous because it often translates into improved pharmacokinetics, including reduced plasma protein binding and faster blood clearance.

To facilitate conjugation and radiolabeling under mild conditions, we employed the commercially available p-isothiocyanatobenzyl derivative of NOTA, which carries a reactive isothiocyanate group that couples efficiently to amine-containing ligands without compromising the chelator's binding properties. In contrast, DO3A, a derivative of DOTA containing three acetate arms, is generally regarded as kinetically more sluggish in radiolabeling reactions compared to NOTA. DOTA-based chelators require harsher conditions (higher temperature and longer reaction time) for efficient ^{68}Ga incorporation due to their large cavity size and less optimal fit for Ga^{3+}.

However, once formed, the resulting DOTA–Ga complexes are exceptionally stable and resistant to demetallation under physiological conditions. Thus, while NOTA offers rapid labeling kinetics under mild conditions—a valuable feature when labeling heat-sensitive biomolecules—DO3A provides a complementary option, balancing slightly slower labeling kinetics with excellent *in vivo* stability.

Including both chelators in this study allowed for a broader evaluation of labeling efficiency, stability, and biological behavior. Previous reports have shown that NOTA-containing ligands, such as TPP-xy-Bn-NOTA and TPEP-xy-Bn-NOTA, can be efficiently labeled with ^{64}Cu to yield thermodynamically stable, irreversibly bound complexes even at room temperature.[25,26] Building on this, we applied a consistent radiolabeling protocol to all four designed ligands, TPP-xy-DO3A, TPP-xy-Bn-NOTA, TPEP-xy-DO3A, and TPEP-xy-Bn-NOTA, to enable direct comparisons between DO3A- and NOTA-based tracers in subsequent biodistribution studies.

Radiochemical analysis using iTLC-SG showed that the crude labeling yields of the four complexes, tracers 1–4, were within 45–65% (Figure 3A-D). Although these crude yields were moderate, subsequent purification on a C-18 Sep-Pak cartridge effectively removed free gallium and by-products, increasing the radiochemical purity of all tracers to higher than 98%. This was confirmed through radio-HPLC analysis, as illustrated for Tracer 1 (Figure 3E). Moreover, the purified radiolabeled products demonstrated excellent short-term stability, remaining intact in saline for at least 2 h with no detectable dissociation. Such stability is essential for *in vivo* imaging applications, as it ensures that the radioactive signal accurately reflects the biodistribution

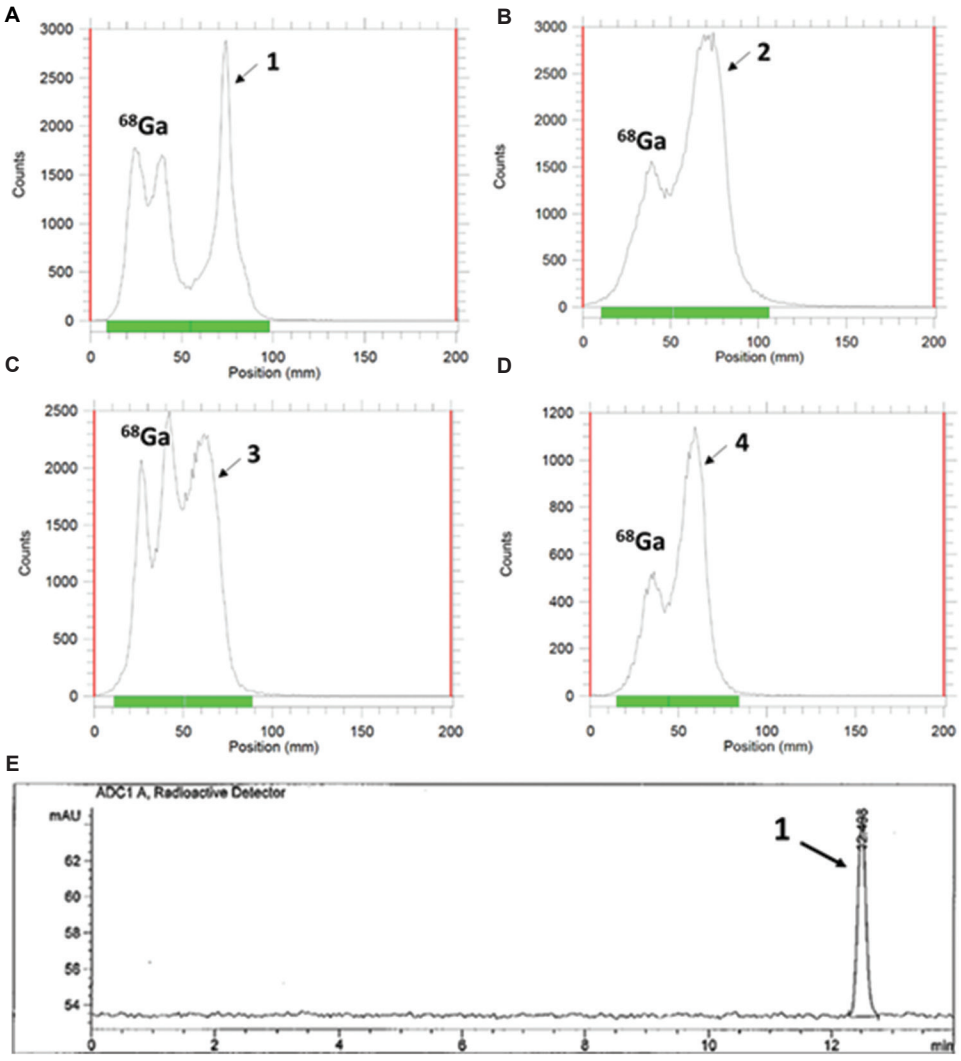

Figure 3. Chromatograms of tracers 1–4. (A–D) Chromatograms of instant thin-layer chromatography for (A) tracer 1, (B) tracer 2, (C) tracer 3, and (D) tracer 4, showing radiochemical yield analysis. (E) The radio-high-performance liquid chromatography chromatogram of tracer 1.

of the targeting ligands rather than free radionuclides. Taken together, these findings highlight that while NOTA offers the advantage of fast and efficient ^{68}Ga labeling under mild conditions, DO3A provides an additional layer of robustness *in vivo*, making both chelators valuable scaffolds for the development of reliable radiotracers.

The biodistribution profiles of tracers 1–4 at 15, 30, 60, and 90 min post-injection are summarized in Figure 4. Among the four candidates, tracer 3 demonstrated the most favorable tumor-targeting properties. It showed an early tumor uptake of 1.45 ± 0.92 %ID/g at 15 min and was maintained over time, with only a modest decline to 0.57 ± 0.62 %ID/g at 90 min. This stability suggests effective and sustained retention in tumor tissue, confirming its strong tumor selectivity.

The clearance characteristics of tracer 3 further support its suitability as a lead candidate. It exhibited efficient renal clearance, with kidney uptake peaking at 26.78 ± 7.89 %ID/g at 15 min, followed by rapid washout to 8.04 ± 2.75 %ID/g at 90 min. This rapid excretion profile minimizes long-term renal retention, reducing potential nephrotoxicity concerns. In addition, tracer 3 showed rapid blood clearance, as circulating activity decreased sharply from 3.32 ± 2.06 %ID/g at 15 min to 0.37 ± 0.25 %ID/g at 90 min. The combination of stable tumor retention, rapid blood clearance, and efficient renal excretion is highly desirable for imaging tracers, as it enhances tumor visibility while reducing background signals.

By comparison, tracer 1 demonstrated less favorable tumor-targeting characteristics. At 90 min, the tumor uptake was 0.36 %ID/g, lower than that of tracer 3 (0.57 ± 0.62 %ID/g). Blood clearance of tracer 1 was also slower, with a value of 0.53 ± 0.27%ID/g at 90 min compared to 0.37 ± 0.25 %ID/g for tracer 3. In addition, tracer 1 showed higher kidney retention (6.21 ± 2.56 vs. 5.39 ± 2.75 %ID/g for tracer 3 at 90 mins) and produced poorer tumor-to-background contrast, as reflected by a tumor-to-blood ratio of only 0.68, compared to 1.54 for tracer 3. Collectively, these findings indicate that tracer 1 is less efficient in differentiating tumors from background tissues, limiting its potential utility.

The NOTA-containing analogs (tracers 2 and 4) displayed distinct biodistribution patterns compared to their DO3A-based counterparts. Tracer 2 showed a tumor uptake rate (1.30 ± 0.46 %ID/g at 15 min) that was initially comparable to tracer 3, but declined more steeply to 0.60 ± 0.33 %ID/g by 90 min, suggesting a less stable tumor retention. Notably, tracer 2 exhibited substantial liver accumulation (10.39 ± 1.83 %ID/g at 90 min), which may reflect differences in lipophilicity or chelator-dependent biodistribution. Such high hepatic uptake is undesirable, as it may interfere with the imaging of abdominal lesions and may complicate dosimetry for therapeutic applications. On the other hand, tracer 4 was particularly notable for its persistent blood pool activity, with values remaining at 1.94 ± 0.81 %ID/g at 90 min. In contrast, tracer 3, its DO3A-based analog, demonstrated significantly lower blood activity (0.37 ± 0.25 %ID/g; p=0.003). This slow clearance limits the tumor-to-blood contrast for tracer 4 and may hinder effective imaging. Both tracers 2 and 4 consistently showed slower clearance from circulation relative to their DO3A analogs, underscoring the impact of chelator selection on pharmacokinetics. Across all

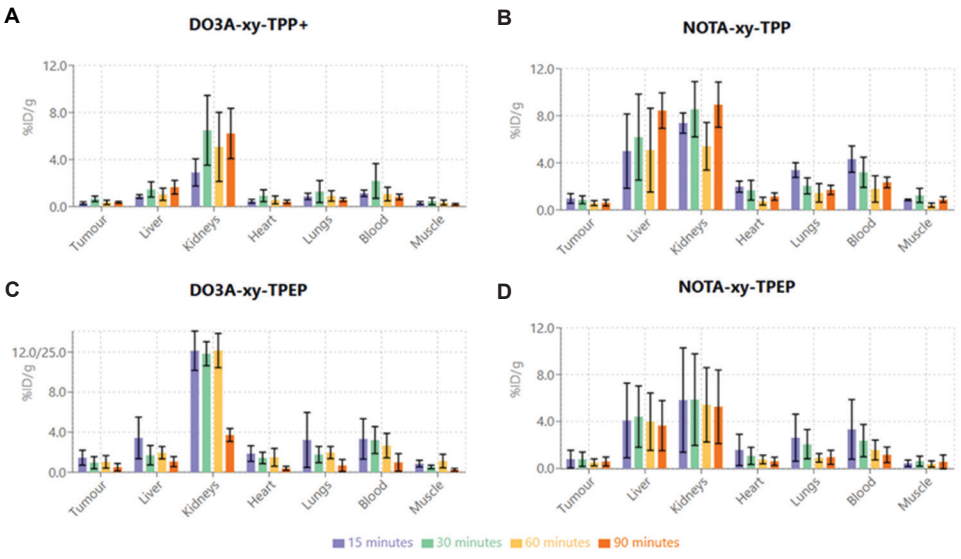

Figure 4. *In vivo* biodistribution of (A) tracer 1, (B) tracer 2, (C) tracer 3, and (D) tracer 4 in rhabdomyosarcoma patient-derived xenograft tumor-bearing mice (n = 3/group), at 15 min (blue bars), 30 min (orange bars), 60 min (gray bars), and 90 min (yellow bars) post-injection

tracers, heart and lung uptake remained low (<2 %ID/g after 30 min), indicating minimal non-specific retention in these organs and favorable distribution profiles with respect to cardiopulmonary safety.

Taken together, the comparative biodistribution analysis highlights tracer 3 as the most promising candidate. Its combination of sustained tumor retention, rapid clearance from blood and non-target tissues, efficient renal excretion, and superior tumor-to-background ratios provides a strong rationale for prioritizing tracer 3 for further pre-clinical development and potential translation to clinical imaging studies.

In addition, the biodistribution data suggest that the chelator NOTA, when complexed with ^{68}Ga, does not significantly contribute to tumor uptake, indicating that its high thermodynamic stability and fast complexation kinetics may not directly translate into effective tumor targeting. In contrast, the chelator DO3A used in tracer 3 demonstrated favorable tumor uptake, maintaining stable retention and yielding high tumor-to-muscle ratios. This difference highlights that beyond radiometal complex stability, the choice of chelator can influence pharmacokinetics, tracer biodistribution, and target accessibility, ultimately affecting tumor accumulation. Thus, DO3A may provide more suitable biological characteristics for tumor imaging compared to NOTA in this regard. Our data demonstrated that ^{68}Ga-labeled tracers show biodistribution patterns comparable to those previously reported with ^{64}Cu,[24-26] indicating that the intrinsic targeting mechanism is preserved across different radionuclides. While ^{68}Ga does not inherently increase tumor accumulation compared to ^{64}Cu, it offers the advantage of rapid imaging with lower background retention due to its short half-life.

4. Conclusion

Radiolabeling of TPP and TPEP ligands with ^{68}Ga can be achieved with high radiochemical efficiency, demonstrating the feasibility of these compounds as potential PET imaging agents. Importantly, the modification of TPP-based ligands and their associated chelators was found to significantly influence the biodistribution and targeting characteristics of the resulting ^{68}Ga-radiotracers, highlighting the critical role of ligand design in optimizing tumor selectivity and minimizing off-target accumulation. Comparative analysis demonstrated that the biodistribution profiles of the ^{68}Ga-labeled tracers were generally consistent with those in previously reported studies that used the same ligands labeled with ^{64}Cu, suggesting that the intrinsic targeting properties of TPP and TPEP scaffolds are preserved across different radiometals. *In vivo* studies conducted in NOD scid mice bearing rhabdomyosarcoma PDX tumors further confirmed appreciable tumor uptake and favorable tumor-to-normal tissue ratios, thereby underscoring the potential utility of these tracers for oncological imaging. The current results provide an important proof of concept, and ongoing optimization of ligand structure and chelation strategy is expected to enhance tumor accumulation and further improve the translational potential of these tracers. Such refinements are essential to advance these radiotracers from the pre-clinical stage toward clinical translation, where they may serve as valuable tools for tumor detection, molecular characterization, and potentially for guiding therapeutic interventions.

Acknowledgments

The authors thank Ms Aiswariya Vadivellu, VIVA-KKH Paediatric Brain and Solid Tumour Programme, for assistance with experiments.

Funding

This study was funded by the SingHealth Duke-NUS Radiological Sciences Academic Clinical Programme Grant: Pitch for Funds (2020) and the VIVA-KKH Paediatric Brain and Solid Tumour Programme (Viva Foundation for Children with Cancer).

Conflict of interest

Chang-Tong Yang is an Editorial Board Member of this journal and Guest Editor of this special issue, but was not in any way involved in the editorial and peer-review process conducted for this paper, directly or indirectly. Separately, other authors declared that they have no known competing financial interests or personal relationships that could have influenced the work reported in this paper.

Author contributions

Conceptualization: Chang-Tong Yang, Amos Hong Pheng Loh, Yiu Ming Khor
Data curation: Bin Xia, Tao He, Zhao Liu, Chang-Tong Yang
Formal analysis: Chang-Tong Yang, Amos Hong Pheng Loh, David Chee Eng Ng, Yiu Ming Khor
Investigation: Chang-Tong Yang, Amos Hong Pheng Loh, Yiu Ming Khor
Methodology: Chang-Tong Yang, Bin Xia, Zhao Liu
Project administration: Chang-Tong Yang
Resources: Chang-Tong Yang, Bin Xia, Tao He
Supervision: Chang-Tong Yang, Yiu Ming Khor
Validation: Chang-Tong Yang, Bin Xia, Zhao Liu
Writing–original draft: Chang-Tong Yang, Bin Xia
Writing–review & editing: Chang-Tong Yang, Bin Xia, Amos Hong Pheng Loh, Yiu Ming Khor

Ethics approval and consent to participate

The study acquired approval from the SingHealth Duke NUS CIRB protocol 2014/2079 (Modeling, Analysis, and Translational Therapeutics for Tumors of Childhood) (Case ID RHB24-0521). All experiments were performed under the approval of the Institutional Animal Care and Use Committee (IACUC No.: 2016/SHS/1468).

Consent for publication

Not applicable.

Availability of data

Data are available from the corresponding author upon reasonable request.

Further disclosure

Parts of the findings were presented in the 37th Annual Congress of the European Association of Nuclear Medicine EANM´24, October 19–23, 2024, Hamburg, Germany; and in the 26th International Symposium of Radiopharmaceutical Science (iSRS 2025), May 11-15, 2025, Gold Coast, Australia.

References

1. Dedkova EN, Blatter LA. Measuring mitochondrial function in intact cardiac myocytes. *J Mol Cell Cardiol.* 2012;52: 48-61.

   doi: 10.1016/j.yjmcc.2011.08.030

2. Duchen MR, Surin A, Jacobson J. Imaging mitochondrial function in intact cells. *Meth Enzymol.* 2003;361:353-389.

   doi: 10.1016/S0076-6879(03)61019-0

3. McCluskey S, Haslop A, Coello C, *et al.* Imaging of chemotherapy-induced acute cardiotoxicity with ^{18}F-labeled lipophilic cations. *J Nucl Med.* 2019;60:1750-1756.

   doi: 10.2967/jnumed.119.226787

4. Pelletier-Galarneau M, Petibon Y, Ma C, *et al. In vivo* quantitative mapping of human mitochondrial cardiac membrane potential: A feasibility study. *Eur J Nucl Med Mol Imaging*. 2021;48:414-420.

   doi: 10.1007/s00259-020-04878-9

5. Hüttemann M, Lee I, Pecinova A, *et al*. Regulation of oxidative phosphorylation, the mitochondrial membrane potential, and their role in human disease. *J Bioenerg Biomembr.* 2008;40:445-456.

   doi: 10.1007/s10863-008-9169-3

6. Rottenberg H. Membrane potential and surface potential in mitochondria: Uptake and binding of lipophilic cations. *J Membr Biol.* 1984;81:127-138.

   doi: 10.1007/bf01868977

7. Zorova LD, Popkov VA, Plotnikov EY, *et al*. Mitochondrial membrane potential. *Anal Biochem*. 2018;552:50-59.

   doi: 10.1016/j.ab.2017.07.009

8. Modica-Napolitano JS, Apprille JR. Delocalized lipophilic cations selectively target the mitochondria of carcinoma cells. *Adv Drug Deliv Rev*. 2001;49:63-70.

   doi: 10.1016/s0169-409x(01)00125-9

9. Mannella CA. The relevance of mitochondrial membrane topology to mitochondrial function. *Biochim Biophys Acta*. 2006;1762:140-147.

   doi: 10.1016/j.bbadis.2005.07.001

10. Dhanasekaran S, Venugopal D, Al-Dayan N, *et al.* Emerging insights into mitochondria-specific targeting and drug delivering strategies: Recent milestones and therapeutic implications. *Saudi J Biol Sci*. 2020;27:3581-3592.

    doi: 10.1016/j.sjbs.2020.07.030

11. Zielonka J, Joseph J, Sikora A, *et al*. Mitochondria-targeted triphenylphosphonium-based compounds: Syntheses, mechanisms of action, and therapeutic and diagnostic applications. *Chem Rev.* 2017;117:10043-10120.

    doi: 10.1021/acs.chemrev.7b00042

12. Min J, Biwal S, Deroose C, Gambhir SS. Tetraphenylphosphonium as a novel molecular probe for imaging tumors. *J Nucl Med*. 2004;45:636-643.

13. Madar I, Ravert H, Nelkin B, *et al.* Characterization of membrane potential-dependent uptake of the novel PET tracer 18F-fluorobenzyl triphenylphosphonium cation. *Eur J Nucl Med Mol Imaging*. 2007;34:2057-2065.

    doi: 10.1007/s00259-007-0500-8

14. Cheng X, Feng D, Lv J, *et al.* Application prospects of triphenylphosphine-based mitochondria-targeted cancer therapy. *Cancers (Basel)*. 2023;15:666.

    doi: 10.3390/cancers15030666

15. Fukuda H, Syrota A, Charbonneau P, *et al*. Use of 11C-triphenylmethylphosphonium for the evaluation of membrane potential in the heart by positron-emission tomography. *Eur J Nucl Med*. 1986;11:478-483.

    doi: 10.1007/BF00252793

16. Krause BJ, Szabo Z, Becker LC, *et al*. Myocardial perfusion with [11C]methyl triphenyl phosphonium: Measurements of the extraction fraction and myocardial uptake. *J Nucl Biol Med (1991)*. 1994;8:521-526.

17. Kim DY, Kim HJ, Yu KH, *et al*. Synthesis of [18F]-labeled (2-(2 fluoroethoxy)-ethyl)-tris(4-methoxyphenyl)-phosphonium cation as a potential agent for positron emission tomography myocardial imaging. *Nucl Med Biol*. 2012;39:1093-1098.

doi: 10.1016/j.nucmedbio.2012.03.008

18. Kim DY, Kim HJ, Yu KH, Min JJ. Synthesis of [18F]-labeled (2-(2-fluoroethoxy)-ethyl)-triphenylphosphonium cation as a potential agent for myocardial imaging using positron emission tomography. *Bioorg Med Chem Lett.* 2012;22: 319-322.

doi: 10.1016/j.bmcl.2011.11.005

19. Kim DY, Kim HS, Le UN, *et al*. Evaluation of a mitochondrial voltage sensor, (18F-fluoropentyl) triphenylphosphonium cation, in a rat myocardial infarction model. *J Nucl Med.* 2012;53:1779-1785.

doi: 10.2967/jnumed.111.102657

20. Zhao Z, Yu Q, Mou T, *et al.* Highly efficient one-pot labeling of new phosphonium cations with fluorine-18 as potential PET agents for myocardial perfusion imaging. *Mol Pharm*. 2014;11:3823-3831.

doi: 10.1021/mp500216g

21. Kim DY, Kim HS, Min JJ. Radiosynthesis and evaluation of 18F-labeled aliphatic phosphonium cations as a myocardial imaging agent for positron emission tomography. *Nucl Med Commun*. 2015;36:747-754.

doi: 10.1097/MNM.0000000000000315

22. Kim DY, Min JJ. Synthesis and evaluation of 18F-labeled fluoroalkyl triphenylphosphonium salts as mitochondrial voltage sensors in PET myocardial imaging. *Methods Mol Biol.* 2015;1265:59-72.

doi: 10.1007/978-1-4939-2288-8_5

23. Kim DY, Min JJ. Radiolabeled phosphonium salts as mitochondrial voltage sensors for positron emission tomography myocardial imaging agents. *Nucl Med Mol Imaging*. 2016;50:185-195.

doi: 10.1007/s13139-016-0397-x

24. Wang J, Yang CT, Kim YS, *et al*. ^{64}Cu-labeled triphenylphosphonium and triphenylarsonium cations as highly tumor-selective imaging agents. *J Med Chem*. 2007;50:5057-5069.

doi: 10.1021/jm0704088

25. Kim YS, Yang CT, Wang J, *et al*. Effects of targeting moiety, linker, bifunctional chelator, and molecular charge on biological properties of ^{64}Cu-labeled triphenylphosphonium cations. *J Med Chem*. 2008;51:2971-2984.

doi: 10.1021/jm7015045

26. Yang CT, Kim YS, Wang J, *et al.* ^{64}Cu-labeled 2-(diphenyl-phosphoryl)-ethyl-diphenyl-phosphonium cations as highly selective tumor imaging agents: Effects of linkers and chelates on radiotracer biodistribution characteristics. *Bioconjug Chem*. 2008;19:2008-2022.

doi: 10.1021/bc8002056

27. Yang CT, Liu S. Synthesis and structural characterization of complexes of a DO3A-conjugated triphenylphosphonium cation with diagnostically important metal ions. *Inorg Chem.* 2007;46:8988-8997.

doi: 10.1021/ic7010452

28. Chandrasekharan P, Yong CX, Poh Z, *et al*. Gadolinium chelate with DO3A conjugated 2-(diphenylphosphoryl)-ethyldiphenylphosphonium cation as potential tumor-selective MRI contrast agent. *Biomaterials.* 2012;33:9225-9231.

doi: 10.1016/j.biomaterials.2012.08.071

29. Hall AJ, Robertson AG, Hill LR, *et al*. Synthesis and tumour cell uptake studies of gadolinium(III)-phosphonium complexes. *Sci Rep.* 2012;11:598.

doi: 10.1038/s41598-020-79893-9

30. Clarke ET, Martell AE. Stabilities of the Fe(III), Ga(III) and In(III) chelates of N, N',N"-triazacyclononanetriacetic acid. *Inorg Chim Acta*. 1991;181:273.

doi: 10.1016/S0020-1693(00)86821-8

31. Kim J, Kim SK, Kim HK, *et al.* Mitochondrial function in human neuroblastoma cells is up-regulated and protected by NQO1, a plasma membrane redox enzyme. *PLoS One*, 2013;8:e69030.

doi: 10.1371/journal.pone.0069030

32. Titova E, Shagieva G, Ivanova O, *et al.* Mitochondria-targeted antioxidant SkQ1 suppresses fibrosarcoma and rhabdomyosarcoma tumour cell growth. *Cell Cycle.* 2018;17:1797-1811.

doi: 10.1080/15384101.2018.1496748

33. Manskikh VN, Krasilshchikova MS, Vygodin VA, Egorov MV. Effect of the mitochondria-targeted antioxidant SkQ1 on development of spontaneous tumors in BALB/c mice. *Biochemistry (Mosc).* 2014;79:1136-1139.

doi: 10.1134/S0006297914100162

34. Morrison DE, Aitken JB, De Jonge MD, Ioppolo JA, Harris HH, Rendina LM. High mitochondrial accumulation of new gadolinium(III) agents within tumour cells. *Chem Commun (Camb)*. 2014;50:2252-2254.

doi: 10.1039/c3cc46903d

35. Tsionou MI, Knapp CE, Foley CA, *et al.* Comparison of macrocyclic and acyclic chelators for gallium-68 radiolabelling. *RSC Adv*. 2017;7:49586-49599.

doi: 10.1039/c7ra09076e

36. Studer M, Meares CF. Synthesis of novel 1,4,7-triazacyclononane-N, N',N"-triacetic acid derivatives suitable for protein labeling. *Bioconjug Chem*. 1992;3: 337-341.

doi: 10.1021/bc00016a013

37. Hu A, Wilson JJ. Advancing chelation strategies for large metal ions for nuclear medicine applications. *Acc Chem Res*. 2022;55(6):904-915.

doi: 10.1021/acs.accounts.2c00003

38. Roesch F, Riss PJ. The renaissance of the ^{68}Ge/^{68}Ga radionuclide generator initiates new developments in ^{68}Ga radiopharmaceutical chemistry. *Curr Top Med Chem*. 2010;10:1633-1668.

doi: 10.2174/156802610793176738

39. Ray Banerjee S, Chen Z, Pullambhatla M, *et al.* Preclinical comparative study of (68)Ga-labeled DOTA, NOTA, and HBED-CC chelated radiotracers for targeting PSMA. *Bioconjug Chem*. 2016;27:1447-1455.

doi: 10.1021/acs.bioconjchem.5b00679

Appendix

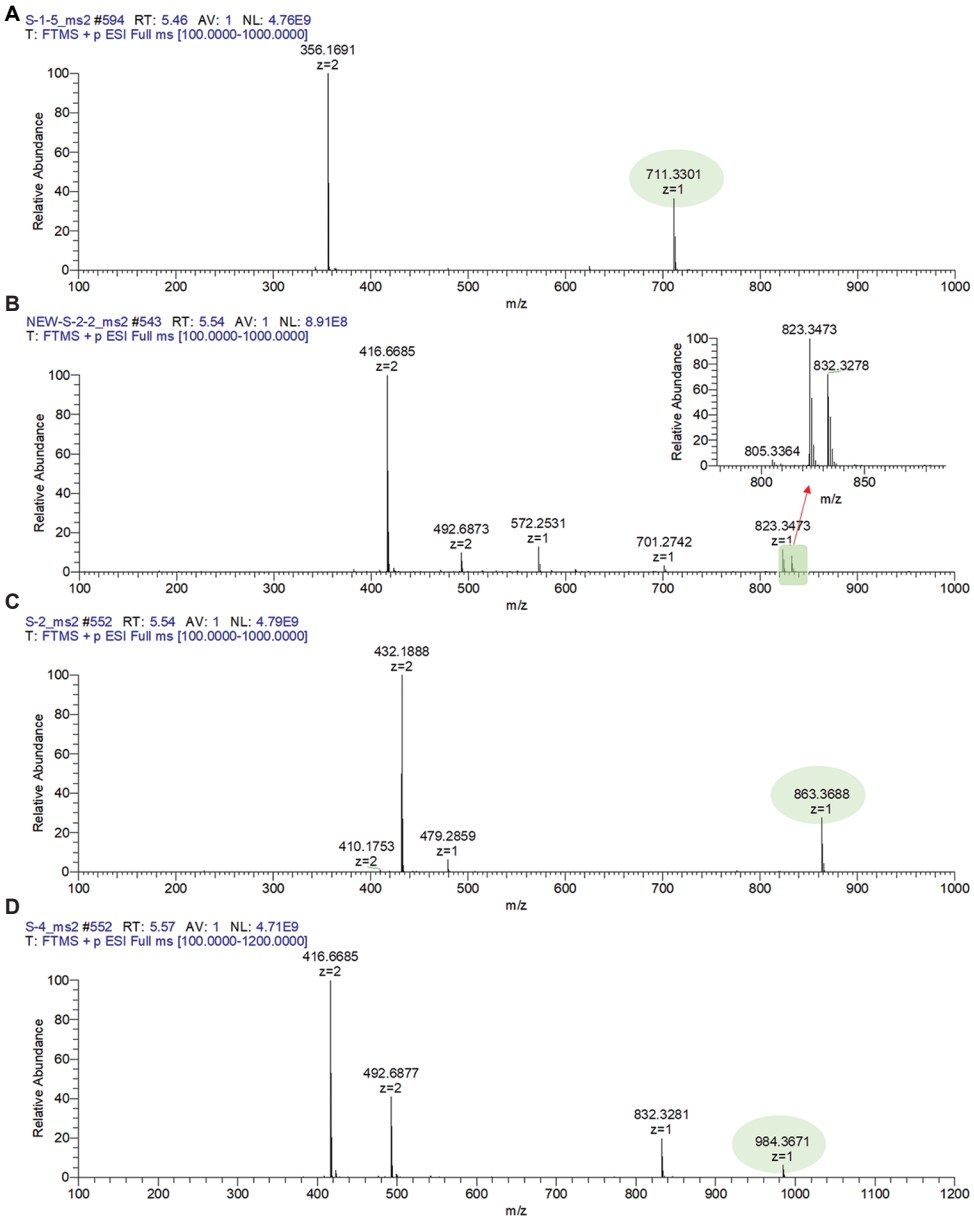

Figure A1. Electrospray ionization-mass spectrometer (ESI-MS) results of the four ligands: (A) ^{68}Ga-labeled triphenyl(4-((4,7,10-tris(carboxymethyl)-1,4,7,10-tetraazacyclododecan-1-yl)methyl)benzyl)-phosphonium acetate: C40H47N4O6P, (B) triphenyl(4-((3-(4-(((1,4,7-tris(carboxymethyl)-1,4,7-triazonan-2-yl)methyl)phenyl)thioureido)methyl)benzyl)-phosphonium acetate: C46H53N5O6PS, (C) (2-(diphenylphosphoryl)ethyl) diphenyl(4-((4,7,10-tris(carboxymethyl)-1,4,7,10-tetraazacyclododecan-1-yl)methyl)benzyl)-phosphonium acetate: C48H56N4O7P2, and (D) TPEP-xy-Bz-NOTA: C54H59N5O7P2S

ACCSCIENCE PUBLISHING

Advances in Radiotherapy & Nuclear Medicine

ORIGINAL RESEARCH ARTICLE

Radiotherapy using diagnostic computed tomography scans: A phantom-based end-to-end evaluation

Fabian Krause[1]*, Stephan Wolff[2], Sören Semrau[1], and Frank-André Siebert[1]

[1]Department of Radiotherapy, University Medical Center Schleswig-Holstein, Kiel, Schleswig-Holstein, Germany

[2]Department of Radiology and Neuroradiology, University Medical Center Schleswig-Holstein, Kiel, Schleswig-Holstein, Germany

Abstract

Palliative patients receiving radiotherapy often experience significant pain. Nevertheless, they must be transported for a planning computed tomography (CT) scan and endure additional waiting times because treatment planning is time-consuming. New artificial intelligence (AI)-assisted radiotherapy devices enable simplified workflows. Using cone-beam CT data, an adaptive treatment plan based on the current patient anatomy can be generated within minutes. This study examines how technical innovations can shorten radiation treatment planning using diagnostic images instead of planning CT (pCT) scans. The entire treatment planning chain was evaluated using an Alderson phantom in an end-to-end test with dose measurements for an AI-supported adaptive workflow. Different diagnostic CT acquisitions were used, and the resulting dose calculations were compared with those obtained from a pCT calibrated for radiotherapy. In Report 24, the International Commission on Radiation Units and Measurements (ICRU) specifies a tolerance for radiotherapy dose delivery of ±5% relative to the prescribed dose. To evaluate if an adaptive workflow with diagnostic images on the Varian's Ethos system (v1.1) meets these requirements, ionization chamber measurements in a phantom were compared to planned doses. Comparison of the results showed that the requirements of ICRU Report 24 were met. When diagnostic CT images were used instead of a dedicated treatment pCT, increased dose deviations of up to 2% were observed, although these remained within the ICRU tolerance. The end-to-end test presented here provides a practical approach to assessing the impact of using diagnostic CT data in adaptive treatment planning. The findings indicate that the observed dose deviations remain within the 5% limit defined by ICRU Report 24.

Keywords: End-to-end study; Ethos; Adaptive radiotherapy; Simulation-free radiation

***Corresponding author:**
Fabian Krause
(fabian.krause@uksh.de)

Citation: Krause F, Wolff S, Semrau S, Siebert F. Radiotherapy using diagnostic computed tomography scans: A phantom-based end-to-end evaluation. *Adv Radiother Nucl Med*. 2025;3(4):72-82.
doi: 10.36922/ARNM025370047

Received: September 13, 2025

Revised: November 3, 2025

Accepted: November 25, 2025

Published online: December 9, 2025

1. Introduction

As a result of the ongoing demographic change and the associated increase in the average age of the population, an increasing rate of cancer diagnoses is predicted. This trend, together with longer survival times attributable to medical progress, means that further development of therapeutic approaches for treating metastatic disease in the palliative

setting will become increasingly important.[1,2] Palliative radiotherapy has proven to be an effective treatment for partial pain relief and other local symptoms.[3] Shortening the delay of the palliative treatment has a positive effect on the quality of life and survival of patients.[4] A new generation of artificial intelligence (AI)-supported radiotherapy systems[5,6] offers fast workflows,[7-9] which, combined with modern palliative treatment concepts (e.g., 8 Gy in a single fraction[10,11]), could reduce both treatment delay and overall duration, enabling rapid and effective treatment, potentially on the same day if the indication is established. These workflows commonly use diagnostic computed tomography (dCT) images for treatment planning.

A standard palliative radiotherapy treatment concept involves creating a computed tomography (CT) dataset specifically for radiation treatment planning (pCT) before the planning process takes place. The data from the pCT serve as a geometric reference for the subsequent radiation treatments on the linear accelerator and provide density information for the dose calculation. The CT density (Hounsfield unit [HU]) of a given tissue depends on the CT and the tube voltage used for the scan. To accurately depict the influence of CT parameters and the resulting physical uncertainties on dose calculation, a device-specific CT calibration curve is used by the treatment planning system (TPS) for each pCT setup. The CT calibration curve includes HU values, determined using a phantom with defined-density inserts, plotted against the known electron/physical density values of the inserts.

Especially in the advanced metastatic stage of the disease, the patients being treated are often in great pain. Nevertheless, due to this workflow, they not only have to be transported, which is sometimes extremely complex (medical transport inside or outside the clinic)[12] but also have to accept treatment delays of 1–2 days, as the radiation treatment planning process is time-consuming.[13]

Our proposed workflow using dCT scans mitigates some potential uncertainties associated with the absence of a pCT through the utilization of AI-supported tools that enable the generation of adaptive treatment plans. Instead of using cone-beam CT (CBCT) data solely for verifying patient positioning, an adaptive treatment plan based on the current patient anatomy can be calculated within minutes. Dose calculation is still based on the density information (HU) from the planning imaging (dCT or pCT). However, the contours of targets and organs from the treatment planning images are transferred to the current imaging using deformable registration algorithms and AI-based organ contouring[14] to generate a synthetic CT (sCT). Geometric uncertainties are thus reduced to a minimum.

Only a few publications[15-19] have addressed how the use of dCT data influences dose calculations in the TPS. Unlike previous approaches, which primarily focus on replanning existing pCT-based treatment plans on a dCT and comparing dose parameters, thus restricting the analysis to dose calculation effects within the TPS, the present study introduces a novel and more clinically relevant methodology. It evaluates the impact of dCTs across the entire treatment chain undergone by patients during treatment planning and delivery. The methodology is realized through an end-to-end test that includes dose measurements within an AI-supported adaptive workflow. Multiple dCT scanners were assessed under identical experimental conditions, allowing a direct and robust comparison. This setting not only offers deeper insights into the specific influence of each dCT scanner but also captures the variability in model-specific dose effects. By extending the analysis beyond the planning phase, this study provides a more holistic understanding of the clinical impact when using dCTs.

2. Materials and methods

2.1. Phantom

The entire radiotherapy treatment chain includes the initial imaging, radiation planning (simulation), patient positioning on the radiation device using imaging, and subsequent dose application. In its Report 24, the International Commission on Radiation Units and Measurements (ICRU) specifies that the accuracy of patient irradiation, as demonstrated by quality assurance (QA) measurements, should be within ±5% of the prescription dose.[20] However, this value applies not only to the dose delivery step itself but also to the entire treatment chain. To assess whether radiation treatment planning based on diagnostic imaging meets these requirements, the entire treatment chain for an AI-supported adaptive workflow was simulated in an end-to-end test using a male Alderson–Rando phantom with 2.5 cm-thick slices.[21] The phantom was scanned with the pCT and multiple dCT scanners, and all dCT datasets were evaluated using the HU calibration curve derived from the pCT. The simulated results were verified using a Farmer ionization chamber 30013 (PTW Freiburg GmbH, Germany). A custom-made chamber holder, manufactured from two drilled polymethyl methacrylate slabs, was used as an insert for the Farmer chamber (Figure 1). A tension belt was used to secure the phantom slabs.

Even though the Alderson phantom does not replicate physiological functions and cannot fully replace living human tissue, it can be considered representative of the human body. The primary focus of this study is on the

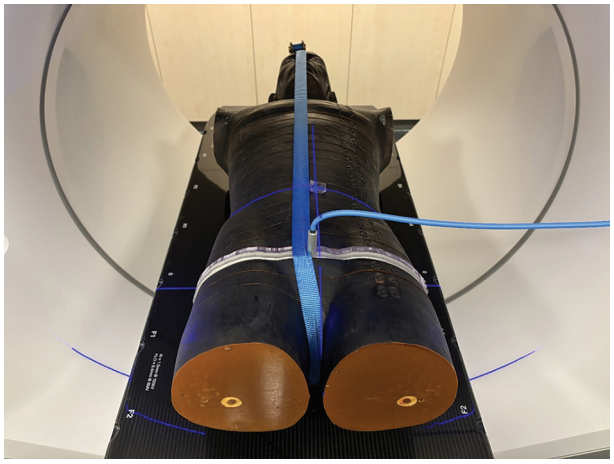

Figure 1. Alderson phantom with a custom-made polymethyl methacrylate Farmer chamber holder (view during phantom positioning)

physical dose distribution rather than geometry changes due to biological responses. Since the phantom consists of tissue-equivalent materials that closely imitate how radiation interacts with real human tissue, it enables accurate and reproducible dose measurements. The absence of physiological motion is advantageous in this context, as it reduces variability and allows for a more precise assessment of the dosimetric effects of dCTs. With the phantom remaining static, any observed dose differences are more likely tied to the treatment planning rather than patient movement, making the sources of discrepancies more apparent and easier to analyse. While the absence of biological processes improves reproducibility, the results may not fully apply to extreme clinical scenarios (e.g., patients with unusual body types).

2.2. Workflow of end-to-end test

The treatment planning chain of this study consisted of a SOMATOM go.Sim dual-energy CT simulator (Siemens Healthineers, Germany); the TPS Ethos Treatment Management v.1.1 by Varian (United States of America [USA]), a Siemens Healthineers company that utilizes the model-based dose calculation algorithm Ethos Acuros XB v.1.1.1001 (Varian, USA); and an Ethos linear accelerator (Varian, USA) equipped with a 6 MV FFF beam. First, a CT scan of the Alderson phantom was performed with the SOMATOM go.Sim using DirectDensity,[22] and the data were imported into the TPS (Figure 2). To minimize imaging artifacts, the CT scan was acquired without the insertion of the Farmer ionization chamber. This approach helps to improve image quality by avoiding metal artifacts caused by the chamber during initial scanning. The subsequently determined dose values were referenced to the effective measuring point of the Farmer chamber, which was located within the air-filled sensitive volume of

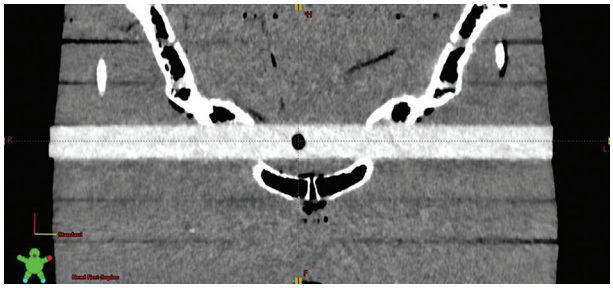

Figure 2. Alderson phantom with a custom-made polymethyl methacrylate Farmer chamber holder (frontal computed tomography view)

the chamber. For this reason, no water-equivalent insert was used during image acquisition. The pCT scanner, with the DirectDensity module, was initially calibrated using a Gammex density phantom to ensure accurate quantification of tissue density. During calibration, an energy spectrum from 70 kV to 140 kV was applied to account for variations in beam energy and its impact on density measurements. This approach allows a calibration across the clinically relevant energy range, enhancing the reliability of density-based imaging and dose calculations. Based on this pCT dataset, plans were then computed in the TPS. Afterward, the phantom was placed on the linear accelerator. The adaptive workflow, which uses planning directives based on the current CBCT geometry and patient positioning, was then initiated. A customized adaptive treatment plan was calculated for each treatment fraction.

The TPS used, Ethos Treatment Management, integrates multiple AI components into its framework, enabling rapid adaptation to changing patient anatomy and treatment conditions. The main components are a deep learning-based auto-segmentation, a feedback loop with the physician enabling continuous monitoring and adjustment of the contours, and an intelligent optimization engine (IOE) that allows fast treatment plan creation. The auto-segmentation uses a convolutional neural network and structure-guided deformation for structure segmentation and automatic contouring in situations where volume changes are present.[23,24] The contour suggestions generated through this process were reviewed by the physician and adjusted if necessary. The IOE was used to generate automated treatment plans based on the given contours by emulating the decision-making process of a human planner, defining the objective function for photon optimization, and supervising the optimization. For this purpose, clinical goals defined in the radiotherapy prescription were converted into optimization objectives by the engine.[25] Existing studies have shown clinically acceptable results for Ethos auto-contouring,[23,24] with

a reported Dice similarity of 0.93 ± 0.05.[23] In this work, planning target volume (PTV) reproducibility was visually verified through the feedback loop, with adjustments made in case of noticeable deviations, as in clinical practice. With a PTV that generously covered the chamber's sensitive volume (the PTV was approximately 83 times larger than the sensitive volume of the chamber) and provided a homogeneous dose distribution, slight variations in the PTV were not expected to affect the dose significantly. Therefore, no independent Dice analysis was performed as part of this work.

Finally, in the sCTs of the adaptive treatment plans, the calculated dose at the reference point within the ionization chamber was compared with the measured dose at this point using a Farmer ionization chamber 30013. Despite its relatively large sensitive volume compared to other chambers, the Farmer chamber was used to minimize angular dependence within the chosen experimental setting. This procedure was then repeated using the following dCT scanners instead of the SOMATOM go.Sim CT simulator to employ dCTs for the plan calculation and creation of an adaptive sCT (Figure 3): SOMATOM Sensation 64 Open single-energy CT scanner (Siemens Healthineers, Germany), Biograph mCT 40 positron emission tomography (PET)/CT scanner (Siemens Healthineers, Germany), and IQon Spectral CT scanner (Philips, The Netherlands). For the acquisition of CT images, the standard abdomen/pelvis profile of the scanners was used, resulting in a uniform tube voltage of 120 kV for all scans and a slice thickness of 0.1–0.3 cm. The presented procedure was used to review the entire treatment planning chain. Table 1 provides a detailed overview of the scan parameters used by the different CT scanners.

2.3. Data analysis

The treatment plan calculation was performed with the HU calibration curve of the SOMATOM go.Sim (pCT) using the DirectDensity module. As DirectDensity enables the use of a single calibration curve for all tube voltages, the chosen tube voltage should have only a minor influence, even if different tube voltages are used. The planning technique for the creation of the treatment plans was similar to that used in daily clinical practice. For comparability across all CT datasets, an artificial nine-field intensity-modulated radiotherapy (IMRT) plan with sliding-window modulation was used. Short on-couch times are particularly important for online adaptive radiotherapy. Not only may adapted organ contours change over time (e.g., rectum or bladder) but also this is even more relevant in emergency radiotherapy, as patients are often in significant pain. Calculation of online adaptive treatment plans using IMRT fields is faster than using volumetric modulated arc therapy.[25,26] Hence, many clinics prefer seven-, nine-, or 12-field IMRT plans, as they offer an excellent compromise between plan quality and treatment planning time.[23,25,26] At our clinic, we primarily utilize nine-field IMRT plans, as this configuration provides an optimal balance between achieving highly conformal dose distributions and maintaining manageable planning and treatment delivery times. This helps minimize patient discomfort from prolonged on-couch

Table 1. Overview of essential parameters that can affect Hounsfield unit accuracy and thus dose calculation for the different computed tomography scanners

CT scanner	Tube voltage (kV)	Slice thickness (cm)	Reconstruction kernel
go.Sim (pCT)	120	0.2	Sd40
S64 (dCT)	120	0.2	B31s
mCT 40 (dCT)	120	0.3	Br38
IQon (dCT)	120	0.1	B

Abbreviations: CT: Computed tomography; dCT: Diagnostic computed tomography; pCT: Planning computed tomography.

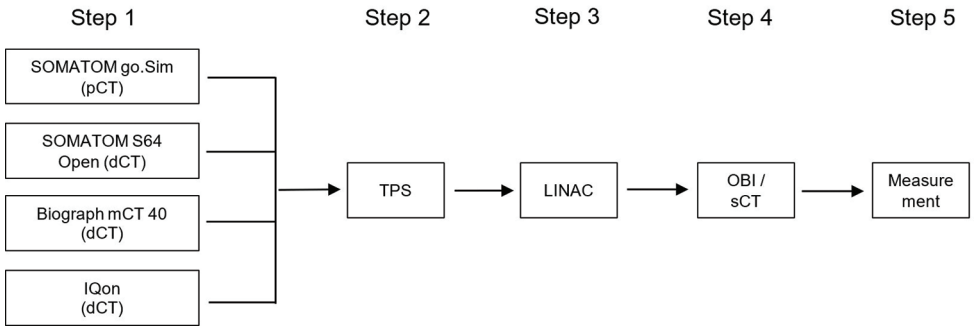

Figure 3. Schematically workflow: Step 1: CT scan; Step 2: contouring and dose calculation in the TPS; Step 3: data transfer to the LINAC; Step 4: Use OBI for creation of phantoms sCT; and Step 5: dose measurement with Farmer chamber and comparison with dose calculated on sCT
Abbreviations: CT: Computed tomography; dCT: Diagnostic computed tomography; LINAC: Linear accelerator; OBI: Onboard imaging; pCT: Planning computed tomography; sCT: Synthetic computed tomography; TPS: Treatment planning system.

times while maintaining the clinical effectiveness of the adapted treatment by reducing variations in organs at risk.

To achieve a homogeneous dose distribution over the whole sensitive volume of the ionization chamber, the PTV covered the ionization chamber (PTV volume of 50 cm^3 covering the 0.6 cm^3 sensitive volume of the Farmer chamber; Figure 4) and was optimized with the criteria, as shown in Table 2. Modern hypofractionated palliative treatment protocols,[10,11] particularly those applied in emergency radiotherapy settings such as cases of impending spinal cord compression or tumor-related bleeding, are typically designed to deliver a homogeneous dose distribution within the PTV. Consequently, the desired dose distribution was both physically suitable for the selected measurement method and consistent with clinical reality.

Since the dose measurement was performed using a Farmer-type ionization chamber containing air within its sensitive volume, no additional density overrides were applied during dose calculation. This ensures that the measured dose accurately corresponds to the dose computed in the TPS, without the need for manual correction for tissue heterogeneities in the measurement region. The dose distribution was comparable to that of a real patient case with a homogeneous dose prescription within the PTV as typically prescribed in palliative radiotherapy.

The prescription dose for this test plan was 8 Gy. For each CT scanner, 10 identical adaptive treatment plans, including corresponding dose measurements, were generated to allow assessment of statistical variability. To compare the measured doses of the adaptive treatment plans with the calculated doses planned on the sCT, the point dose at the reference location of the chamber on the chamber axis—1.30 cm from the chamber tip according to the PTW datasheet—was used (Figure 4). The reference location was taken as the effective point of measurement because it lies at the center of both the nine-field IMRT and the ionization chamber.

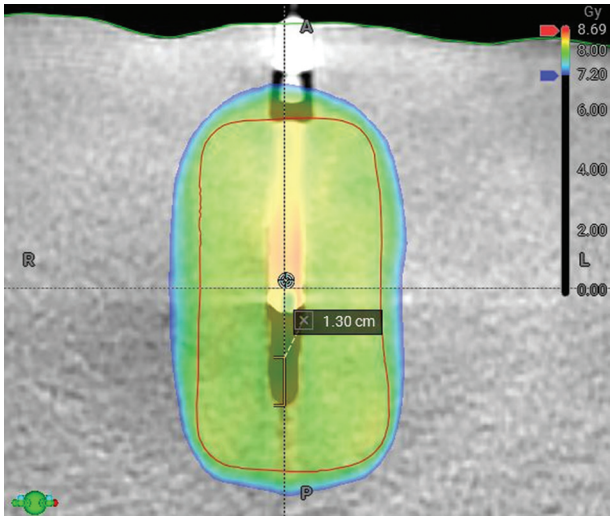

Figure 4. Transversal computed tomography slice of the polymethyl methacrylate insert with the chamber cavity, including dose distribution and reference point

An uncertainty analysis for our study, considering dose calculation in the TPS and dose measurement (uncertainties for the Farmer chamber, detector positioning, and dose calibration), was conducted.

3. Results

3.1. Experimental results

The deviations between the TPS-calculated adaptive plans and dose measurements, as well as the differences between pCT (Table 3) and dCT (Tables 4-6) plans, are shown in Tables 3-6. As every adaptive plan was unique, the average and standard deviation were reported only for the percentage deviations.

The results indicate that the use of diagnostic images affects dose calculation in the TPS. As expected, treatment

Table 2. Optimization criteria for the test treatment plan calculated in Ethos v1.1

Volume	Optimization criteria		
PTV	D0.1% ≤105%; variation 107%	D99% ≥100%; variation 95%	V95% ≥100%; variation 95%

Abbreviations: D0.1%: 0.1% of the volume received this dose or more; D99%: Dose received by 99% of the volume; PTV: Planning target volume; V95%: Volume receiving≥95% of the prescribed dose.

Table 3. Results from SOMATOM go.Sim (planning computed tomography)

Adaptive plan	Dose TPS (Gy)	Measurement (Gy)	Deviation (%)
1	8.15	8.20	0.61
2	8.15	8.17	0.25
3	8.19	8.21	0.24
4	8.17	8.22	0.61
5	8.14	8.21	0.86
6	8.20	8.26	0.73
7	8.19	8.24	0.61
8	8.16	8.23	0.85
9	8.20	8.26	0.77
10	8.19	8.25	0.75
Average±SD (%)			0.63±0.21

Abbreviations: TPS: Treatment planning system; SD: Standard deviation.

Table 4. Results from SOMATOM S64 Open (diagnostic computed tomography)

Adaptive plan	Dose TPS (Gy)	Measurement (Gy)	Deviation (%)
1	8.28	8.52	2.86
2	8.36	8.47	1.31
3	8.22	8.34	1.45
4	8.22	8.36	1.69
5	8.30	8.38	0.96
6	8.21	8.39	2.17
7	8.35	8.44	1.07
8	8.24	8.30	0.73
9	8.24	8.34	1.21
10	8.08	8.28	2.44
Average±SD (%)			1.59±0.66

Abbreviations: TPS: Treatment planning system; SD: Standard deviation.

Table 5. Results from Biograph mCT 40 (diagnostic computed tomography)

Adaptive plan	Dose TPS (Gy)	Measurement (Gy)	Deviation (%)
1	7.99	8.12	1.61
2	8.05	8.19	1.72
3	8.09	8.31	2.68
4	8.19	8.32	1.57
5	8.12	8.31	2.31
6	8.09	8.26	2.08
7	8.04	8.26	2.70
8	8.14	8.31	2.07
9	8.11	8.34	2.80
10	8.13	8.36	2.79
Average±SD (%)			2.23±0.47

Abbreviations: TPS: Treatment planning system; SD: Standard deviation.

Table 6. Results from IQon (diagnostic computed tomography)

Adaptive plan	Dose TPS (Gy)	Measurement (Gy)	Deviation (%)
1	8.10	8.31	2.56
2	8.07	8.30	2.81
3	8.07	8.29	2.69
4	8.12	8.27	1.83
5	8.02	8.25	2.83
6	8.11	8.30	2.32
7	8.01	8.23	2.71
8	8.07	8.30	2.81
9	8.17	8.33	1.94
10	8.04	8.29	3.06
Average±SD (%)			2.56±0.38

Abbreviations: TPS: Treatment planning system; SD: Standard deviation.

plans using HU-calibrated pCT images showed slightly smaller deviations between calculated and measured doses than plans based on diagnostic images (Figure 5). Although a slight dose underestimation was observed, excellent agreement with an average deviation of 0.63 ± 0.21% between dose calculations using the Acuros XB algorithm on pCT data and measurements was found (Table 3). The underestimation increased when using dCT data for plan creation; however, it remained in good agreement with measured doses for all three uncalibrated diagnostic imaging devices. The average dose deviation ranged from 1.59 ± 0.66% (Table 4) to 2.56 ± 0.38% (Table 6). Compared with the initial pCT-based dose calculation, only minor differences in dose of up to 2% were observed.

The CT scanners used in this study differ in their technical principles. A PET/CT scanner, a spectral CT scanner, a dual-energy scanner, and a single-energy scanner were used. Although substantially different behavior from other devices cannot be definitively excluded, it appears unlikely based on current evidence. In radiotherapy treatment planning, the accuracy of dose calculations depends on a consistent and precise HU-to-density conversion. The differences in deviations relative to the pCT were influenced by a variety of factors. Differences in HU for the same material across dCT scanners can occur even under identical scan parameters due to variations in detector design, beam-hardening, scatter correction algorithms, and reconstruction methods. In addition, manufacturer-specific calibration procedures and spectral differences can affect the results. The precise origin of these differences is challenging to predict and depends, among other factors, on the pCT scanner used as the reference.

3.2. Transferability to 2D dose measurements

To assess the transferability of point-dose measurements obtained with the Farmer ionization chamber to 2D dose distributions and to minimize the risk of underestimating local dose variations, a prostate clinical case treatment plan was generated using the pCT calibration curve applied

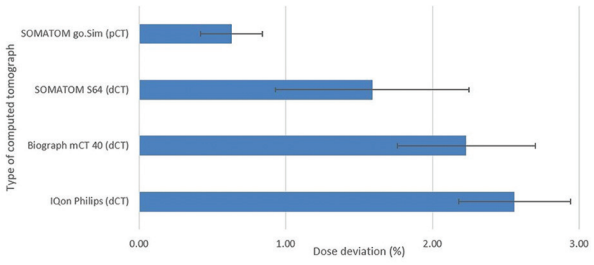

Figure 5. Mean dose deviation between calculated and measured doses for the planning computed tomography and three diagnostic computed tomography datasets

to dCT data acquired with the Biograph mCT 40. The corresponding QA plan was then calculated and measured using the high-precision 2D ionization chamber array OCTAVIUS 1500 (PTW Freiburg GmbH, Germany). The Biograph mCT 40 scanner was selected because it falls within the range of previously measured deviations, avoiding both extremes. To increase the complexity of the case, a prostate cancer treatment plan based on the conventional or hypofractionated high-dose intensity modulated radiotherapy for prostate cancer (CHHiP) protocol with two integrated boosts was selected. Using 2D gamma criteria with a 3 mm distance and 3% dose difference resulted in a passing rate of 94.1%, demonstrating a clinically acceptable agreement within the irradiated PTV. When applying gamma criteria with a 3 mm distance and a reduced dose difference of 2%, the passing rate decreased to 79.4 %. Reducing the threshold for the permissible dose deviation from 3% to 2% inevitably results in a lower gamma passing rate. This effect was expected, as stricter criteria made the comparison more sensitive to minor discrepancies. In this case, the observed reduction in passing rate is consistent with the previously measured dose deviation of 2.2% using the Farmer ionization chamber for the Biograph 40 mCT, indicating that the decrease remains within the range expected from the earlier measurement. Given a previously measured dose deviation of 2.2%, reducing the tolerance threshold to no more than 2% resulted in a significant increase in the number of failed points. This relationship is illustrated in Figure 6, which shows the agreement for the corresponding 2D gamma analysis results obtained with the OCTAVIUS 1500 array, demonstrating the transferability of the ionization chamber measurements to 2D dose distributions.

3.3. Uncertainty analysis

To gain a comprehensive understanding of the overall uncertainty associated with the presented end-to-end test, the uncertainties at each step of the workflow were systematically evaluated and quantified (Table 7). This approach provides a more detailed insight into the overall reliability and accuracy of the presented workflow.

The results indicate that the dose calculated with Acuros XB might underestimate the dose systematically, even if the deviations were small. This effect has been described previously when comparing Acuros XB calculations with measurements in or beyond air cavities.[27] The situation here is comparable. When using a Farmer ionization chamber, an air-filled cavity was brought into the measurement environment. Therefore, an uncertainty of 1.5% in the TPS dose calculation was estimated.[28] According to Castro *et al.*,[29] the uncertainty of dose measurement with the Farmer chamber was assumed to be 1.6% for the absorbed dose to water. Furthermore, a systematic error of 0.02 cm was estimated for the uncertainty in determining the effective point of measurement within the ionization chamber. This results in a dose uncertainty of 0.5% for the effective dose. Through periodic in-house QA measurements with the Farmer chamber on the Ethos platform, an uncertainty for the dose calibration of up to 0.1% was determined.

Table 7. Uncertainty budget for dose calculation and measurement

Procedure	Origin of uncertainty	Type	Uncertainty (%)
Dose calculation	Calculation of dose in the TPS	B	1.5
Dosimetry	Uncertainty of the Farmer chamber	B	1.6
	Chamber position	A	0.5
	Dose calibration	A	0.1
Combined standard uncertainty			2.3

Abbreviation: TPS: Treatment planning system.

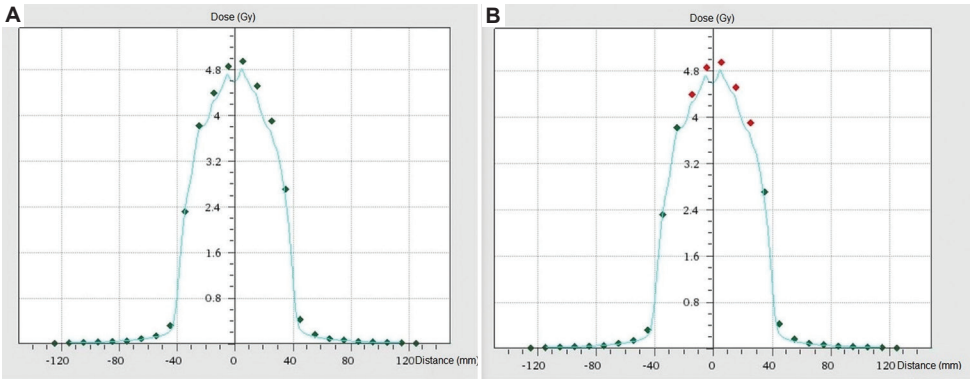

Figure 6. Comparison of 2D gamma analysis results for the prostate quality assurance plan using gamma criteria of (A) 3 mm/3% and (B) 3 mm/2%. The figure shows the spatial distribution of passing (green) and failing (red) points within the irradiated planning target volume for the different evaluation criteria, displayed in a cross-section through the treatment volume.

4. Discussion

To improve quality and safety in radiotherapy, monitoring of dosimetry is essential.[30] In the ICRU Report 24, it is concluded that in the dose delivery to a target volume, a point dose accuracy of ±5% should be achieved.[20] Even though the need for updated accuracy requirements has been discussed extensively since the release of the ICRU report in 1976, this value is still regarded as a compromise between clinical needs and technical feasibility.[31,32] Especially when introducing new and complex techniques, an end-to-end test provides an independent check to prevent dosimetric failures at the institutional level and verify that dosimetric requirements are met.[33,34] The experimental results of the end-to-end test show that the requirements of ICRU Report 24 for point-dose accuracy were met. Even though some dosimetry audits define stricter criteria for a good score in an end-to-end test, an accuracy of 5% is sufficient to pass according to Lehmann *et al.*[35] The outcome presented here even fulfills the requirements for an optimal passing score (deviations within 3.3%) defined in that work. The results shown here are in good accordance with the study by Nelissen *et al.*[18] for the Ethos platform, who recalculated patients' initial clinical treatment plans on an sCT basis using an existing dCT and also found minor differences of up to 2% in film measurements. This further suggests that the results obtained from point measurements are transferable to 2D measurements. Machine commissioning had already demonstrated this by systematically comparing point doses from treatment plans with corresponding 2D dose distributions (2D dose maps). In the present work, this is further illustrated using a clinical prostate plan as an example, proving the consistency and transferability of the ionization chamber results to 2D dose distributions. These comparisons confirmed the consistency and applicability of the point measurement results. Therefore, it can be concluded that the use of dCTs is feasible for a fast and sufficiently safe workflow in some adaptive radiotherapy cases. The dose deviations are within a threshold of 5% and thus clinically acceptable. In palliative emergency cases, rapid dose delivery is often the primary concern.[36] As a result, uncertainties caused by the dCT data used appear acceptable if dose deviations remain within an admissible range[37] (e.g., ±5%) and treatment delay associated with the planning process is reduced.[8,12] Whether the deviations are acceptable must be decided on a case-by-case basis by the physicist and physician together, taking the patient's situation into account. It can be stated that, in particular, palliative emergency patients could benefit from faster treatment without the need for prior pCT. Early outcome results from the FAST-METS study by Nelissen *et al.*,[7] including 47 patients treated with an accelerated workflow, demonstrated reasonable patient satisfaction. In their analysis of 1,000 consecutive palliative radiation courses without simulation, Schuler *et al.*[8] found a pain response comparable to that reported for conventional pCT-based plans. These findings suggest that patients derive benefits that go beyond simple time savings. However, the prerequisite is that an actual dCT is available. This is the case for most of the affected patients. Using an adaptive workflow, the geometrical and anatomical changes in the body contour and the target volume can be tracked and adapted, enabling the application of organs-at-risk-sparing modulated plans.[18] As part of periodic QA, the test procedure presented here also appears feasible for consistency checks of the entire treatment planning chain in clinical practice. The dosimetric uncertainties when using an air-filled ionization chamber in combination with Acuros could be reduced using a thermoluminescent dosimeter or a liquid-filled ionization chamber in further studies.

Although the upcoming Ethos platform version 2.0 is expected to obviate the need for a sCT generation,[38] the findings presented in this study remain valid and relevant. A significant number of radiotherapy departments are expected to remain on version 1.1 for an extended period. Other manufacturers are also developing online adaptive solutions nearing market readiness that rely on sCTs.[39] Magnetic resonance imaging (MRI)-based approaches for adaptive radiotherapy continue to rely on sCT images to enable accurate dose calculation and treatment planning. Despite advancements in MRI technology and image processing, sCT generation remains a critical step to provide electron density information that MRI alone cannot provide.[40,41] In this context, there is also a growing interest in fast, adaptive workflows, and the results demonstrated herein are expected to be transferable.

Furthermore, the findings regarding the influence of dCTs on the treatment planning process are transferable to emergency radiotherapy scenarios on conventional linear accelerators. While our study was performed on the Varian Ethos platform v1.1 using dCT data for treatment planning, the underlying principles regarding the impact of density information and image reconstruction on dose calculation are principally system-independent. Dose calculation accuracy relies on the fidelity of CT HUs to electron density, a factor that remains critical across AI-based radiotherapy devices, regardless of the vendor. Provided that the primary source for dose calculation is the initial planning imaging, as in the case for workflows on conventional C-arm accelerators or AI-based devices utilizing sCTs for adaptive workflows, the effect of using dCTs is expected to be comparable.

5. Conclusion

The phantom-based end-to-end test presented in this study provides a practical approach to better understand the influence of using diagnostic datasets for treatment planning in adaptive workflows. Using the presented test procedure, it is possible to accurately verify the point dose within the irradiated target volume, thereby ensuring compliance with the planned dose distribution and the precision of the treatment delivery. The workflow also appears suitable for use in periodic system tests. The results indicate that dCTs have the potential to be used in clinical applications while meeting the recommendations of ICRU Report 24. The use of dCTs appears feasible for enabling fast workflows, especially for single-fraction palliative treatment of metastases, although dosimetric accuracy is reduced by up to 2% compared to pCT. In our clinic, we have already implemented an emerging workflow for adaptive radiotherapy on dCTs as a time-saving technique for palliative emergency treatments. The initial cohort of patients treated according to this workflow completed their therapy successfully, demonstrating the feasibility and clinical applicability of this technique in urgent palliative care settings. By the time of submission, 12 patients had been treated with this technique. As our cohort remains small for a statistical analysis of clinical data, no such data are currently available. However, the results reported by Nelissen *et al*.[7] and Schuler *et al*.[8] demonstrated favourable clinical outcomes. With an increasing number of patients in our cohort, similar favorable outcomes may be expected, further substantiating the effectiveness of the described technique.

Acknowledgments

None.

Funding

None.

Conflict of interest

Frank-André Siebert is an Editorial Board Member of this journal, but was not in any way involved in the editorial and peer-review process conducted for this paper, directly or indirectly. Separately, other authors declared that they have no known competing financial interests or personal relationships that could have influenced the work reported in this paper.

Author contributions

Conceptualization: Fabian Krause
Formal analysis: Fabian Krause
Investigation: Fabian Krause
Methodology: Fabian Krause
Project administration: Fabian Krause
Resources: All authors
Supervision: Frank-André Siebert
Validation: Fabian Krause
Visualization: Fabian Krause
Writing–original draft: Fabian Krause
Writing–review & editing: Stephan Wolff, Sören Semrau, Frank-André Siebert

Ethics approval and consent to participate

Not applicable.

Conflict of interest

Not applicable.

Availability of data

The data that support the findings of this study are available from the corresponding author on reasonable request.

References

1. Etkind SN, Bone AE, Gomes B, *et al*. How many people will need palliative care in 2040? Past trends, future projections and implications for service. *BMC Med*. 2017;15:102.

   doi: 10.1186/s12916-017-0860-2

2. Dennis K, Harris G, Kamel R, *et al*. Rapid access palliative radiotherapy programmes. *Clin Oncol (R Coll Radiol)*. 2020;32(11):704-712.

   doi: 10.1016/j.clon.2020.08.002

3. Lutz S, Balboni T, Jones J, *et al*. Palliative radiation therapy for bone metastases: Update of an ASTRO evidence-based guideline. *Pract Radiat Oncol*. 2017;7(1):4-12.

   doi: 10.1016/j.prro.2016.08.001

4. Van Tol FR, Suijkerbuijk KPM, Choi D, Verkooijen HM, Oner FC, Verlaan JJ. The importance of timely treatment for quality of life and survival in patients with symptomatic spinal metastases. *Eur Spine J*. 2020;29:3170-3178.

   doi: 10.1007/s00586-020-06599-x

5. Sibolt P, Andersson LM, Calmels L, *et al*. Clinical implementation of artificial intelligence-driven cone-beam computed tomography-guided online adaptive radiotherapy in the pelvic region. *Phys Imaging Radiat Oncol*. 2021;17:1-7.

   doi: 10.1016/j.phro.2020.12.004

6. Wegener S, Exner F, Weick S, *et al*. Prospective risk analysis of the online-adaptive artificial intelligence-driven workflow using the Ethos treatment system. *Z Med Phys*. 2024;34(3):384-396

   doi: 10.1016/j.zemedi.2022.11.004

7. Nelissen KJ, Versteijne E, Senan S, *et al*. Same-day adaptive

palliative radiotherapy without prior CT simulation: Early outcomes in the FAST-METS study. *Radiother Oncol*. 2023;182:109538.

doi: 10.1016/j.radonc.2023.109538

8. Schuler T, Roderick S, Wong S, *et al*. Real-world implementation of simulation-free radiation therapy (SFRT-1000): A propensity score-matched analysis of 1000 consecutive palliative courses delivered in routine care. *Int J Radiat Oncol Biol Phys*. 2025;121(3):585-595.

doi: 10.1016/j.ijrobp.2024.09.041

9. Yu L, Zhao J, Xia F, *et al*. Technical note: First implementation of a one-stop solution of radiotherapy with full-workflow automation based on CT-linac combination. *Med Phys*. 2023;50(5):3117-3126.

doi: 10.1002/mp.16324

10. Howell DD, James JL, Hartsell WF, *et al*. Single-fraction radiotherapy versus multifraction radiotherapy for palliation of painful vertebral bone metastases-Equivalent efficacy, less toxicity, more convenient: A subset analysis of radiation therapy oncology group trial 97-14. *Cancer*. 2013;119(4):888-896.

doi: 10.1002/cncr.27616

11. Hartsell WF, Scott CB, Bruner DW, *et al*. Randomized trial of short- versus long-course radiotherapy for palliation of painful bone metastases. *J Natl Cancer Inst*. 2005;97(11):798-804.

doi: 10.1093/jnci/dji139

12. O'Neil M, Laba JM, Nguyen TK, *et al*. Diagnostic CT-enabled planning (DART): Results of a randomized trial in palliative radiation therapy. *Int J Radiat Oncol Biol Phys*. 2024;120(1):69-76.

doi: 10.1016/j.ijrobp.2024.03.005

13. Kawamura M, Kamomae T, Yanagawa M, *et al*. Revolutionizing radiation therapy: The role of AI in clinical practice. *J Radiat Res*. 2024;65(1):1-9.

doi: 10.1093/jrr/rrad090

14. Koenig L, Derksen A, Papenberg N, Haas B. Deformable image registration for adaptive radiotherapy with guaranteed local rigidity constraints. *Radiat Oncol*. 2016;11:122.

doi: 10.1186/s13014-016-0697-4

15. Giacometti V, King RB, Agnew CE, *et al*. An evaluation of techniques for dose calculation on cone beam computed tomography. *Br J Radiol*. 2019;92(1096):20180383.

doi: 10.1259/bjr.20180383

16. Glober G, Kubli A, Kielbasa J, *et al*. Technical report: Diagnostic scan-based planning (DSBP), a method to improve the speed and safety of radiation therapy for the treatment of critically ill patients. *Pract Radiat Oncol*. 2020;10(5):e425-e431.

doi: 10.1016/j.prro.2020.01.009

17. Ho, QA, Smith-Raymond L, Locke A, Robbins JR. Dosimetry comparison of palliative radiation plans generated from available diagnostic CT images versus dedicated CT simulation for inpatients. *Cureus*. 2021;13(9):e17799.

doi: 10.7759/cureus.17799

18. Nelissen KJ, Versteijne E, Senan S, Hoffmans D, Slotman BJ, Verbakel WFA. Evaluation of a workflow for cone-beam CT-guided online adaptive palliative radiotherapy planned using diagnostic CT scans. *J Appl Clin Med Phys*. 2023;24(3):e13841.

doi: 10.1002/acm2.13841

19. Larjavaara S, Strengell S, Seppälä T, Tenhunen M, Anttonen A. Palliative intensity modulated radiotherapy of bone metastases based on diagnostic instead of planning computed tomography scans. *Phys Imaging Radiat Oncol*. 2023;27:100456.

doi: 10.1016/j.phro.2023.100456

20. ICRU International Commission on Radiation Units and Measurements. *Determination of Absorbed Dose in a Patient Irradiated by Beams of X or Gamma Rays in Radiotherapy Procedures. ICRU Report 24*. Bethesda, MD: ICRU; 1976.

21. Alderson SW, Lanzl LH, Rollins M, Spira J. An instrumented phantom system for analog computation of treatment plans. *Am J Roentgenol Radium Ther Nucl Med*. 1962;87:185-195.

22. Nelson G, Pigrish V, Sarkar V, Su FC, Salter B. Technical note: The use of DirectDensity™ and dual-energy CT in the radiation oncology clinic. *J Appl Clin Med Phys*. 2019;20(3):125-131.

doi: 10.1002/acm2.12546

23. Mao W, Riess J, Kim J, *et al*. Evaluation of auto-contouring and dose distributions for online adaptive radiation therapy of patients with locally advanced lung cancers. *Pract Radiat Oncol*. 2022;12(4):e329-e338.

doi: 10.1016/j.prro.2021.12.017

24. Prunaretty J, Mekki F, Laurent PI, *et al*. Clinical feasibility of Ethos auto-segmentation for adaptive whole-breast cancer treatment. *Front Oncol*. 2024;14:1507806.

doi: 10.3389/fonc.2024.1507806

25. Pokharel S, Pacheco A, Tanner SM. Assessment of efficacy in automated plan generation for Varian Ethos intelligent optimization engine. *J Appl Clin Med Phys*. 2022;23(4):e13539.

doi: 10.1002/acm2.13539

26. Kubiatowicz A, Sherer M, Owaga A, Sharabi A, Ray X. Assessing dosimetric benefit from daily online adaptive radiation therapy for esophageal cancer. *J Appl Clin Med Phys*. 2025;26(10):e70244.

doi: 10.1002/acm2.70244

27. Koo T, Chung JB, Eom KY, Kim IH, Kim JS. Dosimetric

effects of the acuros XB and anisotropic analytical algorithm on volumetric modulated arc therapy planning for prostate cancer using an endorectal balloon. *Radiat Oncol*. 2015;10:48.

doi: 10.1186/s13014-015-0346-3

28. Bush K, Gagne IM, Zavgorodni S, Ansbacher W, Beckham W. Dosimetric validation of Acuros XB with Monte Carlo methods for photon dose calculations. *Med Phys*. 2011;38(4):2208-2221.

doi: 10.1118/1.3567146

29. Castro P, García-Vicente F, Mínguez C, *et al*. Study of the uncertainty in the determination of the absorbed dose to water during external beam radiotherapy calibration. *J Appl Clin Med Phys*. 2008;9(1):70-86.

doi: 10.1120/jacmp.v9i1.2676

30. Johnson D, Li HH, Kimler BF. Dosimetry: Was and is an absolute requirement for quality radiation research. *Radiat Res*. 2024;202(2):102-129.

doi: 10.1667/rade-24-00107.1

31. Mijnheer BJ, Battermann JJ, Wambersie A. What degree of accuracy is required and can be achieved in photon and neutron therapy? *Radiother Oncol*. 1987;8(3):237-252.

doi: 10.1016/s0167-8140(87)80247-5

32. Thwaites D. Accuracy required and achievable in radiotherapy dosimetry: Have modern technology and techniques changed our views? *J Phys Conf Ser*. 2013;444:012006.

doi: 10.1088/1742-6596/444/1/012006

33. Schmitt D, Blanck O, Gauer T, *et al*. Technological quality requirements for stereotactic radiotherapy: Expert review group consensus from the DGMP working group for physics and technology in stereotactic radiotherapy. *Strahlenther Onkol*. 2020;196:421-443.

doi: 10.1007/s00066-020-01583-2

34. Krause F, Risske F, Bohn S, Delaperriere M, Dunst J, Siebert FA. End-to-end test for computed tomography-based high-dose-rate brachytherapy. *J Contemp Brachytherapy*. 2018;10(6):551-558.

doi: 10.5114/jcb.2018.81026

35. Lehmann J, Alves A, Dunn L, *et al*. Dosimetric end-to-end tests in a national audit of 3D conformal radiotherapy. *Phys Imaging Radiat Oncol*. 2018;6:5-11.

doi: 10.1016/j.phro.2018.03.006

36. Christian E, Adamietz IA, Willich N, *et al*. Radiotherapy in oncological emergencies--final results of a patterns of care study in Germany, Austria and Switzerland. *Acta Oncol*. 2008;47(1):81-89.

doi: 10.1080/02841860701481554

37. Nierer L, Walter F, Niyazi M, *et al*. Radiotherapy in oncological emergencies: Fast-track treatment planning. *Radiat Oncol*. 2020;15:215.

doi: 10.1186/s13014-020-01657-6

38. MacDonald RL, Fallone C, Chytyk-Praznik K, Robar JL, Cherpak A. The feasibility of CT simulation-free adaptive radiation therapy. *J Appl Clin Med Phys*. 2025;25(9):e14438.

doi: 10.1002/acm2.14438

39. Groot Koerkamp ML, Bol GH, Kroon PS, *et al*. Bringing online adaptive radiotherapy to a standard C-arm linac. *Phys Imaging Radiat Oncol*. 2024;31:100597.

doi: 10.1016/j.phro.2024.100597

40. Winkel D, Bol GH, Kroon PS, *et al*. Adaptive radiotherapy: The Elekta Unity MR-linac concept. *Clin Transl Radiat Oncol*. 2019;18:54-59.

doi: 10.1016/j.ctro.2019.04.001

41. Klüter S. Technical design and concept of a 0.35 T MR-Linac. *Clin Transl Radiat Oncol*.2019;18:98-101.

doi: 10.1016/j.ctro.2019.04.007

ACCSCIENCE PUBLISHING

Advances in Radiotherapy & Nuclear Medicine

MINI-REVIEW

Diagnostics and treatment of thyroid nodules after the Chernobyl accident

Sirion Robertson[1] and Sergei Jargin[2]*

[1]Department of Pharmacy, Faculty of Pharmacy, Rhodes University, Makhanda, Eastern Cape, South Africa

[2]Department of Pathology, Faculty of Medicine, RUDN University, Moscow, Russia

Abstract

Thyroid cancer is rare in children but often presents at an advanced stage with aggressive features. Following the Chernobyl accident (CA), a marked increase in pediatric papillary thyroid carcinoma (PTC) was reported in contaminated areas, coinciding with the initiation of mass screening and heightened diagnostic scrutiny. This review summarizes prior publications on thyroid lesions related to the CA and examines potential biases in associated epidemiological research. Based on the linear no-threshold theory, an increase in the incidence of various malignancies was predicted after the accident. In reality, however, no elevation in cancer frequency has been conclusively linked to Chernobyl-related radiation exposure, except for PTC in residents exposed at a young age. It remains plausible that a considerable proportion of these thyroid cancers were indeed caused by ionizing radiation from the accident. Before the CA, pediatric thyroid cancer was infrequently diagnosed in Belarus and Ukraine. It is well established that screening can significantly increase the detection rate of thyroid tumors. Post-accident screening efforts identified not only small lesions but also previously undiagnosed cancers – some of which were labeled as aggressive radiogenic carcinomas. This labeling contributed to the perception of exceptional tumor aggressiveness. Such interpretations influenced clinical practice: certain experts recommended more radical approaches for thyroid nodules diagnosed as radiogenic carcinoma, diverging from standard international guidelines. Overestimations of the medical and environmental consequences of low-dose ionizing radiation have played a role in constraining the development of nuclear energy. Several studies on Chernobyl-related thyroid malignancies warrant reassessments. Lifelong animal studies represent a promising approach for elucidating dose–response relationships.

Keywords: Radioactivity; Chernobyl accident; Thyroid carcinoma; Thyroidectomy

***Corresponding author:**
Sergei Jargin
(sjargin@mail.ru)

Citation: Robertson S, Jargin S. Diagnostics and treatment of thyroid nodules after the Chernobyl accident. *Adv Radiother Nucl Med*. 2025;3(4):83-93.
doi: 10.36922/ARNM025120013

Received: March 18, 2025

1st revised: April 15, 2025

2nd revised: June 23, 2025

Accepted: June 24, 2025

Published online: July 15, 2025

1. Introduction

Thyroid cancer is rare in the pediatric population. In comparison to adults, children more frequently present with aggressive or advanced-stage disease. Papillary thyroid carcinoma (PTC), which accounts for ~90% of pediatric thyroid cancer, is commonly associated with extensive extrathyroidal spread. Children tend to present with either locoregional or distant metastases and exhibit a higher risk of recurrence than adults with PTC.[1] An increase in the detection rate of thyroid cancer in contaminated regions

began approximately 4 years after the Chernobyl accident (CA), with PTC being by far the most predominant subtype.[2-4] While iodine-131 therapy for Graves' disease in adults was known to cause hypothyroidism, it was not linked to cancer. However, studies of children exposed to radiation from atomic bombs, medical X-rays, or therapeutic radiation reported increased thyroid cancer incidence, typically after latencies of ~10 years or more.[5] Although radiogenic malignancies likely occurred following the CA, their incidence has been overestimated in some reports.[6-8] Before CA, the detection rate of pediatric thyroid tumors in the former Soviet Union (SU) was lower than in other industrialized nations (Table 1), likely due to insufficient attention to thyroid health during medical checkups, as well as differences in diagnostic quality and imaging technology.[6] In contaminated regions, the rise in incidence coincided with the launch of mass screening programs in 1989. Some experts questioned the reliability of morphological diagnostics used at the time.[4] Mechanisms of false positivity are discussed below and have been explored in earlier publications.[6-8] The mass screenings uncovered not only small nodules but also previously neglected late-stage cases. Moreover, there was a tendency among individuals to register as Chernobyl victims to access state-provided benefits.[9] In 1990, the year regulations on Chernobyl-related social protections were issued, a rapid increase in the diagnosis of thyroid conditions eligible for such benefits was observed. Some international observers noticed that many of these claims lacked sufficient clinical validation.[9] It is important to note that thyroid cancer cases brought from other regions may have been, on average, more advanced than those identified through local mass screenings. This aligns with findings that the first wave of post-accident thyroid cancers tended to be larger and less differentiated than those diagnosed 10 years later.[2,3]

Table 1. Thyroid cancer incidence in children and adolescents

Country	Period	Age <(years)	Incidence (per million/ year)	References
Belarus	1981 – 1985	14	0.3	11,12
Belarus	1991 – 1995	18	Female: 57.2; male: 27.5	16
Belarus	2001 – 2005	18	Female: 118.8; male: 34.4	16
Ukraine	1981 – 1985	14	0.5	11,12
Ukraine (northern regions)	1981 – 1985	14	0.1	11,12
Ukraine	1991 – 1995	18	Female: 14.0; male: 5.0	16
Ukraine	2001 – 2005	18	Female: 44.0; male: 10.0	16
Bulgaria	1980 – 1989	14	0.7	17,18
Canada	1982 – 1991	14	1.6	17,18
Costa Rica	1984 – 1992	14	0.7	17,18
Czech Republic	1980 – 1989	14	1.1	17,18
Nigeria (Ibadan)	1983 – 1992	14	0.2	17,18
Norway	1980 – 1989	14	1.4	17,18
Thailand	1983 – 1993	14	0.8	17,18

Note: Data for countries outside the former Soviet Union reflect pre-CA periods for comparison. In Russia, thyroid cancer began to be recorded as a separate diagnostic category in 1989.[4]

A commonly cited but potentially misleading statement reads: "With regard to the size of the primary tumor, 77% were >1 cm, suggesting that these were not incidental thyroid cancers detected by aggressive screening."[10(p269])] In reality, mass screening detected both incidental tumors and advanced, previously undiagnosed malignancies. Some argue that the screening cannot fully explain the age-related differences in incidence, as increases in Chernobyl-related malignancy were most notable among those exposed at younger ages. However, this may be explained by prioritization: children and adolescents received focused attention,[4] were easily accessible through kindergartens, schools, and colleges, and were often examined hastily by teams not uniformly proficient, under an atmosphere of anticipation regarding thyroid malignancies.

2. Diagnostics and epidemiology

Thyroid cancer was rarely diagnosed in children and adolescents in the former SU before the CA. For instance, between 1981 and 1985 in Belarus, only three cases were recorded in children under 15, corresponding to an annual incidence of 0.3 per million. In Ukraine during the same period, 25 cases were recorded (0.5 per million), and in the northern, later-contaminated regions, only 1.0 and 0.1 per million, respectively (Table 1).[11,12] According to the International Agency for Research on Cancer, "In the whole of Belarus, by 1995, the incidence of childhood thyroid carcinoma had increased to 4 cases per 100000 per year compared to 0.03 – 0.05 cases per 100000 per year before the Chernobyl accident."[13(p290])] Table 1 presents comparative incidence data from other countries. Based on 2000 – 2004 data, the United States Surveillance, Epidemiology, and End Results Program reported an annual age-adjusted thyroid cancer incidence of 8.5/100,000, with 2.1% of cases diagnosed under age 20 – equating to 1.8 per million annually.[14] According to the American Thyroid Association (ATA), thyroid cancer incidence increases with age, from ≤1 cases per million per year in children ≤10 years old, to 3.5 in children aged 10 – 14, and 15.4 in adolescents aged 15 – 19.[15]

The post-CA rise in PTC incidence was so marked that even an increase in the baseline incidence by a few cases per million annually would have had a minimal impact on interpretation. Assuming a pre-existing background incidence of 2 – 4 cases per million, the hypothetical pool of undiagnosed PTCs would have been 30 – 60 per million. If all were detected within 5 years following the sharp incidence rise (1991 – 1995), the resulting annual rate would be ~8 – 16 per million – still well below the actual figures observed (Table 1). Despite the unexpectedly brief latency period, there is little doubt that radiogenic cancers did emerge post-accident, although quantifying their proportion remains difficult. It is plausible that a considerable portion of thyroid cancers was indeed caused by ionizing radiation from the CA. However, other factors likely contributed to the surge, including false positives, reclassification of dormant or ambiguous cases (e.g., papillary thyroid microcarcinoma [mPTC]), misclassification of unexposed individuals as exposed, and various methodological biases. It was already well understood before the CA that intensive screening could significantly inflate recorded thyroid cancer incidence.[19] Furthermore, lower thyroid-stimulating hormone levels – particularly in iodine-deficient regions like those affected by the CA – are associated with increased thyroid nodule prevalence and malignancy risk. Independent of radiation exposure, studies have shown that PTC frequency is higher in iodine-deficient areas than in iodine-sufficient ones.[20,21]

The number of thyroid cancer cases in Ukraine between 1981 and 1985, as reported by the United Nations Scientific Committee on the Effects of Atomic Radiation (UNSCEAR), was 25.[16] This figure, also cited in Tronko *et al.*,[22] could not be independently verified through online databases, the journal's website, or academic libraries. According to an email from the UNSCEAR Secretariat (October 2013), hard copies of the article were supplied directly to the Secretariat. It has repeatedly been stated or implied in the literature that thyroid cancer incidence in Belarus before the accident was comparable to that in other countries.[23-25] – that is, much higher than the figures listed in Table 1. For example, Fridman *et al.*[25] makes such a claim citing Williams,[26] yet no such statement appears in Williams.[26] This discrepancy suggests an effort to obscure the comparatively low pre-CA thyroid cancer incidence in the former SU. Following the CA, more than 90% of children in contaminated areas underwent annual screening for thyroid nodules using ultrasonography and other diagnostic methods. This mass screening effort – arguably the most extensive in the history of medicine – resulted in the detection of thousands of previously undiagnosed or "occult" cancers.[19] In some institutions, frozen or celloidin-embedded tissue sections were used instead of paraffin-embedded ones, which is suboptimal for the histological diagnosis of PTC. As mentioned in Section 1, PTC was the predominant pediatric thyroid malignancy following the CA.[2-4] A pathologist trained in the former SU would recognize that the diagnosis of minimally invasive follicular carcinoma requires numerous thin sections through the nodule capsule to detect invasive growth – an approach rarely implemented in practice, resulting in the underdiagnosis of follicular carcinoma. Furthermore, advanced PTCs often contain solid or follicular architectural components. The high prevalence of such features in post-CA PTC supports the likelihood of delayed diagnosis.

Considering this context, the assertion that "in children born a year after the Chernobyl disaster, the age-specific incidence rates were comparable to those expected based on the incidence trend of 1978 – 1986"[27(p5)] is unfounded. Pre-accident thyroid cancer incidence was low, and there was no apparent upward trend. Despite the return to normal background radiation levels, thyroid cancer detection rates in Belarus have remained elevated,[24,27] likely due to increased awareness among both physicians and the public. Indeed, the graph presented in Fridman *et al.*[27] shows sustained elevation in detection rates through 2020. Remarkably, after 2003, the highest incidence was observed in individuals over 45 years of age at diagnosis,[27] likely due to the discontinuation of mass screening in younger populations, combined with increased health-seeking behavior and medical coverage in older adults.

The lack of a comparable increase in thyroid malignancies among children born after the CA likely has non-radiation-related explanations. This cohort was not subject to mass screening at levels comparable to those exposed during childhood. In the meantime, diagnostic standards improved, the reservoir of undetected cases was gradually depleted, and there were no longer institutional or professional incentives to artificially inflate case numbers. As has been noted by internal observers, exaggerating the scale of thyroid cancer facilitated the completion of numerous scientific theses, secured international funding, and attracted foreign aid. Furthermore, the CA has been used politically to undermine nuclear power worldwide,[19] supporting higher market prices for petroleum and natural gas. According to interviews with local professionals, manipulation of statistical data and pathological specimens contributed to overestimating the health consequences of the CA – an issue not uncommon in SU-era medical science.[28-30]

One citation that warrants further scrutiny reads: "It is also important to note that the increase in morbidity was primarily noted in the southern regions of Belarus, which

were most contaminated with radioactive iodine"[27(p5)] This pattern can be explained by the disproportionately intense screening efforts conducted in those regions. An insightful example appears in Okeanov *et al.*,[31(p654],648])] commented upon in Jargin,[32] which claims: "A significant increase in the incidence of cancer morbidity of colon, lung, urinary bladder and thyroid gland, as well as cancers of all sites, was observed in the population of the contaminated areas. This increase is significant in inhabitants of the most contaminated Gomel region." and "The overall cancer morbidity rate in all organs, including colon, urinary bladder, and thyroid, was significantly higher in the Gomel region than in Vitebsk (the minimally contaminated province of Belarus)." In reality, the difference was negligible: 225/100,000 in Gomel versus 219/100,000 in Vitebsk.

Furthermore, the healthcare system in Minsk was more advanced than in rural areas, prompting many patients to migrate to the capital for diagnosis and treatment – sometimes even obtaining official residence there. As a result, tumor incidence in Minsk city was significantly higher than in the heavily contaminated Gomel province (263.7 ± 1.76 vs. 224.6 ± 6.3; $p<0.001$) as well as in the surrounding Minsk province (263.7 ± 1.76 vs. 216.6 ± 3.9; $p<0.001$).[31]

Mechanisms of false positivity have been previously discussed.[6,7,32] When a thyroid nodule was detected through screening, fine-needle aspiration biopsy (FNAB) was typically followed – although FNAB was introduced only after mass screening had begun. Data on its diagnostic sensitivity for detecting post-CA childhood thyroid malignancy are presented in a dissertation.[33] Out of 238 cases, a definitive or presumptive diagnosis of thyroid carcinoma was confirmed in 161. PTC was correctly identified using FNAB in 69.5% of cases, and its follicular subtype in only 36.5%. From the context, it appears that presumptive diagnoses were included among the "correctly" diagnosed cases. Suspicious cytological findings often prompted surgical intervention. The surgical specimens were submitted for histopathological analysis, where malignancy was sometimes confirmed – even in cases of diagnostic uncertainty. As discussed below, histological verification confirmed the cancer diagnosis in ~78% of surgical specimens.[33] The actual proportion was likely higher, given the tendency to obscure false positives. Notably, "low quality of histological sections, impeding the evaluation of cell nuclei,"[34(p5)] contributed to overdiagnosis. In the 1990s, cyto- and histopathological criteria for certain thyroid carcinoma variants were still insufficiently defined. Some cases were overdiagnosed based on cellular atypia, which can also occur in benign thyroid nodules. Misleading diagnostic labels such as "non-invasive follicular carcinoma" or "follicular carcinoma *in situ*" were occasionally used.[35] Papillary hyperplastic[36] and other benign thyroid nodules were sometimes misclassified as cancers. At the time, foreign cytology and histopathology reference materials were rarely constituted.[37]

3. Surgical treatment

According to the ATA Pediatric Guidelines, total or near-total thyroidectomy is recommended for children with differentiated thyroid cancer, due to the increased risk of bilateral (30%) and multifocal (65%) disease, as well as recurrence – which would necessitate a second operation if thyroidectomy had not been performed initially.[15] However, some experts advocate for lobectomy, citing comparable survival outcomes to total thyroidectomy and a lower risk of complications such as hypocalcemia and recurrent laryngeal nerve injury. This position is countered by evidence suggesting a lower recurrence rate after total thyroidectomy.[38] In adults, the recommended approach for differentiated thyroid cancer may include either lobectomy or total thyroidectomy. In the case of mPTC, treatment options for adults include lobectomy, ethanol ablation, or active surveillance.[39] Pediatric mPTC; however, remains understudied. Some experts argue that lobectomy with isthmusectomy is adequate for unifocal pediatric mPTC.[38] Of note, the frequency of treatment regret among mPTC patients following thyroidectomy was reported as 24.2%, compared to 3.4% among those managed with active surveillance. According to the authors of that study, greater caution should be exercised when scheduling thyroidectomy for low-risk mPTC, and patients should be fully informed of the potential risks.[40] Recommendations for clinical management are intentionally avoided in this section.

In the post-CA context, the following quotations are particularly illustrative: "Practically all nodular thyroid lesions, independently of their size, were regarded at that time in children as potentially malignant tumors, requiring an urgent surgical operation" and "Aggressiveness of surgeons contributed to the shortening of the minimal latency period"[4(p47)] In some institutions, thyroid surgery became more extensive,[41,42] and a "maximally radical approach" was recommended.[43] Recommended treatment protocols included the following: "Total thyroidectomy combined with neck dissection followed by radioiodine ablation"[18(p759])] and irradiation with 40 Gy.[44] Completion thyroidectomy was performed in previously operated children, even in the absence of demonstrable residual tumor.[45,46] Renowned experts recommended total thyroidectomy with neck dissection for presumed radiogenic PTC independently of tumor size.[46-48] This

aggressive approach contrasts with that applied in other countries, including Japan, following the Fukushima accident.[49] Some sources[50-52] were inaccurately cited to support the recommendation: "The most prevailing opinion calls for total thyroidectomy regardless of tumor size and histopathology"[42(p530])] In fact, the cited publications discuss near-total rather than total thyroidectomy. Similarly, Danese *et al*., La Quaglia *et al*., Segal *et al*.[52-54] were misquoted in Demidchik and Kontratovich.[46]

The problem of overdiagnosis and "excessive activity in thyroid surgery" – that is, overtreatment and avoidable post-operative complications – was acknowledged by the Health Ministry of the Russian Federation in 1998.[55] Nevertheless, overtreatment persisted, especially in Belarus and Ukraine. The Ministry mandated a histological revision of thyroidectomy specimens from pediatric patients residing in the partly contaminated Bryansk province.[55] This verification revealed substantial false-positive rates: The diagnosis of thyroid cancer was confirmed in 79.1% of cases (federal level of verification: 354 cases) and 77.9% (international level: 280 cases).[33] As mentioned above, the actual percentages may have been even higher. A 2009 monograph compared the proportion of thyroidectomies in which some functioning thyroid parenchyma was preserved in children and adolescents, including those from contaminated areas of Chernobyl and the Urals. The percentages of parenchyma preservation were as follows: 87.2% in Chelyabinsk, 64.3% in St. Petersburg, 35.0% in Minsk, 14.2% in Moscow, and 13.9% in Kyiv.[56] After the Fukushima accident, the corresponding figure in Japan was 92%.[57] Japanese pediatric PTCs have shown significant differences from those observed in Belarus and Ukraine, including a lower frequency of de-differentiated solid and solid-trabecular growth patterns.[58,59] In contrast to CA-related tumors, most PTCs detected after the Fukushima accident were of the classical, well-differentiated papillary type,[60,61] indicating earlier tumor detection in Japan. In this regard, international comparisons of cancer grade are arguably more informative indicators of diagnostic quality than comparisons of stage, since large nodules with uncertain malignant potential could be classified as advanced-stage cancers in contexts of overdiagnosis and suboptimal histological quality.

An earlier study led by Edward D. Williams reported that "The exposed and unexposed tumors from the same geographical area are essentially identical morphologically and in their degree of aggressiveness… childhood PTC from Japan were much more highly differentiated (p<0.001), showed more papillary differentiation (p<0.001) and were less invasive (p<0.01) than Chernobyl tumors."[58(p847])] In subsequent publications by the same group – authored without Williams – the interpretation shifted: "Childhood Japanese PTC differed from Ukrainian PTC by more pronounced invasive properties… higher morphological aggressiveness of PTC in young Japanese patients."[59(p983])] In a more recent paper, the authors acknowledged that Ukrainian "radiogenic" or "radiation-related" PTCs "had a solid-trabecular growth pattern and displayed morphological features of aggressive biological behavior"[62(p1330])] However, no compelling evidence was presented to demonstrate that a considerable part of the tumors in residents of Kyiv, Chernihiv, and Zhytomyr provinces were caused by or significantly influenced by radiation. Importantly, Kyiv was not officially designated as a contaminated territory. What truly distinguished these regions was not the radiation exposure itself, but rather extensive screening that facilitated detection of previously neglected cases, elements of overdiagnosis, heightened radiophobia leading to increased self-reporting, and the registration of some unexposed individuals as the CA victims.[6]

In one study, 69% of post-CA pediatric thyroid cancer patients underwent total thyroidectomy.[57] In another, "given the presence of radiation exposure in the patients' histories,"[63(p14)] total thyroidectomy was performed in 405 out of 465 (87.1%) patients with mPTC. Of these, 76.1% received post-operative radioiodine therapy, and neck dissection was performed in ~50% of cases. Notably, disease recurrence was recorded in only 1.3% of patients over a median follow-up of 5.2 years. The authors acknowledged that mPTCs in their series were "rather indolent"[63(p17)] Some experts have recommended radioiodine therapy for patients with mPTC[64] or for PTC in general,[46] a practice that diverges from prevailing international guidelines. Given the potential adverse effects of radioiodine, the 2009 ATA Guidelines advocate for selective rather than universal administration of iodine-131, especially in younger patients (≤45 years of age) with intrathyroidal PTC and no or minimal lymph node involvement.[65] This selective approach is generally recommended for PTC patients with intermediate risk.[66]

A separate study spanning 1990 – 2005 with an average follow-up of 12.4 years included 936 Belarusian thyroid cancer patients (600 females, 336 males; mean age at surgery: 14.4 years). During the observation period, 17 deaths were recorded – seven due to suicide and five from trauma/accident cases. Only two patients died from cancer progression (pulmonary metastases).[25] In young female patients, cosmetic concerns, visible post-operative scarring or deformity, cancer-related stigma, permanent hypothyroidism, and anxiety regarding radiation effects may contribute to depression.[9,67] Of note, suicide is often

underreported – both intentionally and unintentionally – with official rates potentially 2 – 3 times lower than actual figures, as suicides may be concealed by policymakers/authorities, healthcare providers, or families.[68] A persistent tendency to downplay the social and psychological consequences of CA has been documented.[5,69] Given the excellent long-term prognosis of pediatric thyroid cancer, it is unlikely that screening reduces cancer-specific mortality. Furthermore, it remains unclear whether early detection significantly improves quality of life. The harm resulting from overdiagnosis of thyroid cancer is particularly concerning in pediatric populations, where active surveillance is difficult to implement and a cancer diagnosis may lead to significant stigma.[70] Finally, total thyroidectomy is contraindicated in settings where access to lifelong levothyroxine replacement cannot be guaranteed – a relevant concern in regions currently affected by the war in Ukraine.

4. Discussion

Certain claims attributing the global increase in thyroid cancer incidence – including in the United States and other countries – to radioiodine exposure from nuclear accidents or weapons testing are indicative of ideological bias. For example, it has been stated that the CA "resulted in the development of thyroid cancer in more than 4,000 individuals"[71(p1626])] Other statements include: "Any minimal radiation dose causes damage to heredity;" "there are no genetically inefficient low doses of radiation;"[72(p10,12)] "Contamination of the territory with long-lived radionuclides after CA was comparable to that from 200 to 300 Hiroshima bombs."[73(p1493])] These assertions have been critically challenged on theoretical and empirical grounds in earlier analyses.[6,8,32] CA has also been framed as a catalyst for halting the global expansion of nuclear energy,[19] thereby contributing to sustained high prices for fossil fuels. While deliberate intent cannot be confirmed, negligence and violations of operational protocols were among the direct causes of CA.[74,75]

Historically, geopolitical crises have driven up fossil fuel prices. Similarly, the destruction and shutdown of the Zaporozhie Nuclear Power Plant – the largest in Europe – during the ongoing conflict in Ukraine has further intensified reliance on fossil fuels. The vulnerability of nuclear infrastructure to military attacks remains one of the most significant arguments against its proliferation. Some analysts have suggested that the maintenance of elevated fossil fuel prices may be among the underlying motives behind the war in Ukraine and the associated nuclear threats.[76] A parallel may be drawn with earlier Middle East conflicts: by 1976, in the aftermath of the Arab–Israeli wars, host governments gained control of national fossil fuel reserves, leading to the revocation of foreign concessions and a steep rise in oil prices. This outcome was likely foreseeable and may have been one of the concealed motivations for the wars. Despite the conflict, both Israel and several neighboring countries have received consistent foreign aid.

From the perspective of public health and environmental risks, coal and oil remain the most damaging energy sources, followed by natural gas, with nuclear energy presenting significantly lower risks.[19] This hierarchy is also reflected in their respective contributions to greenhouse gas emissions.[77] Looking ahead, nuclear fission may eventually be supplanted by nuclear fusion, which offers the promise of intrinsically safer, cleaner, and more sustainable energy production, with an abundant supply of raw materials.[78,79] Progress toward such large-scale technological transitions will require lasting peace and robust international cooperation.

Epidemiologists have long warned against the overdiagnosis of thyroid cancer from mass screening using modern imaging technologies. As noted: "The extent to which opportunistic thyroid cancer screening is converting thousands of asymptomatic persons to cancer patients without any known benefit to them needs to be examined carefully."[80(p1535])]

The present author concurs with the conclusions drawn by Cléro *et al.*:[81(p1,4)]

- "After the Chernobyl and Fukushima nuclear accidents, thyroid cancer screening was implemented mainly for children, leading to case overdiagnosis."
- "The existence of a natural reservoir of latent thyroid carcinomas, together with advancements in diagnostic practices leading to case overdiagnosis, explains, at least partially, the rise in thyroid cancer incidence in many countries."
- "Total thyroidectomy, as performed after CA, implies that patients must live the rest of their lives with thyroid hormone supplementation. Additional treatment using radioactive iodine-131 therapy in some cases may result in potentially short- or long-term adverse effects."

These conclusions are consistent with points previously made by the present authors[6,8,32] Importantly, acknowledging diagnostic inflation does not negate the role of ionizing radiation as a potential cause of thyroid cancer and other malignancies following CA.

Some reviews and meta-analyses have methodological limitations, including insufficient consideration of data reliability, bias, and confounding factors. The present authors agree with Little,[82(p12)] who stated that data of

equivocal reliability "should therefore probably not be used for epidemiologic analysis, in particular for the Russian worker studies considered here.[83-86]" Similar concerns may apply to certain studies discussed in this review.

5. Conclusion

The UNSCEAR evaluation of low-dose radiation risks appears susceptible to bias – for example, through potential overestimation of CA-related consequences. Given the present abundance of literature, it is essential that future reviews and meta-analyses incorporate rigorous evaluation of research quality, selection criteria, self-selection effects, and potential ideological bias in determining which studies merit inclusion.

Acknowledgments

None.

Funding

None.

Conflict of interest

The authors declare that they have no competing interests.

Author contributions

Conceptualization: All authors
Writing – original draft: Sergei Jargin
Writing – review & editing: All authors

Ethics approval and consent to participate

Not applicable.

Consent for publication

Not applicable.

Availability of data

Not applicable.

References

1. Paulson VA, Rudzinski ER, Hawkins DS. Thyroid cancer in the pediatric population. *Genes* (*Basel*). 2019;10(9):723.

   doi: 10.3390/genes10090723

2. Williams ED, Abrosimov A, Bogdanova T, *et al*. Thyroid carcinoma after Chernobyl latent period, morphology and aggressiveness. *Br J Cancer*. 2004;90(11):2219-2224.

   doi: 10.1038/sj.bjc.6601860

3. Nikiforov Y, Gnepp DR. Pediatric thyroid cancer after the Chernobyl disaster. Pathomorphologic study of 84 cases (1991-1992) from the Republic of Belarus. *Cancer*. 1994;74:748-766.

   doi: 10.1002/1097-0142(19940715)74:2<748:aid-cncr2820740231>3.0.co;2-h

4. Lushnikov EF, Tsyb AF, Yamashita S. *Thyroid Cancer in Russia after the Chernobyl*. Moscow: Meditsina; 2006.

5. Tapia JA. *Chernobyl and the Mortality Crisis in Eastern Europe and the Former USSR*. Boston: De Gruyter; 2022.

6. Jargin SV. The Overestimation of Medical Consequences of Low-Dose Exposure to Ionizing Radiation. Newcastle Upon Tyne: Cambridge Scholars Publishing; 2022.

7. Jargin S. Thyroid cancer after chernobyl: Re-evaluation needed. *Turk Patoloji Derg*. 2021;37(1):1-6.

   doi: 10.5146/tjpath.2020.01489

8. Jargin SV. Chernobyl-related cancer and precancerous lesions: Incidence increase vs. late diagnostics. *Dose Response*. 2014;12(3):404-414.

   doi: 10.2203/dose-response.13-039.Jargin

9. Bay IA, Oughton DH. Social and economic effects. In: Smith J, Beresford NA, editors. *Chernobyl - Catastrophe and Consequences*. Chichester: Springer; 2005. p. 239-266.

10. Tuttle RM, Vaisman F, Tronko MD. Clinical presentation and clinical outcomes in Chernobyl-related paediatric thyroid cancers: What do we know now? What can we expect in the future? *Clin Oncol (R Coll Radiol)*. 2011;23:268-275.

    doi: 10.1016/j.clon.2011.01.178

11. Stsjazhko VA, Tsyb AF, Tronko ND, Souchkevitch G, Baverstock KF. Childhood thyroid cancer since accident at Chernobyl. *BMJ*. 1995;310:801.

    doi: 10.1136/bmj.310.6982.801

12. Andersson M, Blettner M, Boecker BB, *et al*. Ionizing radiation, part 2: Some internally deposited radionuclides. Views and expert opinions of an IARC Working Group on the evaluation of carcinogenic risks to humans. Lyon, 14-21 June 2000. *IARC Monogr Eval Carcinog Risks Hum*. 2001;78(Pt 2):233-236.

13. IARC Working Group. Internalized β-Particle Emitting Radionuclides. IARC Monographs. Radiation. Vol. 100. France: IARC; 2012. p. 285-303.

14. Luster M, Lassmann M, Freudenberg LS, Reiners C. Thyroid cancer in childhood: Management strategy, including dosimetry and long-term results. *Hormones* (*Athens*). 2007;6:269-278.

    doi: 10.14310/horm.2002.1111023

15. Parisi MT, Eslamy H, Mankoff D. Management of differentiated thyroid cancer in children: Focus on the American Thyroid association pediatric guidelines. S*emin Nucl Med*. 2016;46:147-164.

    doi: 10.1053/j.semnuclmed.2015.10.006

16. UNSCEAR. *2008 Report. Annex D. Health Effects Due to Radiation from the Chernobyl Accident*. New York: United Nations; 2008.

17. Parkin DM, Kramárová E, Draper GJ, Masuyer E, editors. *International Incidence of Childhood Cancer IARC Scientific Publication No 144*. Lyon: IARC Press; 1998.

18. Demidchik YE, Saenko VA, Yamashita S. Childhood thyroid cancer in Belarus, Russia, and Ukraine after Chernobyl and at present. *Arq Bras Endocrinol Metabol*. 2007;51:748-762.

doi: 10.1590/s0004-27302007000500012

19. Jaworowski Z. Observations on the chernobyl disaster and LNT. *Dose Response*. 2010;8:148-171.

doi: 10.2203/dose-response.09-029.Jaworowski

20. Cao LZ, Peng XD, Xie JP, Yang FH, Wen HL, Li S. The relationship between iodine intake and the risk of thyroid cancer: A meta-analysis. *Medicine* (*Baltimore*). 2017;96:e6734.

doi: 10.1097/MD.0000000000006734

21. Yildirim Simsir I, Cetinkalp S, Kabalak T. Review of factors contributing to nodular goiter and thyroid carcinoma. *Med Princ Pract*. 2020;29(1):1-5.

doi: 10.1159/000503575

22. Tronko ND, Bogdanova TI, Komissarenko I. Thyroid cancer in children and adolescents in Ukraine having been exposed as a result of the Chornobyl accident (15-year expertise of investigations). *Int J Radiat Med*. 2002;4:222-232.

23. Balonov M. The Chernobyl accident as a source of new radiological knowledge: Implications for Fukushima rehabilitation and research programmes. *J Radiol Prot*. 2013;33:27-40.

doi: 10.1088/0952-4746/33/1/27

24. Fridman MV, Kras'ko OV, Man'kovskaia SV, Savva NN, Demidchik IE. The increase of non-cancerous thyroid tissue in children and adolescents operated for papillary thyroid cancer: Related factors. *Vopr Onkol*. 2013;59(2):121-125.

25. Fridman MV, Man'kovskaia SV, Kras'ko OV, Demidchik IE. Clinical and morphological features of papillary thyroid cancer in children and adolescents in the Republic of Belarus: analysis of 936 post-Chernobyl carcinomas. *Vopr Onkol*. 2014;60(2):43-46.

26. Williams D. Radiation carcinogenesis: Lessons from chernobyl. *Oncogene*. 2008;27(Suppl 2):S9-S18.

doi: 10.1038/onc.2009.349

27. Fridman M, Krasko O, Veyalkin I. The incidence trends of papillary thyroid carcinoma in Belarus during the post-Chernobyl epoch. *Cancer Epidemiol*. 2025;95:102745.

doi: 10.1016/j.canep.2025.102745

28. Jargin SV. Overestimation of Chernobyl consequences: Poorly substantiated information published. *Radiat Environ Biophys*. 2010;49(4):743-745.

doi: 10.1007/s00411-010-0313-1

29. Jargin SV. *Misconduct in Medical Research and Practice*. New York: Nova Science Publishers; 2020.

doi: 10.52305/giez3244

30. Jargin SV. Urological concern after nuclear accidents. *Urol Ann*. 2018;10:240-242.

doi: 10.4103/0974-7796.236525

31. Okeanov AE, Sosnovskaya EY, Priatkina OP. National cancer registry to assess trends after the chernobyl accident. *Swiss Med Wkly*. 2004;134:645-649.

doi: 10.4414/smw.2004.10221

32. Jargin SV. Some aspects of thyroid neoplasia after Chernobyl. *Hamdan Med J*. 2020;13(2):69-77.

doi: 10.4103/hmj.hmj_73_19

33. Abrosimov AI. *Rak Shhitovidnoizhelezy u Detei i Podrostkov Rossii Posle Avarii na Chernobylskoi AES (Problem Diagnostici i Verifikacii Diagnoza, Morfologicheskaia Harakteristika)* [*Thyroid Cancer in Children and Adolescents in Russia after Chernobyl Accident (Problems of Diagnosis and Verification, Morphological Characteristics)*]. [Dissertation]. Obninsk: Medical Research Radiological Centre; 2004.

34. Abrosimov AI, Lushnikov EF, Frank GA. Radiogenic (Chernobyl) thyroid cancer. *Arkh Patol*. 2001;63(4):3-9.

35. Demidchik EP, Tsyb AF, Lushnikov EF. *Rak Shhitovidnoi Zhelezy u Detei. Posledstvia avarii na Chernobylskoi AES [Thyroid Carcinoma in Children. Consequences of Chernobyl Accident]*. Moscow: Meditsina; 1996.

36. Khurana KK, Baloch ZW, LiVolsi VA. Aspiration cytology of pediatric solitary papillary hyperplastic thyroid nodule. *Arch Pathol Lab Med*. 2001;125(12):1575-1578.

doi: 10.5858/2001-125-1575-ACOPSP.

37. Murphy J, Jargin S. International trends in health science librarianship part 20: Russia. *Health Info Libr J*. 2017;34(1):92-94.

doi: 10.1111/hir.12172

38. Christison-Lagay ER, Baertschiger RM, Dinauer C, *et al*. Pediatric differentiated thyroid carcinoma: An update from the APSA cancer committee. *J Pediatr Surg*. 2020;55(11):2273-2283.

doi: 10.1016/j.jpedsurg.2020.05.003

39. Haugen BR. 2015 American thyroid association management guidelines for adult patients with thyroid nodules and differentiated thyroid cancer: What is new and what has changed? *Cancer*. 2017;123(3):372-381.

doi: 10.1002/cncr.30360

40. Li G, Li R, Zhong J, *et al*. A multicenter cohort study of

thyroidectomy-related decision regret in patients with low-risk papillary thyroid microcarcinoma. *Nat Commun*. 2025;16(1):2317.

doi: 10.1038/s41467-025-57627-7

41. Iakovleva IN, Shishkov RV, Poliakov VG, Pankova PA. Clinico-morphological peculiarities of thyroid cancer among children exposed to the Chernobyl disaster radiation. *Vopr Onkol*. 2008;54:315-320.

42. Demidchik YE, Demidchik EP, Reiners C, *et al*. Comprehensive clinical assessment of 740 cases of surgically treated thyroid cancer in children of Belarus. *Ann Surg*. 2006;243:525-532.

doi: 10.1097/01.sla.0000205977.74806.0b

43. Fridman MV, Demidchik IE, Papok VE, *et al*. Cryptogenic and iatrogenic papillary thyroid carcinoma in children and adolescences: Comparative study. *Arkh Patol*. 2011;73(6):26-29.

44. Mamchich VI, Pogorelov AV. Surgical treatment of nodular goiter after the accident at the Chernobyl nuclear power station. *Klin Khir* (*1962*). 1992;59(12):38-40.

45. Romanchishen AF, Bagaturiia GO, Gostimskii AV, Bagatikov AA. Epidemiology and specificity of thyroid carcinoma clinical course before and after the chernobyl accident. *Vestn Khir Im I I Grek*. 2010;169(1):68-72.

46. Demidchik IE, Kontratovich VA. Repeat surgery for recurrent thyroid cancer in children. *Vopr Onkol*. 2003;49:366-369.

47. Romanchishen AF. Actual questions of endocrinous surgery: A viewpoint of a participant of international congresses in 2003-2004. *Vestn Khir Im I I Grek*. 2005;164(3):52-55.

48. Fridman MV. *Papillarnyi Rak Shhitovidnoi Zhelezy u Detei i Podrostkov: Diagnostika, Lechenie, Prognoz* [*Papillary Thyroid Cancer in Children and Adolescents: Diagnostics, Treatment, Prognosis*]. Dissertation. Minsk: Republican Center of Oncology and Medical Radiology; 2014.

49. Sugitani I. Management of papillary thyroid carcinoma in Japan. In: Yamashita S, Thomas G, editors. *Thyroid Cancer and Nuclear Accidents. Long-Term After-Effects of Chernobyl and Fukushima*. London: Elsevier; 2017. p. 185-194.

50. Arici C, Erdogan O, Altunbas H, *et al*. Differentiated thyroid carcinoma in children and adolescents. Clinical characteristics, treatment and outcome of 15 patients. *Horm Res*. 2002;57:153-156.

doi: 10.1159/000058375

51. Giuffrida D, Scollo C, Pellegriti G, *et al*. Differentiated thyroid cancer in children and adolescents. *J Endocrinol Invest*. 2002;25:18-24.

doi: 10.1007/BF03343956

52. Danese D, Gardini A, Farsetti A, Sciacchitano S, Andreoli M, Pontecorvi A. Thyroid carcinoma in children and adolescents. *Eur J Pediatr*. 1997;156:190-194.

doi: 10.1007/s004310050580

53. La Quaglia MP, Corbally MT, Heller G, Exelby PR, Brennan MF. Recurrence and morbidity in differentiated thyroid carcinoma in children. *Surgery*. 1988;104:1149-1156.

54. Segal K, Arad-Cohen A, Mechlis S, Lubin E, Feinmesser R. Cancer of the thyroid in children and adolescents. *Clin Otolaryngol Allied Sci*. 1997;22:525-528.

doi: 10.1046/j.1365-2273.1997.00060.x

55. Starodubov VI. *(Health Minister 1998-1999). Ordinance (Prikaz) No. 301 of October 09, 1998. O Sovershenstvovanii Organizacii Medicinskoi Pomoshhi Bolnym s Zabolevaniami Shhitovidnoi Zhelezy, Prozhivaiushchim na Radioaktivno Zagriaznennoi Territorii Brianskoi Oblasti [On Improving the Organization of Medical Care for Patients with Thyroid Diseases Living in the Radioactively Contaminated Territory of the Bryansk Province*]. Moscow: Health Ministry; 1998.

56. Romanchishen AF, Demidchik IE, Poliakov VG. Hirurgicheskoe lechenie detei i podrostkov s patogeneticheski raznym rakom shhitovidnoi zhelezy. Surgical treatment of children and adolescents with pathogenetically different thyroid cancer. In: Romanchishen AF, editor. *Hirurgia shchitovidnoi i Okoloshchitovidnyh Zhelez [surgery of Thyroid and Parathyroid]*. St. Petersburg: Vesti; 2009. p. 367-369.

57. Drozd V, Saenko V, Branovan DI, Brown K, Yamashita S, Reiners C. A search for causes of rising incidence of differentiated thyroid cancer in children and adolescents after Chernobyl and Fukushima: Comparison of the clinical features and their relevance for treatment and prognosis. *Int J Environ Res Public Health*. 2021;18:3444.

doi: 10.3390/ijerph18073444

58. Williams ED, Abrosimov A, Bogdanova T, *et al*. Morphologic characteristics of Chernobyl-related childhood papillary thyroid carcinomas are independent of radiation exposure but vary with iodine intake. *Thyroid*. 2008;18(8):847-852.

doi: 10.1089/thy.2008.0039

59. Bogdanova TI, Saenko VA, Hirokawa M, *et al*. Comparative histopathological analysis of sporadic pediatric papillary thyroid carcinoma from Japan and Ukraine. *Endocr J*. 2017;64(10):977-993.

doi: 10.1507/endocrj.ej17-0134

60. Suzuki S. Childhood and adolescent thyroid cancer in Fukushima after the Fukushima Daiichi nuclear power plant accident: 5 years on. *Clin Oncol (R Coll Radiol)*. 2016;28(4):263-271.

doi: 10.1016/j.clon.2015.12.027

61. Yamashita S, Suzuki S, Suzuki S, Shimura H, Saenko V. Lessons from Fukushima: Latest findings of thyroid cancer after the Fukushima nuclear power plant accident. *Thyroid*. 2018;28(1):11-22.

doi: 10.1089/thy.2017.0283

62. Bogdanova TI, Saenko VA, Hashimoto Y, *et al*. Papillary thyroid carcinoma in Ukraine after Chernobyl and in Japan after Fukushima: Different histopathological scenarios. *Thyroid*. 2021;31(9):1322-1334.

doi: 10.1089/thy.2020.0308

63. Bogdanova T, Chernyshov S, Zurnadzhy L, *et al*. The relationship of the clinicopathological characteristics and treatment results of post-Chornobyl papillary thyroid microcarcinomas with the latency period and radiation exposure. *Front Endocrinol (Lausanne)*. 2022;13:1078258.

doi: 10.3389/fendo.2022.1078258

64. Gamolina LI, Achinovich SL, Pyshnyak VL. Mikrokarcinoma Shhitovidnoi Zhelezy. Taktika Lecheniia i Dispansernogo Nabliudenia [Thyroid Microcarcinoma. Treatment Tactics and Follow-Up] In: Thyroid Cancer: Current Concepts of Diagnostics and Treatment. In: *Proceedings of the International Scientific Forum*. St. Petersburg, June 12-13, 2009. St. Petersburg University; 2008. p. 40-41.

65. Francis GL, Waguespack SG, Bauer AJ, *et al*. Management guidelines for children with thyroid nodules and differentiated thyroid cancer. *Thyroid*. 2015;25(7):716-759.

doi: 10.1089/thy.2014.0460

66. Matrone A, Campopiano MC, Nervo A, Sapuppo G, Tavarelli M, De Leo S. Differentiated thyroid cancer, from active surveillance to advanced therapy: Toward a personalized medicine. *Front Endocrinol (Lausanne)*. 2020;10:884.

doi: 10.3389/fendo.2019.00884

67. Kim H, Kim Y, Shin MH, Choi KW, Chung MK, Jeon HJ. Risk of suicide attempt after thyroidectomy: A nationwide population study in South Korea. *Psychiatry Investig*. 2021;18(1):39-47.

doi: 10.30773/pi.2020.0174

68. Holinger PC, Offer D. Toward the prediction of violent deaths among the young. In: Howard S, Sudak HS, Amasa B, Ford AB, Norman B, Rushforth NB, editors. *Suicide in the Young*. Boston: John Wright; 1984. p. 15-30.

69. Smith J, Beresford NA, editors. Conclusions. In: *Chernobyl - Catastrophe and Consequences*. Chichester: Springer; 2005. p. 289-305.

70. Takano T. Overdiagnosis of juvenile thyroid cancer. *Eur Thyroid J*. 2020;9(3):124-131.

doi: 10.1159/000503323

71. Nikiforov YE. Is ionizing radiation responsible for the increasing incidence of thyroid cancer? *Cancer*. 2010;116:1626-1628.

doi: 10.1002/cncr.24889

72. Dubinin NP, Arsenieva MA, Kerkis II. *Geneticheskaia Opasnost Malyh Doz Radiacii Dlia Cheloveka i ih Effekt na Nasledstvennost Obezian i Gryzunov [Genetic Danger of Low Radiation doses for Humans and their Effect in Heredity of Primates and Rodents]*. Moscow: Akademia Nauk SSSR; 1960.

73. Dubinin NP. The genetic risk of ionizing radiation. *Dokl Akad Nauk SSSR*. 1990;314(6):1491-1494.

74. Beliaev IA. *Chernobyl. Vahta smerti [Death shift]*. Moscow: IzdAT; 2006.

75. Semenov AN. *Chernobyl. Desiat' let Spustia: Neizbezhnost ili Sluchainost? [Ten Years Later: Inevitability or Coincidence?]* Moscow: Energoatomizdat; 1995.

76. Jargin SV. *The Conflict in Ukraine: Psychopathology and Social Aspects*. New York: Nova Science Pulishers; 2023.

doi: 10.52305/FGMY4468

77. Markandya A, Wilkinson P. Electricity generation and health. *Lancet*. 2007;370:979-990.

doi: 10.1016/s0140-6736(07)61253-7

78. Duffy DM. Fusion power: A challenge for materials science. *Philos Trans A Math Phys Eng Sci*. 2010;368(1923):3315-3328.

doi: 10.1098/rsta.2010.0060

79. Llewellyn Smith C, Ward D. The path to fusion power. *Philos Trans A Math Phys Eng Sci*. 207;365(1853):945-956.

doi: 10.1098/rsta.2006.1956

80. Ahn HS, Kim HJ, Kim KH, *et al*. Thyroid cancer screening in South Korea increases detection of papillary cancers with no impact on other subtypes or thyroid cancer mortality. *Thyroid*. 2016;26:1535-1540.

doi: 10.1089/thy.2016.0075

81. Cléro E, Ostroumova E, Demoury C, *et al*. Lessons learned from Chernobyl and Fukushima on thyroid cancer screening and recommendations in case of a future nuclear accident. *Environ Int*. 2021;146:106230.

doi: 10.1016/j.envint.2020.106230

82. Little MP. Radiation and circulatory disease. *Mutat Res*. 2016;770(Pt B):299-318.

doi: 10.1016/j.mrrev.2016.07.008

83. Azizova TV, Grigoryeva ES, Haylock RG, Pikulina MV, Moseeva MB. Ischaemic heart disease incidence and mortality in an extended cohort of Mayak workers first employed in 1948-1982. *Br J Radiol*. 2015;88(1054):20150169.

doi: 10.1259/bjr.20150169

84. Ivanov VK, Maksioutov MA, Chekin SY, *et al*. The risk of radiation-induced cerebrovascular disease in Chernobyl emergency workers. *Health Phys*. 2006;90(3):199-207.

doi: 10.1097/01.hp.0000175835.31663.ea

85. Kashcheev VV, Chekin SY, Maksioutov MA, *et al*. Radiation-

epidemiological study of cerebrovascular diseases in the cohort of Russian recovery operation workers of the Chernobyl accident. *Health Phys*. 2016;111(2):192-197.

doi: 10.1097/HP.0000000000000523

86. Moseeva MB, Azizova TV, Grigoryeva ES, Haylock R. Risks of circulatory diseases among Mayak PA workers with radiation doses estimated using the improved Mayak Worker dosimetry system 2008. *Radiat Environ Biophys*. 2014;53(2):469-477.

doi: 10.1007/s00411-014-0517-x

ACCSCIENCE PUBLISHING

Advances in Radiotherapy & Nuclear Medicine

SHORT COMMUNICATION

Performance of neutron beam system for accelerator-based boron neutron capture therapy

Vladislav Veksleman[1]*, Mark Harrison[1], Kirill Martianov[2], Anatoly B. Muchnikov[1], Aleksandr Makarov[2], Yong Jiang[3], Ken Franzen[1], Alexander Ivanov[1], Michael Meekins[1], Chad Lee[2], and Alexander Dunaevsky[1]

[1]TAE Technologies Inc., Foothill Ranch, California, United States of America

[2]TAE Life Sciences, Irvine, California, United States of America

[3]TAE TLS China, Xiamen, Fujian, China

(This article belongs to the *Special Issue: Boron Neutron Capture Therapy: A Renaissance*)

Abstract

A neutron beam system (NBS) based on an electrostatic proton accelerator designed for accelerator-based boron neutron capture therapy has been installed in Xiamen Humanity Hospital in China. The NBS has been used for patient treatments since October 2023, after more than a year of preliminary studies. By the end of 2024, more than 50 treatments had been executed. NBS uptime during 2024 was above 96%. Repeatability of the beam parameters was well within 2%. At present, configuration with only one treatment room operational, the overall machine usage, including clinical use, physics and dosimetry measurements, and biological experiments, has reached 27% of its capacity.

Keywords: Boron neutron capture therapy; Accelerator-based boron neutron capture therapy; Neutron beam system; Tandem accelerator; Proton beam; Lithium target

***Corresponding author:**
Vladislav Veksleman
(vvekselman@tae.com)

Citation: Veksleman V, Harrison M, Martianov K, *et al.* Performance of neutron beam system for accelerator-based boron neutron capture therapy. *Adv Radiother Nucl Med*. 2025;3(4):94-101. doi: 10.36922/ARNM025190022

Received: May 6, 2025

1st revised: June 5, 2025

2nd revised: July 30, 2025

Accepted: August 4, 2025

Published online: August 18, 2025

1. Introduction

Boron neutron capture therapy (BNCT) has re-emerged as a promising cancer treatment enabled by recent breakthroughs in compact accelerator technology. BNCT enables highly selective tumor cell destruction, employing the nuclear reaction of boron-10, delivered to and accumulated in malignant tissue, with thermal or epithermal neutrons. Resulting particles with high linear energy transfer (LET) deposit energy over a subcellular distance, effectively damaging tumor cells while sparing adjacent healthy tissues.

Historically, the clinical advancement of BNCT has been limited by the availability of suitable neutron sources. Conventional neutron sources relied on nuclear research reactors, which presented substantial limitations in terms of footprint, regulation, accessibility, and hospital integration. Emergence of accelerator-based BNCT (ab-BNCT) systems capable of producing an epithermal neutron beam in compact, shielded facilities renewed interest in the field. In 2020, Japan approved the first ab-BNCT system

(NeuCure™, Sumitomo Heavy Industries)[1] followed by installations in Finland, China, and South Korea. Systems such as NeuCure™, CICS (Japan),[2] nuBeam (Finland),[3] A-BNCT (Korea),[4] and NeuPex (China)[5] differ in beam energy, neutron yield, target design, and facility layout. However, they collectively represent a transition from experimental treatment toward a more standardized and accessible cancer therapy. The role of the accelerator, specifically, its ability to deliver stable proton beams to the neutron-generating targets, remains central to these systems.

TAE Life Sciences has developed AlphaBeam™, a turnkey clinical solution for BNCT treatment centers. AlphaBeam™ includes an accelerator-based neutron beam system (NBS), a beam shaping assembly, a neutron dosimetry system, a patient positioning system, a treatment planning software, and a radiation safety system. The NBS is based on a proton accelerator designed for high operational stability, safety, and efficiency to meet the strict demands of clinical workflows.

AlphaBeam™ NBS is also used as a neutron source for the NeuPex™ BNCT platform offered in China by Neuboron Medtech. The NeuPex™ system installed at Xiamen Humanity Hospital in Xiamen, China, has been used to treat patients since October 2023.[5] By the end of 2024, more than 50 treatments had been successfully delivered with clinical performance and dosimetry data reported.[5]

Through this paper, we aim to provide insight into the real-world performance of accelerator-driven NBS and highlight its key parameters, including beam stability, system availability, reliability, and power consumption.

2. NBS methodology: Design and implementation

The concept of the AlphaBeam™ NBS is based on the generation of neutrons by the nuclear reaction of protons accelerated to 2.2–2.4 MeV with a lithium target: ^{7}Li(p,n)^{7}Be. Spectrum of neutrons generated in this reaction suits well for moderation to the epithermal energies required by standards for BNCT treatment.[6]

The NBS is built around a tandem-type electrostatic accelerator (Figure 1). It consists of: (i) A source of negative ions of hydrogen mounted on a high-voltage platform to provide pre-acceleration of the negative ions before injection to the accelerator, (ii) A tandem accelerator powered by a 25 kW SF6-filled high-voltage power supply, (iii) A high-energy beamline to deliver the proton beam to the lithium targets, and (iv) The lithium target assemblies where neutrons are generated. Before implementation, this architecture of the NBS and the design of its components underwent a detailed experimental study.[7]

While low-energy proton beams coupled with lithium targets are a common method for neutron generation in BNCT, they are not the only approach. An alternative widely adopted method involves higher energy proton beams in combination with beryllium targets employing ^{9}Be(p,n)^{9}B reaction. Electrostatic accelerators are typically employed for low-energy proton beam generation, whereas radiofrequency linacs and cyclotrons are preferred for higher energy proton beams.

The specific implementation of the accelerator systems varies across platforms, each presenting distinct advantages and limitations, but the parameters of the epithermal neutron beams are comparable for all architectures.[8,9] Our selection of the transformer type tandem electrostatic accelerator was based on simplicity, reliability, and cost-effectiveness of this specific technology.[10] We believe that this architecture offers meaningful advantages in achieving higher beam power necessary for increasing the fluence of epithermal neutrons as a way to increase throughput in BNCT treatment facilities.

2.1. H^- ion source

As a source of negative ions of hydrogen, a cesium-free, filament-driven ion source was chosen. Sources with volumetric formation of negative ions have limited output ion current but are drastically simpler in terms of maintenance than caesiated sources with surface ion formation.[11] The use of a filament-based design offers simpler construction and improved electrical efficiency, translating to lower power consumption.[12]

Hardware of the negative ion source used in the NBS is manufactured by D-Pace Inc.[13] The downstream beam optics have been upgraded to optimize beam quality and transport efficiency. Power supply system and the control algorithm were developed by TAE Life Sciences. The power system ensures precise control of beam parameters, enables real-time tuning of beam current, and supports fully automated, operator-free operation aligned for routine clinical use.

The ion source is capable of delivering direct current (DC) of the negative ions of hydrogen up to 15 mA at ion energy of 30 keV.

2.2. Injector

The injector plays a critical role in preparing the H^- beam for efficient acceleration. It consists of a pre-acceleration stage, adaptive beam matching optics, and beam diagnostics (Figure 2).

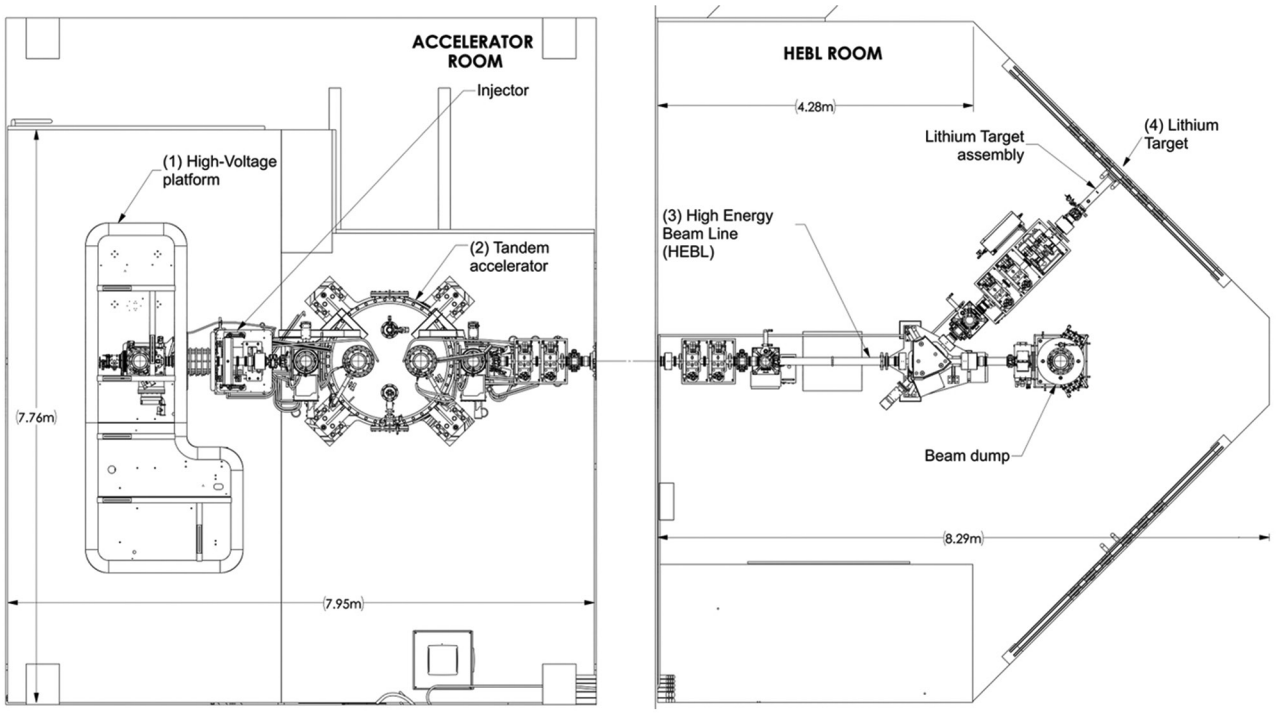

Figure 1. Structure of the AlphaBeam™ Neutron Beam System. Reproduced with permission of TAE Life Sciences. Copyright (C) 2020 TAE Life Sciences.

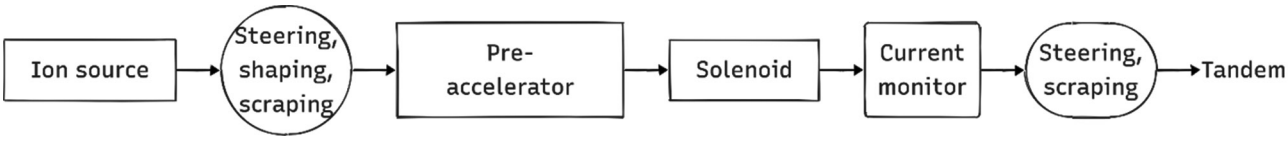

Figure 2. Injector schematics

A pre-accelerator stage utilizes an electrostatic tube to boost the beam energy up to 200 keV. This step is essential to minimize space-charge effects and reduce beam stripping losses. In addition, coupling with a solenoid magnet ensures optimal transverse beam matching of the acceptance angle of the tandem accelerator. Dual-axis steering magnets are used to align the beam along the accelerator longitudinal axis, offering alignment within 0.1 mrad.

Beam dual-axis optical diagnostics is integrated into the injector to provide real-time feedback on beam position (accuracy within ±100 μm) and profile (resolution 250 μm) at the injection point of the tandem accelerator. Beam current is measured using a high-precision current monitor with ±20 μA accuracy.

The ion beam is injected into the tandem accelerator through a beam limiter (aperture). The limiter removes beam halo, improving transport efficiency and reducing heat load of the internal elements of the tandem accelerator.

2.3. Tandem-type electrostatic accelerator

The tandem accelerator is designed to deliver a proton beam with adjustable proton energies of 1.8–2.4 MeV and beam currents of 0–10 mA (Figure 3). The accelerator employs a two-stage (tandem) acceleration mechanism. First, H^- ions are accelerated toward the high-voltage terminal, which is biased to a DC voltage equivalent to half of the required beam energies. Within the terminal, a gaseous charge-exchange target strips both electrons of the negative ions of hydrogen, forming protons, which are further accelerated toward ground potential to achieve the final energy. NBS uses argon as a stripping gas. A high gradient of the Ar pressure along the acceleration path is achieved by the concept of vacuum insulation of tandem accelerators.[7]

DC power supply of a transformer type is used to power the tandem accelerator.[14] AC current with a frequency of several kHz supplied by a 40 kW frequency converter drives the primary winding of the transformer. Secondary sections with rectifiers are connected in series to achieve

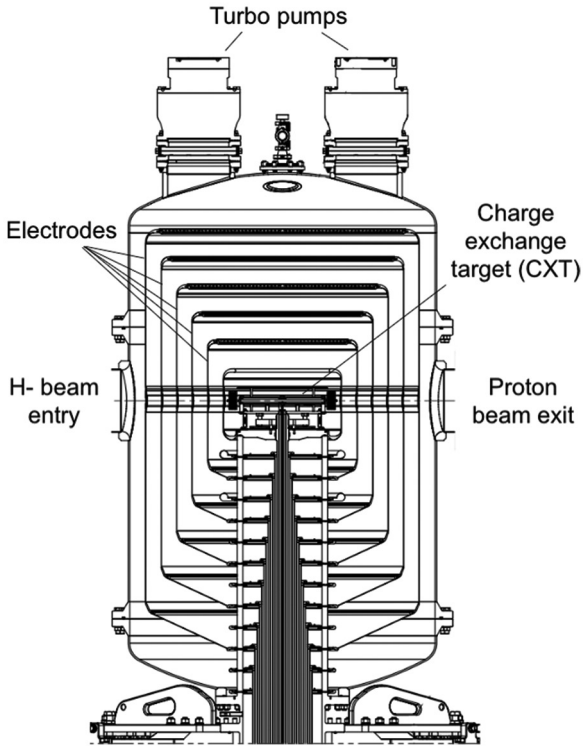

Figure 3. Tandem electrostatic accelerator. Reproduced with permission of TAE Life Sciences. Copyright (C) 2020 TAE Life Sciences.

voltages up to 1.3 MV. The output voltage is applied to electrodes of the tandem accelerator through a 1.3 MV coaxial feedthrough. The entire power supply is placed into a vessel filled with SF6 to achieve the necessary high-voltage insulation.

After acceleration, the proton beam is ejected from the tandem through the exit aperture, which also scrapes off a minimal halo of the proton beam. Beam size, position, and current are monitored by the same optical beam diagnostics and the current monitor as at the injection of the accelerator. Current balance of the input and output current, as well as power absorbed by the charge-exchange target, allows monitoring of the accelerator efficiency and provides reliable interlocks for protection of the system.

2.4. High-energy beamline

From the exit of the tandem accelerator, the high-energy proton beam is transported to the lithium targets by a high-energy beamline. The beamline incorporates a series of quadrupole magnets that control the beam envelope along the beamline. Dual-axis steering magnets help to align the beam with the axis of the beamline.

Dipole magnets are used to deflect the beam towards lithium targets in the treatment rooms. The installation in the Xiamen Humanity hospital has three treatment rooms: two horizontal rooms at 90° to each other and one vertical, placed underneath the high-energy beamline hall. Deflection of the beam toward the horizontal treatment rooms is done by a single 45° Y-shaped dipole. Beam weldment of the dipole also has a beamline continuation to deliver the beam to the full-power beam dump when the dipole is not powered. Deflection of the beam to the vertical treatment room is done by a 90° dipole.

Dedicated high-speed raster magnets sweep the beam over the lithium target surface at a predefined two-dimensional pattern. Parameters of the rastering pattern—frequency, amplitude, and shape—are adjustable to evenly distribute power over the surface of the lithium target.[15]

Beam position, size, and current are monitored by the optical beam diagnostics and the DC current monitors, similar to those used in the tandem accelerator.

2.5. Lithium target

The neutron production target consists of a 100 μm thick layer of lithium vacuum-deposited on an oxygen-free copper substrate (Figure 4). The substrate incorporates a special pattern of cooling channels with turbulent water flow, capable of removing up to 25 kW of thermal load while maintaining the lithium layer below 130°C.[16] The target assembly integrates multiple embedded thermocouples in a radial pattern to monitor thermal gradients. A target imaging diagnostics based on IR-VIS optical imaging of beam-induced luminescence provides live visualization of the rastering pattern and beam coverage on the lithium surface. In addition, it is used to assess changes in target surface reflectivity, uniformity, and wear over time. These diagnostics capabilities enable proactive maintenance and scheduling of target replacement to maintain consistent neutron generation while minimizing NBS downtime.

2.6. Ancillary and control

In addition to the accelerator itself, the NBS includes a set of ancillary systems needed to provide the accelerator with electric power, cooling water, compressed air, and specialty gases.

The NBS is driven by a control system developed to provide completely automated, operator-independent operation of the NBS. The control system collects and analyzes data of all NBS subsystems in real time, providing the proton beam of current and energy stability better than 2%. The system supports multiple layers of safety interlocks to protect the hardware from failures and personnel and patients from hazards. The human interface of the control system provides the technical personnel with access to the NBS subsystems needed for periodic preventive maintenance.

3. NBS performance evaluation: Results and discussion

3.1. Operational workflow

The system is designed to minimize manual intervention and operates under an automated workflow depicted in Figure 5.

The day begins with a System Check to verify all subsystems' health status and followed by Tandem Conditioning to stabilize high-voltage operation. A Beam Quality Assurance (QA) procedure then confirms beam parameters and transport efficiency before allowing Patient Treatment Sessions. Currently, treatment delivery follows Medical User Control System (MUCS) requests with 20-min inter-session intervals. At the end of the day, the machine cools down and a final NBS health check is performed. After that, the NBS is transitioned into a safe standby mode until the next operational cycle.

3.2. Beam QA

The Beam QA protocol ensures consistent treatment delivery through verification of accelerator performance and beam characteristics. Executed automatically before patient treatments, this 10-min procedure validates all critical beam parameters. Any significant deviation from nominal values triggers the beam deviation protocol.

The beam QA procedure includes the following key elements:

(i) Beam validation: Beam current is measured at several beamline locations, including pre- and post-acceleration. Beam energy is calculated. Measured values are compared with setpoints to confirm beam delivery meets clinical tolerances. Figure 6 shows beam current measurements acquired during routine beam QA sessions
(ii) Beam transport efficiency: The efficiency of the beam transport in NBS is assessed
(iii) Beam losses: Beam losses are measured at beam limiters (apertures) distributed along the NBS beamline. This data are analyzed to detect and localize abnormal beam interactions with the beamline and log loss patterns
(iv) Beam alignment: Beam position and shape are verified using optical diagnostics.

3.3. Beam operation and stability

The standard clinical operation protocol consists of up to six treatment sessions per day, each running for up to 50 min at a proton beam energy of 2.35 MeV and a beam current of 10 mA at the lithium target. Between sessions, automated system procedures allow for a brief cooldown, machine status check, and diagnostics verification.

Figure 7 shows representative waveforms of beam current and energy acquired during a day of operation (6 treatment sessions at 2.35 MeV, 10 mA, ~45 min/session).

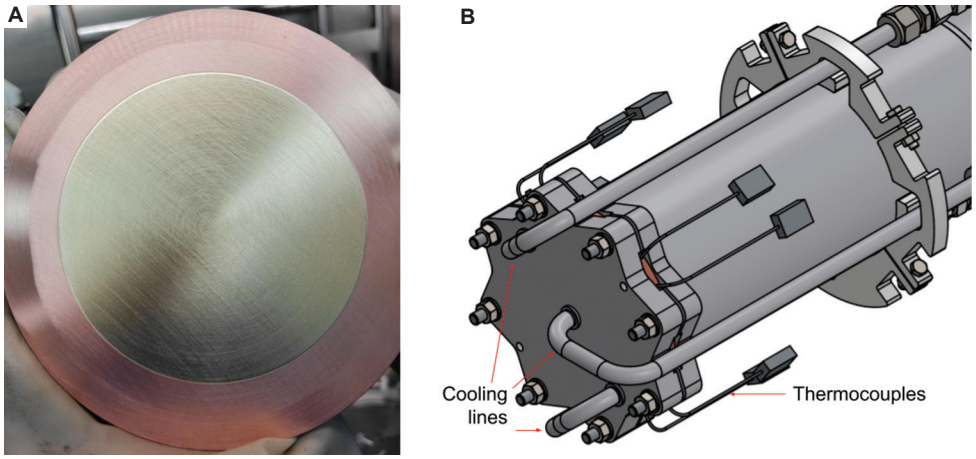

Figure 4. Lithium layer on copper substrate (A) and partial view of the target assembly (B)

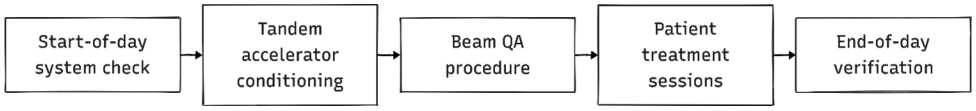

Figure 5. Operational workflow of the neutron beam system
Abbreviation: QA: Quality assurance.

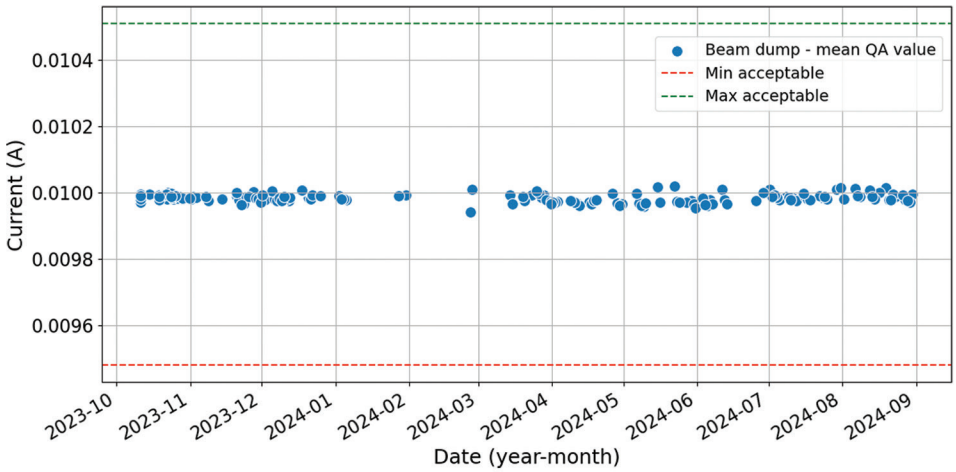

Figure 6. Beam current at the beam dump over 12 months as measured during beam QAs. Dashed lines show tolerances. Abbreviation: QA: Quality assurance.

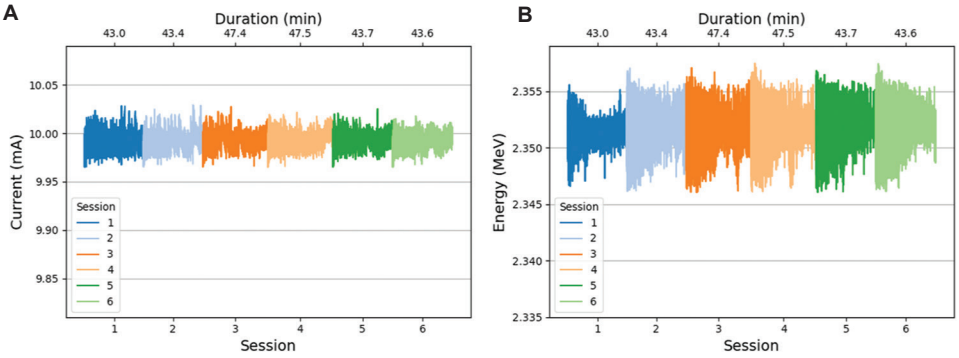

Figure 7. Representative waveforms of beam current (A) and energy (B) acquired during a day of operation in April 2025

A summary of the beam parameter statistics is provided in Table 1.

3.4. Beam transport efficiency through the tandem

Since the NBS is based on an electrostatic tandem accelerator, its performance is critically important for reliable proton beam delivery to the lithium target. Unlike conventional vacuum-insulated accelerators, the NBS accelerator operates in a gas-moderated vacuum state that introduces distinct beam physics and transport dynamics.

Efficiency is defined as the ratio of the extracted proton beam current to the injected H^- beam current, thus accounting for charge-exchange processes and beam losses on internal components. During the charge-exchange process, H^- ions are stripped of their electrons, with some fraction lost due to incomplete stripping and scattering effects. Additional losses arise from internal apertures within the accelerator.

The efficiency trend collected during a treatment is presented in Figure 8, illustrating the stability and efficiency close to 90%.

3.5. System availability and reliability

Over the past 12 months, the NBS has demonstrated a consistently high level of operational reliability. Beam uptime, defined as the fraction of scheduled operational hours during which a clinical-quality proton beam was successfully delivered to the lithium target, is 98.3% on average. Figure 9 shows the monthly uptime data distribution over the evaluation period.

At the end of the year of 2024, the average daily system usage for clinical and research purposes reached 27%. In the clinical mode, Xiamen Humanity Hospital scheduled up to three patient treatments a day. More than 50 patient treatments were delivered, with the number continuously growing. It is proven to be critical to have at least two treatment rooms to support high patient throughput.

Table 1. Beam parameter statistics

Session	Beam current		Beam energy	
	Mean value (mA)	STD (μA)	Mean value (MeV)	STD (keV)
1	9.993	8.5	2.3513	0.7
2	9.994	9.4	2.3515	1.1
3	9.994	8.2	2.3516	1.1
4	9.994	7.6	2.3517	1.1
5	9.994	7.2	2.3518	1.2
6	9.993	6.8	2.3518	1.1

Abbreviations: mA: Milliamperes; μA: Microamperes; MeV: Mega electron-volt; keV: Kilo electron-volt; STD: Standard deviation.

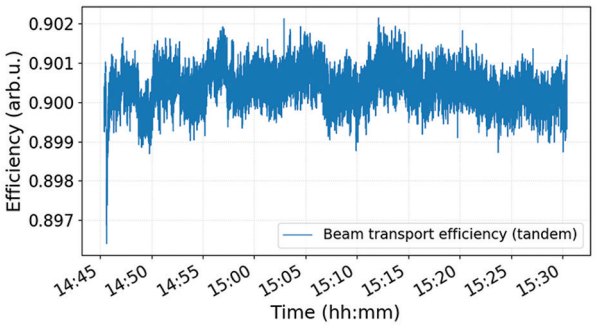

Figure 8. Beam transport efficiency through the tandem. Beam energy = 2.35 MeV, current = 10 mA, and duration = 45 min.

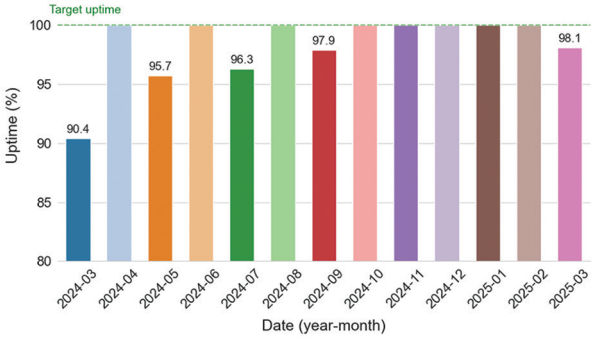

Figure 9. The neutron beam system monthly uptime data

3.6. Power budget

The NBS operational efficiency directly supports clinical and economic feasibility. At the standard clinical operating condition of 23.5 kW proton beam, the system demonstrates:

- Total active power consumption: 54 kW (excluding cooling systems)
- Tandem accelerator electrical efficiency: 72%
- Net electrical efficiency of all NBS subsystems: 44% from wall-plug to beam power
- Operational power ratio: 2.3 kW per kW of the proton beam on the target
- Standby (overnight) power consumption: 13 kW

With 44% overall electrical efficiency, NBS represents a significant advancement in accelerator efficiency. It makes it possible to achieve the total power budget of the facility to be below 80 kW at a typical clinical installation.

4. Conclusion

AlphaBeam™ NBS was put into operation at the Xiamen Humanity Hospital in October 2022, when First-in-Human treatment was delivered. Full performance of the system was achieved in September 2023. The NBS passed all regulatory tests and entered the warranty period in December 2023. Over 50 patient treatments had been delivered. Phase 1A of the clinical trials was successfully completed. At the time of submission of the manuscript, Phase 1b of the clinical trials was ongoing. Clinical results are expected to be published by the medical team soon.

After more than a year of continuous use, average daily usage of the NBS reached 27%. Actual annual downtime of the NBS was <4%. The NBS was proven to deliver the proton beam with stability better than 2% with high reliability and reproducibility. The overall electrical efficiency of the entire NBS system is as high as 44%, providing a low cost of ownership. The system is operated by local personnel trained and certified by TAE Life Sciences.

Acknowledgments

None.

Funding

This work was fully funded by TAE Life Sciences.

Conflict of interest

Kirill Martianov, and Aleksandr Makarovand Chad Lee work for TAE Life Sciences in United States of America. This has not influenced the content of the manuscript. No reference to the author's company is made, but it is declared for full transparency. Other authors declare no conflict of interest.

Author contributions

Conceptualization: Alexander Dunaevsky, Alexander Ivanov

Data curation: Yong Jiang, Vladislav Veksleman

Investigation: Vladislav Veksleman, Mark Harrison, Kirill Martianov, Anatoly B. Muchnikov, Aleksandr Makarov, Yong Jiang, Ken Franzen, Alexander Dunaevsky

Resources: Michael Meekins, Alexander Ivanov
Writing–original draft: Vladislav Vekselman, Aleksandr Makarov
Writing–review & editing: Vladislav Vekselman, Alexander Dunaevsky, Chad Lee

Ethics approval and consent to participate

Not applicable.

Consent for publication

Not applicable.

Availability of data

Data is available from the corresponding author upon reasonable request.

References

1. Hirose K, Konno A, Hiratsuka J, *et al*. Boron neutron capture therapy using cyclotron-based epithermal neutron source and borofalan (10B) for recurrent or locally advanced head and neck cancer (JHN002): An open-label phase II trial. *Radiother Oncol*. 2021;155:182-187.

   doi: 10.1016/j.radonc.2020.11.001

2. Kurosaki H, Okazaki K, Takemori M, Tate E, Nakamura T. The effects of boron neutron capture therapy on the lungs in recurrent breast cancer treatment. *Cureus*. 2024;16(4):e57417.

   doi: 10.7759/cureus.57417

3. Porra L, Wendland L, Seppälä T, *et al*. From nuclear reactor-based to proton accelerator-based therapy: The finnish boron neutron capture therapy experience. *Cancer Biother Radiopharm*. 2023;38(3):184-191.

   doi: 10.1089/cbr.2022.0059

4. Bae Y soon, Kim DS, Seo HJ, *et al*. Advances of LINAC-based boron neutron capture therapy in Korea. *AAPPS Bull*. 2022;32(1):34.

   doi: 10.1007/s43673-022-00063-2

5. Zhang Z, Chong Y, Liu Y, *et al*. A review of planned, ongoing clinical studies and recent development of BNCT in mainland of China. *Cancers (Basel)*. 2023;15(16):4060.

   doi: 10.3390/cancers15164060

6. International Atomic Energy Agency Physics Section. *Advances in Boron Neutron Capture Therapy*. IAEA; 2023. Available from: https://www.iaea.org/publications/15339/advances-in-boron-neutron-capture-therapy [Last accessed on 2025 Jul 28].

7. Ivanov AA, Smirnov AN, Taskaev SY, *et al*. Accelerator-based neutron source for boron neutron capture therapy. *Phys Usp*. 2021;65:834-851.

   doi: 10.3367/ufne.2021.02.038940

8. Kumada H, Sakae T, Sakurai H. Current development status of accelerator-based neutron source for boron neutron capture therapy. *EPJ Techn Instrum*. 2023;10(1):18.

   doi: 10.1140/epjti/s40485-023-00105-5

9. Dziura D, Tabbassum S, Macneil A, *et al*. Boron neutron capture therapy in the new age of accelerator-based neutron production and preliminary progress in Canada. *Can J Phys*. 2023;101(8):363-372.

   doi: 10.1139/cjp-2022-0266

10. Sauerwein WAG, Wittig A, Moss RL, Nakagawa Y, Ono K. *Neutron Capture Therapy: Principles and Applications*. 2nd ed. Switzerland: Springer Nature; 2025.

    doi: 10.1007/978-3-031-82591-0

11. Bacal M, Wada M. Negative hydrogen ion production mechanisms. *Appl Phys Rev*. 2015;2(2):021305.

    doi: 10.1063/1.4921298

12. Melanson S, Dehnel M, Potkins D, McDonald H, Philpott C. HΣ, DΣ, C2Σ: A Comparison of RF and Filament Powered Volume-Cusp Ion Sources. In: *IPAC 2017 - Proceedings of the 8th International Particle Accelerator Conference*. JACoW; 2017. p. 1685-1687.

    doi: 10.18429/JACoW-IPAC2017-TUPIK002

13. Kuo T, Yuan D, Jayamanna K, *et al*. On the development of a 15 mA direct current H- multicusp source. *Rev Sci Instrum*. 1996;67:1314-1316.

    doi: 10.1063/1.1146704

14. Domarov EV, Ivanov AA, Kuksanov NK, *et al*. A sectioned high-voltage rectifier for a compact tandem accelerator with vacuum insulation. *Instrum Exp Tech*. 2017;60(1):70-73.

    doi: 10.1134/S0020441216060130

15. Dunaevsky A, Snitchler G, Eggers H, Styron J, Leon Lee C. *Ion Beam Exclusion Paths on the Target Surface to Optimize Neutron Beam Performance*; 2023. https://patentcenter.uspto.gov/applications/18177528 [Last accessed on 2025 Aug 06].

16. Jauregui F, Meekins M, Bhanderi S, Muchnikov A. *Neutron Generating Target for Neutron Beam Systems*; 2023. Available from: https://patentcenter.uspto.gov/applications/17004742 [Last accessed on 2025 Aug 06].

ACCSCIENCE PUBLISHING

Advances in Radiotherapy & Nuclear Medicine

CASE REPORT

Recurrent adult-type granulosa cell tumor of the ovary: A case report

Phuong Pham Cam[1,2,3*], Khoa Mai Trong[1,2,3], Thai Pham Van[1,3], Hung Nguyen Thanh[1,2], Khiem Nguyen Thanh[4], Khuy Doan Minh[1,5], Huyen Tong Thi[1], Lanh Pham Minh[1,2], Ngan Tran Thi Thuy[1,2], and Ha Le Thanh[2]

[1]The Nuclear Medicine and Oncology Center, Bach Mai Hospital, Hanoi, Vietnam

[2]Department of Oncology and Nuclear Medicine, University of Medicine and Pharmacy, Vietnam National University, Hanoi, Vietnam

[3]Department of Nuclear Medicine, Hanoi Medical University, Hanoi, Vietnam

[4]The Digestive Surgery Center, Bach Mai Hospital, Hanoi, Vietnam

[5]The Pathology and Cytology Center, Bach Mai Hospital, Hanoi, Vietnam

Abstract

Adult ovarian granulosa cell tumors (AGCTs) are among the most common types of gonadal sex cord-stromal tumors. This pathological entity is generally associated with a favorable prognosis but only accounts for about 2–5% of all malignant ovarian tumors. Disease stage is the most important prognostic factor, with patients diagnosed at an early stage exhibiting a good prognosis. Surgery remains the cornerstone of treatment, both for primary and recurrent cases, while chemotherapy is typically reserved for inoperable or advanced progressive situations. Despite treatment, about one-third of patients experience relapse or progression within 4–7 years, and approximately 50% of these cases result in mortality. We report a case of recurrent AGCT occurring three years after initial surgery and chemotherapy. The patient underwent secondary cytoreductive surgery for recurrent lesions, with postoperative recovery achieved. Further chemotherapy will be administered based on clinical condition and treatment response.

Keywords: Granulosa cell tumor; Adult-type; Ovarian neoplasm; Recurrence; Cytoreductive surgery

***Corresponding author:**
Phuong Pham Cam
(phamcamphuong@hmu.edu.vn)

Citation: Cam PP, Trong KM, Van TP, *et al*. Recurrent adult-type granulosa cell tumor of the ovary: A case report. *Adv Radiother Nucl Med.* 2025;3(4):102-108. doi: 10.36922/ARNM025240029

Received: June 14, 2025

Revised: July 29, 2025

Accepted: August 19, 2025

Published online: September 23, 2025

1. Introduction

Granulosa cell tumor (GCT) is one of the most common subtypes of gonadal sex cord-stromal tumors, characterized by distinct clinical and molecular features. Within the pathological classification of ovarian neoplasms, GCTs belong to a group associated with a favorable prognosis, accounting for about 2–5% of malignant ovarian tumors.[1] Most patients are diagnosed at an early stage and generally have favorable clinical outcomes. Surgical management of GCTs is tailored to tumor stage and the patient's age. In pre-menopausal women or those of reproductive age, fertility-sparing surgery is often performed, typically involving unilateral salpingo-oophorectomy. In contrast, for postmenopausal women or patients who have completed childbearing, the standard

surgical approach frequently includes a total abdominal hysterectomy with bilateral salpingo-oophorectomy, depending on the stage of the disease.

Stage remains the most important prognostic factor, with a 10-year survival rate ranging from 84% to 95% for stage I tumors, 50–65% for stage II, and only 17–33% for stages III and IV.[1] Patients with low-risk stage I tumors are generally managed with surveillance. In contrast, high-risk stage I cases—such as those involving large tumors (≥10–15 cm), stage IC disease, poor differentiation, high mitotic index, or tumor rupture—may warrant consideration of adjuvant chemotherapy due to elevated risk of recurrence.[1] However, the prognostic impact of these factors and the benefits of chemotherapy remain uncertain. For stage II–IV, adjuvant chemotherapy is generally recommended following surgery. Nevertheless, its efficacy remains unclear due to the rarity of these cases and the limited availability of studies and clinical trials. However, in select high-risk cases, adjuvant chemotherapy or radiation therapy may contribute to improved disease-free survival (DFS).[1] Given the tendency for GCTs to recur years after the initial diagnosis, prolonged follow-up is essential. Routine physical examinations and monitoring of serum tumor markers, such as estradiol and inhibin, play a crucial role in the early detection of recurrence.

Recent advances in molecular pathology have further elucidated the biology of adult-type GCTs (AGCTs). A recurrent somatic mutation in the *FOXL2* gene—c.402C>G (p.C134W)—has been identified in approximately 95–97% of AGCTs and is now considered a pathognomonic molecular hallmark for this tumor type. This mutation plays a crucial role in AGCT tumorigenesis and is widely used in modern diagnostic pathology to distinguish AGCT from other ovarian neoplasms with overlapping histologic features.[2,3] In this case report, we present a 46-year-old woman who developed recurrent AGCT three years after initial surgery and chemotherapy, and was subsequently managed with secondary cytoreductive surgery and planned chemotherapy. Although *FOXL2* mutation analysis was not performed in the present case, its relevance is discussed below.

2. Case presentation

A 46-year-old woman (born in 1975) with a history of left ovarian cystectomy in 2018 presented with prolonged menstrual bleeding, fatigue, poor appetite, and rapid weight loss of 3 kg/month in January 2021. She had no significant past medical history and had not yet reached menopause. On physical examination, she exhibited signs of anemia, and a firm, immobile mass measuring approximately 10 × 6 cm was palpable in the right lower abdominal region.

2.1. Before treatment

Abdominal computed tomography (CT) revealed a subhepatic mass measuring 71 × 113 mm with ill-defined borders and heterogeneous contrast enhancement. Additional findings included multiple peritoneal metastases (the largest measuring 46 × 69 mm) and a right ovarian tumor measuring 52 × 48 mm. Chest CT and gastrocolonoscopy showed no abnormalities or lesions suggestive of malignancy.

At the time of initial diagnosis, the disease had already spread beyond the ovary, with hepatic metastases present, corresponding to advanced-stage disease (FIGO stage IV). The case was reviewed by the Gastroenterology and Oncology Council, and the patient underwent laparoscopic surgery, which included resection of the right ovarian tumor, the left subhepatic mass, and peritoneal nodules.

Histopathological analysis confirmed the diagnosis of an adult-type GCT.

The patient recovered well postoperatively and was discharged on day 6 after surgery. The patient subsequently received adjuvant chemotherapy consisting of paclitaxel (175 mg/m^2, administered intravenously on day 1) and carboplatin (AUC 6, administered intravenously on day 1).

2.2. Post-treatment review: Six cycles of chemotherapy

After completing six cycles of chemotherapy, the patient remained stable, with no shortness of breath or abnormal vaginal bleeding. Weight gain was observed, and the patient's general physical condition improved.

Subclinical findings showed improvement in anemia, and no severe chemotherapy-related side effects were noted. Whole-body CT revealed no evidence of recurrent lesions.

Following discharge, the patient was placed under regular follow-up. Abdominal ultrasound and biochemical/hematological testing were performed every three months, while chest and abdominal CT scans were conducted every 6 months, all of which were normal.

By September 2024, the patient underwent a routine abdominal CT scan for lesion surveillance and re-evaluation. Clinically, the patient remained asymptomatic, with no abnormal vaginal bleeding, no abdominal pain, and maintained good physical condition, mobility, and daily activities.

Abdominal CT showed a 65 × 64 mm pelvic mass with unclear boundaries involving the posterior cervical wall and high rectal wall (Figure 1). An infusion-enhancing mass (42 × 29 mm) was also detected between the right liver

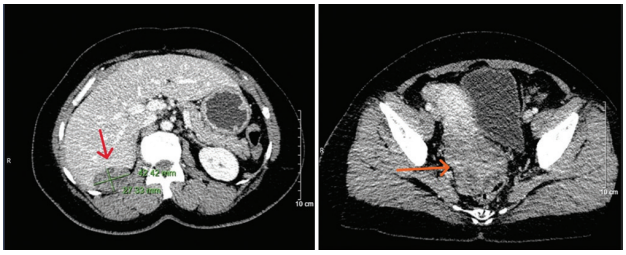

Figure 1. Contrast-enhanced axial computed tomography images demonstrating two enhancing soft-tissue masses. (Left) A well-enhancing peritoneal implant measuring approximately 42 × 29 mm is located in the right subphrenic space, between the right hepatic lobe and the right hemidiaphragm (red arrow). (Right) A heterogeneously enhancing pelvic mass measuring approximately 65 × 64 mm with ill-defined borders abuts the posterior cervical wall and the anterior wall of the upper rectum (orange arrow), suggestive of local invasion or dense adhesions.

and right diaphragm. Magnetic resonance imaging (MRI) revealed a heterogeneous mass (59 × 83 × 78 mm) located posterior to the uterus, with clear boundaries separating it from the uterus (Figure 2). Abdominal wall nodules of a similar nature were observed, the largest measuring 23 × 24 mm. Thoracic CT was normal (Figure 3). Endoscopic examinations were also performed. Gastroscopy and colonoscopy revealed no tumors, and cystoscopy showed normal findings.

Given these results, the case was reviewed by the Gastroenterology and Oncology Council, and surgery was recommended for the removal of the recurrent tumor lesions, the right subhepatic mass, and peritoneal nodules. Multiple metastatic nodules were found on the peritoneum of the pelvic and diaphragmatic arches. The liver had two metastatic nodules, with one located on the surface of the posterior lobe (2 × 2.5 cm). A small skeletal tumor (4 × 5 cm) showed a significant invasion into the rectal membrane. The surgical interventions included (Figure 4) resection of recurrent tumors, hysterectomy, resection of pelvic and right diaphragmatic peritoneal metastases, liver metastasis excision, and appendectomy (Figure 5).

Gross pathological examination revealed: (1) The pelvic tumor measured 7 × 5 × 3.5 cm, with a solid gray-white cut surface and focal cystic dilation (1.5 cm); (2) The uterus measured 12 × 8 × 6 cm. The cervical mucosa and endometrium appeared smooth, with no identifiable appendages. A 2 × 1.5 × 1 cm mass was located on the edge of the uterine body, exhibiting a yellowish-white, slightly firm texture with signs of bleeding; (3) The mass at the liver base measured 3.5 × 3 × 2 cm, appeared brown, and was firm in consistency; (4) The appendix measured 2.5 × 1 cm, with a congested serosal surface but no identifiable tumor; (5) Right diaphragmatic nodules ranged from 0.4 cm to

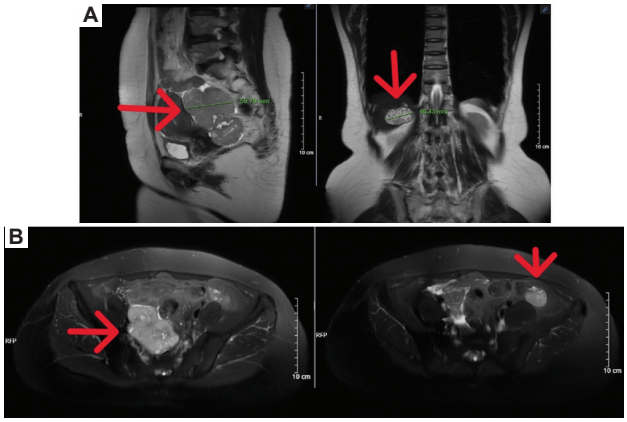

Figure 2. Pelvic magnetic resonance imaging findings. (A) Sagittal and coronal T2-weighted images demonstrate a well-defined, lobulated mass posterior to the uterus, measuring approximately 59 × 83 × 78 mm, with heterogeneous signal intensity, internal septations, and possible hemorrhagic or cystic components, suggestive of a recurrent granulosa cell tumor. (B) Axial T2-weighted fat-saturated and diffusion-weighted images show multiple enhancing nodular lesions within the anterior abdominal wall, the largest measuring approximately 23 × 24 mm (red arrows). These findings are consistent with peritoneal implants or metastatic deposits.

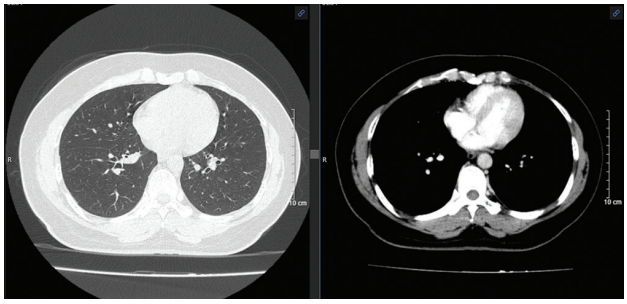

Figure 3. Contrast-enhanced thoracic computed tomography demonstrating normal thoracic anatomy with no radiological evidence of metastatic disease. The bilateral lung parenchyma demonstrates a homogeneous appearance, with no evidence of either focal or diffuse pulmonary lesions (left). The mediastinal structures are well-aligned and symmetrical. The chest wall, including the bony structures and surrounding soft tissues, shows no abnormal findings (right).

2.3 × 1.5 cm, appearing soft and gray; (6) Omental tissue weighing 200 g contained multiple firm brown lesions ranging from 1–3 cm.

Microscopic findings revealed tumor cells with round or oval nucleid, some with nuclear grooves. The cells exhibited scant cytoplasm, high nuclear density, and mitotic activity. They were arranged in clusters, bands, or Call–Exner bodies. Immunohistochemistry (IHC) showed tumor cells were positive for CD99 and inhibin, and negative for cytokeratin (CK), CD56, Wilms tumor 1 (WT1), synaptophysin, myogenic markers, S100, calretinin, and epithelial membrane antigen (EMA).

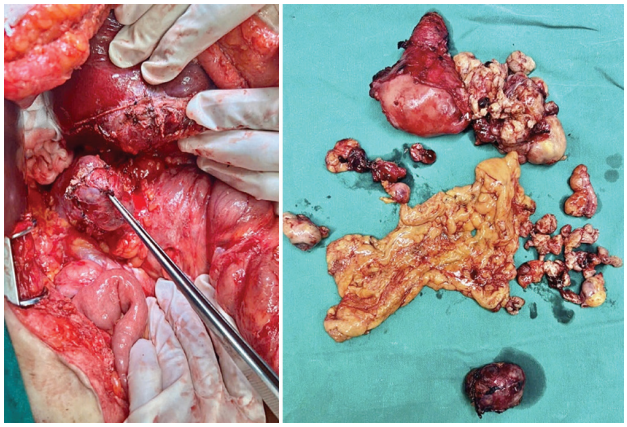

Figure 4. Intraoperative and gross pathological findings. (Left) Intraoperative photograph reveals multiple peritoneal metastatic nodules on the liver surface, peritoneum, and omentum. A visible metastatic implant is being dissected from the pelvic peritoneum using forceps. The liver surface shows deposits at the diaphragmatic aspect, suggestive of tumor implants or adhesions. The surgical field demonstrates widespread peritoneal dissemination. (Right) Gross specimen after cytoreductive surgery shows multiple nodular tumor deposits of varying sizes, including the uterus, tumor-infiltrated omentum, and numerous peritoneal metastatic nodules, characteristic of disseminated adult-type granulosa cell tumor recurrence.

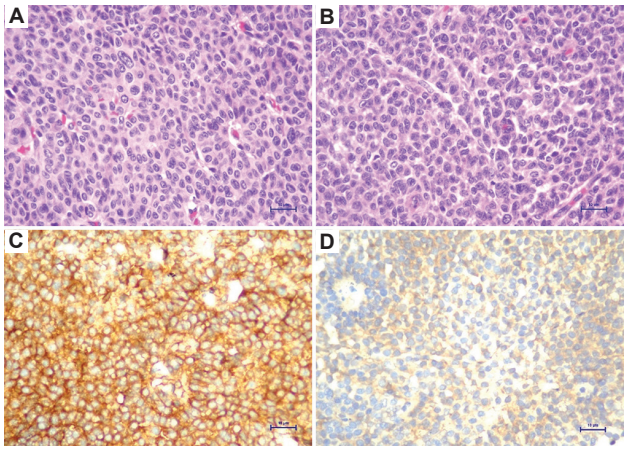

Figure 5. Histopathological and immunohistochemical findings. Depicts the microscopic features of the tumor tissue, which comprises cells with round to oval nucleic, some exhibiting notching, scant cytoplasm, frequent mitoses, and high cellularity. (A and B) The cells are arranged in clusters, cords, and exhibit areas suggestive of Call-Exner bodies, (magnification: ×400). (C) Immunohistochemical analysis revealed CD99 positivity (magnification: ×400) and (D) inhibin alpha positivity (magnification: ×400); the tumor cells were negative for cytokeratin, CD56, Wilms tumor 1, synaptophysin, myogenin, S100, calretinin, and epithelial membrane antigen.

The diagnosis was ovarian AGCT, with metastases to the liver, peritoneum, diaphragm, and omentum. The patient is currently recovering postoperatively and is expected to proceed with chemotherapy once her condition stabilizes.

3. Discussion

GCTs are rare neoplasms, often presenting with nonspecific or no obvious symptoms. Due to their rarity, most available research comprises case reports and retrospective studies, with no randomized clinical trials conducted to establish an optimal treatment regimen for this histopathological type.

GCTs exhibit a bimodal age distribution, with the highest incidence observed in postmenopausal women. The average age at diagnosis is approximately 50–55 years. Patients with GCTs may present with symptoms such as abdominal pain, bloating, self-detection of tumors, and menstrual irregularities. In some cases, the condition is asymptomatic.[1] In the present case, the patient was diagnosed at the age of 46 years and presented with prolonged menstrual bleeding, fatigue, and vaginal bleeding.

GCTs are classified into two types based on clinical and histopathological characteristics: juvenile and adult (AGCT). The present case is consistent with AGCT, which typically occurs in middle-aged women. This aligns with findings from Ayhan *et al.*,[4] who reported a median age of 47.6 years for adult CGT cases. The most common symptom noted in the study was abnormal uterine bleeding, observed in 53.7% of patients. Endometrial pathology is frequently identified in patients with GCTs, occurring in 51.2% of cases before surgery. Hyperplasia, found in 25–50% of cases, is a result of excess estrogen produced by the tumor. In addition, endometrial adenocarcinoma may coexist in 5–10% of GCTs. These adenocarcinomas are typically well-differentiated, diagnosed at early stages, and often associated with favorable outcomes.[1,5]

While the histopathological and immunoprofile features in the present case were typical of AGCT, molecular confirmation through *FOXL2* mutation testing was not performed. IHC plays a pivotal role in the diagnosis of AGCTs, particularly in distinguishing them from other sex cord-stromal tumors and epithelial ovarian neoplasms. The immunoprofile of AGCTs typically includes strong positivity for inhibin-α and CD99, with variable expression of calretinin, steroidogenic factor-1, and FOXL2. In contrast, AGCTs are generally negative for epithelial markers such as CK and EMA, as well as neuroendocrine and muscle markers such as synaptophysin, S100, desmin, and WT1. In the present case, the tumor was positive for inhibin and CD99, and negative for CK, WT1, CD56, synaptophysin, calretinin, and EMA—findings consistent with AGCT. While calretinin is frequently positive in AGCTs, its absence does not exclude the diagnosis when supported by classic histopathological and immunophenotypic features. This IHC panel, comprising

positive markers (inhibin and CD99) and negative markers (CK, WT1, CD56, synaptophysin, calretinin, and EMA), is essential to rule out differential diagnoses such as epithelial ovarian carcinoma, Sertoli–Leydig cell tumors, or neuroendocrine neoplasms.

One limitation of this case is the absence of *FOXL2* (C134W) mutation testing, which has become an important diagnostic adjunct in the evaluation of AGCTs. Although the histopathological and immunohistochemical features in our patient were classic and consistent with AGCT, *FOXL2* analysis could have provided molecular confirmation, especially in the context of recurrent disease. This mutation, located in exon 1 of the *FOXL2* gene, is highly specific to AGCT and has been validated in multiple studies as a reliable marker with both diagnostic and potential prognostic implications.[2,3] In resource-limited settings, as in our institution, *FOXL2* testing may not always be available. In recent years, FOXL2 IHC using validated antibodies—such as the rabbit polyclonal anti-FOXL2 (C134W) antibody developed by BioSB—has emerged as a practical alternative to DNA-based mutation analysis, particularly in recurrent or morphologically ambiguous tumors.[6] Moreover, circulating tumor DNA harboring *FOXL2* mutations has shown promise as a non-invasive biomarker for disease monitoring and early relapse detection in AGCT. These molecular advances highlight the evolving diagnostic landscape of AGCT and underscore the importance of integrating molecular tools into clinical practice whenever feasible.

Prognostic factors in GCT include tumor stage, patient age, tumor size, tumor rupture, cell division index, presence of residual disease, and degree of differentiation.[7] Research by Haltia *et al.*[8] provided insights into the biological characteristics of GCT, showing that follicle-stimulating hormone and estradiol may promote tumor growth through activation of endocrine signaling pathways, thereby increasing the risk of recurrence. This highlights the potential for hormone-modulating therapies as therapeutic or surveillance strategies. Aromatase inhibition, in particular, has shown promising outcomes as a treatment strategy.[9]

The recurrence rate of GCT generally increases with the disease stage. Evans *et al.*[10] found that only 9% of women with stage IA disease experienced tumor recurrence, compared to 30% for those with more advanced stages. Similarly, Ayhan *et al.*[4] reported recurrence rates of 5.4%, 21%, and 40% for stages I, II, and III, respectively. Further findings from Mangili *et al.*[7] revealed that recurrence in advanced stages (II–IV) occurred in 43% of patients within 5 years of diagnosis and 57% of cases between 5–10 years post-diagnosis. These findings highlight the critical importance of long-term follow-up in GCTs to monitor and manage the risk of recurrence.

In terms of tumor size, while some studies suggest a correlation—independent of disease stage—between large tumor (diameter >10–15 cm) and increased risk of recurrence and/or decreased progression-free survival (PFS),[11] others indicate that size loses prognostic significance when adjusted for stage.[4] Established adverse prognostic factors include advanced stage, incomplete surgical resection (R1/R2 resection), and elevated levels of serum biomarkers such as inhibin B and anti-Müllerian hormone.

Recurrence in GCTs typically occurs locally or within the peritoneal cavity. However, distant metastases to the lungs, liver, and brain have been reported in approximately 10% of cases.[12] This underscores the necessity of comprehensive surveillance strategies incorporating diagnostic imaging modalities such as CT and MRI.

Surgery is considered the first-line treatment for GCTs, as it provides accurate information about the initial severity of the disease, thereby identifying patients who may benefit from adjuvant interventions. A retrospective study conducted in 2014–2022 involving 44 patients with GCTs reported a 5-year overall survival rate of 90.9% and a 5-year DFS rate of 79.4%.[13] Disease stage and completeness of surgical resection are important prognostic factors; patients with stage I disease demonstrated a superior 5-year DFS compared to those with stage II–III disease (100% vs. 54.1%), while patients without residual lesions had a markedly better 5-year DFS than those with residual lesions (94.7% vs. 0%).[13] Consistent with other studies, non-radical surgery has been associated with poor outcomes and survival after surgery.[4,11] In the presented case, the tumor measured 7 × 6 × 5 cm and was associated with synchronous hepatic and peritoneal metastases at initial diagnosis, indicating advanced-stage disease and a high risk of recurrence. Consistent with the literature, the patient experienced disease recurrence after 3 years of treatment and periodic monitoring, highlighting the aggressive potential of advanced GCTs and the importance of long-term follow-up.

Adjuvant chemotherapy regimens commonly employed include bleomycin, etoposide, and cisplatin (BEP); etoposide/cisplatin; and paclitaxel with carboplatin (TC/PC).[1] The role of adjuvant radiation therapy remains controversial. Mangili *et al.*[7] reported an average recurrence interval of 53 months (ranging from 9 to 332 months), with the pelvis as the most frequent site of recurrence. Surgical resection may offer long-term disease control in cases of localized recurrence (*in situ* disease).[9] However, treatment becomes significantly more challenging in the setting of intraperitoneal dissemination or distant metastases. Pelvic or whole-abdominal radiotherapy may

be considered in patients with persistent or recurrent GCT, particularly following surgical debulking of peritoneal or pelvic recurrences.[1]

Platinum-based chemotherapy is the preferred systemic treatment for advanced-stage GCTs.[1] BEP is historically regarded as the standard regimen, supported by the Gynecologic Oncology Group (GOG) phase II trial.[14] The overall response rates to different combination chemotherapy regimens in advanced or recurrent ovarian GCTs are reported to range from 50% to 92%.[15] However, BEP carries substantial toxicity—such as bleomycin-induced pulmonary fibrosis, nephrotoxicity, and neurotoxicity—making it less suitable for older patients or those with comorbidities.

Alternative regimens, such as TC/PC, cyclophosphamide, and other taxane-based combinations, have been shown to offer improved tolerability with encouraging efficacy in recent reports.[11,16-18] Retrospective data from the MITO-9 study demonstrated that taxane-based regimens, including TC/PC, showed promising efficacy with improved tolerability in recurrent AGCT.[7] Moreover, a recent randomized phase II trial conducted by NRG Oncology (GOG-0264) found TC/PC demonstrating non-inferior efficacy and better tolerability compared to BEP in patients with sex cord-stromal tumors—including AGCT.[19] The National Comprehensive Cancer Network recommends taxane-based regimens, with or without carboplatin, for recurrent GCTs. The cisplatin, vinblastine, and bleomycin (PVB) regimen, investigated in a European Organisation for Research and Treatment of Cancer trial,[16] is another alternative. However, despite favorable initial response rates, the PVB regimen was associated with limited PFS and significant toxicity.

In our practice, treatment strategies and surveillance protocols are individualized following surgical intervention, based on a comprehensive clinical status. In the present case, TC/PC was chosen to balance therapeutic efficacy and long-term tolerability. This choice is supported by evolving clinical evidence and may be appropriate for selected patients who are not suitable candidates for intensive regimens such as BEP. The limited institutional access to certain BEP components was another reason for the choice.

This case adds to the current understanding of AGCTs by highlighting several clinically relevant insights. First, it underscores the potential for late recurrence—even after prolonged remission—reinforcing the need for lifelong surveillance. Second, the successful application of secondary cytoreductive surgery in our patient emphasizes the continued role of surgical resection in managing localized or symptomatic relapse. Third, the case reflects the growing role of individualized treatment decisions, balancing efficacy, tolerability, and resource availability. Finally, the absence of *FOXL2* mutation testing, despite classical histopathological features, highlights the ongoing challenges of applying molecular diagnostics in resource-limited settings and the growing importance of molecular profiling in this rare tumor type.

4. Conclusion

Ovarian GCT is a rare malignancy, typically diagnosed at an early stage, and primarily treated with comprehensive surgical staging and complete cytoreductive surgery. In recurrent cases, surgical intervention remains the most effective therapeutic approach, while the role of chemotherapy continues to evolve in the absence of randomized clinical trials. This case illustrates the indolent yet unpredictable clinical behavior of AGCT, emphasizing the need for long-term surveillance. The selection of an appropriate adjuvant chemotherapy regimen should be tailored based on the tumor's histopathological and molecular features, as well as the patient's tolerance and the safety profile of each regimen. The use of taxane–carboplatin in this case underscores its growing role as an effective and tolerable alternative to BEP. The lack of *FOXL2* molecular testing in this context underscores the importance of expanding access to molecular diagnostics, which are increasingly relevant for prognostication and therapeutic decision-making in this rare tumor.

Acknowledgments

The authors gratefully acknowledge the patient for her participation. We also thank our colleagues and nursing staff, whose dedication contributed to the successful management of this patient.

Funding

None.

Conflict of interest

Phuong Pham Cam is an Editorial Board Member of this journal, but was not in any way involved in the editorial and peer-review process conducted for this paper, directly or indirectly. Separately, other authors declared that they have no known competing financial interests or personal relationships that could have influenced the work reported in this paper.

Author contributions

Conceptualization: Phuong Pham Cam, Huyen Tong Thi
Investigation: All authors
Writing–original draft: All authors
Writing–review & editing: Phuong Pham Cam

Ethics approval and consent to participate

This study was approved by the Ethics Committee of Bach Mai Hospital (Approval No.18/BM-HĐĐĐ). Written informed consent was obtained from the patient.

Consent for publication

Informed consent was obtained from the patient for publishing her data.

Availability of data

Data is available from the corresponding author upon reasonable request.

References

1. Schumer ST, Cannistra SA. Granulosa cell tumor of the ovary. *J Clin Oncol*. 2003;21(6):1180-1189.

   doi: 10.1200/JCO.2003.10.019

2. Shah SP Köbel M, Senz J, *et al*. Mutation of FOXL2 in granulosa-cell tumors of the ovary. *N Engl J Med*. 2009;360(26):2719-2729.

   doi: 10.1056/NEJMoa0902542

3. Jamieson S, Butzow R, Andersson N, *et al*. The FOXL2 C134W mutation is characteristic of adult granulosa cell tumors of the ovary. *Mod Pathol*. 2010;23(11):1477-1485

   doi: 10.1038/modpathol.2010.145

4. Ayhan A, Salman MC, Velipasaoglu M, Sakinci M, Yuce K. Prognostic factors in adult granulosa cell tumors of the ovary: A retrospective analysis of 80 cases. *J Gynecol Oncol*. 2009;20(3):158-163.

   doi: 10.3802/jgo.2009.20.3.158

5. Sehouli J, Drescher FS, Mustea A, *et al*. Granulosa cell tumor of the ovary: 10 years follow-up data of 65 patients. *Anticancer Res*. 2004;24(2C):1223-1229.

6. BioSB Inc. *FOXL2 [C134W] Rabbit Polyclonal Antibody - RPAB*. 2025. Available from: https://www.biosb.com/biosb-products/foxl2-antibody-rpab/[Last accessed on 2025 Aug 28].

7. Mangili G, Ottolina J, Gadducci A, *et al*. Long-term follow-up is crucial after treatment for granulosa cell tumours of the ovary. *Br J Cancer*. 2013;109(1):29-34.

   doi: 10.1038/bjc.2013.241

8. Haltia UM, Pihlajoki M, Andersson N, *et al*. Functional profiling of FSH and estradiol in ovarian granulosa cell tumors. *J Endocr Soc*. 2020;4(4):bvaa034.

   doi: 10.1210/jendso/bvaa034

9. Korach J, Perri T, Beiner M, Davidzon T, Fridman E, Ben-Baruch G. Promising effect of aromatase inhibitors on recurrent granulosa cell tumors. *Int J Gynecol Cancer*. 2009;19(5):830-833.

   doi: 10.1111/IGC.0b013e3181a261d7

10. Evans AT 3rd, Gaffey TA, Malkasian GD Jr., Annegers JF. Clinicopathologic review of 118 granulosa and 82 theca cell tumors. *Obstet Gynecol*. 1980;55(2):231-238.

11. Uygun K, Aydiner A, Saip P, *et al*. Clinical parameters and treatment results in recurrent granulosa cell tumor of the ovary. *Gynecol Oncol*. 2003;88(3):400-403.

    doi: 10.1016/S0090-8258(02)00141-5

12. Homesley HD, Bundy BN, Hurteau JA, Roth LM. Bleomycin, etoposide, and cisplatin combination therapy of ovarian granulosa cell tumors and other stromal malignancies: A Gynecologic Oncology Group study. *Gynecol Oncol*. 1999;72(2):131-137.

    doi: 10.1006/gyno.1998.5304

13. Thieu TK, Nguyen VT, Nguyen TTH, Nguyen QA. Treatment results of granuloblastic ovarian cancer at K Hospital. *Vietnam Med J*. 2024;536(2):42-46.

    doi: 10.51298/vmj.v536i2.8872

14. Autier P, Lhomme C, Culine S, *et al*. Adult granulosa-cell tumor of the ovary: A retrospective study of 45 cases. *Int J Gynecol Cancer*. 1997;7(1):58-65.

    doi: 10.1046/j.1525-1438.1997.00417.x

15. Al-Badawi IA, Brasher PMA, Ghatage P, Nation JG, Schepansky A, Stuart GCE. Postoperative chemotherapy in advanced ovarian granulosa cell tumors. *Int J Gynecol Cancer*. 2002;12(2):119-123.

    doi: 10.1046/j.1525-1438.2002.01067.x

16. Brown J, Sood AK, Deavers MT, Milojevic L, Gershenson DM. Patterns of metastasis in sex cord-stromal tumors of the ovary: Can routine staging lymphadenectomy be omitted? *Gynecol Oncol*. 2009;113(1):86-90.

    doi: 10.1016/j.ygyno.2008.12.007

17. Brown J, Shvartsman HS, Deavers MT, *et al*. The activity of taxanes compared with bleomycin, etoposide, and cisplatin in the treatment of sex cord-stromal ovarian tumors. *Gynecol Oncol*. 2005;97(2):489-496.

    doi: 10.1016/j.ygyno.2005.01.011

18. Chiara S, Merlini L, Campora E, *et al*. Cisplatin-based chemotherapy in recurrent or high-risk ovarian granulosa-cell tumor patients. *Eur J Gynaecol Oncol*. 1993;14(4):314-317.

19. Ray-Coquard I, Oaknin A, Pautier P, *et al*. Paclitaxel-carboplatin compared with bleomycin, etoposide, and cisplatin (BEP) for sex cord-stromal tumors of the ovary: A randomized, phase 2, non-inferiority trial. *J Clin Oncol*. 2024;42(18 Suppl):LBA5506.

    doi: 10.1200/JCO.2024.42.18_suppl.LBA5506

Our Journals

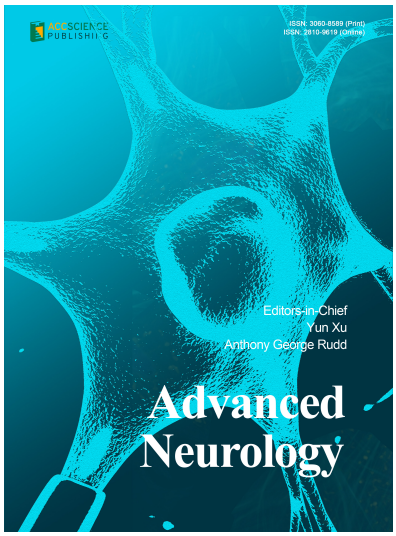

Advanced Neurology is a peer-reviewed and open-access journal that aims to publish and disseminate novel research in the breadth of neurology and neuroscience. The journal aims to advance our understanding in the nervous system and provide a platform to neuroscientists and physicians to showcase their findings in original fundamental and clinical research as well as to present new ideas that highlight the changes in the neurological clinical practice.

Advanced Neurology covers subject areas, including but not limited to the following:

- Neurological disorders
- Neurodegenerative disease
- Cerebrovascular disease
- Epilepsy and movement disorders
- Neuroimmune disease
- Neurological infections
- Muscle disease
- Molecular and cellular neuroscience
- Systems neuroscience
- Cognitive neuroscience
- Computational modeling of nervous system

Global Translational Medicine is a quarterly journal that focuses on medicine, biological sciences, and biomaterials engineering. The goal of *Global Translational Medicine* is to provide a platform to researchers for showcasing their latest research works in translational medicine so as to advance the field towards the betterment of human health. Despite the advancement of omics and new technologies, the process of transforming these technologies and scientific research results into effective therapies and putting them into clinical use still has a long way to go. *Global Translational Medicine* provides a platform to fill the gaps in preclinical and inter-disciplinary research, to promote clinical translation of scientific research results, and to contribute to the conception of new and improved preventive measures as well as diagnostic and therapeutic techniques of diseases.

Global Translational Medicine covers the following themes: cardiovascular disease, metabolism/diabetes/obesity, neuroscience/neurology, cancer, biomaterials and their applications in medicine, proteomics/metabolomics, pharmacogenomics, biomarkers, bioinformatics and data mining, animal and clinical research, and medical methods arising from interdisciplinary crossover.

Start a new journal

Write to us via email if you are interested to start a new journal with AccScience Publishing. Please attach your CV, professional profile page and a brief pitch proposal in your email. We shall inform you of our decision whether we are interested to collaborate in starting a new journal.

Contact: info@accscience.com

https://accscience.com/journal/ARNM

Contact
www.accscience.com
9 Raffles Place, Republic Plaza 1 #06-00 Singapore 048619
Email: editorial@accscience.com
Phone: +65 8182 1586